Master's thesis

2019

Kristoffer Knoph Aamodt

Master's thesis

NTNU
Norwegian University of
Science and Technology
Faculty of Engineering
Department of Civil and Environmental Engineering

NTNU
Norwegian University of
Science and Technology

Kristoffer Knoph Aamodt

Soil reaction curves and damping for monopile design in clay

June 2019

NTNU
Norwegian University of
Science and Technology

NTNU
Norwegian University of
Science and Technology

Soil reaction curves and damping for monopile design in clay

Kristoffer Knoph Aamodt

Geotechnics
Submission date: June 2019
Supervisor: Steinar Nordal, IBM
Co-supervisor: Youhu Zhang, NGI

Norwegian University of Science and Technology
Department of Civil and Environmental Engineering

Abstract

Monopiles are the predominant foundation solution for offshore wind turbines. Due to much smaller *length to diameter ratio (L/D)* compared to conventional piles used in the offshore oil and gas industry, the soil mechanisms mobilized by a monopile under lateral loading are different from those by a slender pile. This has initiated large scale research projects such as the PISA project, which confirmed that the soil reaction curves used for slender pile design (e.g. API) are unsatisfactory and highlighted the need for the soil reaction curves to be calibrated against *finite element analyses (FEA)*.

To address this need, an optimization tool for calibrating site-specific soil reaction curves has been developed in this study. The optimization tool calibrates the reaction curves by scaling the lateral reaction springs (*p-y*), to replicate a target (commonly FEA) pile response. The generality and robustness of the tool is validated through various exercises.

In recent years, the offshore wind industry has seen rapid development in Asia, where soft clays and layered clay profiles are commonly encountered. Noting that most of research on monopile design has been focused on stiff over-consolidated clays in the past, this study investigates the soil reaction curves for monopile design in soft clays and layered profiles. The performance of a proposed multi-spring beam-column framework is tested against a comprehensive parametric finite element analysis. The tested soil strength profiles included normally consolidated clay to lightly over-consolidated clays, and layered profile where a normally consolidated clay is underlain by a more competent over-consolidated clay layer. Four pile geometries were tested, with a length over diameter ratio ranging from 3 to 10. The multi-spring model gave a good match when simulating the longer monopiles (*L/D* of 7 and 10) in all soil profiles. Whereas for the shorter piles (*L/D* of 3 and 5) the proposed framework predicts generally softer response than predicted by FEA. The optimization tool was utilized to investigate the corrections needed. The analyses showed that the accuracy of the predicted monopile response in the soft clay was significantly increased by a simple scaling factor of the displacement variable (*y*) in the *p-y* springs. The scaling factor was found to be more sensitive to the stress-strain behavior of the soil than to the shear strength or monopile geometry. For the layered soil profiles, the only pile geometry noticeably affected by the layering effect was the pile with an *L/D*-ratio of 5, embedded 60% into a stiffer bottom layer. Analyses of the calculated stiffness corrections showed that the weaker upper soil layer experienced an increase in strength, as opposite to the stronger lower soil layer, which experienced a reduction in strength capacity.

The hypothesis of a scaling relationship between the soil damping at element level and at the soil-pile level was tested by comparing the damping calculated by FEA for a horizontal pile slice with the corresponding soil damping curve. Eight different sets of stiffness reduction (stress-strain) and damping curves covering various over consolidation ratios and plasticity indexes, were examined in FEA. The FEA confirms a scaling relationship between soil damping at element level and the soil-pile interaction level. For the same damping ratio, the *normalized pile displacement* (*y/D*) can be scaled from the corresponding shear strain by a factor of 3.3.

Sammendrag

Monopeler er den mest brukte fundamenteringen for havbaserte vindturbiner. En monopel kjennetegnes ved at den har kortere *lengde i forhold til diameter (L/D),* sett i sammenheng med konvensjonelle slanke peler brukt i olje- og gassindustrien. Følgelig er jordmekanismen ved sideveis lasting av monopeler annerledes enn hva som er erfart ved slanke peler. Dette har ført til store forskningsprosjekter slik som PISA prosjektet, som fastslo at reaksjonsfjærene som brukes for å designe slanke peler (for eksempel API) er utilstrekkelige ved dimensjonering av monopeler. Prosjektet trakk også frem behovet for at reaksjonsfjærene blir kalibrert mot analyse utført ved bruk av elementmetoden.

For å imøtekomme dette behovet er det innen denne oppgaven blitt utviklet et optimaliseringsverktøy for å kalibrere reaksjonsfjærer mot stedsspesifikke grunndata. Optimaliseringsverktøyet kalibrerer reaksjonsresponsen fra jorden ved å skalere de laterale reaksjonsfjærene (*p-y*). Ved diverse optimaliseringsoppgaver er generaliteten og allsidigheten til verktøyet bekreftet.

I løpet av de siste årene har offshore vind-bransjen hatt rask utvikling, særlig i Asia. Der består mye av grunnforholdene av svak leire og lagdelte leirprofiler. Som følge av at mesteparten av monopel-forskningen hittil har satt lys på stiv over-konsolidert leire, vil denne oppgaven fokusere på monopel-responsen i svakere og bløtere leire, samt lagdelte leirprofiler. Ytelsen av et foreslått designverktøy bestående av reaksjonsfjærer som beskriver monopelresponsen ved hjelp av bjelketeori er testet mot en omfattende parametrisk analyse utført ved elementmetoden. De simulerte jordprofilene inkluderte styrkeprofiler med normal konsolidert til lett over-konsolidert styrke. Lagdelte leirprofiler, der et normal konsolidert leirlag lå over et stivere over-konsolidert lag ble også testet. Fire pel geometrier ble testet, med et lengde-diameter-forhold varierende mellom 3 og 10. Det foreslåtte designverktøyet ga gode resultater for de lengre monopelene (*L/D* lik 7 og 10). Mens for de kortere pelene (*L/D* lik 3 og 5) ga design-verktøyet generelt en for stor deformasjonsrespons. Optimaliseringsverktøyet ble benyttet for å undersøke hvilke korreksjoner som trengs. Analysene viste at nøyaktigheten i deformasjonsresponsen økte signifikant ved en enkel konstant skaleringsfaktor for forskyvningsvariablen (*y*) i *p-y* fjærene. Skaleringsfaktoren var mer følsom for spenning-tøyningsoppførselen til jorda enn til skjærstyrken eller pel geometrien. For de lagdelte leirprofilene var den eneste pel geometrien som ble merkbart påvirket, pelen med *L/D*-faktor lik 5, med 60% forankret i det stivere bunnlaget. Analyser utført ved bruk av optimaliseringsverktøyet viste at det svakere øvre leirlaget opplevde en økning i styrke, i motsetning til det sterkere nedre leirlaget, som opplevde en reduksjon i styrkekapasitet.

Hypotesen om at det eksisterer et skaleringsforhold mellom jorddempingen på elementnivå og jord-pel nivå ble testet ved å sammenligne dempningen kalkulert ved elementmetoden for et horisontalt stykke av en pel-modell med den tilsvarende jorddempingen. Åtte forskjellige jordprofiler, med forskjellige *over konsoliderings forhold (OCR)* og plastisitetsindekser ble testet i en elementmetode modell. Resultatene bekrefter at det finnes et skaleringsforhold mellom jorddempingen på elementnivå og for jord-pel nivå. For likt dempningsforhold kan den normaliserte pelforskyvningen (*y/D)* bli skalert fra den tilsvarende skjærtøyningen med en faktor på 3.3.

Preface

This master thesis is submitted for the fulfillment of the Master of Science degree in Civil and Environmental Engineering at NTNU within the field of geotechnical engineering. The thesis has been written during the spring semester, 2019, between January and June. In this study, the monopile response in soft clay and layered clay profiles has been investigated using finite element modelling and a multi-spring beam-column model.

The idea for the thematic of this thesis resulted from an internship at NGI in the summer 2018. A specialization project conducted during the autumn 2018 provided the basis for this work. The idea behind the study was raised by Dr. Youhu Zhang at NGI.

Trondheim, 2019

Kristoffer Knoph Aamodt

Acknowledgment

I would like to express my utmost gratitude to my external supervisor Dr. Youhu Zhang at NGI for his constant support, motivation and encouragement over the duration of the thesis, despite his busy schedule. I am grateful for the support and guidance provided by Prof. Amir M. Kaynia and Dr. Jung Chan Choi at NGI. I which to acknowledge the efforts of Prof. Steinar Nordal at NTNU for doing all the administrative work regarding this thesis.

I would also like to thank my friends and family for their continual support and reassurance during my years at NTNU.

Table of Contents

List of Figures xvii

List of Tables xxi

Nomenclature xxiii

1 Introduction 25

1.1 Background 25

1.2 Objectives 26

1.3 Limitations 27

1.4 Structure of the Thesis 27

2 Theoretical foundation 29

2.1 Pile design under lateral loading 29

2.1.1 p-y method 30

2.1.2 API 30

2.1.3 Finite Element Analysis 31

2.2 Soil failure mechanism 31

2.2.1 Wedge failure 31

2.2.2 Plane strain flow-around 32

2.2.3 Rotational mechanism 33

2.3 Ultimate lateral bearing capacity in clay 34

2.3.1 Murff and Hamilton (1993) 35

2.3.2 Jeanjean (2009) 35

2.3.3 Nichols et al. (2014) 36

2.3.4 Zhang et al. (2016) 36

2.4 p-y curves for monopiles 37

2.4.1 Zhang and Andersen (2017) 37

2.4.2 Zhang and Andersen (2019a) 38

2.4.3 A multi-spring model for monopile analysis in soft clays 40

2.4.4 PISA 41

2.5 Layered soil profile 44

2.6 Damping 45

2.6.1 Equation of motion 45

2.6.2 Hysteretic damping 46

2.6.3 Damping ratio, D 46

2.6.4 Darendeli damping curves 47

2.6.5 Estimation of Darendeli Damping variables 48

3 Optimization tool 49

3.1 Methodology 49

3.1.1 Running the tool 50

3.1.2 Implementation of *p*-*y* formulations 52

3.1.3 Iteration procedure 52

3.2 Validation 56

3.2.1 Pile variation 57

3.2.2 Soil strength variation 64

3.2.3 API approach 70

3.3 Summary 77

3.4 Terminology 77

4 Pile response in soft clays and layered clay profiles 79

4.1 Introduction 79

4.2 Multi-spring beam-column model 79

4.3 Finite element model 80

4.3.1 Geometry and meshing 80

4.3.2 Pile geometry 83

4.3.3 Soil model 83

4.3.4 Validation 85

4.4 Methodology 86

4.5 Results 87

4.6 Discussion 94

4.6.1 Performance of the multi-spring model 94

4.6.2 Monopile analyses using the optimization tool 95

4.6.2.1 Normally consolidated clay 96

4.6.2.2 Layered clay profile 97

5 Pile damping 99

5.1 Introduction 99

5.2 Assumption 99

5.3 Finite Element Model 100

5.3.1 Geometry and meshing 100

5.3.2 Soil model 102

5.3.3 Pile damping 105

5.4 Results 106

5.5 Conclusions 112

6 Conclusions and recommendation for further work 113

6.1 Conclusions 113

6.2 Recommendations for further work 113

References 115
Appendices 117

List of Figures

Figure 1.1: Definition of wind turbine components. From DNVGL-ST-0126 (DNVGL, 2018). 26

Figure 2.1 Representation of the shear force H, and lateral resistance p, at different load levels reaching the ultimate lateral bearing capacity (c). Salgado (2008), figure 13-31. 29

Figure 2.2: Modeling the soil-pile system using Winkler springs. Nonlinear springs described by *p-y curves* are used to model the deflected pile shape. From Salgado (2008), figure 13-34. 30

Figure 2.3 (a): Soil deformation mechanism. (b): The conical wedge as seen from above the soil surface. From Murff and Hamilton (1993). 32

Figure 2.4 (a): Flow-around mechanism for a smooth pile (ɑ=0). (b): Flow-around mechanism for a fully rough pile (ɑ=1). From Randolph and Houlsby (1984). 33

Figure 2.5 (a): Typical soil failure mechanisms for a slender pile. (b): Failure mechanisms for a monopile with no plane strain flow-around failure and no tension gap at the rear side. Notice that by pile friction the wedges should have a more curved shape then illustrated. From Zhang and Andersen (2019a). 34

Figure 2.6: Wind farms in the Irish Sea, North Sea and the Baltic Sea, as per 14.10.18. From 4coffshore (2018). 35

Figure 2.7: Illustration of proposed p-y model for calculating the flow-around soil response. From Zhang and Andersen (2017). 37

Figure 2.8: Visualized terminology for proposed framework model by Zhang and Andersen (2019a). 40

Figure 2.9: Illustration of the proposed m-r model for calculation of the spring response. From Zhang (2019b). 41

Figure 2.10: Framework for the proposed finite element model for monopile foundations. Note that displacement y is denoted as v. From Byrne et al. (2015a). 42

Figure 2.11: A distributed moment is included as a function of the vertical shear stress action on the pile surface. From Byrne et al. (2015a). 42

Figure 2.12: Analysis procedure presented by the PISA project. From Byrne et al. (2017). 43

Figure 2.13: A mass-spring damper system. From the Norwegian Geotechnical Institute (NGI). 45

Figure 2.14 (A): Mobilized damping and elastic force for one hysteretic loop. (B): Definition of dissipated energy$\boldsymbol{ED}$ and potential energy $\boldsymbol{ES0}$. From NGI. 46

Figure 2.15: Visualization of the definition of the reference strain, $\boldsymbol{\gamma r}$ at the stiffness reduction curve. Note that G_0 is denoted G_{max}. From Darendeli (2001), figure 6.1. 47

Figure 3.1: Target pile response, for load level H=486 kN for Pile 2, described in section 3.2.1. The target pile responses for load levels H=1098 kN and H=3711 kN are also used as input and has similar spreadsheets. 50

Figure 3.2: Calculated *p*- and *y*-modifiers for the different load levels, along with the optimal (average) modifiers. The upper 30 meters are above mudline. 51

Figure 3.3: Cross-sectional rotation response at the applied load levels. "py with mod" and "py no mod" are the rotation responses with/without modifiers applied calculated by reaction springs. 51

Figure 3.4: Flow chart of the iteration process for the p-modifier for one spring. The same principles are conducted when iterating for the y-modifier. 54

Figure 3.5: The iteration process started at the lower limit with a modification value equal to 0.5, then halving it to 0.75, until it converged toward an optimal modifier value

equal to 1. Hence, the tool applied the upper modifier value equal to 1.5. Following the same halving principle, the solution converged towards 1.0737, and 1.000244 for the p- and y-modifier respectively. NB: To get a better visualization of the iteration process, the iteration started at the lower limit, as opposite of the description above. 56
Figure 3.6: The displacement of pile 1 with and without modifiers and the FEA calculated displacement for three different load levels. 58
Figure 3.7: The modifiers for each load level are calculated separately. The final modifiers are calculated as the average value of the modifiers for each load level, presented as the solid black line. 59
Figure 3.8: Bending moment with and without modifiers, compared to FEA for pile 3. A reduction in accuracy is observed. 60
Figure 3.9: The average change of error for pile 3. An increase in precision is observed at the top 15 meters of the pile below mudline (node 60), thus keeping the calculated spring modifiers at top constant. 61
Figure 3.10: The average change in error for the load levels, when optimizing for all four minimizing variables for pile 1. The bars show the change in error, while the solid lines are the optimal solution for that specific variable corresponding to the same color. 64
Figure 3.11: Assumed strength profile for Cowden test site (Zhang & Andersen, 2019a). 65
Figure 3.12: Cross-sectional rotation of the PISA field pile and the pile response calculated from reaction curves. Please note that the legend wrongfully says that the solid line is FEA Results. The solid line is the field test data......................................66
Figure 3.13: The average change in error for each node/spring of the pile. Note at the mudline and pile bottom, there are no rotation data which led to the gaps in the plot. ..66
Figure 3.14: Bending moment response. Please note that the legend wrongfully says that the solid line is FEA Results. The solid line is the field test data. 67
Figure 3.15: The average change of error. An increase of error prediction is observed at the top 3 meters below mudline (Node 50-65). 68
Figure 3.16 left: Cross-sectional rotation of the pile with and without the modifiers applied. Right: Bending moment of the pile with and without the modifiers applied. Please note that the legend wrongfully says that the solid line is FEA Results. The solid line is the field test data. 69
Figure 3.17: The average change in error for the different load levels, when optimizing for both cross-sectional rotation and bending moment. The bars show the change in error. The solid lines are the optimal solution for that specific variable corresponding to the same color. 69
Figure 3.18: Pile response when minimizing for lateral displacement. 71
Figure 3.19: p- and y-modifiers applied at the stiffness springs. 71
Figure 3.20: Shear force, with and without modifiers. 72
Figure 3.21: Bending moment, with and without modifiers applied. 73
Figure 3.22: The average change in error for each node when minimizing with respect to bending moment. 73
Figure 3.23: Cross-sectional rotation, with and without modifiers applied compared to FEA. Note that the x-axis is plotted in log-scale for a better visualization of the results. 74
Figure 3.24: Shear force response, with and without modifiers applied compared to FEA when minimizing all variables..75
Figure 3.25: Bending moment response, with and without modifiers applied compared to FEA when minimizing all variables. 76

Figure 3.26: The average change in error for the different load levels, when optimizing for all four variables. The bars show the change in error, while the solid lines are the optimal solution for that specific variable, corresponding to the same color. 76
Figure 4.1: Scaling principle for the p-y spring. From Zhang and Andersen (2017). 79
Figure 4.2: Meshing and geometry of the Abaqus model in single-layered soil profiles, L/D = 5. 81
Figure 4.3: Meshing in double-layered soil profiles, L/D = 5. 81
Figure 4.4: Details of the refined mesh area within a radius of 2*D* from the pile. 82
Figure 4.5: Details of the meshing for the transition between pile and soil. 82
Figure 4.6 Pile response comparison for soil profile 5, L/D=10, γfp=0.02 (Appendix A.5.7). 85
Figure 4.7 Pile response comparison for soil profile 5, L/D=10, γfp=0.10 (Appendix A.5.8). 85
Figure 4.8: The soil displacement at failure presented in an undeformed model, without the pile visualized. L/D = 7, soil profile 1, γfp= 0.02. 86
Figure 4.9: Model at failure, showing the displacement. L/D = 7, soil profile 1, γfp= 0.02 87
Figure 4.10: Comparison of lateral pile displacement for pile with an L/D-ratio of 3: (a) soil profile 1; (b) soil profile 2; (c) soil profile 3; (d) soil profile 4. γfp= 0.02 for all soil profiles. The legend wrongfully says “py-calculated”. The pile responses are calculated using the aforementioned multi-spring beam-column model. 88
Figure 4.11: Comparison of lateral pile displacement for pile with an L/D-ratio of 5: (a) soil profile 1; (b) soil profile 2; (c) soil profile 3; (d) soil profile 4. γfp= 0.02 for all soil profiles. The legend wrongfully says “py-calculated”. The pile responses are calculated using the aforementioned multi-spring beam-column model. 89
Figure 4.12: Comparison of lateral pile displacement for pile with an L/D-ratio of 7: (a) soil profile 1; (b) soil profile 2; (c) soil profile 3; (d) soil profile 4. γfp= 0.02 for all soil profiles. The legend wrongfully says “py-calculated”. The pile responses are calculated using the aforementioned multi-spring beam-column model. 90
Figure 4.13: Comparison of lateral pile displacement for pile with an L/D-ratio of 10: (a) soil profile 1; (b) soil profile 2; (c) soil profile 3; (d) soil profile 4. γfp= 0.02 for all soil profiles. The legend wrongfully says “py-calculated”. The pile responses are calculated using the aforementioned multi-spring beam-column model. 91
Figure 4.14: L/D = 10, γfp= 0.02, soil profile 4. Soil stresses mobilized at failure. 92
Figure 4.15: Pile deformation response with/without the soft NC layer. L/D=10, γfp=0.02. 92
Figure 4.16: Predicted deformation using the optimized stiffness springs. Soil profile 1, L/D = 5, γfp= 0.02. The legend wrongfully says “py-calculated”. The pile responses are calculated using the aforementioned multi-spring beam-column model. 93
Figure 4.17: Stiffness spring modifiers applied. 94
Figure 4.18: Average y-modifiers for the normally consolidated clay profile. 96
Figure 4.19: Average p- and y-modifiers for the layered soil profiles, with 60% of the pile embedded into the stiffer bottom soil layer (L/D = 5). The plastic failure strain is denoted as gfp. 97
Figure 5.1: Damping scaling concept. 100
Figure 5.2: Representative horizontal slice of a pile embedded into the ground. 100
Figure 5.3: Geometry of the PLAXIS model. D is the pile diameter. 101
Figure 5.4: Localized flow around mechanism at failure. 101
Figure 5.5: Normalized stiffness reduction curves with an OCR of 1. 102
Figure 5.6: Estimated damping ratio. OCR = 1. 103

Figure 5.7: Normalized stiffness reduction curves with an OCR of 40........................103
Figure 5.8: Estimated damping ratio. OCR = 40. 104
Figure 5.9: Stress-strain comparison between the Darendeli model and the NGI-ADP soil model. 105
Figure 5.10: p-y response predicted by the FE-model along the p-y curves constructed from the stress-strain curves by Zhang and Andersen (2017). 106
Figure 5.11: Back-calculated scaling factor for four different soil profiles with OCR=1 at different displacement levels. Note that the x-axis is log-scaled. 107
Figure 5.12: Back-calculated scaling factor for four different soil profiles with OCR=40 at different displacement levels. Note that the x-axis is log-scaled. 107
Figure 5.13: Estimated pile damping by scaling the soil damping. OCR=1, I_P=10%. ...108
Figure 5.14: Estimated pile damping by scaling the soil damping. OCR=1, I_P=20%. ...109
Figure 5.15: Estimated pile damping by scaling the soil damping. OCR=1, I_P=40%. ...109
Figure 5.16: Estimated pile damping by scaling the soil damping. OCR=1, I_P=60%. ...110
Figure 5.17: Estimated pile damping by scaling the soil damping. OCR=40, I_P=10%...110
Figure 5.18: Estimated pile damping by scaling the soil damping. OCR=40, I_P=20%...111
Figure 5.19: Estimated pile damping by scaling the soil damping. OCR=40, I_P=40%...111
Figure 5.20: Estimated pile damping by scaling the soil damping. OCR=40, I_P=60%...112

List of Tables

Table 2.1: Proposed shear strength of anisotropic clay profiles by Zhang et al. (2016). .37
Table 2.2: Model parameters presented for “Clays”. From Darendeli (2001), Table 8.11. 48
Table 3.1: Soil properties. 57
Table 3.2: Pile geometries used for validation. 58
Table 3.3: Error reduction when minimizing with respect to displacement. 58
Table 3.4: Error reduction when minimizing with respect to shear force. 59
Table 3.5: Error reduction when minimizing with respect to bending moment. 60
Table 3.6: Error reduction when minimizing with respect to cross-sectional rotation. 61
Table 3.7: Error reduction for pile 1 when minimizing with respect to all variables. 62
Table 3.8: Error reduction for pile 2 when minimizing with respect to all variables. 62
Table 3.9: Error reduction for pile 3 when minimizing with respect to all variables. 63
Table 3.10: Soil properties. 65
Table 3.11: Pile geometry. 65
Table 3.12: Error reduction when minimizing with respect to rotation. 65
Table 3.13: Error reduction when minimizing with respect to bending moment. 67
Table 3.14: Error reduction when minimizing with respect to all variables. 68
Table 3.15: Soil parameters. 70
Table 3.16: Error reduction when minimizing with respect to displacement. 70
Table 3.17: Error reduction when minimizing with respect to shear force. 72
Table 3.18: Error reduction when minimizing with respect to bending moment. 72
Table 3.19: Error reduction when minimizing with respect to rotation. 74
Table 3.20: Error reduction when minimizing with respect to all variables. 75
Table 4.1: Summary of the multi-spring beam-column model. 80
Table 4.2: Pile geometries. 83
Table 4.3: Strength profiles used for testing. 84

Nomenclature

Latin Symbols

d	Damping factor
D	Diameter
E	Error function
E_{displ}	Displacement error
E_{rot}	Cross-sectional rotation error
E_{SF}	Shear force error
E_{BM}	Bending moment error
E_D	Dissipated energy
E_{S0}	Potential energy
EI	Bending stiffness
f	Loading frequency
G	Shear modulus
G_0	Initial shear modulus
I_P	Plasticity index
J	empirical API parameter
L	Pile length below mudline
m	Moment
m-r	Moment rotation spring
N	Number of loading cycles
N_p	Bearing capacity factor
N_{pd}	Ultimate bearing capacity factor
p	Resistance
p_{mod}	Spring modifier for the p-response
p_u	Ultimate soil resistance
p-y	Lateral reaction spring
r	Rotation
s	Shear force at pile tip
S_u	Shear strength
s-u	Base shear resistance spring
u	Lateral displacement of pile tip
y	Lateral displacement
y_{mod}	Spring modifier for the y-response

Greek Symbols

α	Pile interface roughness
γ	Shear strain
γ'	Effective unit weight
γ^e	Elastic shear strain
γ^p	Plastic shear strain
γ_f^p	Plastic shear strain at failure
ε_{50}	API parameter
ζ	Damping ratio
ξ	Scaling factor
σ_0'	Pre-consolidation stress
τ	Shear stress

Abbreviations

API	American Petroleum Institute
CPT	Cone Penetration Test
DSS	Direct Simple Shear Strength
FEA	Finite Element Analysis
OC	Over-Consolidated
OCR	Over Consolidation Ratio
NC	Normally Consolidated
NGI	Norwegian Geotechnical Institute
PISA	Pile Soil Analysis Project

1 Introduction

1.1 Background

2018 saw the continuing of the decade-long trend of strong growth in renewable energy sector, which contributed to a third of the added global power generation capacity. This increase was mainly due to new additions from solar and wind energy, which accounted for 84% of the growth (IRENA, 2019). Norwegian Energy Partners (NORWEP) estimated that by 2023 the capacity of the global installed offshore wind to be at 61.3 GW, where the European and Asian market would produce approximately 57% and 39% respectively (NORWEP, 2018). Between the end of 2018 and the end of 2022, the Asian market is expected to increase its capacity from 4.9 GW to 23.9 GW. China is estimated to be the largest contributor, with 55% of the Asian market share.

As Figure 1.1 visualizes, there are several types of foundations for offshore wind turbines, with the monopile foundation having the largest market share (Technavio, 2019). However, from a geotechnical standpoint, there are several challenges related to the design of these monopile structures. Firstly, due to small length over diameter ratio for the monopiles, the soil mechanisms mobilized by a monopile is significantly different from conventional slender piles used for offshore oil and gas platforms. This has led to extensive research on the monopile structure in recent years, such as the PISA project (Byrne et al., 2017) which developed a multi-spring framework by extensive field testing and numerical analyses of monopiles. The model importantly accounts for the contribution of soil resistance from the pile tip and shaft friction, in addition to lateral resistance along the pile, which is the only component considered in conventional slender pile design. Furthermore, in an offshore wind farm which covers a considerable area, large variation in soil conditions is typically encountered. A wind farm consists of many turbine locations and site-specific monopile design is required for each of the locations. Recognizing the important differences in soil mechanisms between a monopile and a conventional slender pile, guidelines by DNVGL for monopile design (DNVGL, 2018) requires that soil springs for monopiles should be calibrated against *finite element (FE)* analyses. This calls for the need of an efficient optimization tool to calibrate soil reaction springs based on finite element analyses.

The past research efforts on monopile design have been mostly devoted to monopiles in stiff over-consolidated clays that are typically encountered in the North Sea. And indeed, the majority of the offshore wind developments to date have concentrated in this region. However, as the industry expands rapidly in Asia, where soft clay and layered soils are commonly encountered, it calls for research on monopile design methods that suit those geotechnical conditions.

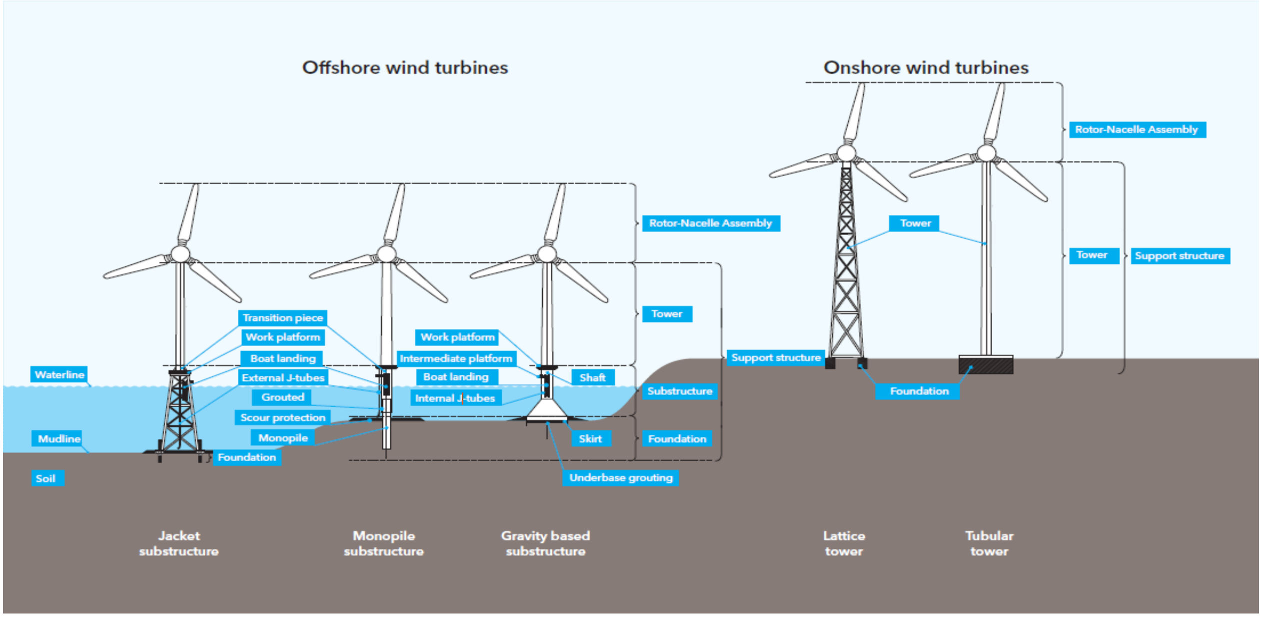

Figure 1.1: Definition of wind turbine components. From DNVGL-ST-0126 (DNVGL, 2018).

1.2 Objectives

Wind turbines are dynamic sensitive structures. Its dynamic response is strongly influenced by the boundary condition provided at the seabed, which is characterized by soil-pile interaction stiffness and damping. The problems investigated in this thesis are divided into three different parts, two focusing on the soil reaction springs (stiffness), and one focusing on the damping:

The first part of this thesis is concerned with an optimization tool. The tool is developed to calibrate soil reaction springs based on pile responses calculated by finite element analyses. The performance and robustness of the tool is verified and tested

The second part of this thesis is concerned with the soil reaction springs for monopile design in soft clay and layered profiles. Most of the existing soil reaction models available in the literature today were derived for a uniform clay. The performance of the existing soil reaction models is yet to be tested in soft clay and layered clay profiles. For this purpose, a comprehensive finite element parametric study is performed, investigating the monopile response in single normally consolidated to lightly over-consolidated soil profile as well as layered clay profiles. The performance of existing soil reaction spring models for capturing the pile response are tested.

The third part of the thesis is concerned with the damping in soil-pile interaction. An investigation is performed to seek the link between the soil damping at element level (damping ratio vs cyclic shear strain) and the damping at the soil-pile interaction level (damping ratio vs normalized pile displacement).

Accordingly, the study has the following three main objectives:

- Develop and validate an optimization for calibrating soil reaction springs based on finite element results.
- Perform FE parametric analyses of monopiles in soft clay and layered clay profiles and test the performance of existing soil reaction models against the FE results.
- See the link between the soil damping at element level and at the soil-pile interaction level.

1.3 Limitations

All geotechnical analyses conducted within this thesis were performed assuming isotropic- strength and stiffness conditions and a fully rough soil-pile interface.

The analyses also assumed the pile to be "wished-in-place", meaning that the pile installation process was not modelled explicitly. Studies have shown that the soil immediately adjacent to the pile wall will be highly remolded during pile installation (Sagaseta et al., 1997), (Renzi et al., 1991). Due to a combination of immediate pore pressure change as the pile tip passes by, thixotropy and pressure dissipation the soil regains some of the initial shear strength. This is commonly accounted for by assigning a representative roughness factor. Despite that this study focused on a fully rough soil-pile interface for simplicity, the effect of interface roughness can be easily incorporated in practice.

1.4 Structure of the Thesis

Each activity and its corresponding methodology are described within a separate chapter with a discussion and a conclusion where it is natural. The thesis is arranged in the following structure:

Chapter 2 gives a theoretical foundation for solving the problems formulated for this thesis. By presenting the development of research activities conducted within the subject of laterally loaded piles, starting from principles derived in the 1960s up to present day, a wide understanding of the subject is achieved. Relevant principles regarding damping is presented at the end of the chapter.

Chapter 3 is a documentation chapter, regarding the developed optimization tool. The principles of the tool are presented, and the tool is validated by various optimization tasks.

Within **chapter 4** the pile response in soft clay, and layered clay profiles are investigated through finite element analyses. The results of the finite element analyses are compared to pile responses calculated by a multi-spring beam-column model. For situations where the multi-spring model did not perform adequately, the optimization tool is used to get a better understanding of the response mechanisms. The chapter ends with a discussion of the results, where the calculated spring modifiers are analyzed further to investigate the effect of the soft clay and soil layering.

Chapter 5 investigates the hypothesis of a scaling relationship between soil damping at element level and the soil-pile interaction level existing. The soil damping is calculated using Darendeli principles (Darendeli, 2001). The pile damping is found through finite element testing.

Chapter 6 concludes by highlighting the findings, and recommendations for further work is discussed.

2 Theoretical foundation

The pile geometry affects the soil deformation patterns, which again affects the pile response. Piles are typically characterized by their *length over diameter (L/D)* ratio, where an *L/D* less than 6 are typically characterized as a monopile. Within this section, the theory of slender pile and monopile behavior is presented by following the historical development and research activities conducted within these subjects. Relevant theory regarding damping is presented at the end of the chapter.

2.1 Pile design under lateral loading

In many constructions where foundation is needed the magnitude of lateral loading may be of a large character. For instance, situations such as traffic, collisions, waves, earthquakes, wind and earth pressure all generate situations in which the lateral loading will be of a significant value. In terms of the foundation of the substructure, piles will be much better suited than, for instance, a shallow foundation to resist these types of forces. The pile mobilizes a resistance in the soil, directly opposite to the direction of the applied lateral load, as it is embedded into the ground.

There are two types of resistance mobilized in the ground: soil-pile interface side resistance (as friction and adhesion), shown as (a) in Figure 2.1 and the soil-pile interface compressive resistance (as normal stress), shown as (b) in Figure 2.1. These two types of resistance generates a *resistance (p)*, which can be measured as a function of the *lateral deflection* (*y)* of the pile (Salgado, 2008). Plotting the resistance against deflection results in a *p-y curve*, shown as (d) in Figure 2.1:

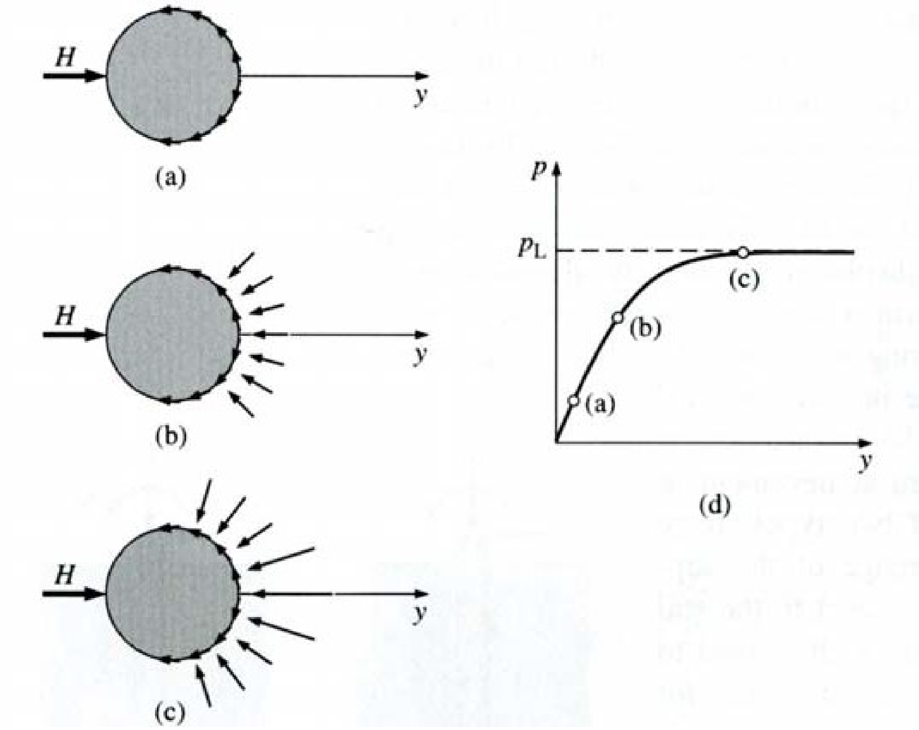

Figure 2.1 Representation of the shear force H, and lateral resistance p, at different load levels reaching the ultimate lateral bearing capacity (c). Salgado (2008), figure 13-31.

2.1.1 p-y method

Based on a "Winkler modelling approach", also known as the *p-y* method, the *p-y* curves are modeled using a series of uncoupled springs along the pile. In reality, the soil is a continuous medium that surrounds the pile. In a Winkler model the pile is divided into different segments, where each segment has its own *p-y curve* described by a non-linear spring. The springs act independently of each other (Caselunghe & Eriksson, 2012). The concept is visualized in Figure 2.2:

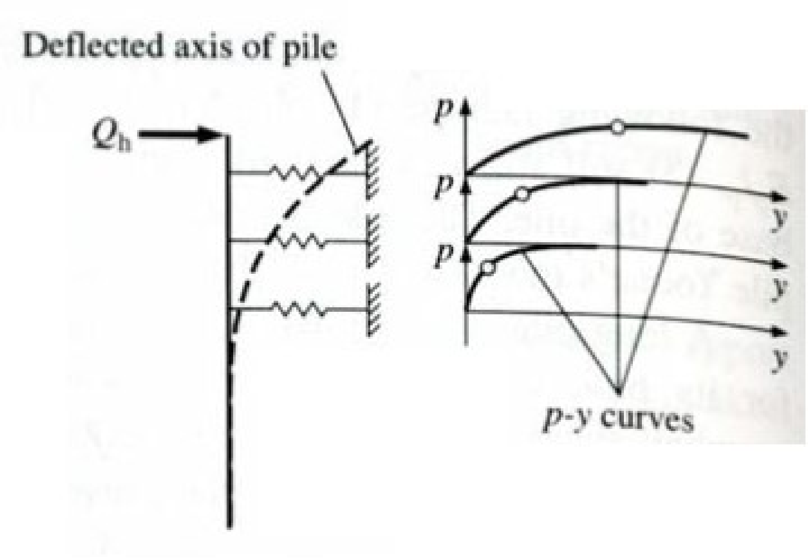

Figure 2.2: Modeling the soil-pile system using Winkler springs. Nonlinear springs described by *p-y curves* are used to model the deflected pile shape. From Salgado (2008), figure 13-34.

The overall pile response is solved by beam-column analysis, following the "Euler-Bernoulli beam" theory (Bauchau & Craig, 2009). The ultimate lateral bearing capacity is defined as the peak value of the *p-y curve*.

2.1.2 API

In the 1950s, a group of five oil companies initiated a research study on laterally loaded piles for offshore structures. The piles were long relative to the pile diameter, commonly known as slender piles. The research included activities such as field testing, laboratory model testing and development of correlations for design. The tests were performed in soft normally consolidated marine clay. The result of the research (Matlock, 1970) provided the basis of the current industry guidelines, published by the American Petroleum Institute (API, 2014). The recommendation is mathematically described as:

$$p_u = \left(3 + \frac{Jz}{D}\right) S_u + \gamma' z$$

$$\frac{p}{p_u} = 0.5 \left(\frac{y}{y_c}\right)^{0.33} \leq 1$$

$$y_c = 2.5\varepsilon_{50} D$$

where J is a dimensionless empirical factor, S_u and γ' is the undrained shear strength and the effective unit weight of the soil respectively at depth z. D is the pile diameter, p_u is the ultimate lateral bearing pressure, denoted p_L in Figure 2.1 (d) and y is the lateral displacement. ε_{50} is defined as axial strain at which 50% of maximum deviator stress is mobilized in an undrained compression test. Full mobilization is achieved at $y=8y_c$.

The *bearing capacity factor* (N_p) is calculated as the resistance over shear strength (p/S_u). The *ultimate bearing capacity* (N_{pd}) is defined as p_u/S_u. The API-recommendation is limited by a "flow-around capacity" of N_{pd} equal to 9, hence the onset depth of flow-around mechanism is the depth in which the N_p is equal to 9.

2.1.3 Finite Element Analysis

The use of *finite element analysis* (*FEA*) is essential when analyzing the monopile response. The pile response provided by FEA is in general seen as the most realistic solution. Thus, in the development of design models the researches strive to capture the FEA soil response with the use of simple and logical design models. Applying the *finite element (FE)* method requires a certain skillset. The use of FEA is costly in terms of computational requirements, and it is time consuming.

The concept of the FEA is to divide a complex geometry into smaller segments, called elements, which are connected by nodes. Within each element, one can apply a set of element equations to describe the desired events. These equations are commonly partial differential equations, which consist of boundary- and/or initial conditions, valued to describe the desired action. The simple equations that model the individual elements are put together in a larger system of equations to model the entire problem. By solving these equations, one may describe numerous physical problems accurately. The division of the geometry may affect the results, as more elements in general gives a more accurate solution but will in return demand higher computational power. The division of elements are commonly known as meshing. A finer mesh will result in more elements and higher accuracy compared to a coarser mesh, which is of larger elements and requires less computational efforts.

There are several commercial finite element programs. The ones relevant for this thesis are Plaxis 3D (Plaxis, 2017) and Abaqus (Abaqus, 2017).

2.2 Soil failure mechanism

A slender pile in clay will experience two soil failure mechanisms (Zhang et al., 2016). In the upper part a conical wedge failure mechanism occurs. At the depth where the bearing capacity, N_P, exceeds the ultimate bearing capacity factor, N_{Pd}, the soil fails in a localized flow-around mechanism. For monopiles, a rotational failure mechanism will form as well, at the lower half of the pile (Hong et al., 2017). The different failure mechanisms are further explained in the following.

2.2.1 Wedge failure

As described in classical Rankine's theory at the ultimate lateral bearing capacity the soil will deform in a wedge failure. At the front of the pile a passive conical wedge will form, as shown in Figure 2.3.

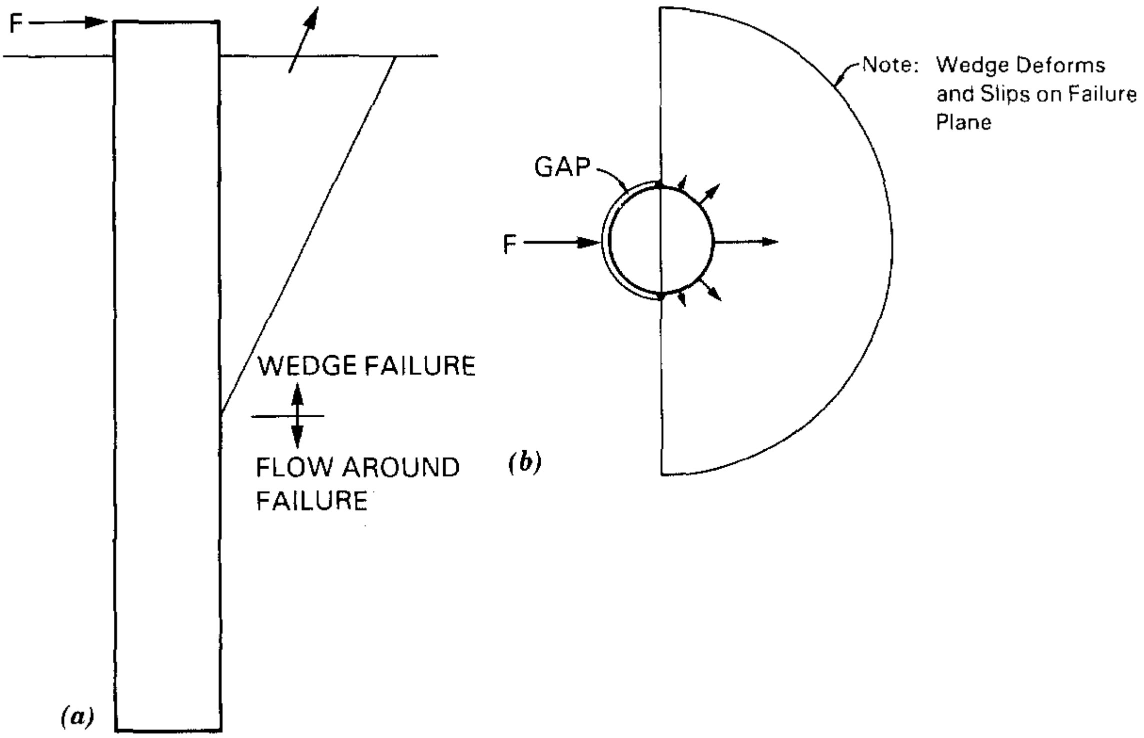

Figure 2.3 (a): Soil deformation mechanism. (b): The conical wedge as seen from above the soil surface. From Murff and Hamilton (1993).

There are two types of wedge failures, with and without suction. For instance, in situations where fast wave loading appears, or if the drainage path is blocked by a mudmat, suction may occur at the rear side. If suction is available, the deformation of the soil on the rear side is assumed to have the shape of an active conical wedge. Murff and Hamilton (1993) showed that this phenomena may have the effect of doubling the unit resistance. If suction is not available, the pile will displace unaffected by the soil at the rear side, and a gap will form as seen in Figure 2.3 (b).

Murff and Hamilton (1993) came up with a set of equations to describe the shapes of the conical wedges, for both passive and active wedges in clay. The equations are applicable when describing cases with both linearly increasing strength, and for two-layered soil systems.

2.2.2 Plane strain flow-around

Below the wedge, the soil is assumed to flow horizontally around the pile. Randolph and Houlsby (1984) investigated the ultimate lateral resistance on a pile in a soil medium, exposed to purely horizontal displacement, and described the failure mechanism as:

> As the pile is pushed laterally through the soil, a region of high mean stress will occur in the front of the pile and of low stress behind the pile. The soil will flow around the pile from front to back. (Randolph & Houlsby, 1984, p. 614).

The deformation patterns will vary as of what *roughness (α)* the pile-soil interface has. Figure 2.4 visualizes the deformation pattern for a smooth interface (α=0), and a fully rough interface (α=1).

Randolph and Houlsby (1984) presented equations for describing the flow-around deformation by lower- and upper bound analysis. Martin and Randolph (2006) presented equations by upper bound analysis.

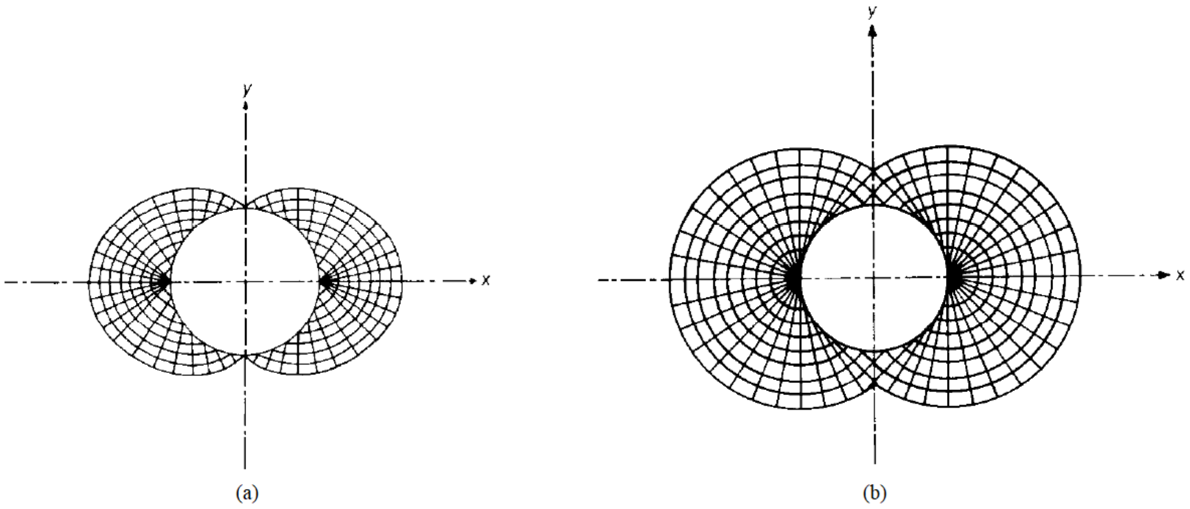

Figure 2.4 (a): Flow-around mechanism for a smooth pile ($\alpha=0$). (b): Flow-around mechanism for a fully rough pile ($\alpha=1$). From Randolph and Houlsby (1984).

The soil will start to deform in a plane strain failure mechanism at the depth where the ultimate lateral bearing capacity factor is mobilized. There are several theories regarding what depth level the soil will start to fail in a plane strain flow-around mechanism, some of these are presented along with the *p-y* frameworks in later sections.

The ultimate bearing capacity factor will vary by the roughness of the pile. In general, N_{pd} is found to vary linearly from 9.14 to 9.20 (lower and upper bounds) for a fully smooth interface, to 11.94 (exact) for a fully rough interface (Zhang et al., 2016).

2.2.3 Rotational mechanism

The characteristic properties of a monopile are relatively different from a slender pile, making an impact on the failure mechanism of the soil located below the wedge failure. Monopiles are, in general, stiffer constructions relative to a slender pile due to a lower *L/D* ratio (typically equal or less than 6 for a monopile, compared to a typical ratio of 20-40 for a slender pile.) The flow-around failure may not be relevant for the monopile at all. The soil around the monopile will react in a wedge failure along the upper part of the pile, and a rotational mechanism along the lower part and the pile tip (Zhang & Andersen, 2019a). As opposite of a slender pile, two additional mechanisms may be of relevance, namely the soil resistance at the pile tip, and the vertical component of the skin friction mobilized along the monopile. The mobilized friction along the pile will shape the wedges into having a more curved shape. The differences are illustrated in Figure 2.5.

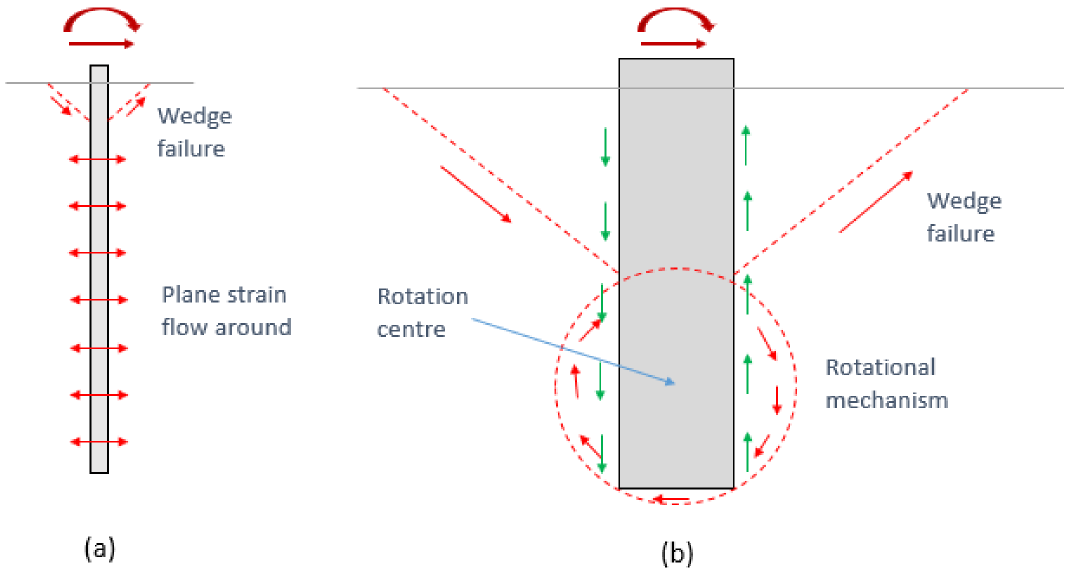

Figure 2.5 (a): Typical soil failure mechanisms for a slender pile. (b): Failure mechanisms for a monopile with no plane strain flow-around failure and no tension gap at the rear side. Notice that by pile friction the wedges should have a more curved shape then illustrated. From Zhang and Andersen (2019a).

As the load level increases, the rotation center of the pile lowers along the pile (Zhang & Andersen, 2019a). The depth of the rotation center impacts the curvature of the rotational scoop mechanism below the pile tip, which may influence the assumed pile tip interaction mechanism. Zhang and Andersen (2019a) showed that the error of replacing the rotational scoop below the pile tip by a pure sliding mechanism is negligible.

Zhang and Andersen (2019a) presented a conceptual framework for analyzing the response of a monopile. The framework includes the tip resistance mobilized by the rotational mechanism by the inclusion of *base shear-displacement* (*s-u*) springs at the pile tip. The mathematical formulation is presented in section 2.4.2.

2.3 Ultimate lateral bearing capacity in clay

The soil properties of the North Sea are commonly described as an over-consolidated stiff clay. As illustrated by Figure 2.6, the North Sea is the main location of the European offshore wind activities. Thus, a lot of the research previously conducted has been trying to capture the soil response in a stiff over-consolidated clay.

The difference in soil properties has led to multiple design recommendations, each trying to describe a site-specific response. In addition to the previously mentioned API-guidelines, a selected set of recommendations are presented in the following.

Figure 2.6: Wind farms in the Irish Sea, North Sea and the Baltic Sea, as per 14.10.18. From 4coffshore (2018).

2.3.1 Murff and Hamilton (1993)

Murff and Hamilton (1993) proposed the following framework for calculating *p-y* curves:

$$N_p = N_1 - N_2 e^{\frac{-\xi * z}{D}}$$

$$\xi = 0.25 + 0.05\lambda \qquad \lambda < 6$$

$$\xi = 0.55 \qquad \lambda \geq 6$$

$$\lambda = \frac{S_{u0}}{S_{u1} * D}$$

where N_1 is the limiting N_p-factor where a flow-around mechanism will occur, N_1-N_2 is the N_p-value at the soil surface. S_{u0} is the shear strength intercept at sea floor, S_{u1} is the rate of increase of shear strength with depth. D is the pile diameter, and z is the depth of interest. No suction was assumed.

2.3.2 Jeanjean (2009)

By carrying out multiple centrifuge tests and finite element analyses, Jeanjean was able to measure the soil response in a lightly over-consolidated clay (Jeanjean, 2009). The study consisted of cyclic loading as well as monotonic push to failure. By measuring the lateral deflection of the pile, the relevant force data was back-calculated using Euler-Bernoulli beam theory (Bauchau & Craig, 2009). Jeanjean further developed the framework proposed by Murff and Hamilton (1993) for a linearly increasing shear strength profile, with a modified expression for the calculation of the bearing capacity factor, N_p. The following framework was proposed:

$$N_P = 12 - 4e^{\frac{-\xi * z}{D}}$$

where ξ is calculated using the same principles as described in the Murff and Hamilton (1993) recommendation. Jeanjean proposed a flow-around capacity of N_{pd} equal to 12, and a N_{pd} of 8 at mudline for double wedge failure.

As discussed by Zhang, Andersen and Tedesco (2016), at mudline a N_p value at approximately 3.5 and 7 for single wedge and double wedge failure respectively, is found to be more realistic. The centrifuge tests did not reveal any sign of a gap developing on the rear side of the pile, thus the framework assumed the development of an active wedge.

2.3.3 Nichols et al. (2014)

Based on literature and finite element analyses, Nichols et al. (2014) proposed a *p-y* formulation including the effect of soil strength anisotropy. The following framework was proposed:

$$p_u = N_{p0}S_u + \gamma' z$$

$$N_{p0} = 4 + 2\left(\frac{z}{D}\right)^{0.6}$$

where γ' is the average submerged unit weight. S_u included the state of anisotropy by describing the undrained shear strength as the average of the triaxial extension strength (S_u^E), and the direct simple shear strength (S_u^{DSS}). A gap was allowed to form at the back of the pile, hence a single passive wedge mechanism occurred. The value of p_u was limited to $11.9S_u$, thus proposing a N_{pd}-factor of 11.9.

2.3.4 Zhang et al. (2016)

By conducting a literature review, Zhang, Andersen and Tedesco discussed the topic of ultimate bearing capacity of laterally loaded piles in clay and concluded with a proposed generalized recommendation for the *p-y* formulation (Zhang et al., 2016). The impact of multiple factors, such as suction, relative pile stiffness, soil weight and onset depth of flow-around mechanism was discussed. In cases where a gap is considered to occur, the bearing capacity factor was proposed as:

$$N_p = N_{p0} + \frac{\gamma' z}{s_{um} + kz} \leq N_{pd}$$

For cases where no gap is considered, the unit weight of the soil will be irrelevant as the active wedge forming on the rear side of the pile will cancel out the passive wedge at the front. The bearing capacity factor was proposed as:

$$N_p = N_{p0} \leq N_{pd}$$

where N_{p0} is the bearing capacity factor in idealized weightless soil with no suction, calculated by:

$$N_{p0} = N_1 - (N_1 - N_2)\left[1 - \left(\frac{z/D}{d}\right)^{0.6}\right]^{1.35}$$

$$N_1 = 11.94$$

$$N_2 = 3.22$$

$$d = 16.8 - 2.3\log_{10}(\lambda) \geq 14.5$$

$$\lambda = \frac{S_{um}}{kD}$$

$$N_{pd} = 9.14 + 2.8\alpha$$

S_{um} is the shear strength at soil surface, k is the shear strength gradient with depth, and α is the pile roughness, varying between 0 and 1 for a smooth to rough pile respectively.

The flow-around mechanism will occur at the depth where $N_p = N_{pd}$. The paper also investigated two practical considerations namely the effect of axial loading, and soil strength anisotropy. The effect of the soil strength anisotropy, was included by defining the shear strength as:

Table 2.1: Proposed shear strength of anisotropic clay profiles by Zhang et al. (2016).

Single wedge (no suction)	$S_u = 0.75S_u^{DSS} + 0.25\ S_u^{E}$
Double wedge (with suction)	$S_u = S_u^{DSS}$, assuming $S_u^{DSS} = S_u^{Average}$
Flow-around	$S_u = S_u^{DSS}$

2.4 p-y curves for monopiles

When designing pile foundations, the current practice is to use the guidelines presented by API (API, 2014). As previously mentioned, the API guidelines were mainly developed for slender pile application. One of the highlighted findings from the PISA-project was the confirmation that the API guidelines are unsatisfactory for design of monopile foundations (Byrne et al., 2017). Thus, a new field of research arose. The most relevant contributions within the field of designing monopiles are presented in the following.

2.4.1 Zhang and Andersen (2017)

Zhang and Andersen (2017) performed a parametric study of the *p-y* response of a pile slice, simulating a stiffness spring, using the FEA-software Plaxis 3D (Plaxis, 2017). By performing a wide range of soil stress-strain behavior and pile-soil interface parameters, they found a set of scaling factors to connect the stress-strain response of the soil and the *p-y* response. By normalizing the mobilization of shear stress given as τ/S_u to a normalized point at the *p-y* curve, p/p_u, the level of mobilization was described as equal ($\tau/S_u = p/p_u$). The shear strain γ was scaled to match the corresponding normalized lateral displacement y/D by using two scaling coefficients, ξ_1 and ξ_2, applied at the elastic shear strain and plastic shear strain, respectively. The connection is illustrated in Figure 2.7 and summarized below.

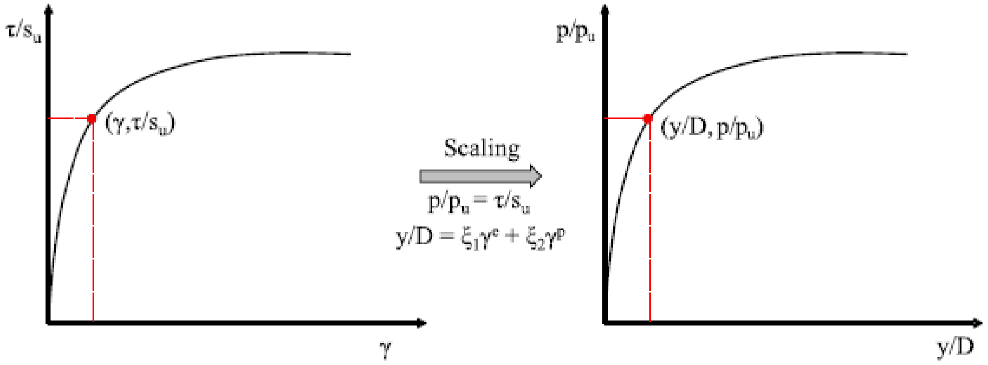

Figure 2.7: Illustration of proposed p-y model for calculating the flow-around soil response. From Zhang and Andersen (2017).

$$\xi_1 = 2.8$$

$$\xi_2 = 1.35 + 0.25\alpha$$

$$\gamma^e = \frac{\tau}{G_0}$$

$$\gamma^p = \gamma - \gamma^e$$

$$p_u = N_p S_u$$

$$N_p = 9.14 + 2.8\alpha$$

Where γ^p and γ^e is the plastic and elastic shear strain respectively. p_u is the ultimate soil resistance. α is the roughness factor, varying from 0 to 1, giving an N_p in the range of 9.14-11.94 for smooth to rough pile interfaces. G_0 is the initial shear modulus.

The model provided an approach to use site-specific *p-y* curves in design, based on simple DSS shear tests without the need of advanced numerical analysis.

2.4.2 Zhang and Andersen (2019a)

Zhang and Andersen (2019a) proposed a conceptual framework specific for monopile analysis in clay. The framework presents a new model for wedge failure analysis and a *base shear model* (*s-u)* to capture the shear forces mobilized at the pile tip. The model divides the soil failure mechanisms into three separate parts:

1. Above the rotation point, *p-y* curves for wedge failures are described as:

$$\frac{p}{p_u} = 1 - 2^{\left[-\left(\frac{y^p}{y^p_{50}}\right)^n\right]}$$

$$n = 0.55 - 0.05\frac{z}{D} \geq 0.325$$

$$y = y^e + y^p;\ y_{50} = y^e_{50} + y^p_{50}$$

Where y_{50} is the displacement at half of the spring mobilization, made up by an elastic and a plastic component.

$$\left(\frac{y^e_{50}}{D}\right)\left(\frac{G_0}{s_u}\right) = 0.6 + 0.28\left(\frac{z}{D}\right) - 0.029\left(\frac{z}{D}\right)^2,\alpha = 1.0$$

$$\left(\frac{y^e_{50}}{D}\right)\left(\frac{G_0}{s_u}\right) = 0.6 + 0.41\left(\frac{z}{D}\right) - 0.039\left(\frac{z}{D}\right)^2,\alpha = 0$$

$$\frac{y^e}{D} = 2\left(\frac{y^e_{50}}{D}\right)\left(\frac{p}{p_u}\right)$$

The normalized plastic displacement at half mobilization is found by scaling the soil stress-strain parameter, described as:

$$\frac{y^p_{50}}{D} = [a + b\left(\frac{z}{D}\right)]\gamma^p_f$$

$$a = 0.01 + 0.015\alpha$$

$$b = 0.10 - 0.06\alpha$$

γ_f^p is the plastic failure strain. As suggested by Yu, Huang and Zhang (2015), the ultimate bearing capacity, p_u is calculated by:

$$p_u = \left(N_{p0} s_u + \gamma' z\right) D$$

where γ' is the effective unit weight.

$$N_{p0} = N_1 - (N_1 - N_2)\left[1 - \left(\frac{z/D}{d}\right)^{0.6}\right]^{1.35} - (1 - \alpha) \leq N_{pd}$$

$$N_1 = 11.94\,; N_2 = 3.22$$

$$d = 14.5; N_{pd} = 9.14 + 2.8\alpha$$

2. Below the rotation point a rotational mechanism occurs. The failure mechanism follows the same formulations as presented by the plane strain flow-around failure by Zhang & Andersen (2017).
3. At the pile tip, a base shear model was proposed. Using the same scaling concept as for the plane strain flow-around *p-y* springs, the established shear force at pile tip, *s,* vs lateral displacement, *u,* is calculated by scaling the stress-strain response at pile tip by the following formulations:

$$\frac{s}{s_{ult}} = \frac{\tau}{S_u}$$

$$\frac{u}{D} = \xi_1 \gamma^e + \xi_2 \gamma^p$$

$$\xi_1 = 0.3$$

$$\xi_2 = 0.12$$

$$s_{ult} = 0.25\pi D^2 S_u$$

The terminology is visualized in Figure 2.8. The depth of the rotation point is found through an iterative procedure. By assuming wedge failure along the entire pile depth, one may calculate the initial rotation point. As discussed in Zhang and Andersen (2019a) the vertical skin friction mobilized by the pile-soil interface initiates a curved wedge (as described in classic earth pressure theory). This effect is included by the bearing capacity factor N_p. The vertical skin friction will also form a resistance against the overturning moment. This effect is accounted for by including a *moment-rotation (m-r)* spring as presented in the next section.

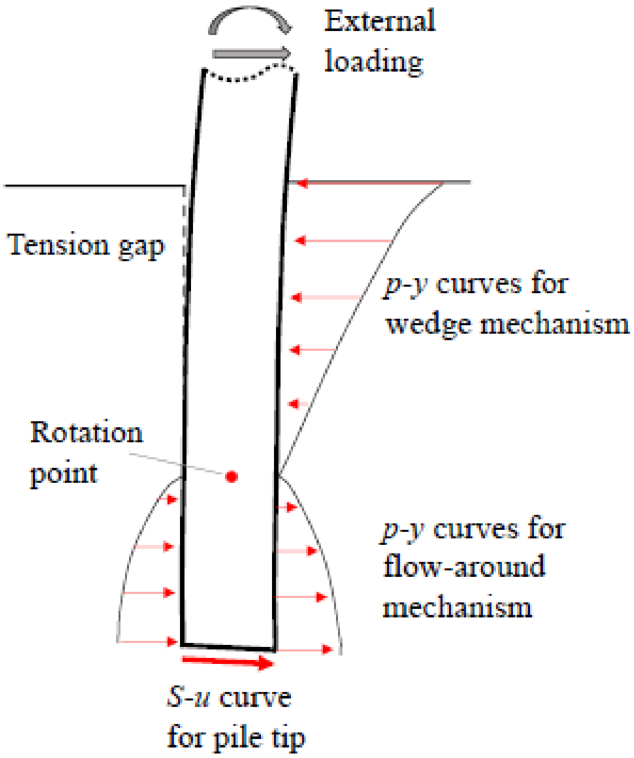

Figure 2.8: Visualized terminology for proposed framework model by Zhang and Andersen (2019a).

2.4.3 A multi-spring model for monopile analysis in soft clays

"A multi-spring model for monopile analysis in soft clays" was submitted by Dr. Zhang on May the 15th 2019 and is not published as of the date of the submission of this thesis. Some of the results presented in the paper were applied in this thesis, thus the relevant literature is presented.

By theoretical derivation, Zhang formulated a theoretical foundation for a moment-rotation spring (Zhang, 2019b). The spring was formulated by the same principles as shown for the flow-around failure mechanism presented by Zhang and Andersen (2017), namely by scaling the stress-strain response of the soil. By defining the level of soil mobilization divided by the interface roughness of the pile, $(\tau/S_u)/\alpha$, as equal to the normalized bending moment M/M_{max}, the corresponding rotation, r (θ in Figure 2.9), could be found by scaling the shear strain. The scaling was done by using two scaling factors, ξ^e and ξ^p, applied at the elastic shear strain, γ^e and the plastic shear strain, γ^p respectively.

The scaling concept is visualized in Figure 2.9, and summarized below:

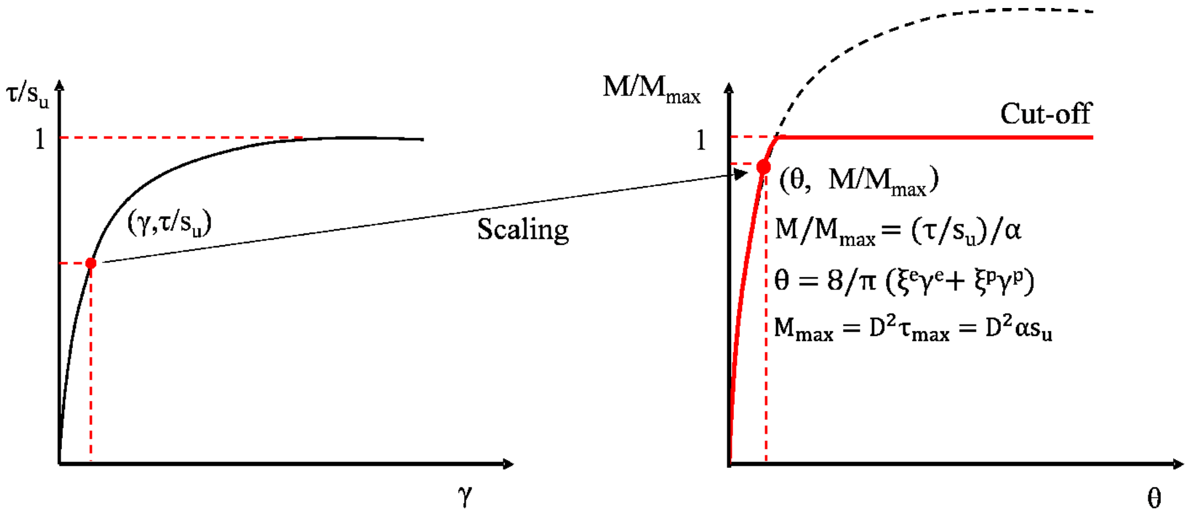

Figure 2.9: Illustration of the proposed m-r model for calculation of the spring response. From Zhang (2019b).

$$\frac{M}{M_{max}} = \left(\frac{\tau}{s_u}\right)/\alpha$$

$$\theta = r = \frac{8}{\pi}(\xi_1\gamma^e + \xi_2\gamma^p)$$

$$\xi^e = 1.15$$

$$\xi^p = 0.45$$

$$M_{max} = D^2\tau_{max} = D^2\alpha s_u$$

For pile roughness, α, below 1, a cut-off was applied at M/M_{max} equal to 1.

2.4.4 PISA

A joint industry project, PISA (Byrne et al., 2015a), was conducted with the purpose of developing a new design method for large diameter monopiles under lateral loading. The project was divided into three separate parts of work:

Field testing (Byrne et al., 2015b)

To replicate typical soil conditions found at many locations in the North Sea, the field testing was conducted at Cowden in north-east England and Dunkirk in northern France. The soil conditions at those areas were stiff to very stiff over-consolidated ductile Quaternary clay, and dense to very dense marine Pleistocene sands respectively. In total, 28 piles were tested, mainly in terms of monotonic loading, although some were tested by cyclic loading. The field tests were used in developing the numerical analysis model.

Numerical modelling (Zdravković et al., 2015)

The soil conditions were simulated using an expanded generalized version of the Modified Cam Clay model, where the model utilized a "*Hvorslev*" surface on the dry side (Zdravković et al., 2015). The numerical study did not consider installation effects.

Development of a new design method

The new design method was based on an extension of the existing *p-y* approach, adding additional soil reaction terms, as visualized in Figure 2.10 and Figure 2.11.

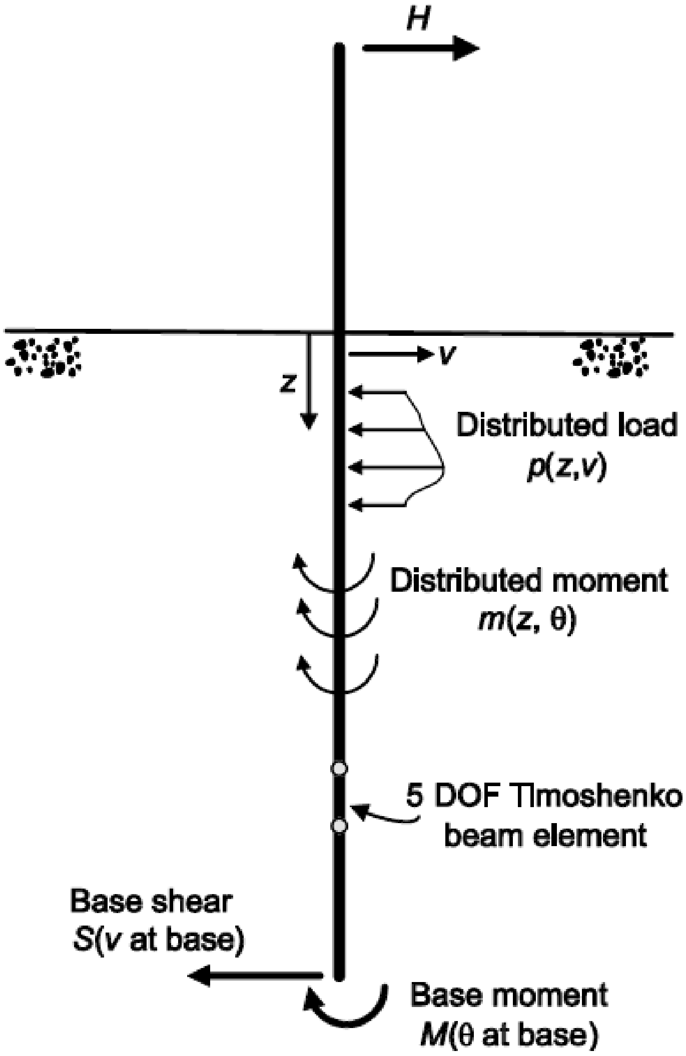

Figure 2.10: Framework for the proposed finite element model for monopile foundations. Note that displacement *y* is denoted as *v.* From Byrne et al. (2015a).

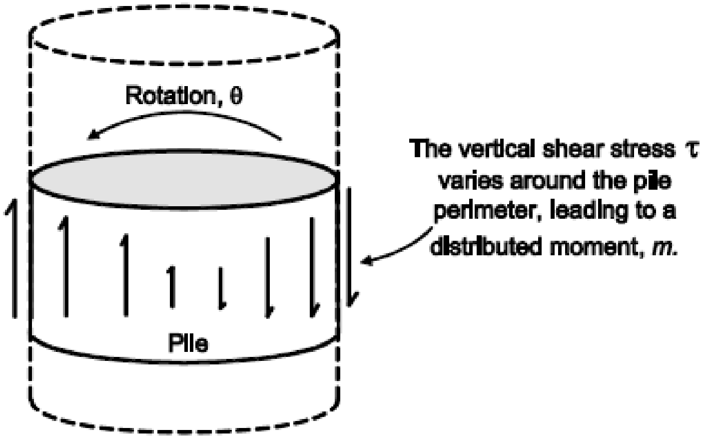

Figure 2.11: A distributed moment is included as a function of the vertical shear stress action on the pile surface. From Byrne et al. (2015a).

With each of the different soil reaction terms defined as:

- Distributed load curve: Defines the *p-y* relationship, having the same function as a conventional *p-y* curve.
- Distributed moment curve: As the pile rotates, a vertical skin friction mobilizes along the pile interface, described by a distributed moment curve.
- Base shear curve. Defines the relationship between the lateral displacement of the pile tip and base shear force.
- Base moment curve. Defines the relationship between moment at base and the rotation of the pile tip.

The pile is modelled using Timoshenko beam theory, which is an extension of conventional Euler-Bernoulli beam theory (Bauchau & Craig, 2009). Timoshenko beam theory includes shear strain effects. The model resulted in a 1D-model of the beam element, which use the lateral response prediction as input parameters.

Results (Byrne et al., 2017)

The lateral response prediction of the soil may be divided into two proposed design methods. The "Rule-based method", and the "Numerical-based method". The rule-based method may be considered the conventional method, where the soil reaction curves are generated using pre-defined mathematical functions. The reaction springs are computed including several complex parameters, such as the variation of the small-strain shear modulus G_0 with depth, typically measured by conducting a seismic cone test. For sands the variation of in-situ vertical effective stress with depth is required in addition to G_0. For clays the method requires data of the undrained shear strength. This may be obtained using CPT- or triaxial-testing, ideally both. The more advanced numerical-based method calculates the soil reaction springs using a 3D FE model. An overview of the analysis procedure is presented in Figure 2.12.

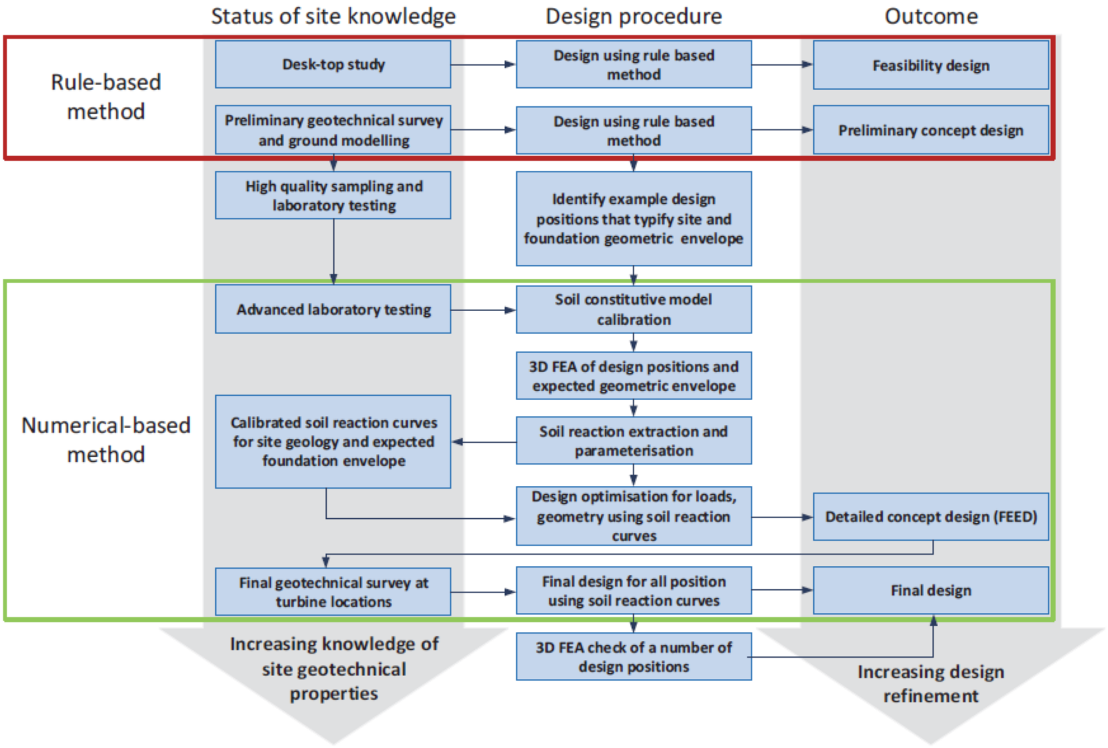

Figure 2.12: Analysis procedure presented by the PISA project. From Byrne et al. (2017).

The design procedure suggests that the rule-based method is applied for the initial feasibility design. Then, the soil reaction curves for monopiles should be validated using FEA. Each monopile at a desired windmill site may be optimized by using site-specific soil reaction curves at the proposed 1D-model.

In addition, the PISA-project highlighted the following findings:

- Confirmation that the current design guidelines (e.g. API) are unsatisfactory for the design of monopile foundations.
- A database of field-testing data with varying diameter and pile length, both monotonic and cyclic loads.
- Less conservatism in the design as the design framework was developed focusing on monopile design, which is likely to promote less costs.

2.5 Layered soil profile

The challenges within the issue of soil layering is yet to be thoroughly investigated by the research community, compared to many of the other subjects within the soil mechanisms regarding laterally loaded piles. Yang and Jeremić (2005) carried out a finite element study of the behavior of a single pile in elastic-plastic soils. The paper researched the pile behavior in two different layered soil profiles, a clay-sand-clay model, and a sand-clay-sand model, which were compared to the pile behavior in uniform clay and sand profiles. The paper discovered a change in the lateral resistance for both models. The clay-sand-clay model provided an increase in the lateral capacity in the upper clay layer up to one pile width above the upper sand interface for small pile displacements ($0.5\%D$). For large pile displacements ($8\text{-}10\%D$), the increase of lateral resistance extended only one finite element above the upper sand interface. The clay layers also effected the lateral resistance of the sand layer. For the sand-clay-sand model, the clay experienced an increase of its lateral resistance by 10%-40%. In addition, the intermediate clay layer had significant effects on the lateral resistance of the upper sand layer.

Murff and Hamilton (1993) considered a two-layered clay profile with l_1 and S_{u1} describing the thickness and strength respectively of the top layer. By calculating the equivalent thickness, l_e, of the top layer with the same strength as the bottom layer, S_{u2}, the soil profile is analyzed by:

$$9\frac{l_e}{D} + 12.72e^{-\frac{0.55l_e}{D}} = 9S_{ur}\frac{l_1}{D} + 12.72e^{-\frac{0.55l_1}{D}} - 12.72(S_{ur} - 1)$$

where $S_{ur} = S_{u1}/S_{u2}$.

2.6 Damping

2.6.1 Equation of motion

For a system that is experiencing external forces, the motion may be described by the equation of motion:

$$m\ddot{u} + c\dot{u} + ku = f(t)$$

The equation of motion is based on equilibrium of forces, namely the inertia ($m\ddot{u}$), damping ($c\dot{u}$) and elastic (ku) force. *k* is the linear elastic stiffness coefficient. *c* is the viscous damper coefficient and *m* is the mass. $u, \dot{u}$ and $\ddot{u}$ is namely the displacement, velocity (*du/dt*) and acceleration (d^2u/dt^2) respectively, of the system. *f(t)* is external force(s). The definitions are visualized in Figure 2.13:

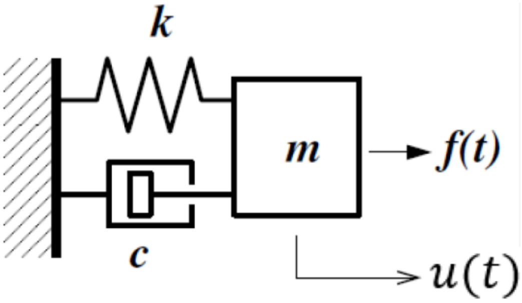

Figure 2.13: A mass-spring damper system. From the Norwegian Geotechnical Institute (NGI).

The undamped natural frequency ω_n of a system is defined as:

$$\omega_n = \sqrt{k/m}$$

with the damped natural frequency defined as:

$$\omega_D = \omega_n\sqrt{1-\zeta^2}$$

where ζ is the damping ratio, defined as:

$$\zeta = \frac{c}{2m\omega_n}$$

The natural period is defined as:

$$T_D = \frac{2\pi}{\omega_D}$$

Damping is defined as the process by which free vibration steadily diminishes in amplitude. There are multiple types of damping:

- Viscous damping
- Hysteretic damping
- Coulomb (or friction) damping
- Radiation (or geometric) damping

For soil damping there are mainly two forms: radiation damping and hysteric material damping, where radiation damping is neglectable for frequencies below 1 Hz. The dominant contributors to dynamic loading of offshore wind turbines are the wind and wave loads (Seidel, 2014). The majority of the wind and wave loads have frequencies below 1 Hz (Carswell et al., 2015), thus making hysteretic damping the most dominant type of soil damping.

2.6.2 Hysteretic damping

By plotting the mobilized force in the damper and the springs: $f_D + f_S = c\dot{u} + ku$ against the displacement u (Figure 2.14 (A)) for one hysteresis loop, the dissipated energy E_D is defined as the area within the loop. The potential energy (or elastic energy) E_{S0} is defined as the maximum potential energy stored in each cycle of motion (area below $f_S(u_{MAX})$) (Figure 2.14 (B)).

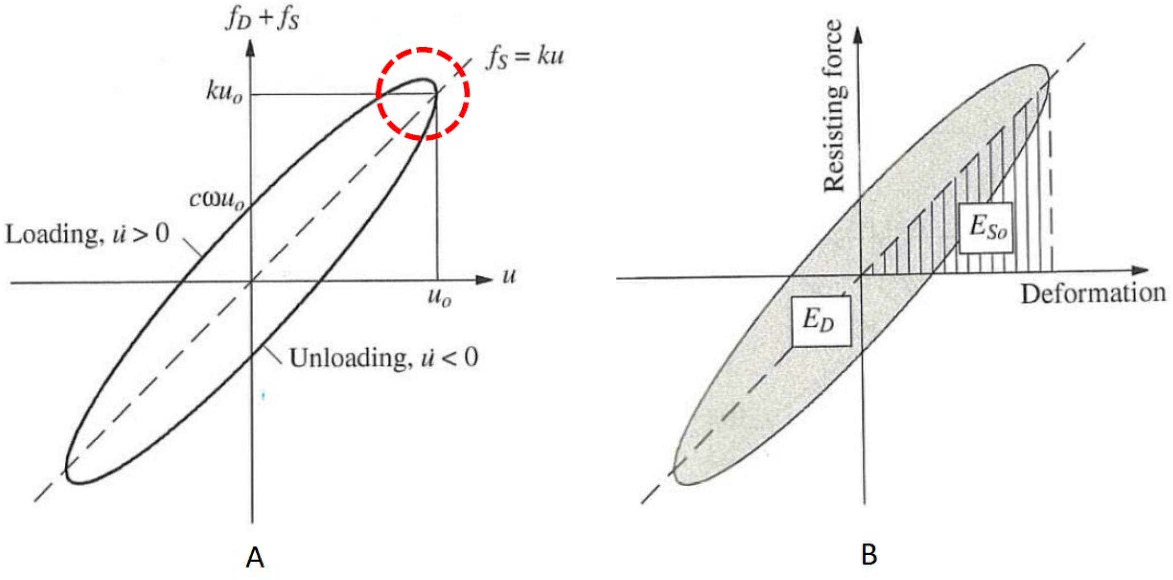

Figure 2.14 (A): Mobilized damping and elastic force for one hysteretic loop. (B): Definition of dissipated energyE_D and potential energy E_{S0}. From NGI.

Using the terminology presented in Figure 2.14, the potential energy $E_{S0}(u)$, and the dissipated energy E_D in one hysteresis loop is mathematically defined as:

$$E_{S0}(u = u_0) = \frac{f_S u_0}{2} = \frac{kuu_0}{2} = \frac{ku_0^2}{2}$$

$$E_D = \int f_D du = \int_0^{T_D} (c\dot{u})\dot{u}dt = \int_0^{\frac{2\pi}{\omega}} c\dot{u}^2 dt = .. = \pi c\omega u_0^2 = 2\pi\zeta\frac{\omega}{\omega_n}ku_0^2$$

2.6.3 Damping ratio, D

By the presented definition of E_D and E_{S0} the damping ratio is rewritten as:

$$\zeta = \frac{1}{4\pi}\frac{1}{\omega/\omega_n}\frac{E_D}{E_{S0}}$$

All activities conducted within this thesis that include damping were assumed to occur at resonance, hence $\omega = \omega_n$. Thus, by rewriting the equation above, the equivalent damping ratio (and hysteretic damping factor *D*) is defined as:

$$\zeta_{eq} = \frac{1}{4\pi}\frac{E_D}{E_{S0}} = D$$

2.6.4 Darendeli damping curves

Darendeli (2001) presented a framework for estimating the damping ratio, *D,* based on soil properties and/or lab testing. The framework utilizes a modulus reduction curve for the given soil, which may be found through lab testing by the Masing principles (MASING, 1926). By using two curvature coefficients the damping curve estimated from Masing behavior may be scaled to fit the experimental observations.

The model expresses the normalized reduction curves as:

$$\frac{G}{G_0} = \frac{1}{1 + \left(\frac{\gamma}{\gamma_r}\right)^a}$$

Where *a* is a curvature coefficient, γ_r is the reference strain at $\gamma_r = \gamma_{G/G_0=0.5}$, as visualized by Figure 2.15.

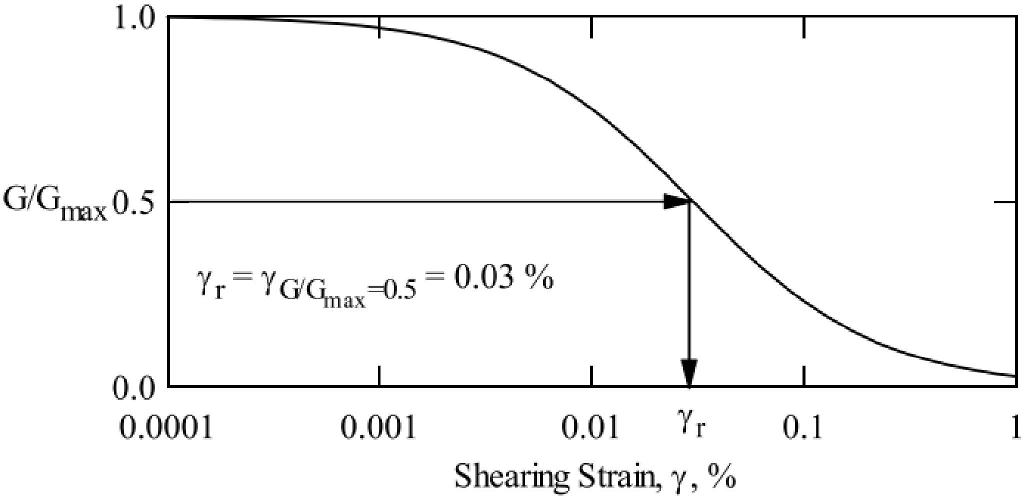

Figure 2.15: Visualization of the definition of the reference strain, γ_r at the stiffness reduction curve. Note that G$_0$ is denoted G$_{max}$. From Darendeli (2001), figure 6.1.

This term is included in the definition of the material damping curve, expressed as:

$$D = b * \left(\frac{G}{G_0}\right)^{0.1} * D_{Masing} + D_{min}$$

Where *b* is a scaling coefficient which accounts for the number of loading cycles. *D$_{min}$* is a constant to adjust the curve to cope with small-strain damping. The definition of *D$_{Masing}$* follow the following mathematical expressions:

$$D_{Masing} = c_1 D_{Masing,a=1.0} + c_2 D_{Masing,a=1.0}{}^2 + c_3 D_{Masing,a=1.0}{}^3$$

Where:

$$D_{Masing,a=1.0} = \frac{100}{\pi}\left[4\frac{\gamma - \gamma_r \ln\left(\frac{\gamma+\gamma_r}{\gamma_r}\right)}{\frac{\gamma^2}{\gamma+\gamma_r}} - 2\right] [\%]$$

$$c_1 = -1.1143a^2 + 1.8618a - 0.2523$$

$$c_2 = 0.0805a^2 - 0.0710a - 0.0095$$

$$c_3 = -0.0005a^2 + 0.0002a + 0.0003$$

2.6.5 Estimation of Darendeli Damping variables

By performing a large number of soil sample tests, Darendeli established a data bank to estimate the input values for his damping model, based on common soil properties. The input parameters were estimated as a function of the *pre-consolidation stress* (σ_0'), *over consolidation ratio* (*OCR*), *plasticity index* (I_p), *number of loading cycles* (*N*), and the *loading frequency* (*f*). The model consists of 18 different model parameters (Φ_{1-18}). The parameters for the damping model are calculated by:

$$\gamma_r = \left(\phi_1 + \phi_2 * I_p * OCR^{\phi_3}\right) * \sigma_0'^{\phi_4}$$

$$a = \phi_5$$

$$D_{min} = \left(\phi_6 + \phi_7 * I_p * OCR^{\phi_8}\right) * \sigma_0'^{\phi_9} * [1 + \phi_{10} * \ln(f)]$$

$$b = \phi_{11} + \phi_{12} * \ln(N)$$

The model parameters (Φ_{1-18}) were estimated by analyzing the response of various soil samples, and derived using the First-order, Second-moment, Bayesian Method (FSBM) (Darendeli, 2001). Relevant for this thesis is the mean value presented for clays by Darendeli (2001), reproduced in Table 2.2:

Table 2.2: Model parameters presented for "Clays". From Darendeli (2001), Table 8.11.

ϕ1	0.0258	**ϕ10**	0.368
ϕ2	0.00195	**ϕ11**	0.466
ϕ3	0.0992	**ϕ12**	0.0223
ϕ4	0.226	**ϕ13**	-5.65
ϕ5	0.975	**ϕ14**	4
ϕ6	0.958	**ϕ15**	-5
ϕ7	0.00565	**ϕ16**	-0.725
ϕ8	-0.1	**ϕ17**	7.67
ϕ9	-0.196	**ϕ18**	2.16

3 Optimization tool

The Hornsea Wind Farm outside of England is one of many large offshore wind farms being developed today. The wind farm will have a capacity of approximately 2400 MW, covering the average daily need for over 2 million British homes. The wind farm spans over a total area of 696 km^2 (Orsted, 2019), thus encountering a large variety of geotechnical conditions, making site-specific analyses a vital part of the design process to keep the costs low. The PISA project (Byrne et al., 2017) carried out extensive field testing and numerical analysis to develop a new multi-spring framework for analyzing the monopile response in a conventional beam-column approach. One of the findings highlighted from the project was a confirmation that the current design guidelines (API, 2014) were unsatisfactory for the design of monopile foundations. The project also called for the necessity of using *finite element analysis (FEA)* when calibrating soil reaction springs. DNVGL-ST0126 (2018) requires that the soil reaction springs are calibrated by FEA. For this purpose, an optimization tool has been developed. The main function of the tool is to calibrate adequate soil reaction springs for any type of pile (slender pile, monopile etc.), in complex soil layering using a target pile response. The following chapter describes the details of the different functions of the tool, as well as verifying the tool itself. To describe the tool, some definitions for the terminology were established. The terminology is presented at the end of this chapter (section 3.4).

3.1 Methodology

To develop the optimization tool, the numerical computing program MATLAB (MATLAB, 2018) is used. The idea is to apply a certain set of modifiers to the calculated *resistance (p)* and *displacement (y)* values derived from a *p-y* formulation and scale the *p-y* curves to get a better fit to a target pile response (often FEA). This is done for each separate *p-y* spring along the pile. Zhang and Andersen (2017) showed that there exists a scaling factor between the stress-strain response of the soil and the *p-y* spring response.

To calculate the pile response by the reaction springs beam-column analyses are conducted, using the software "NGI-Pile". NGI-Pile is written in MATLAB by Dr. Zhang and was originally developed for analyzing piles under lateral cyclic loading. NGI-Pile is an equilibrium solver-based software and gives adequate solutions in terms of pile loading by following the principles of a conventional beam-column model. NGI-Pile follows a response spring approach and contains various *p-y* formulations. The optimization tool is designed to provide calibrated soil reaction springs, independent of any type of *p-y* formulation. The ones applied within this section are the *p-y* frameworks:

- API clay Matlock (1970).
- Zhang and Andersen (2017) flow-around monotonic p-y curves.

3.1.1 Running the tool

To get the desired *p*- and *y*-modifiers, the tool needs minimum one target pile response, which presents the pile response at a specific load level. The pile response is characterized by the deformation response (displacement/rotation) and/or cross-sectional structural forces (shear force/bending moment) along the pile length under a certain load applied laterally at the top (load level, H). This data can be acquired by different methods, e.g. in the validation-section of this chapter, the target pile response is calculated by FEA and field testing (Byrne et al., 2015b). One pile may have multiple target pile responses corresponding to the different load levels the pile has been tested for. An example of a target pile response is presented in Figure 3.1. The values displayed are valid for load level H=486 kN*.* There are two more target pile responses that are going to be accounted for when calculating the modifiers for this example, namely H=1098 kN and H=3711 kN*.* The target pile response for each of these load levels are presented on separate spreadsheets in the same way as for the displayed target pile solution for load level H=486 kN*.*

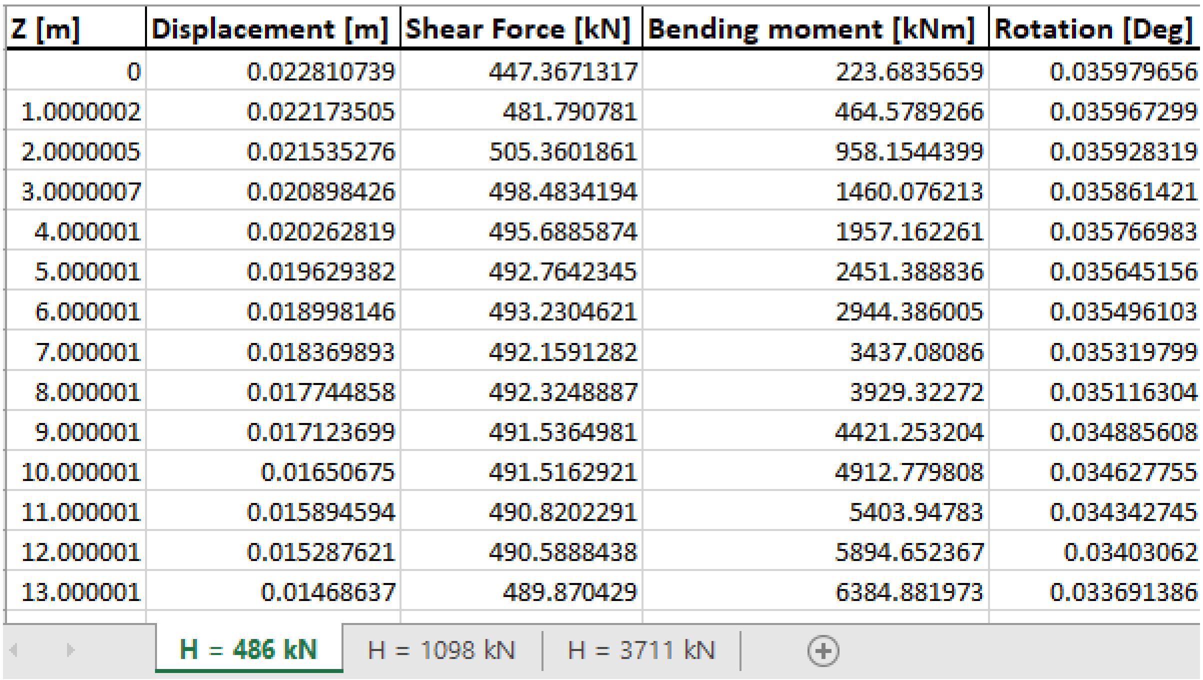

Z [m]	Displacement [m]	Shear Force [kN]	Bending moment [kNm]	Rotation [Deg]
0	0.022810739	447.3671317	223.6835659	0.035979656
1.0000002	0.022173505	481.790781	464.5789266	0.035967299
2.0000005	0.021535276	505.3601861	958.1544399	0.035928319
3.0000007	0.020898426	498.4834194	1460.076213	0.035861421
4.000001	0.020262819	495.6885874	1957.162261	0.035766983
5.000001	0.019629382	492.7642345	2451.388836	0.035645156
6.000001	0.018998146	493.2304621	2944.386005	0.035496103
7.000001	0.018369893	492.1591282	3437.08086	0.035319799
8.000001	0.017744858	492.3248887	3929.32272	0.035116304
9.000001	0.017123699	491.5364981	4421.253204	0.034885608
10.000001	0.01650675	491.5162921	4912.779808	0.034627755
11.000001	0.015894594	490.8202291	5403.94783	0.034342745
12.000001	0.015287621	490.5888438	5894.652367	0.03403062
13.000001	0.01468637	489.870429	6384.881973	0.033691386

Figure 3.1: Target pile response, for load level H=486 kN for Pile 2, described in section 3.2.1. The target pile responses for load levels H=1098 kN and H=3711 kN are also used as input and has similar spreadsheets.

The modifiers for each load level are calculated through an iterative procedure. The tool iterates by testing various modifiers to get the predicted pile response that most resembles the target pile response. Each spring gets the one *p*- and *y*-modifier that best replicates the target pile response at the corresponding load level at that depth. Consequently, each spring will be assigned one *p*- and *y*-modifier (*load level modifiers*) per load level. After the modifiers for each load level are calculated the *optimal modifiers* are calculated as the average of each load level modifier, producing one optimal *p*-modifier and one optimal *y*-modifier per spring. To visualize the process, the modifiers calculated by minimizing, with respect to cross-sectional rotation, are presented in Figure 3.2. The figure presents both the calculated load level modifiers and the average modifiers using the target pile responses presented in Figure 3.1.

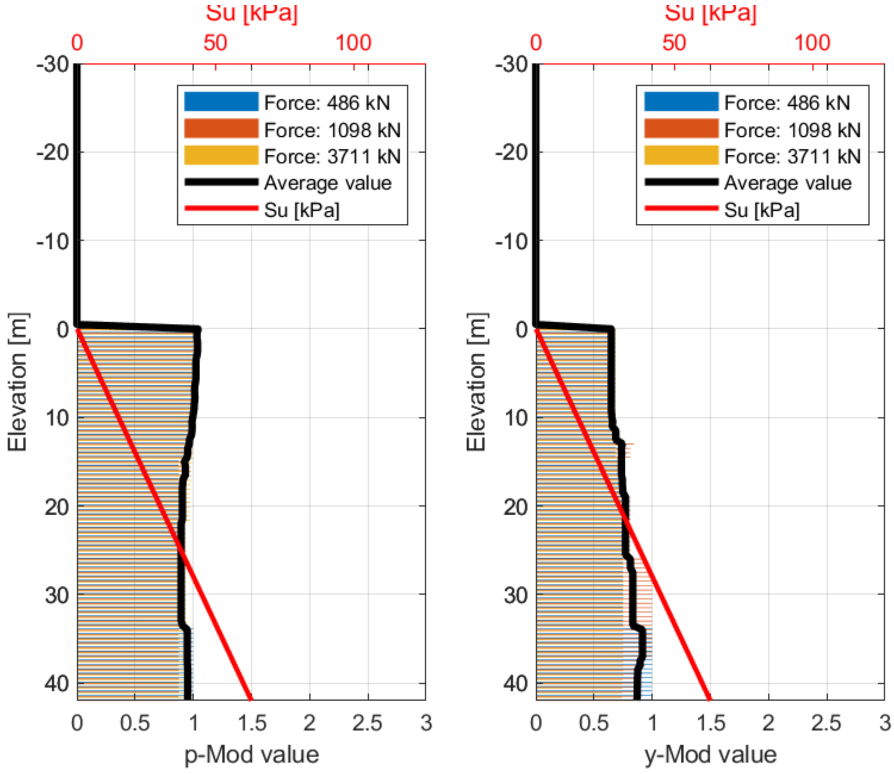

Figure 3.2: Calculated *p*- and *y*-modifiers for the different load levels, along with the optimal (average) modifiers. The upper 30 meters are above mudline.

After the optimal modifiers are calculated, the tool calculates the final pile behavior at the different load levels, and the change of error between the original pile response (no modifiers applied) and the pile response using the modified stiffness springs. Following the calculation of minimizing the cross-sectional rotation, the result of using the average *p*- and *y*-modifiers (Figure 3.2) are presented in Figure 3.3:

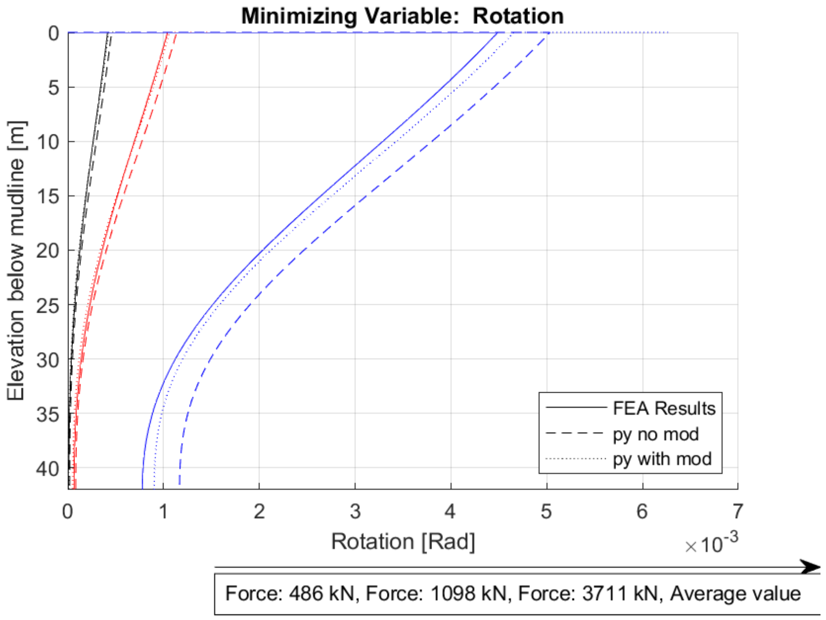

Figure 3.3: Cross-sectional rotation response at the applied load levels. "py with mod" and "py no mod" are the rotation responses with/without modifiers applied calculated by reaction springs.

3.1.2 Implementation of *p-y* formulations

The optimization tool is designed to scale all *p-y* springs, independent of formulation. The modifiers are implemented as direct scaling factors of the calculated *p-* and *y-* curves. For this exercise, the modifiers are applied at the API clay Matlock (1970) and Zhang and Andersen (2017) flow-around formulation by the following mathematical formulations.

API clay Matlock (1970)

The API clay Matlock (1970) recommendation provides equations for calculating p_u and y_c directly. Hence, the modifiers are applied by:

$$p_u = p_{u,0} * p_{mod}$$

$$y_c = y_{c,0} * y_{mod}$$

where $p_{u,0}$ and $y_{c,}$ are calculated by the conventional framework.

Zhang and Andersen (2017) flow-around monotonic p-y curves

The Zhang and Andersen flow-around recommendation (2017) describes the *p-y* response as a function of different variables. Hence, the implementation of the *p-* and *y-* modifiers are somewhat more complicated compared to the API clay Matlock recommendation. The modifiers are implemented by defining:

$$\left(\frac{G_0}{S_u}\right)_{modified} = \left(\frac{G_0}{S_u}\right)_{original} * \frac{1}{y_{mod}}$$

$$(p_u)_{modified} = (p_u)_{original} * p_{mod}$$

$$\left(\gamma_f^p\right)_{modified} = \left(\gamma_f^p\right)_{original} * y_{mod}$$

where p_{mod} and y_{mod} are the scaling factors (modifiers). With a basis on the formulations presented in section 2.4.1. It can be proven mathematically that these implementations lead to the following derivations:

$$P = \frac{p}{p_u} * p_u * p_{mod} = p * p_{mod}$$

$$Y = \frac{y}{D} * D = \left(\left(\xi_1 \frac{\tau}{G_0} + \xi_2 \gamma^p\right) D\right) * y_{mod}$$

The equations describes a specific point (*P,Y*) at the *p-y* curve. For explanation of the different parameters, the reader is directed to section 2.4.1.

3.1.3 Iteration procedure

The iteration procedure is based on principles adopted by the method of least squares. Each spring has one or more squared residual(s) to be minimized by the iteration procedure. For the activities conducted within this thesis, a squared residual is defined as the squared difference between the target pile response and the spring calculated pile response, for a chosen minimizing variable. Four minimizing variables are available: lateral/horizontal displacement, rotation, cross-sectional shear force and bending moment. In the following section the target pile response is denoted as a FEA solution. The squared residual is normalized by dividing it by its corresponding target pile response. The normalized squared residual is denoted as the error regarding the respective minimizing variable. Note that the definitions stated for the terms "residual" and "error" are solely for describing the iteration process conducted herein and are not to be confused with other definitions conducted in conventional statistical theory. Each minimizing variable has its own error calculated by the same principles, e.g. displacement error for a specific spring is calculated as:

$$E_{Displ}(p_{mod,i}) = \sqrt{\left(\frac{Displacement_{FEA} - Displacement_{py}(p_{mod,i})}{Displacement_{FEA}}\right)^2}$$

where $Displacement_{py}(p_{mod,i})$ is the pile displacement at a certain depth, calculated by the reaction springs, using the modifiers at iteration step *i* for the *p-y* spring. $Displacement_{FEA}$ is the target pile response at the corresponding depth, for this example, the pile displacement calculated by FEA. The tool is designed to minimize an error function, *E*. For cases when optimizing for one minimizing variable, the error function is set equal to the error of the chosen variable. If optimizing for multiple minimizing variables, the error function is defined as the sum of the different errors for each variable, equally weighted, e.g. when optimizing for all four minimizing variables the error function at a specific spring with modifiers at iteration step *i* is defined as:

$$E(p_i) = \frac{E_{Displ}(p_{mod,i}) + E_{Rot}(p_{mod,i}) + E_{SF}(p_{mod,i}) + E_{BM}(p_{mod,i})}{4}$$

where $E_{Rot}(p_{mod,i})$, $E_{SF}(p_{mod,i})$ and $E_{BM}(p_{mod,i})$ is the rotation-, shear force- and bending moment error respectively, with modifier p_i applied. The minimizing errors are defined by the same approach as presented for the displacement error above. This may lead to a situation where the modifiers will improve one error, while decreasing the accuracy of another. The tool finds the solution adequate as the improvement of one error is of a larger size than the decrease of the other.

The user decides if the tool iterates for the *p*- or the *y*- modifier first. The overall iteration process is conducted by iterating all springs for the chosen modifier first, then, using the iterated modifiers, the other modifier is iterated. For instance, when iterating for the *p*-modifier first, the *y*-modifiers are kept equal to one, until individual *p*-modifiers for all springs are found. The iteration for the *y*-modifier are then conducted using the iterated *p*-modifier for all springs while iterating for the *y*-modifiers. The section below describes the iteration process when iterating for the *p*-modifiers first. For clarification, Figure 3.4 presents the iteration process by a flow chart. The mathematical formulations are presented after a description.

The iteration procedure starts by performing two actions. A calculation of the *p-y* response with all modifiers equal to one and a calculation of the corresponding error function for each spring as defined in the equation(s) above. The second step of the iteration is performed by setting all the *p*-modifiers equal to an *upper limit* defined by the user and calculating the corresponding pile response and error function. If the error function has decreased, the tool registers the new value of the error function as the lowest, along with the modifier. If the error function has increased it is assumed that the optimal modification value is below the upper limit, and a new round of calculations is started by setting the *p*-modifier equal to the middle of the previous tested parameter, and the optimal solution at that time. When a spring has a new all-time low value for the error function, the *p*-modifier is stored as the new optimal modifier along with the value of the error function. The tool calculates the next *p*-modifier value to be tested as the middle of the new optimal modifier, and the one tested prior to the optimal modifier. The

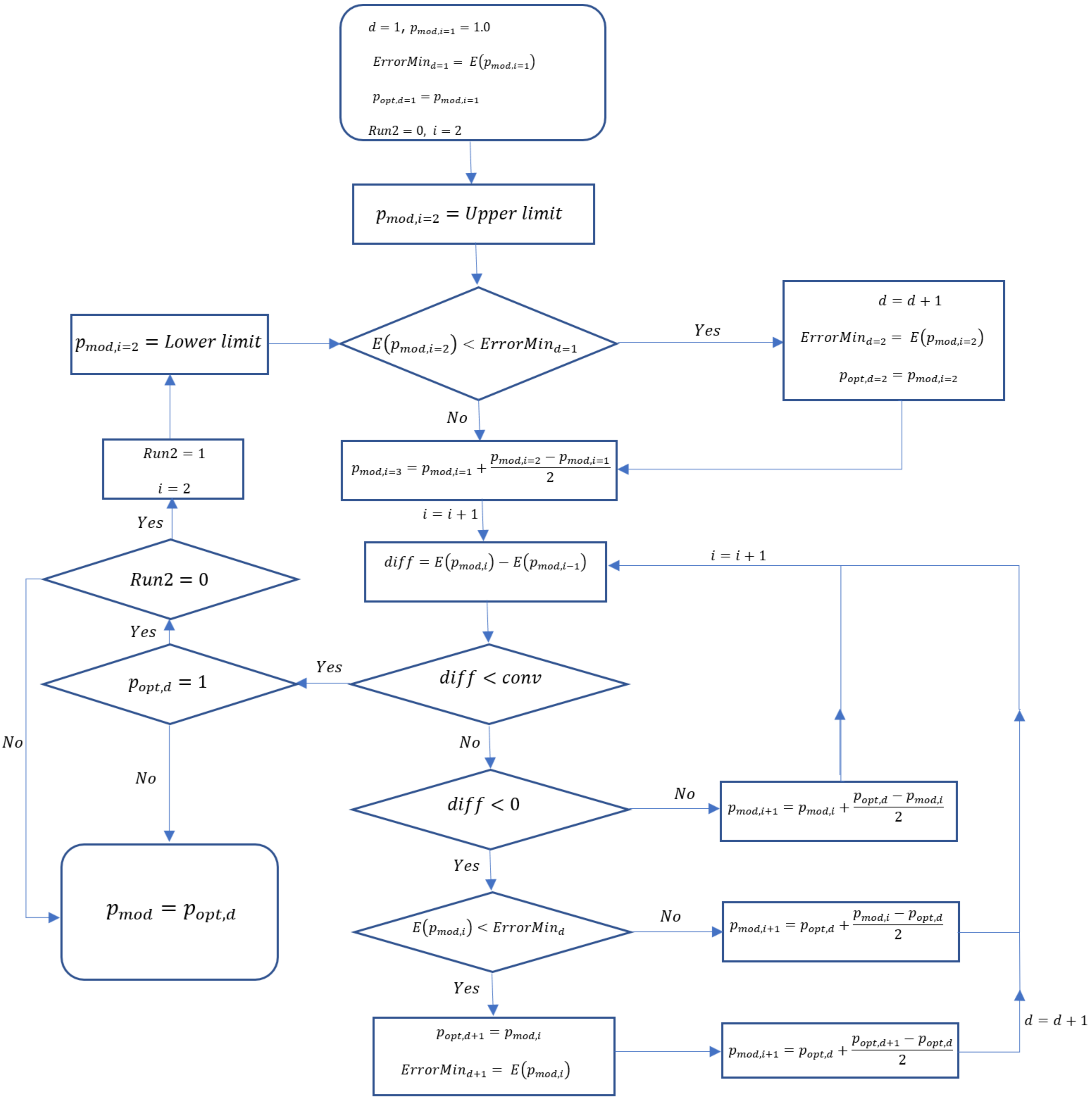

Figure 3.4: Flow chart of the iteration process for the p-modifier for one spring. The same principles are conducted when iterating for the y-modifier.

solution has converged when the difference between the value of the error function calculated for the previous and the current modifier are below a user set value, named the *convergence limit* (*conv*). If the iteration converges towards the initial modifier value of 1, a new round of iterations is started by changing the modifier to the *lower limit*, defined by the user. The tool will follow the same principles, calculating a converged modifier solution based on the same halving principle procedure as described for the upper limit solution. After finding the optimal *p*-modifiers, the iteration process is repeated by the same principles for the *y*-modifiers. By applying this procedure for each separate spring along the pile embedded into the ground, *p*- and *y*-modifiers are found for each separate spring. By defining *i* as the iteration step, the process of iterating the *p*-modifier for one spring is mathematically described as:

$i = 1$:

$$d = 1$$

$$p_{mod,i=1} = 1.0$$

$$ErrorMin_{d=1} = E(p_{mod,i=1})$$

$$p_{opt,d=1} = p_{mod,i=1}$$

$i = 2$:

$$p_{mod,i=2} = Upper\ limit$$

$$d = d + 1, \qquad E(p_{mod,i=2}) < ErrorMin_{d=1}$$

$$ErrorMin_{d=2} = E(p_{mod,i=2}), \qquad E(p_{mod,i=2}) < ErrorMin_{d=1}$$

$$p_{opt,d=2} = p_{mod,i=2}, \qquad E(p_{mod,i=2}) < ErrorMin_{d=1}$$

$$p_{mod,i=3} = p_{mod,i=1} + \frac{p_{mod,i=2} - p_{mod,i=1}}{2}$$

$i \geq 3$:

$$diff = E(p_{mod,i}) - E(p_{mod,i-1})$$

$$p_{opt,d+1} = p_{mod,i}, \qquad E(p_{mod,i}) < ErrorMin_d$$

$$ErrorMin_{d+1} = E(p_{mod,i}), \qquad E(p_{mod,i}) < ErrorMin_d$$

$$p_{mod,i+1} = \begin{cases} p_{mod,i} + \dfrac{p_{opt,d} - p_{mod,i}}{2}, & diff > 0 \\ p_{opt,d} + \dfrac{p_{opt,d+1} - p_{opt,d}}{2}, & E(p_{mod,i}) < ErrorMin_d \\ p_{opt,d} + \dfrac{p_{mod,i} - p_{opt,d}}{2}, & diff < 0 \ \ and\ E(p_{mod,i}) > ErrorMin_d \end{cases}$$

$$d = d + 1, \qquad E(p_{mod,i}) < ErrorMin_d$$

The iteration procedure continues until the *difference* (*diff*) value is below the user defined *convergence limit* (*conv*). As previously mentioned, if the solution converges towards a modifier equal to one, the tool repeats the same procedure setting the modifier equal to the lower limit, instead of the upper limit at iteration step two. To capture neighboring trends, the tool performs the iteration process at all springs simultaneously. Meaning that step one (*i=1*) is applied at all springs, followed by step two (*i=2*) applied at all springs, then step three etc. After a spring-modifier has converged, the modifier for that specific spring is kept constant. The tool iterates until all springs have converged towards a specific modifier. When iterating for the *p*-modifier at first, the tool will find all converged *p*-modifiers before it starts to iterate the *y*-modifier by the same principles as for the *p*-modifiers. The different *p*-modifiers are kept constant equal to the pre-calculated converged value during the *y*-modifier iteration.

Figure 3.5. presents an example of the error function for one specific spring, plotted against the modifier values. Upper- and lower limit were chosen as 1.5 and 0.5 respectively. The points display the calculated error function at different modification values. The optimal solution was found to be 1.0737, and 1.000244 for the *p*- and *y*-modifiers respectively.

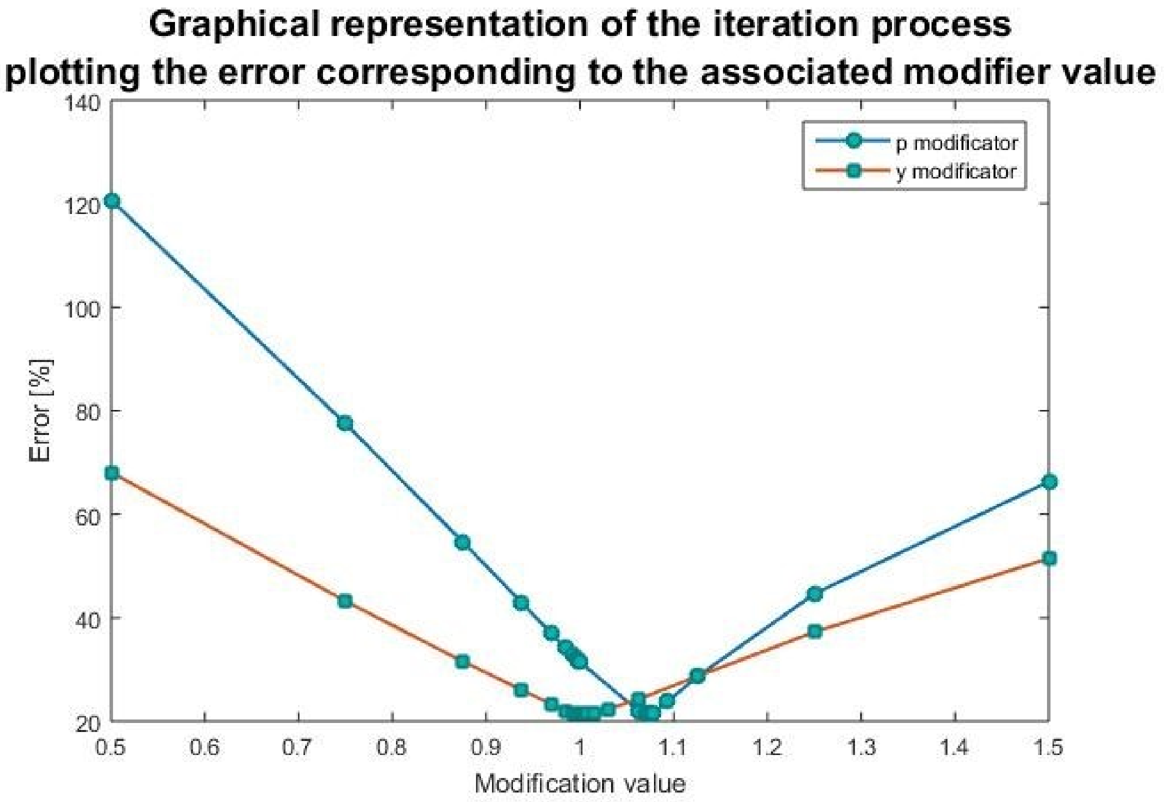

Figure 3.5: The iteration process started at the lower limit with a modification value equal to 0.5, then halving it to 0.75, until it converged toward an optimal modifier value equal to 1. Hence, the tool applied the upper modifier value equal to 1.5. Following the same halving principle, the solution converged towards 1.0737, and 1.000244 for the p- and y-modifier respectively. NB: To get a better visualization of the iteration process, the iteration started at the lower limit, as opposite of the description above.

Due to numerical issues, the tool excludes a minimizing variable for a spring if the FEA-result is below a certain value. For lateral displacement and cross-sectional rotation, the minimum values were defined as 5% of the maximum value of the corresponding minimizing variable. For bending moment and shear force, the error calculation is excluded if the FEA-calculated response is below 1% of the maximum value of the corresponding minimizing variable.

3.2 Validation

The tool serves its purpose if it is able to find adequate soil reaction springs that would have an improved prediction of the chosen minimizing variable(s) for the pile response. To achieve this goal, the tool needs to calculate adequate soil reaction springs independent of the chosen *p-y* formulation, and the pile- and soil properties. Thus, the tool is validated by three parts:

- Pile geometry variation: The robustness of the tool is tested by calculating adequate modifiers for several pile geometries in an idealized normally consolidated clay profile.
- Site-specific soil profile: The tool is tested by using field data from the PISA-project as the target pile response. The soil profile has a large variation of shear strength.
- Alternative *p-y* formulation: The generality of the tool is tested by calculating reaction springs with a basis on the API clay Matlock (1970) formulation.

In all cases, each minimizing variable is tested separately, before all available minimizing variables are tested combined. The reduction of error for each spring is normalized by:

$$Error\ reduction\ [\%] = \frac{E(p_{i=1}) - E(p_{opt})}{E(p_{i=1})} * 100$$

where *E* is the error function as described in section 3.1.3. Hence, an error reduction of 100% indicates that the spring-calculated pile response, with the modifiers applied is completely alike the target pile response. An error reduction of 0% indicates that there is no change in the pile behavior, consequently a negative error reduction indicates that the difference between the FEA- and spring calculated pile response have increased. The error reductions presented in the sections below, are calculated as the average error reduction of all pile-springs. The results are discussed, and noticeable results are visualized by various plots.

3.2.1 Pile variation

The tool should be as robust and versatile as possible. Therefore, it should be able to calculate accurate modifiers, independent of pile properties. Hence, the tool is validated by optimizing three different piles with various *length relative to diameter* (*L/D)* ratios. The pile response is calculated using three spring components. The *p-y* formulation presented by Zhang and Andersen (2017), the *base shear* (*s-u*) and *moment rotation* (*m-r*) springs, presented in Zhang and Andersen (2019a) and (2019b) respectively. The iteration is conducted by optimizing the *y*-modifier first.

The target pile response solutions were calculated in the finite element software Abaqus (Abaqus, 2017), by Dr. Zhang. To limit the complexity of the problem, the soil was modeled based on the following assumptions:

- The soil is described with an isotropic stress-strain profile with linearly increasing shear strength with depth.
- No tension gap occurring, hence the soil is assumed weightless.

For more details on the methodology regarding the soil model and Abaqus calculations, the reader is referred to the description of the Abaqus model used in Zhang and Andersen (2019a, p. 100). The remaining relevant soil parameters are summarized in Table 3.1.

Table 3.1: Soil properties.

G_0/S_u [-]	$\gamma^p{}_f$ [-]	α (Pile-soil interface roughness factor)	Shear strength [kPa] z = depth below mudline [m]	ϕ [°]
1000	0.10	1	0.1 + 1.5z	0

Three different piles are tested, ranging from a *L/D*-ratio of 5 to 10. The load is applied laterally at the pile top. Young's modulus for the pile is set equal to 210 GPa*.* The element length is chosen to be 0.5 m, giving one node/spring every half. Upper limit is equal to 2, lower limit is equal to 0.5. Other relevant properties are summarized in Table 3.2.

Table 3.2: Pile geometries used for validation.

	Diameter [m]	Stick-up [m]	Penetration depth [m]	*L/D* [-]	Wall thickness [m]
Pile 1	6	30	30	5	0.06
Pile 2			42	7	
Pile 3			60	10	

Displacement

Table 3.3: Error reduction when minimizing with respect to displacement.

	Load level [kN]	Error reduction [%]
Pile 1	486	56.18
	1098	88.56
	1648	80.36
Pile 2	486	47.03
	1098	64.68
	3711	59.77
Pile 3	973	22.05
	2195	67.58
	7423	60.37

The tool provides more accurate solutions for each of the load levels across the different pile geometries. To visualize the results the displacement with/without modifiers along with the FEA displacement for pile 1 and its associated modifiers are presented in Figure 3.6. and Figure 3.7.

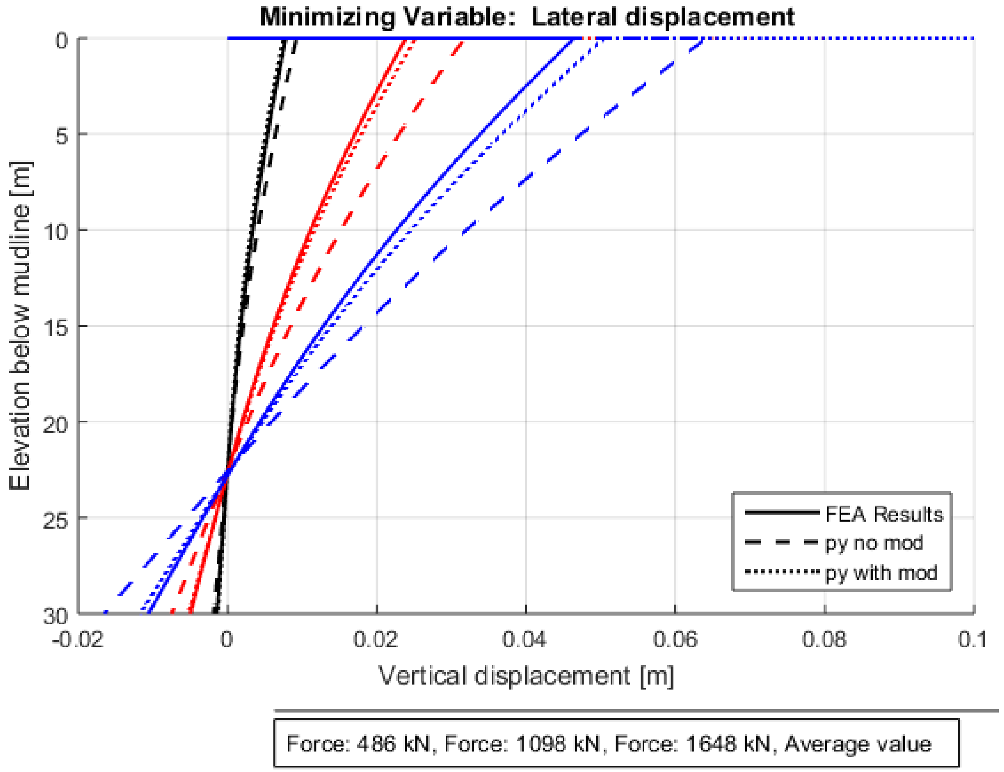

Figure 3.6: The displacement of pile 1 with and without modifiers and the FEA calculated displacement for three different load levels.

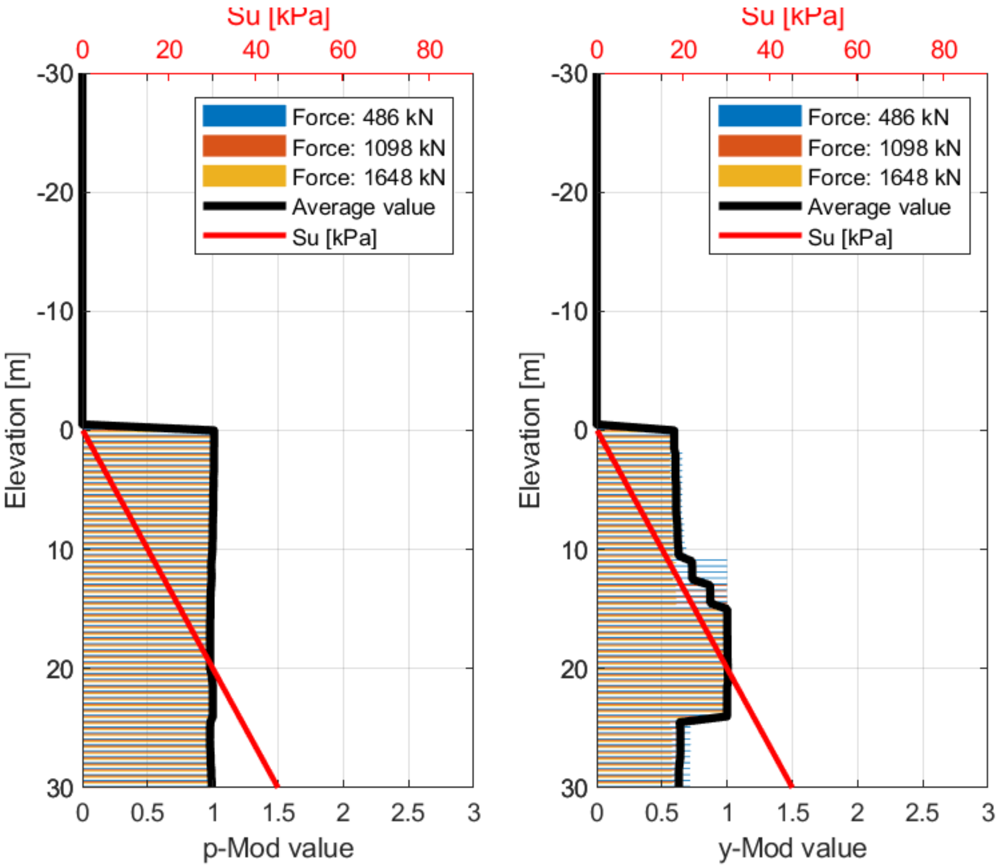

Figure 3.7: The modifiers for each load level are calculated separately. The final modifiers are calculated as the average value of the modifiers for each load level, presented as the solid black line.

Shear force

Table 3.4: Error reduction when minimizing with respect to shear force.

	Load level [kN]	Error reduction [%]
Pile 1	486	27.62
	1098	21.20
	1648	16.21
Pile 2	486	45.10
	1098	29.07
	3711	-45.41
Pile 3	973	36.17
	2195	21.94
	7423	-131.91

The tool performs adequately when minimizing with respect to shear force.

Bending moment

Table 3.5: Error reduction when minimizing with respect to bending moment.

	Pile Load [kN]	Error reduction [%]
Pile 1	486	-21.15
	1098	-24.57
	1648	-67.70
Pile 2	486	-106.35
	1098	-81.41
	3711	-112.47
Pile 3	973	-179.88
	2195	-563.60
	7423	-455.16

Even though the Zhang and Andersen (2017) formulation was developed with a basis on stiffer clay profiles, the formulation gives a good prediction of the pile response with no modifiers applied, especially for the longer piles (pile 3). For this case, a weakness of the tool is observed. The tool finds adequate modifiers at the top section of the pile and stop iterating this section. These modifiers were kept constant, while the rest of the pile iteration continued. These top modifiers influenced the calculated bending moment further down the pile, making the pile response with the modifiers applied worse off. The incident is visualized in Figure 3.8 and Figure 3.9 for pile 3 by presenting the calculated bending moment, and the *average change of error* $(E(p_{i=1}) - E(p_{opt}))$. As the bending moment prediction is precise initially, the normalized bending moment error is highly sensitive, giving error reductions of a large negative magnitude.

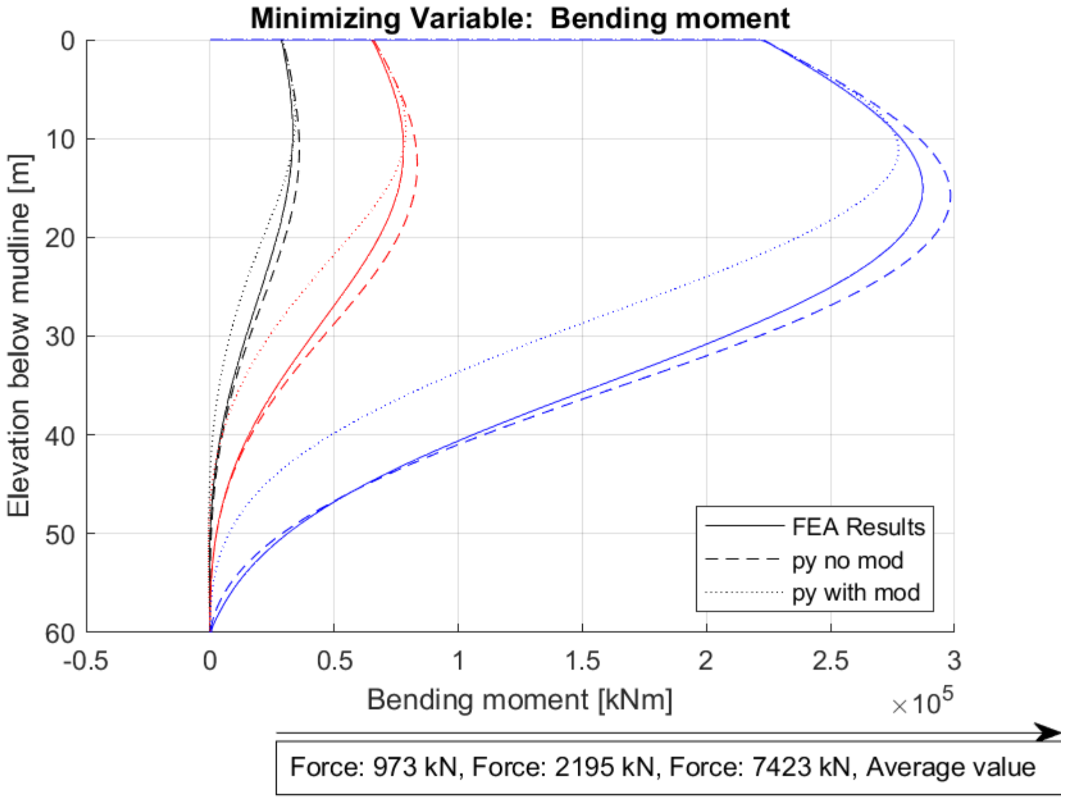

Figure 3.8: Bending moment with and without modifiers, compared to FEA for pile 3. A reduction in accuracy is observed.

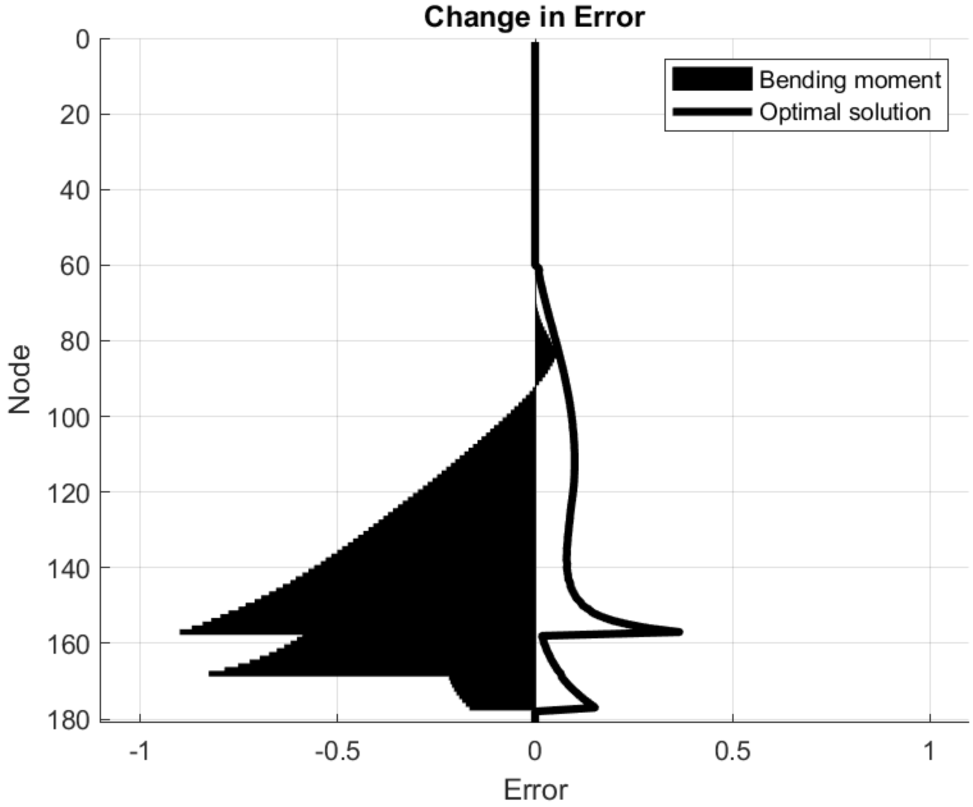

Figure 3.9: The average change of error for pile 3. An increase in precision is observed at the top 15 meters of the pile below mudline (node 60), thus keeping the calculated spring modifiers at top constant.

Rotation

Table 3.6: Error reduction when minimizing with respect to cross-sectional rotation.

	Load level [kN]	Error reduction [%]
Pile 1	486	64.61
	1098	53.43
	1648	62.88
Pile 2	486	70.65
	1098	38.26
	3711	74.81
Pile 3	973	43.80
	2195	54.00
	7423	73.37

The tool performs adequately when minimizing with respect to cross-sectional rotation.

Combined displacement, shear force, rotation and bending moment

Table 3.7, 3.8 and 3.9 presents the calculated error reduction for pile 1, 2 and 3 respectively when minimizing with respect to all variables.

Table 3.7: Error reduction for pile 1 when minimizing with respect to all variables.

Pile load [kN]		Error reduction [%]
486	Displacement	55.62
	CS Rotation	58.67
	Bending moment	18.94
	Shear force	7.09
	Combined	**35.25**
1098	Displacement	64.56
	CS Rotation	55.81
	Bending moment	17.50
	Shear force	20.26
	Combined	**36.92**
1648	Displacement	65.79
	CS Rotation	62.19
	Bending moment	-9.57
	Shear force	28.00
	Combined	**39.85**

Table 3.8: Error reduction for pile 2 when minimizing with respect to all variables.

Pile load [kN]		Error reduction [%] (Change of error)
486	Displacement	-33.81 (-2.19)
	CS Rotation	83.29
	Bending moment	-10.21 (-0.72)
	Shear force	46.71
	Combined	**34.70**
1098	Displacement	11.66
	CS Rotation	80.84
	Bending moment	17.36
	Shear force	53.18
	Combined	**48.65**
3711	Displacement	-5.13
	CS Rotation	-5.35
	Bending moment	5.91
	Shear force	36.01
	Combined	**21.65**

Table 3.9: Error reduction for pile 3 when minimizing with respect to all variables.

Pile load [kN]		Error reduction [%] (Change of error)
973	Displacement	-41.61 (-1.32)
	CS Rotation	61.92
	Bending moment	55.64
	Shear force	25.81
	Combined	**20.13**
2195	Displacement	70.45
	CS Rotation	76.70
	Bending moment	51.56
	Shear force	52.84
	Combined	**43.50**
7423	Displacement	32.55
	CS Rotation	39.62
	Bending moment	34.67
	Shear force	47.27
	Combined	**33.37**

As previously discussed, the spring model performed very good, resulting in large negative normalized error reductions at small deteriorations. For instance, for the displacement response for pile 3 (Table 3.9.). At load level 973 kN, the average error reduction is -41.61%, even though the change of error is only -1.32%.

To visualize the results, the average change in error for each minimizing variable for pile 1 is presented below in Figure 3.10. The solid lines show the optimal error change, while the bars show the error change with the modifiers applied. The error reduction may be visualized as the area of the bars “divided” by the area created by the optimal line.

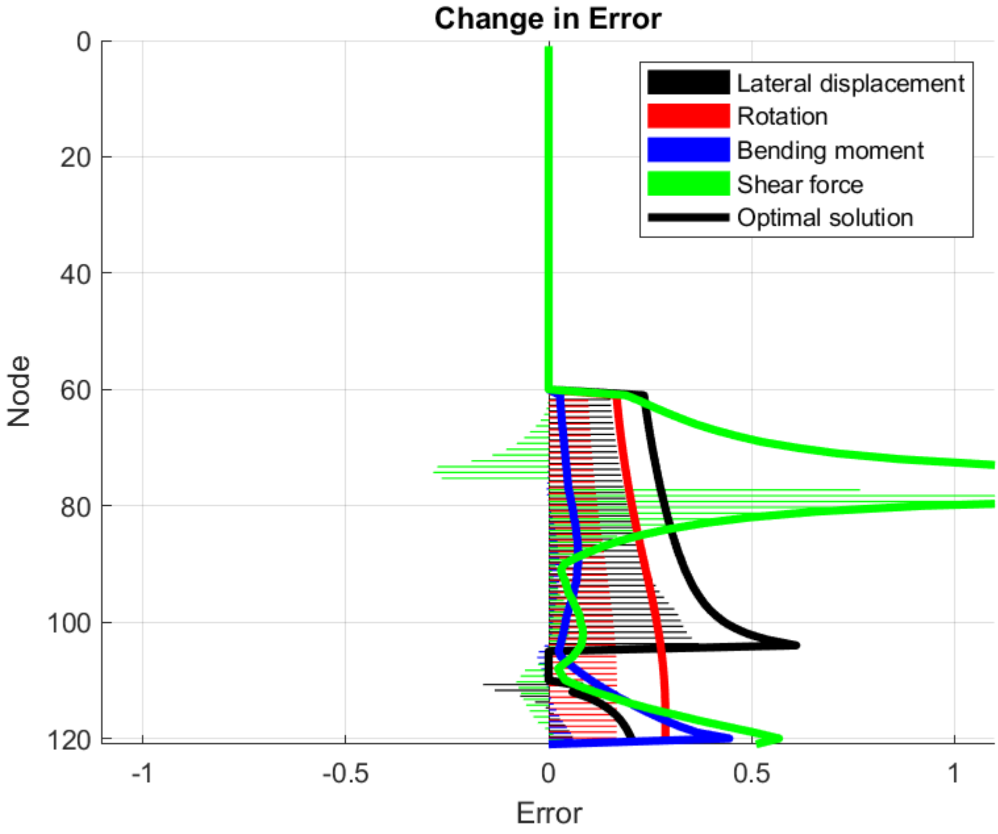

Figure 3.10: The average change in error for the load levels, when optimizing for all four minimizing variables for pile 1. The bars show the change in error, while the solid lines are the optimal solution for that specific variable corresponding to the same color.

3.2.2 Soil strength variation

To validate the robustness of the tool, field test data from the PISA project (Byrne et al., 2015b) is used as the target pile response. The pile response is calculated using three spring components. The *p-y* formulation presented by Zhang and Andersen (2017), the base shear and moment rotation springs, presented in Zhang and Andersen (2019a) and (2019b) respectively. The iteration was conducted by optimizing the *y*-modifier first.

FEA-data is in general considered the most accurate description of reality achievable by a computer simulation. But it may give an idealized picture which may lead to a smooth and theoretical numerical connection for force- and displacement values along the pile depth. In reality the case may be different. Factors and variables which are out of our hands to control and measure are hard to model in a finite element model. Hence, to validate the robustness of the tool, field test data from the PISA project is used as the target pile response.

The methodology and execution of the field testing are presented by Byrne et al. (2015b). The target response is the rotation and bending moment data from field testing at a glacial till site in Cowden, tested by monotonic loading. The strength profile varies between 40-128 kPa (Byrne et al., 2017). The stiffness profile is based on the stiffness degradation data reported by Powell and Butcher (2003) and by the experience of Dr. Zhang, based on soil plasticity and over consolidation ratio. Due to relatively short piles (7.6m embedded into the ground), the element length is equal to 0.2.

The validation is conducted by optimizing with respect to rotation and bending moment. First separately, then combined. The results are presented by the average error reduction for all springs at the various load levels, along with figures showing the pile response and the average change in error for each node/spring. The soil properties and pile geometry are summarized in Table 3.10, Table 3.11 and Figure 3.11:

Table 3.10: Soil properties.

G_0/S_u [-]	γ^{p}_{f} [-]	α (Pile-soil interface roughness factor)	γ' [kPa]	ϕ [°]
500	0.20	0.3	0 (No tension crack behind the pile)	0

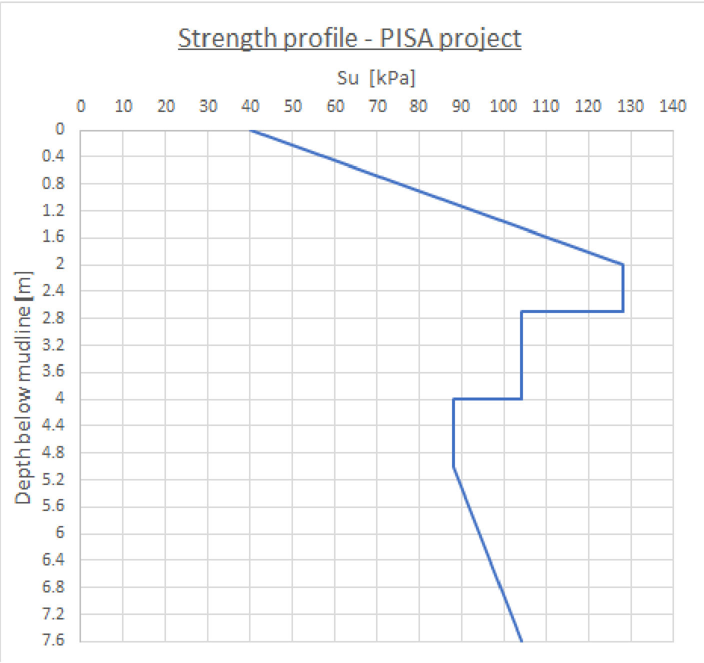

Figure 3.11: Assumed strength profile for Cowden test site (Zhang & Andersen, 2019a).

Table 3.11: Pile geometry.

Diameter [m]	Stick-up [m]	Penetration depth [m]	*L/D* [-]	Wall thickness [m]
0.762	10	7.6	10	0.025

Rotation

Table 3.12: Error reduction when minimizing with respect to rotation.

Pile load [kN]	Error reduction [%]
113	73.55
395	87.05

The results are visualized in Figure 3.12 and Figure 3.13 by the pile cross-sectional rotation and change of error.

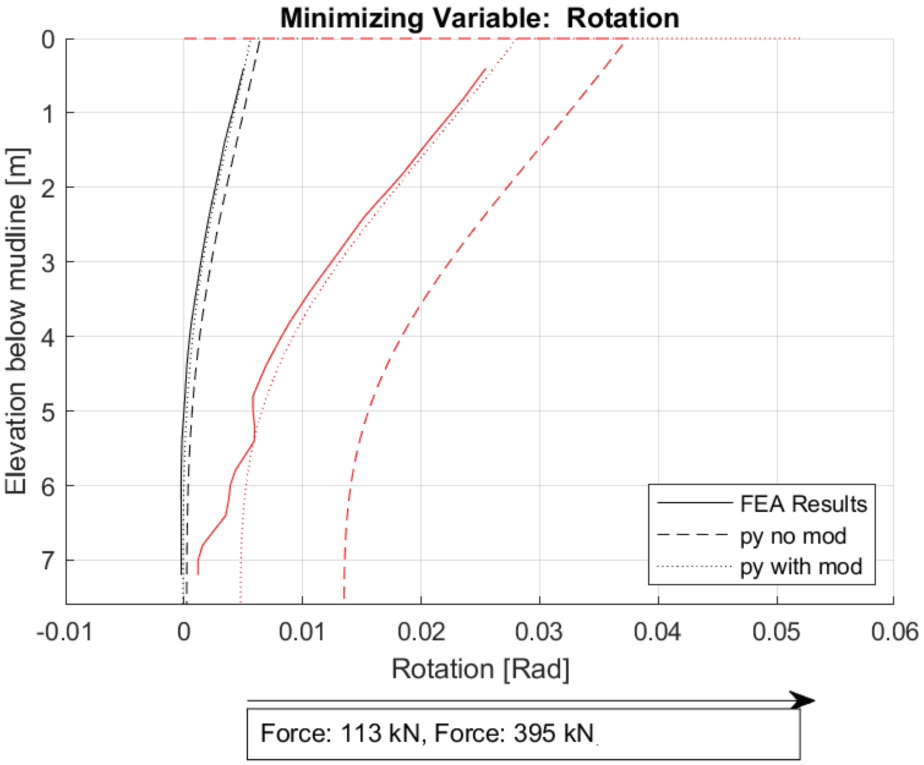

Figure 3.12: Cross-sectional rotation of the PISA field pile and the pile response calculated from reaction curves. Please note that the legend wrongfully says that the solid line is FEA Results. The solid line is the field test data.

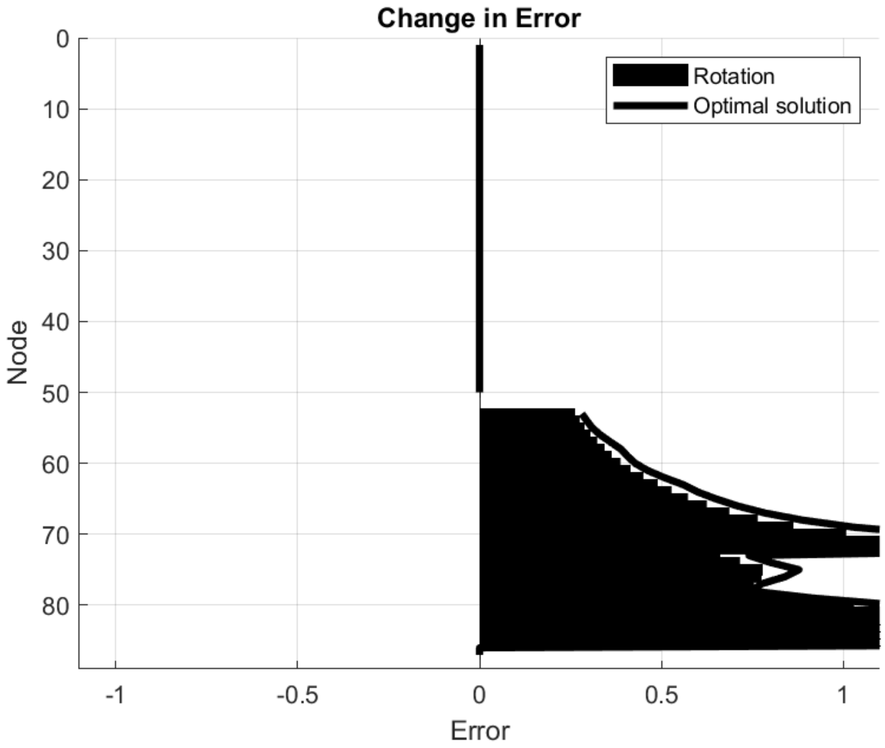

Figure 3.13: The average change in error for each node/spring of the pile. Note at the mudline and pile bottom, there are no rotation data which led to the gaps in the plot.

Bending moment

Table 3.13: Error reduction when minimizing with respect to bending moment.

Pile load [kN]	Error reduction [%]
113	-196.35
395	-85.33

As visualized by Figure 3.14 and Figure 3.15, the same phenomena as discussed in section 3.2.1. occurred when minimizing for bending moment solely.

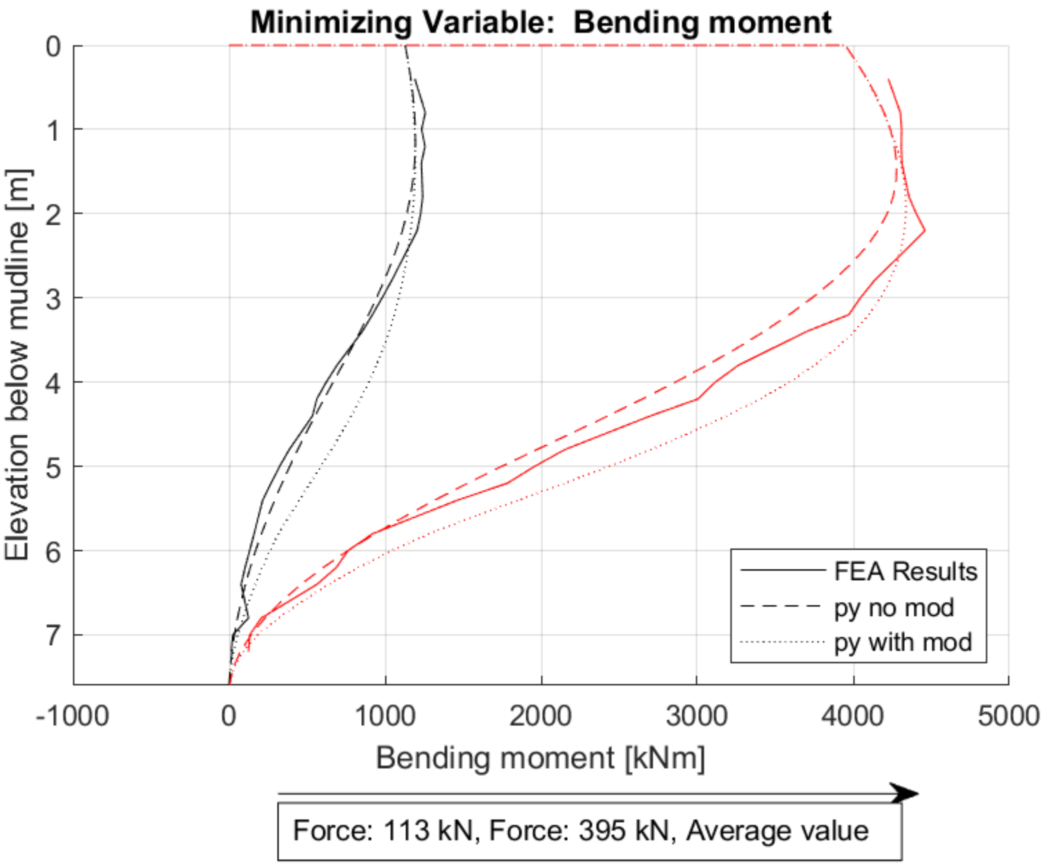

Figure 3.14: Bending moment response. Please note that the legend wrongfully says that the solid line is FEA Results. The solid line is the field test data.

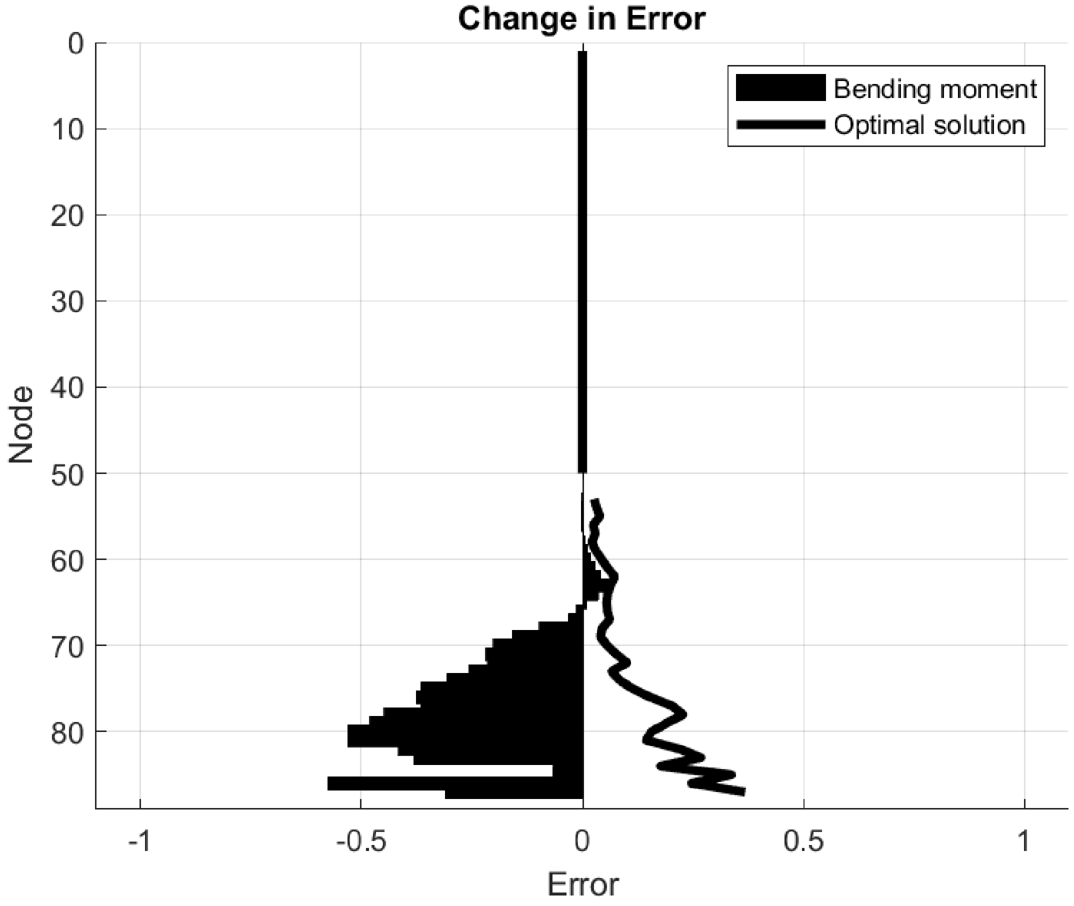

Figure 3.15: The average change of error. An increase of error prediction is observed at the top 3 meters below mudline (Node 50-65).

Combined rotation and bending moment

Table 3.14: Error reduction when minimizing with respect to all variables.

Pile load [kN]		Error reduction [%] (Error change)
113	Rotation	70.95
	Bending moment	4.55
	Combined	**49.95**
395	Rotation	76.37 (+94.64)
	Bending moment	-80.87 (-5.71)
	Combined	**66.93 (44.25)**

The optimization tool calculates adequate modifiers that increase the accuracy of all variables, except for the bending moment at load level 395 kN. The pile rotation and bending moment are visualized in Figure 3.16.

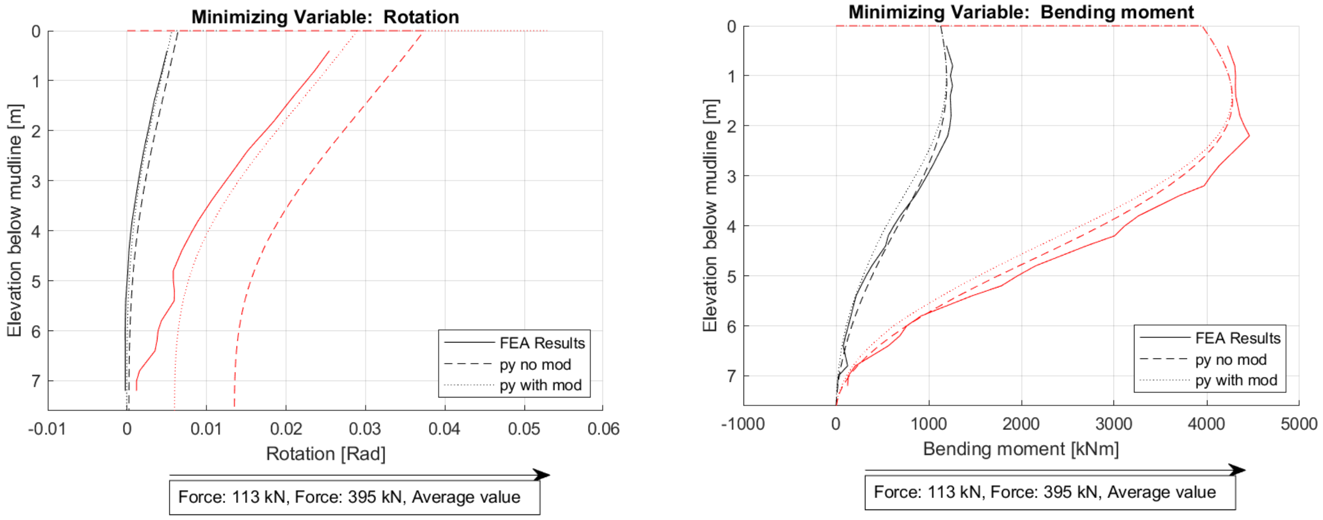

Figure 3.16 left: Cross-sectional rotation of the pile with and without the modifiers applied. Right: Bending moment of the pile with and without the modifiers applied. Please note that the legend wrongfully says that the solid line is FEA Results. The solid line is the field test data.

The average change in error per spring is presented in Figure 3.17.

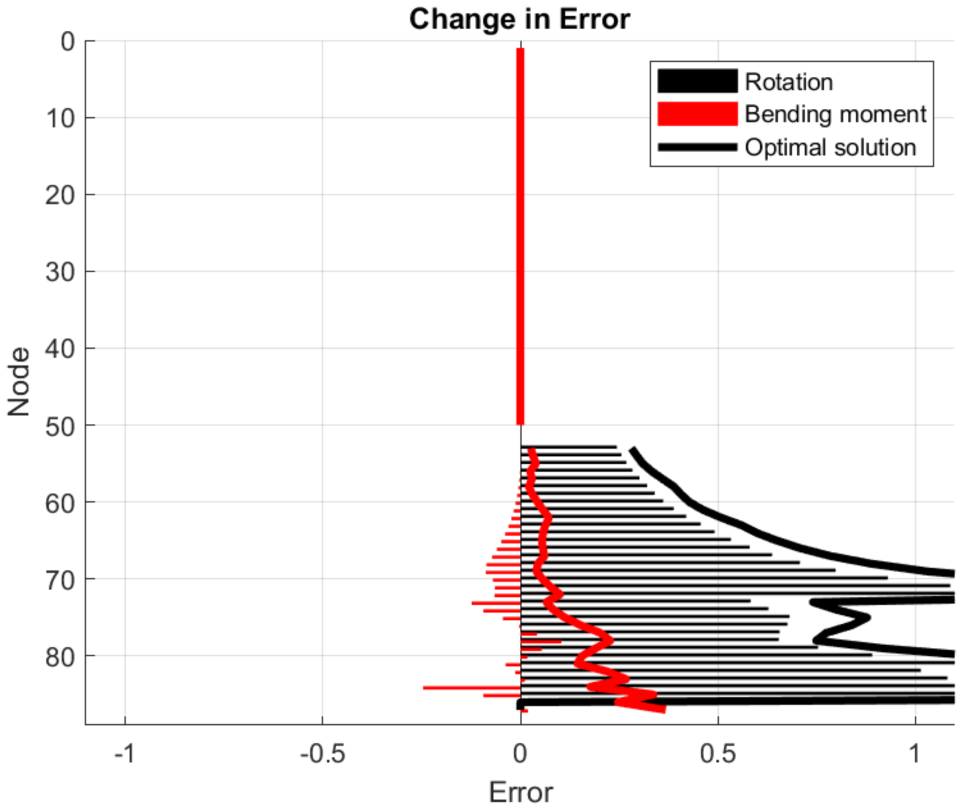

Figure 3.17: The average change in error for the different load levels, when optimizing for both cross-sectional rotation and bending moment. The bars show the change in error. The solid lines are the optimal solution for that specific variable corresponding to the same color.

3.2.3 API approach

To validate the generality, the tool is tested using the API clay Matlock (1970) formulation. The FEA results for pile 1, as described in section 3.2.1., are used as the target pile response.

The API clay Matlock (1970) formulation has proven to perform inadequately when calculating the pile response of a monopile (Byrne et al., 2017), (Zhang et al., 2016). Hence, the tool will serve its purpose if it can provide adequate soil reaction springs, by scaling the API stiffness curves.

Pile 1 is chosen as it has the lowest *L/D* of the tested piles. The pile geometry is presented in section 3.2.1., Table 3.2.

The API-framework assumes wedge failure with no suction occurring. Thus, an effective unit weight of the soil layer of 7 kN/m^3 is assumed. The relevant parameters for the are presented in Table 3.15.

Table 3.15: Soil parameters.

Shear strength [kPa] z = depth [m]	J [-]	ε_{50} [-]	γ' [kN/m^3]	α	γ^p_f [-]	G_0/S_u [-]	ϕ [°]
0.1 + 1.5z	0.5	0.01	7	1	0.10	1000	0

Displacement

Table 3.16: Error reduction when minimizing with respect to displacement.

Pile load [kN]	Error reduction [%]
486	93.11
1098	91.17
1648	93.91

As seen in Figure 3.18, the API *p-y* formulation with optimal spring modifiers applied provide a good match to the finite element analysis. The modifiers increase the accuracy through the entire pile depth.

As seen by Figure 3.19, the tool did not calculate modifiers at the depth of 21 to 25 m. Within this depth, the displacement was below 5% of the maximal FEA-pile displacement value, thus validating the exclusion function of the tool.

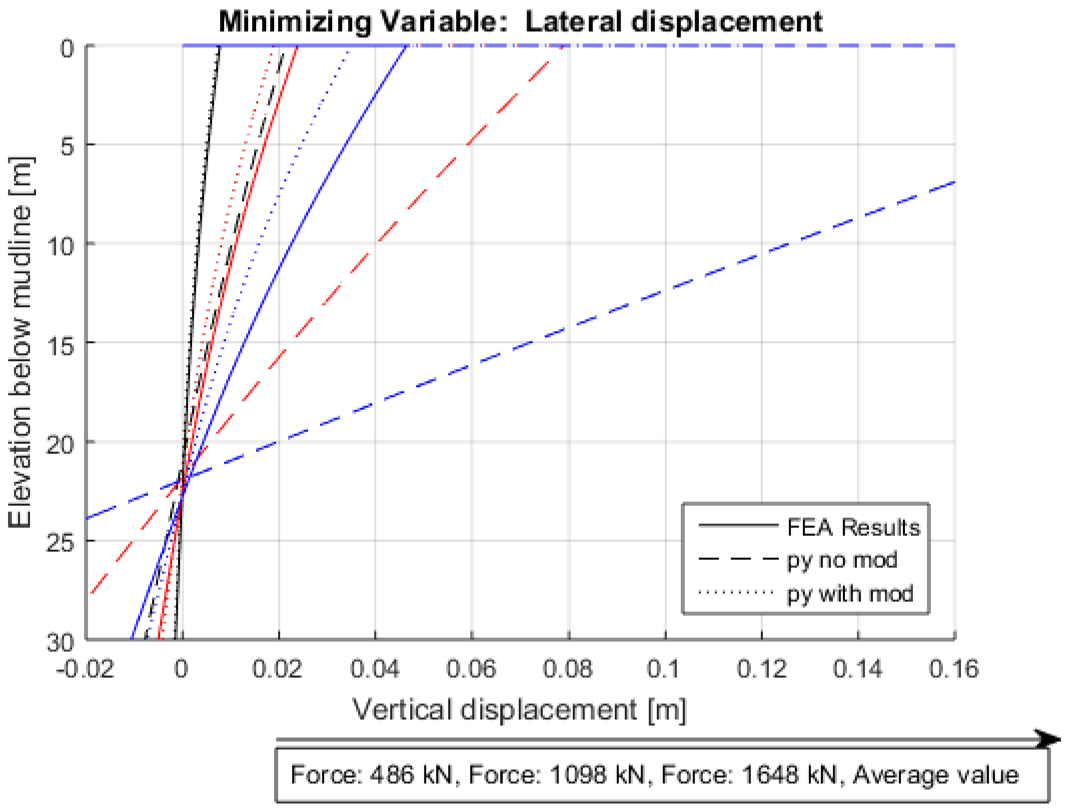

Figure 3.18: Pile response when minimizing for lateral displacement.

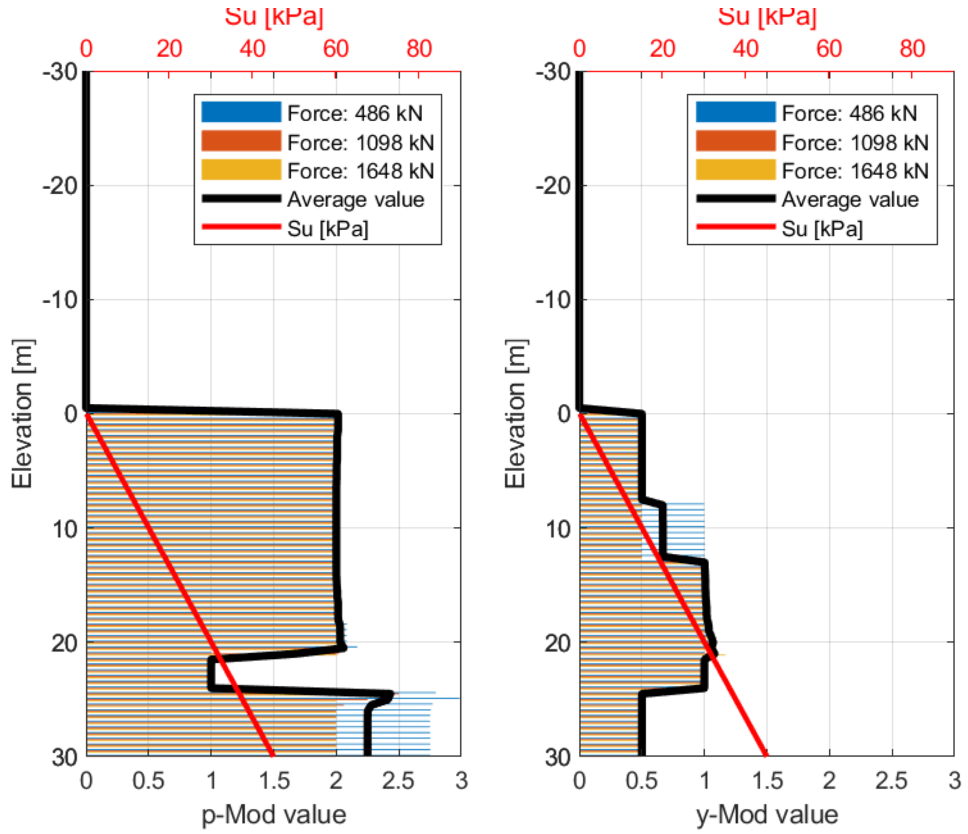

Figure 3.19: p- and y-modifiers applied at the stiffness springs.

Shear force

Table 3.17: Error reduction when minimizing with respect to shear force.

Pile load [kN]	Error reduction [%]
486	-196.94
1098	-44.34
1648	-27.90

The tool does not perform well when minimizing with respect to shear force solely. As seen by Figure 3.20, the pile response with the modifiers applied at the reaction springs follows no specific pattern.

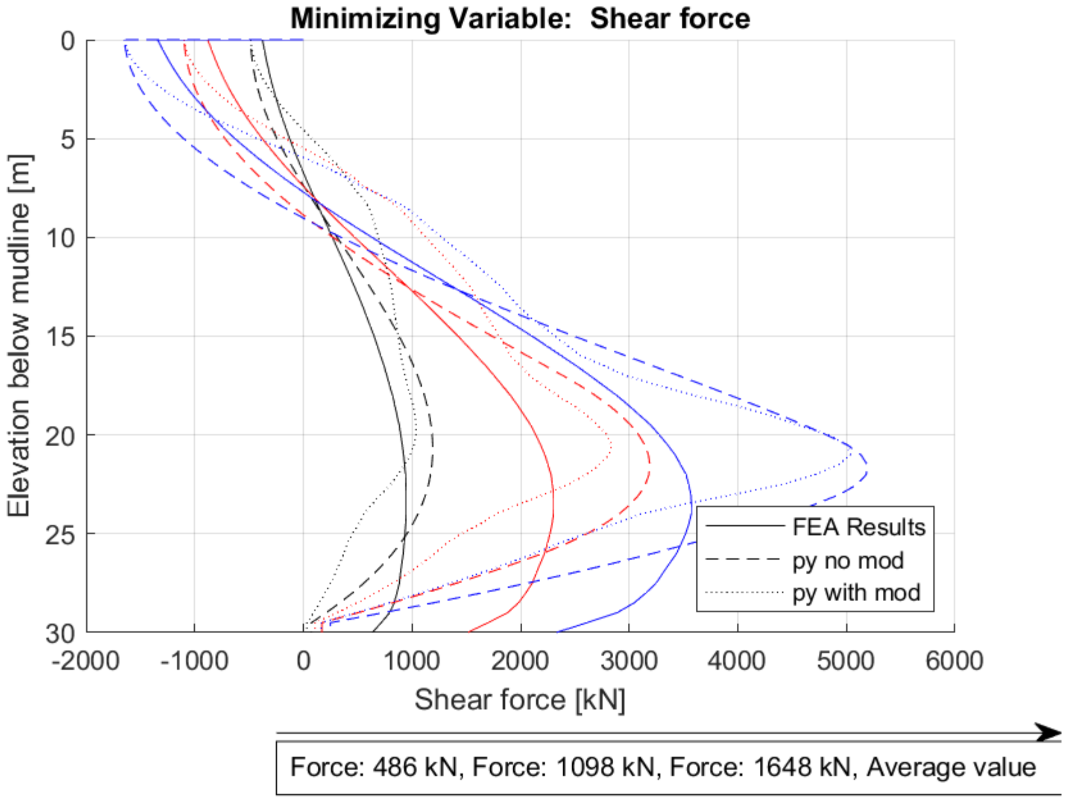

Figure 3.20: Shear force, with and without modifiers.

Bending moment

Table 3.18: Error reduction when minimizing with respect to bending moment.

Pile load [kN]	Error reduction [%]
486	-18.67
1098	-23.75
1648	-15.68

As visualized by the change of error in Figure 3.22, the same phenomena as previously discussed (section 3.2.1.) occurred when optimizing with respect to bending moment.

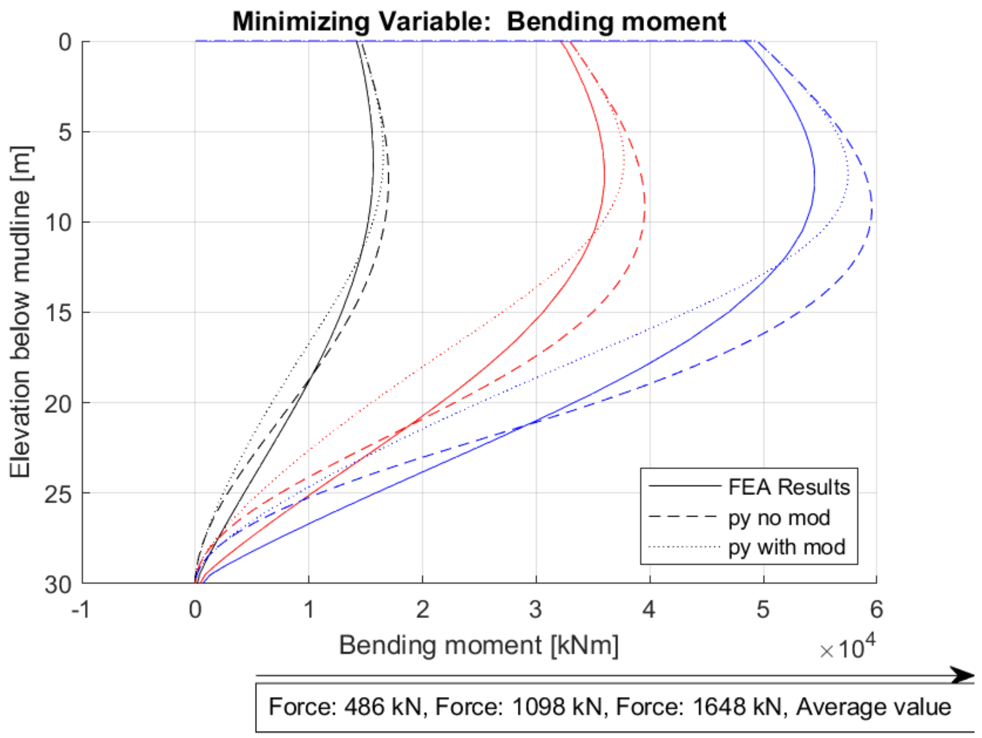

Figure 3.21: Bending moment, with and without modifiers applied.

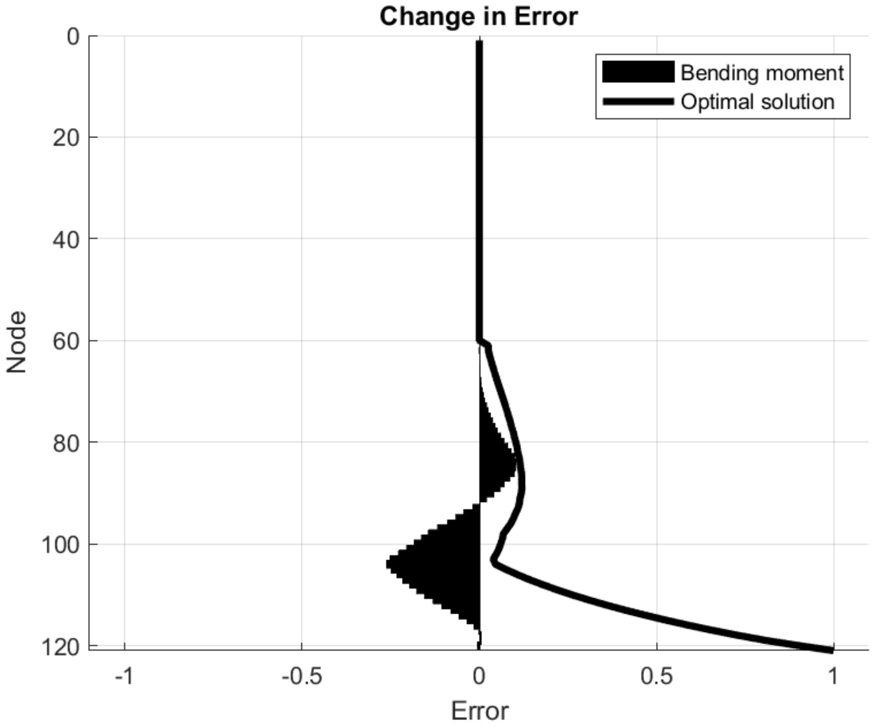

Figure 3.22: The average change in error for each node when minimizing with respect to bending moment.

Rotation

Table 3.19: Error reduction when minimizing with respect to rotation.

Pile load [kN]	Error reduction [%]
486	95.83
1098	88.91
1648	92.02

The modified stiffness springs give a good math to the FEA-calculated pile response.

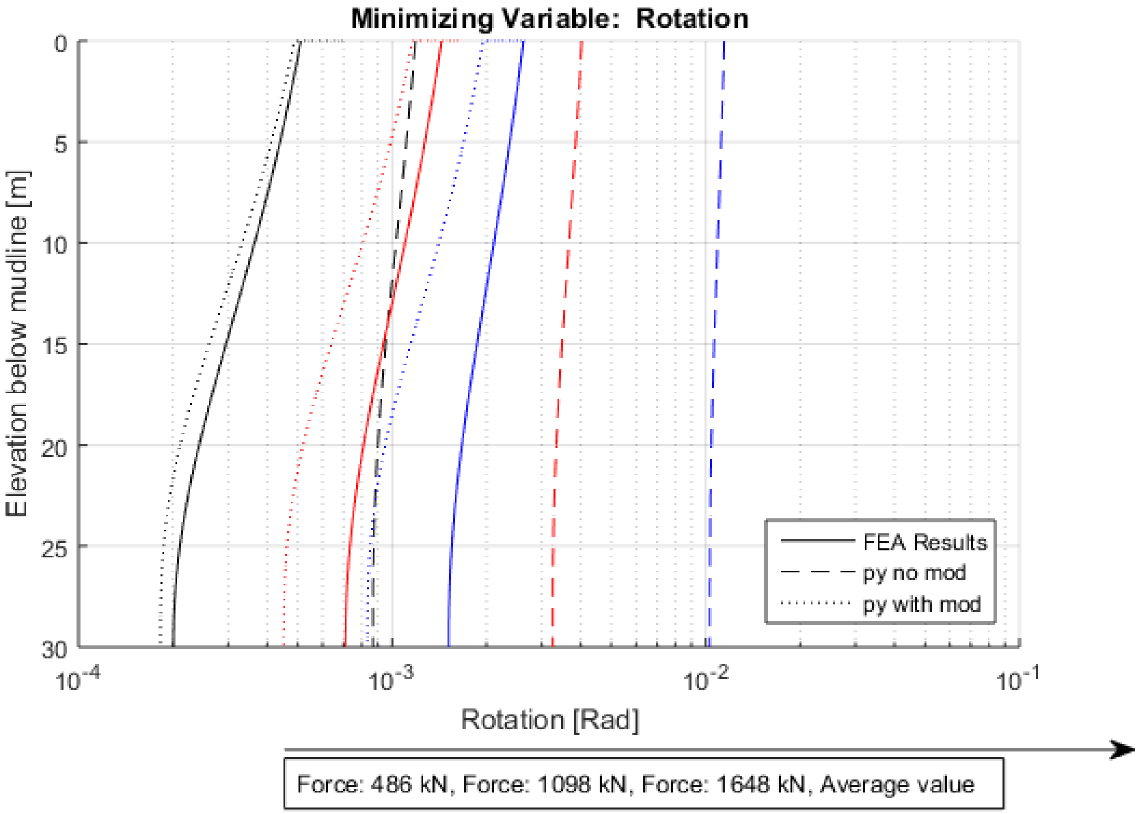

Figure 3.23: Cross-sectional rotation, with and without modifiers applied compared to FEA. Note that the x-axis is plotted in log-scale for a better visualization of the results.

Combined displacement, shear force, bending moment and rotation

Table 3.20: Error reduction when minimizing with respect to all variables.

Pile load [kN]		Error reduction [%] (Error change)
486	Displacement	86.34
	CS Rotation	93.90
	Bending moment	-8.14 (-1.47)
	Shear force	9.08
	Combined	**79.03**
1098	Displacement	84.68
	CS Rotation	87.47
	Bending moment	-6.28
	Shear force	20.79
	Combined	**77.46**
1648	Displacement	90.16
	CS Rotation	91.24
	Bending moment	4.42
	Shear force	46.91
	Combined	**86.16**

When optimizing the stiffness springs for all minimizing variables, the tool performs very well. In particular, the cross-sectional structural forces have better response relative to the ones calculated optimizing for one force response solely. As visualized by Figure 3.24 and Figure 3.25, the force responses follow a smooth pattern and are matching the FEA-calculated pile response better. The lateral displacement and cross-sectional rotation do perform very well, as previously seen in conducted validation tests.

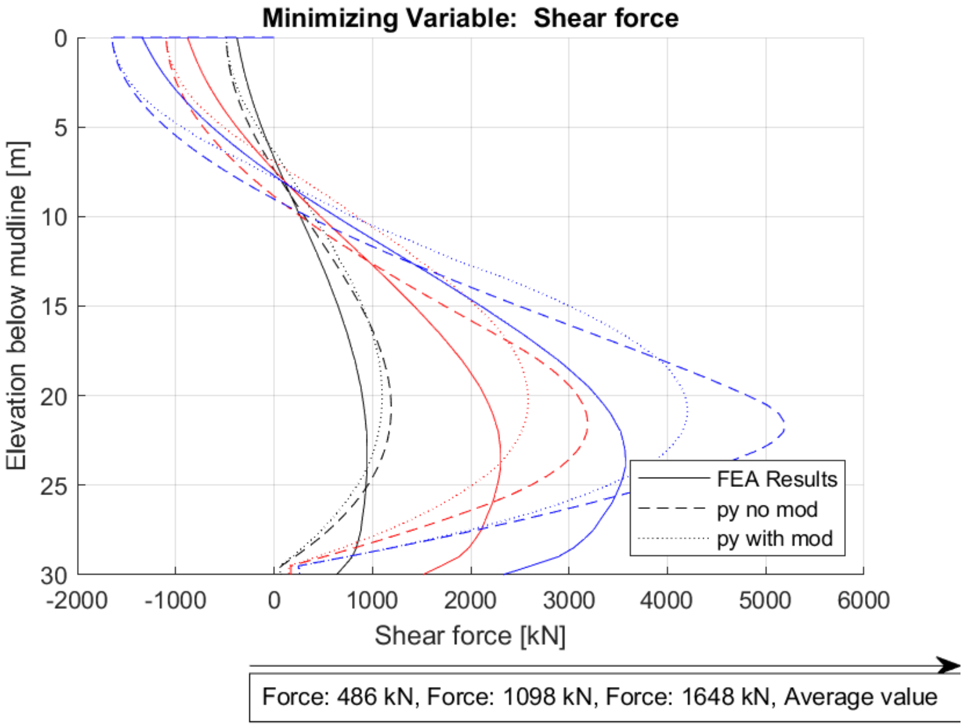

Figure 3.24: Shear force response, with and without modifiers applied compared to FEA when minimizing all variables.

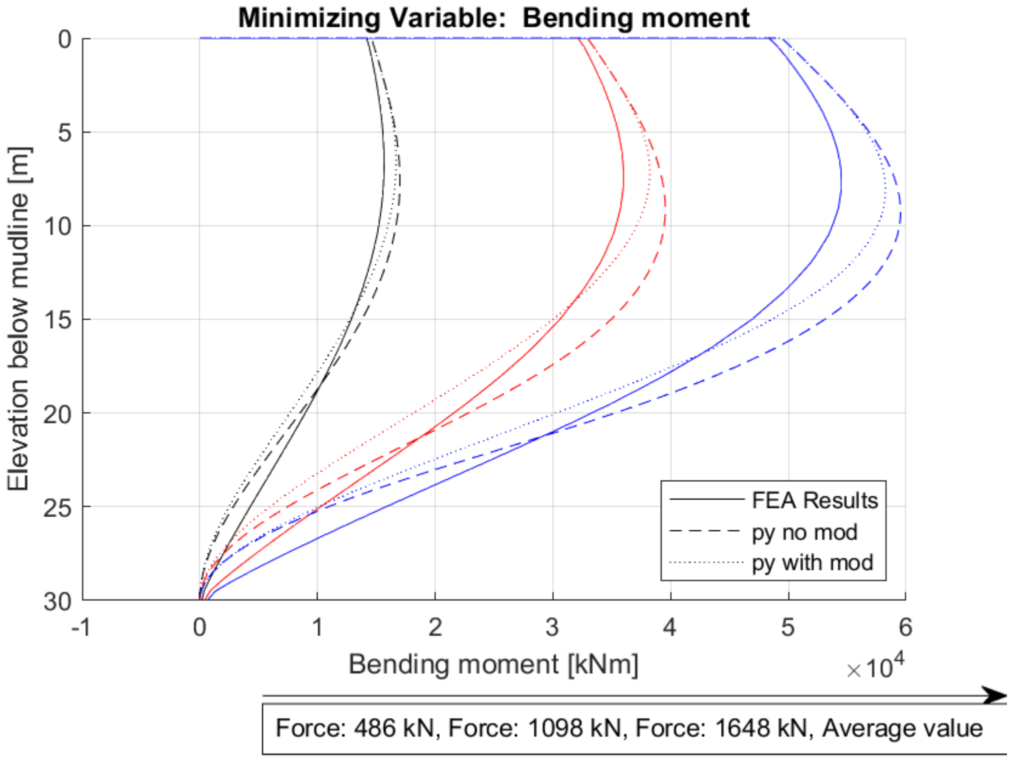

Figure 3.25: Bending moment response, with and without modifiers applied compared to FEA when minimizing all variables.

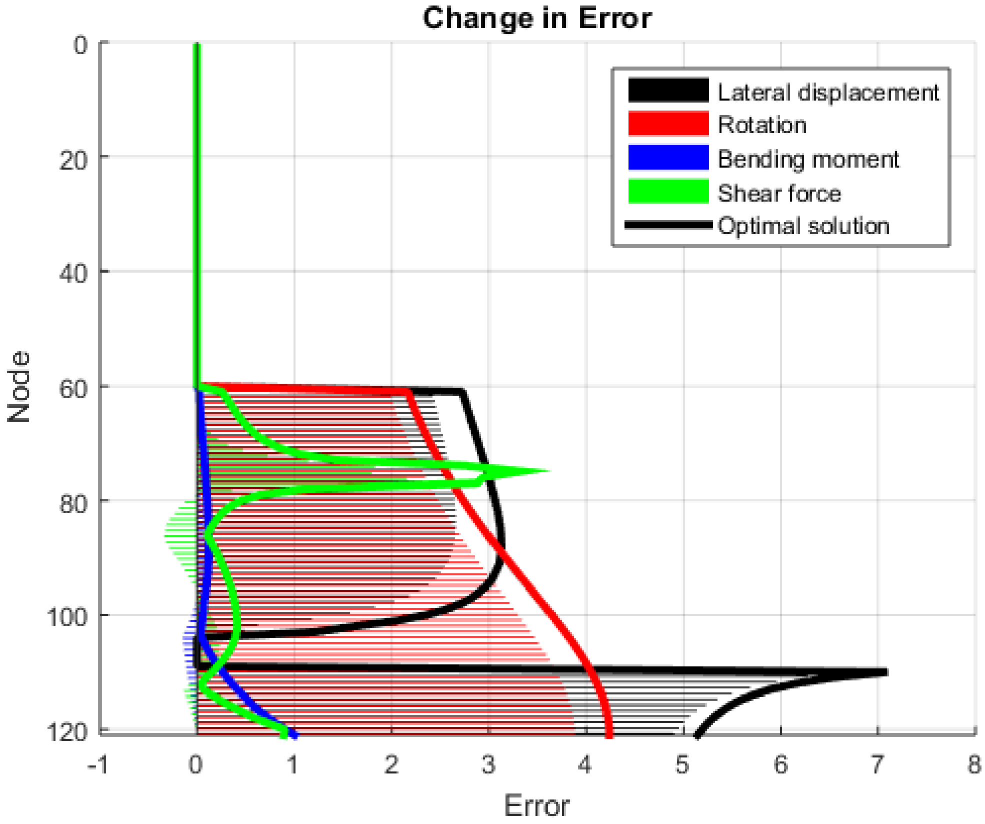

Figure 3.26: The average change in error for the different load levels, when optimizing for all four variables. The bars show the change in error, while the solid lines are the optimal solution for that specific variable, corresponding to the same color.

3.3 Summary

When optimizing the variables separately, the tool gives adequate results when minimizing with respect to the deformation variables. The accuracy of the shear force prediction has some various results, decreasing in some, while increasing in others. The decrease was particularly visible when using the API clay Matlock (1970) formulation, indicating that the tool has difficulties to converge towards an optimal solution. The bending moment response decreases in accuracy for all cases. The tool should be used with caution when minimizing with respect to either of the two cross-sectional structural force variables separately.

When minimizing for all variables combined, the tool gives good results for all cases tested. The calculated stiffness spring modifiers provides an increase of accuracy for both deformation response and cross-sectional structural forces. When minimizing with respect to all the variables the tool performs well, thus fulfilling its purpose of finding effective soil reaction springs, to get a more precise pile response.

3.4 Terminology

Minimizing variable – What error one wants to minimize (displacement, shear force, rotation, bending moment or a combination free of choice.)

Target pile response/load level – The solution the tool tries to duplicate, by using reaction springs with modifiers applied (for the stiffness spring). The target pile response is presented at a certain load level. One pile may have multiple target pile responses.

Error – The difference between the target pile response and the calculated pile response using response springs, for a given variable, divided by the target pile response value.

Error function – The value that the tool tries to minimize through iteration. For multiple errors, each error is equally weighted and summarized, forming the error function.

Load level modifiers – The modifiers calculated for each load level.

Optimal modifiers – The final modifiers, calculated as the average modifier value of the load level modifiers.

Upper limit – Upper limit value for the modifiers.

Lower limit – Lower limit value for the modifiers.

Convergence limit – When the difference between the value of the error function between the latest iteration steps are below the convergence limit, the solution for that specific spring has converged, and the optimal modifier is registered.

4 Pile response in soft clays and layered clay profiles

4.1 Introduction

To date, most of the offshore wind turbine activities has been concentrated in the North Sea in Europe, where the soil conditions mostly consists of stiff *over-consolidated (OC)* clay or very dense sand, because of previous glacier activities. However, in recent years, the offshore wind industry has seen a rapid expansion in Asia, and particularly in China. These regions present geotechnical conditions that are different from what typically encountered in Europe. Soft clays and layered soil profiles are commonly encountered. The research published in public domain has mostly concentrated on modelling the monopile response in single layered clay, with uniform strength. Very little research has looked at monopile response in soft *normally consolidated (NC)* clay, and the effect of layering.

In this chapter, the performance of a multi-spring beam-column framework for modelling monopile response is tested for a range of pile geometries in soil profiles consisting of NC clay and layered soil profiles. The test is performed by comparing the pile response calculated by *finite element analyses (FEA)* and the predictions by the multi-spring beam-column model. For cases where the existing framework does not perform adequately, the optimization tool is used to find what stiffness corrections is needed to get a better match.

4.2 Multi-spring beam-column model

The multi-spring beam-column model consist of three components, namely the *stiffness spring* (*p-y*) presented by Zhang and Andersen (2017), a *base shear* (*s-u*) component for the pile tip resistance presented by Zhang and Andersen (2019a) and a *moment rotation spring* (*m-r*), mobilized by the side friction of the pile, presented in Zhang (2019b). All spring components are based on a principle of scaling the stress-strain response of the soil. This principle is illustrated for the *p-y* spring in Figure 4.1.

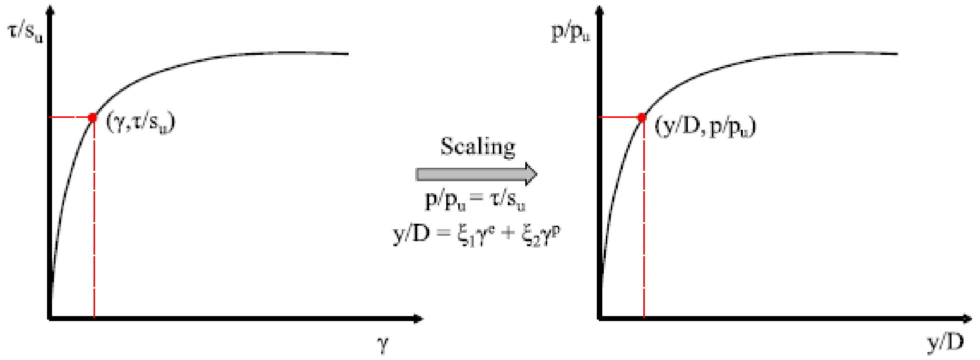

Figure 4.1: Scaling principle for the p-y spring. From Zhang and Andersen (2017).

The elastic and plastic shear strains are scaled by separate scaling factors. A summary of the model components and their corresponding scaling factors is presented in Table 4.1. For explanation of the different variables, the reader is directed to section 2.4. The pile response is found by a conventional beam-column analysis.

Table 4.1: Summary of the multi-spring beam-column model.

Model component	Description
p-y	$\frac{p}{p_u} = \frac{\tau}{s_u}$ $\frac{y}{D} = \xi_1 \gamma^e + \xi_2 \gamma^p$ $\xi_1 = 2.8$ $\xi_2 = 1.35 + 0.25\alpha$ $\gamma^e = \frac{\tau}{G_0}$ $\gamma^p = \gamma - \gamma^e$ $p_u = N_p s_u$ $N_p = 9.14 + 2.8\alpha$ where α is the pile roughness
s-u	The base shear resistance is calculated by the same principles as for the *p-y* spring, namely by scaling the stress-strain response of the soil at the pile tip by the following set of equations: $\frac{s}{s_{ult}} = \frac{\tau}{s_u}$ $\frac{u}{D} = \xi_1 \gamma^e + \xi_2 \gamma^p$ $\xi_1 = 0.3$ $\xi_2 = 0.12$ $s_{ult} = 0.25\pi D^2 s_u$ where D is the pile diameter
m-r	$\frac{M}{M_{max}} = \left(\frac{\tau}{s_u}\right)/\alpha$ $r = \frac{8}{\pi}(\xi_1 \gamma^e + \xi_2 \gamma^p)$ $\xi_1 = 1.15$ $\xi_2 = 0.45$ $M_{max} = D^2 \tau_{max} = D^2 \alpha s_u$ if α is below 1, a cut-off is applied at M/M_{max} equal to 1.

4.3 Finite element model

The finite element analyses are conducted in the commercial finite element software Abaqus (Abaqus, 2017). Different soil profiles and pile geometries are tested.

4.3.1 Geometry and meshing

The *finite element (FE)* models are discretized using C3D8R (first order, reduced integration brick) elements. Abaqus allows the user to prescribe biased seeding along an edge. To achieve adequate numerical efficiency and accuracy, a cylindrical zone with a radius of 2*D* from pile center is meshed with a finer mesh, with the element size decreasing towards the pile-soil interaction. At the pile tip level, the mesh is divided into thin horizontal layers to improve the accuracy of base shear resistance. For the layered soil profiles, the same approach is taken at the transition between the layers. Figure 4.2 and Figure 4.3 illustrate the FEA model in single-layered and double-layered soil profiles respectively. The details of the meshing are presented in Figure 4.4 and Figure 4.5.

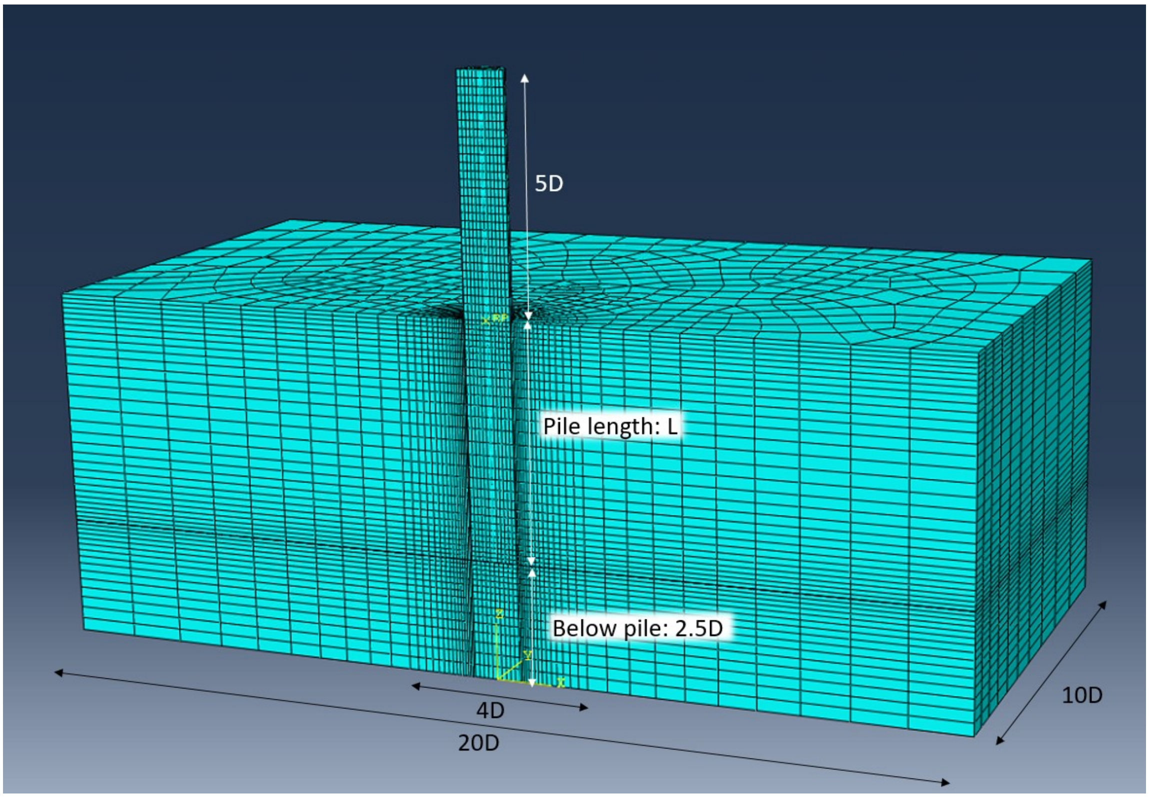

Figure 4.2: Meshing and geometry of the Abaqus model in single-layered soil profiles, L/D = 5.

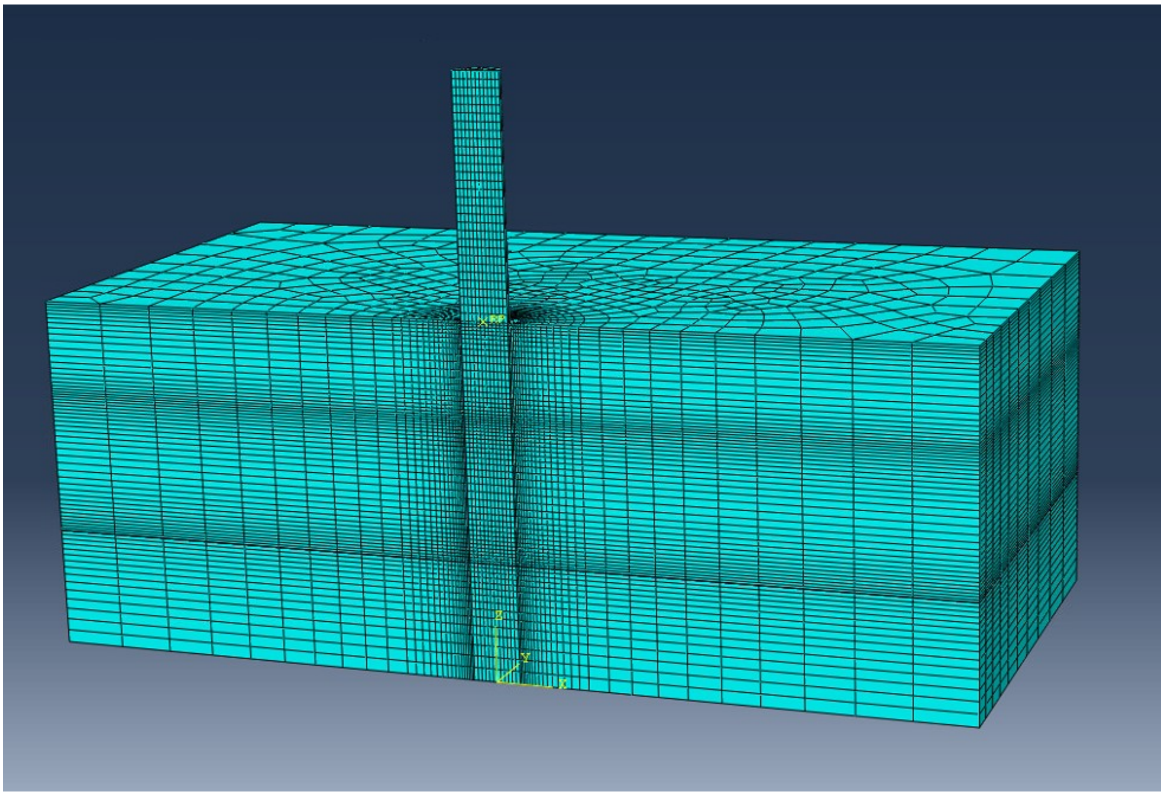

Figure 4.3: Meshing in double-layered soil profiles, L/D = 5.

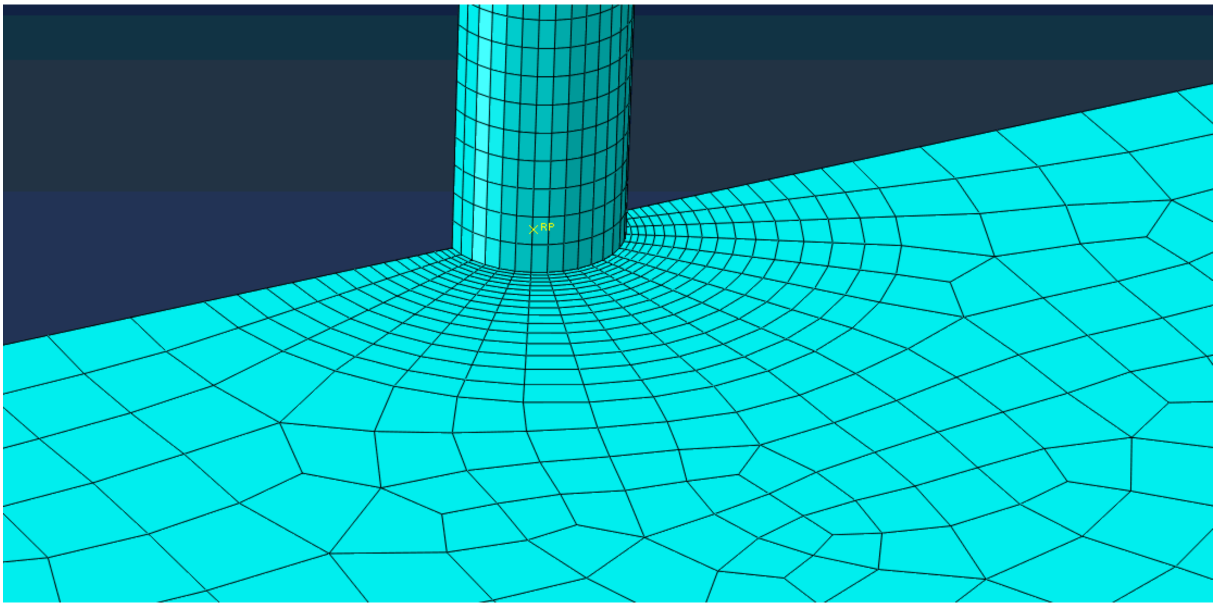

Figure 4.4: Details of the refined mesh area within a radius of 2*D* from the pile.

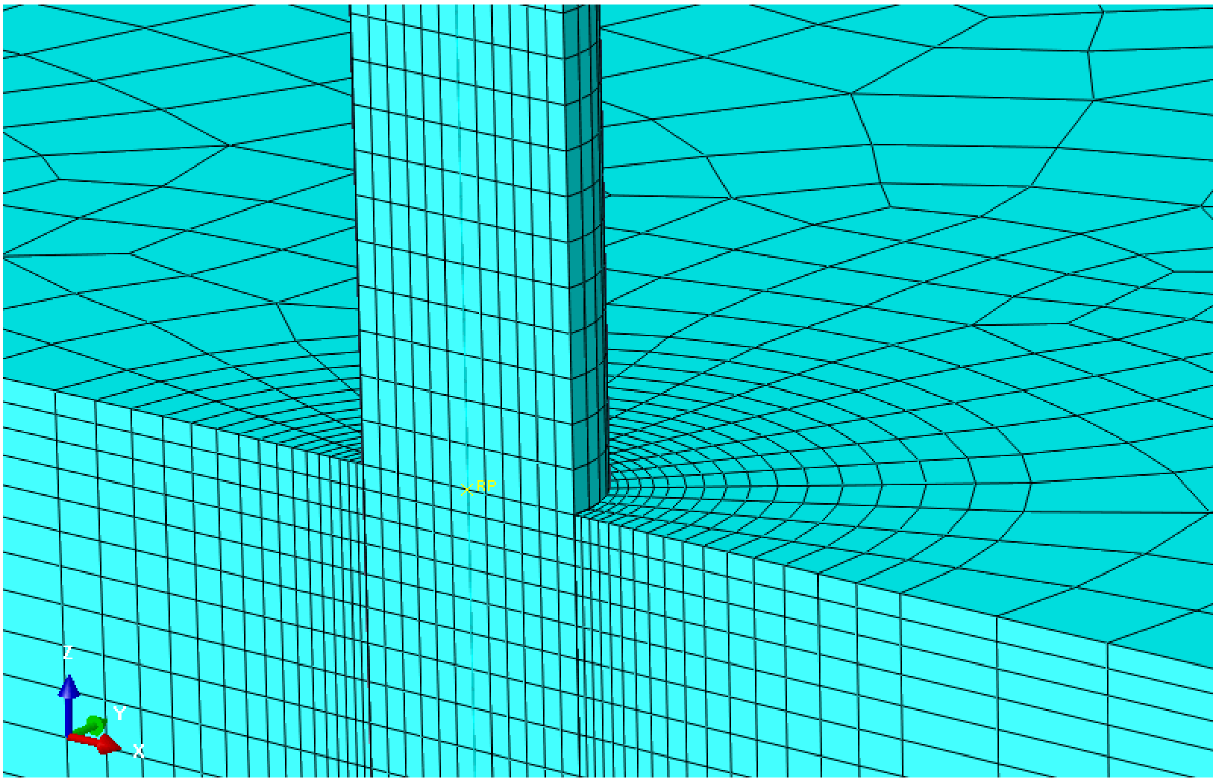

Figure 4.5: Details of the meshing for the transition between pile and soil.

By defining surface to surface contact pairs, the pile-soil surfaces are modeled as fully rough interfaces. Thus, the two surfaces (front and back of the pile under loading) will not slide relative to the soil. These conditions lead to the failure mechanism occurring in the soil, and not at the interface. Separation after contact is not allowed, meaning there is no gap occurring. The tested pile is assumed to be at an offshore location, with weak (low shear strength) clay at the mudline. Thus, the soil at the active side of the failure mechanism collapses, and suction occurs on the rear side. This suction may be visualized by the phenomena of walking barefoot on the sea floor. If the foot is raised quickly, one feels a sort of suction underneath the foot, pulling it back towards the sea floor. This is explained by the fact that most clays at the sea floor have a relatively low permeability. Hence, there is not enough time for the water that was squeezed out of the pores when the foot stamped down to return to its equilibrium state when the foot is raised, and a vacuum within the pores is established. The same phenomena is assumed to occur under pile loading, and the interface of the backside of the pile will stay connected through the loading process. Thus, a gap is not allowed to occur.

4.3.2 Pile geometry

Due to symmetric conditions, only half of the pile is modeled. Hence, the vertical face of the pile side is given symmetric boundary conditions (no rotation or displacement out of the plane.) The pile is modeled as a solid pile, with isotropic elastic material behavior. The Youngs modulus of the solid pile was recalculated to match the *bending stiffness* (*EI*) of the pipe pile that is modeled (Table 4.2). The Poisson's ratio is equal to 0.3. The force is applied laterally at the pile head 30 meters above mudline.

To capture the effect of the pile size, four different piles are simulated. The following properties are tested.

Table 4.2: Pile geometries.

L/D [-]	Diameter [m]	Penetration depth [m]	Wall thickness [m]	Stick-up [m]
3	6	18	0.06	30
5	6	30	0.06	30
7	6	42	0.06	30
10	6	60	0.06	30

4.3.3 Soil model

The response of the soil is modeled using the Mohr-Coulomb model. Friction and dilatancy angles are set equal to 0°, thus simplifying to a Tresca model. Undrained conditions are assumed, specifying the Poisson's ratio as 0.48. The elastic Youngs modulus *E* is kept constant through the calculations, making the elastic strain component equal to:

$$\gamma^e = \frac{\tau}{G}$$

where *G* is the equivalent shear modulus found through the relationship:

$$G = \frac{E}{2(1+\nu)} \approx \frac{E}{3}$$

Abaqus allows the user to specify the plastic shear strains, γ^p, at different mobilization stages described by the shear stress, τ, relative to the shear strengths, S_u. Thus, the non-linear plastic soil response is captured by pre-calculating the soil response using the NGI-ADP model (Grimstad et al., 2012) at different mobilization levels.

The NGI-ADP model is a total stress soil model. It is commonly used when simulating undrained anisotropic behavior of clay. The model follows a Tresca type yield criterion. The model assumes the following plastic hardening rule:

$$\frac{\tau}{S_u} = 2\frac{\sqrt{\gamma^p/\gamma_f^p}}{1+\gamma^p/\gamma_f^p}$$

where τ is the currently mobilized shear stress, S_u is the *DSS (direct simple shear)* strength of the soil, γ^p is the current plastic shear strain, and the γ_f^p is the plastic shear strain at failure. For elastic shear strain it follows:

$$\gamma^e = \frac{\tau}{G_0} = \frac{\tau/S_u}{G_0/S_u}$$

where the relationship G_0/S_u describes the ratio between the strain stiffness at low mobilization over shear strength and is assumed constant. Thus, the soil behavior may be described by the parameters γ_f^p, G_0/S_u and S_u. γ_f^p and G_0/S_u may be used as curve fitting parameters, to capture the stress-strain behavior of any site-specific soil.

For simplicity the soil is assumed to be weightless and have isotropic strength and stiffness properties. There is no gap occurring. Thus, the contribution from the passive and active wedge cancels each other out, making the weightless soil assumption valid.

To capture the response of different stress-strain behaviors, the soil profiles are tested for two different values of plastic shear strain at failure, γ_f^p. G_0/S_u is kept constant equal to 1000. Five different shear strength soil properties are established, making it ten different soil profiles to be tested in total. The soil profiles are presented in Table 4.3.

Table 4.3: Strength profiles used for testing.

Identification	Shear strength, S_u [kPa] z is the depth below mudline [m]	Plastic shear strain at failure, γ_f^p [-]
Soil profile 1	$S_u = 0.1 + 1.5z$	0.02
		0.10
Soil profile 2	$S_u = 10 + 1.5z$	0.02
		0.10
Soil profile 3	$S_u = 0.1 + 1.5z, \quad 0 < z \leq 12$ $S_u = 50, \quad z > 12$	0.02
		0.10
Soil profile 4	$S_u = 0.1 + 1.5z, \quad 0 < z \leq 12$ $S_u = 100, \quad z > 12$	0.02
		0.10
Soil profile 5	$S_u = 100$	0.02
		0.10

Soil profiles 1 and 2 are designed to simulate normally consolidated to lightly over-consolidated clay profiles. Soil profile 1 is defined as an ideally normally consolidated soft clay profile with shear strength linearly increasing with depth. Soil profile 2 is defined as a lightly over-consolidated clay profile, with the same linearly increasing strength gradient as for soil profile 1.

Soil profiles 3 and 4 are designed as two layered soil profiles. Each soil profile consists of the identical normally consolidated soil profile as for soil profile 1 to the depth of 12 meters, where the strength increases rapidly, simulating a stiffer soil profile.

Soil profile 5 is included to validate the FE-model, and to investigate how the reaction springs performs when calculating shorter monopiles in a stiffer clay profile.

Each pile is tested in each soil profile, in total 40 FE-analyses.

4.3.4 Validation

The *p-y* spring component of the multi-spring beam-column model was developed to capture the flow-around soil failure mechanism in stiffer OC clays with an uniform shear strength (Zhang & Andersen, 2017). Thus, it is assumed that the multi-spring beam-column model performs well when calculating the pile response for the longer monopiles, which experiences a larger amount of flow-around soil failure. By this assumption, soil profile 5 (Table 4.3) is used for validation of the finite element calculated pile response. A comparison between the multi-spring model and the finite element calculated pile response for the longer piles (*L/D* of 10) is presented in Figure 4.6 and Figure 4.7, with the plastic failure strain equal to 0.02 and 0.10 respectively. Note that the legends in the plots below wrongfully says "py-calculated". The pile responses are calculated using the aforementioned multi-spring beam-column model.

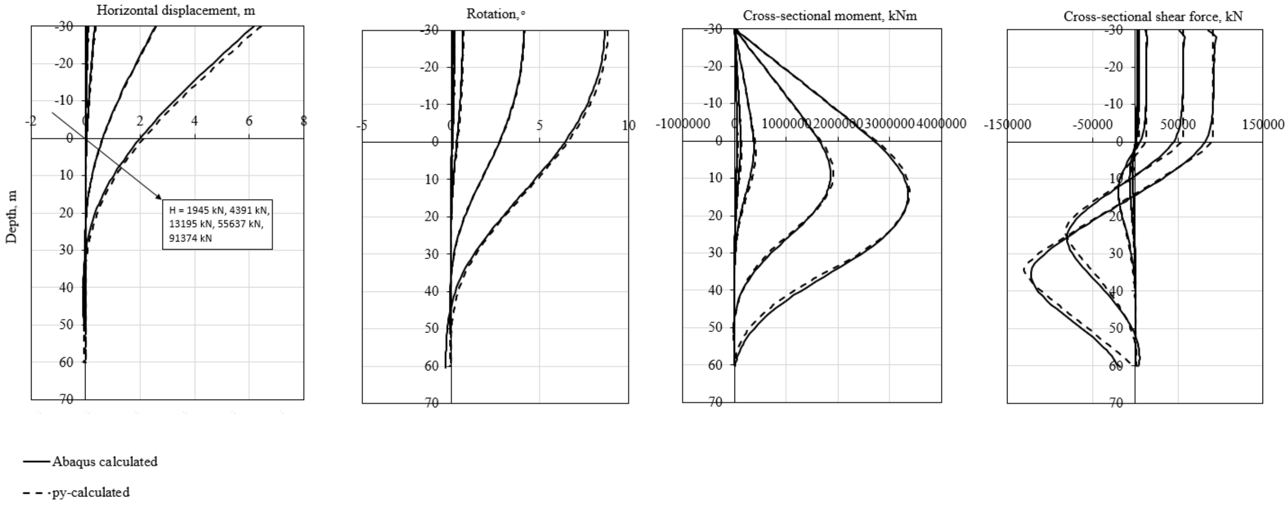

Figure 4.6 Pile response comparison for soil profile 5, L/D=10, γ_f^p=0.02 (Appendix A.5.7).

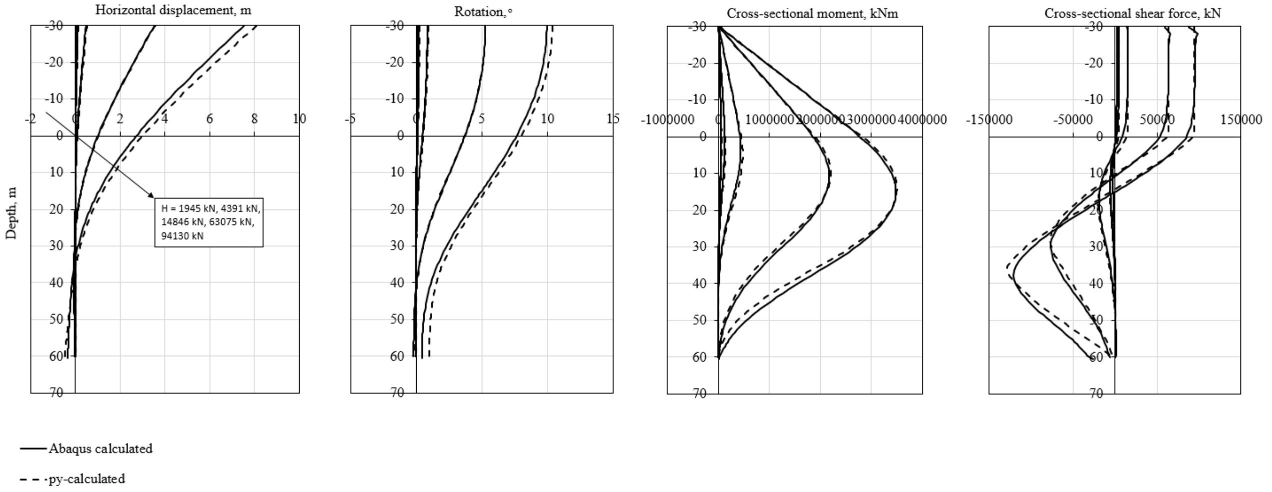

Figure 4.7 Pile response comparison for soil profile 5, L/D=10, γ_f^p=0.10 (Appendix A.5.8).

A good match is demonstrated for the predicted lateral displacement, rotation and cross-sectional bending moment, while the cross-sectional shear force predicted by the finite element model is not as precise. The force is applied at pile head 30 meters above mudline, and is the only force influencing the pile above mudline. Thus, the cross-sectional shear force should be equal to the corresponding load level until reaching mudline, which is the case for the spring calculated piles. The results of the comparison are presented in Appendix A.5. It is assumed that the deformation response from the finite element model is captured correctly, while the shear force response is not fully captured.

4.4 Methodology

The pile is loaded monotonically at the pile-top by a lateral distributed pressure over the pile head until reaching soil failure. The equivalent point load, *F,* at different load levels is calculated by:

$$F = \pi \frac{D^2}{4} q t * 2$$

where q is the applied distributed pressure, *D* is the diameter, and t is the time step, ranging from 0 to 1, where the load is applied proportional to the time steps. Hence, t=0.25 implies a load level where 25% of q is applied, and t=1 equals the final load level. As the model is a half-pipe model, the force is multiplied by 2 to find the equivalent force for a full circular pile. Abaqus allows the user to extract results at various time steps, making it possible to extract the pile response at different load levels. The corresponding pile response calculated by the multi-spring beam-column model is found by conventional beam-column analyses. For cases where the multi-spring model does not perform adequately, the finite element calculated pile responses and their corresponding load levels are used as the target pile responses in the optimization tool.

Figure 4.8. shows the soil displacement at failure for soil profile 1, *L/D*=7. The active and passive wedges are clearly visible, and they tend to have the same size. A rotational soil failure mechanism is observed, forming at the lower half of the pile embedment. Similar results are observed in the other models as well. The deformed model at failure is presented in Figure 4.9. Note that the color scaling used for plotting is different, thus the color plots of Figure 4.8. and Figure 4.9. cannot be directly compared.

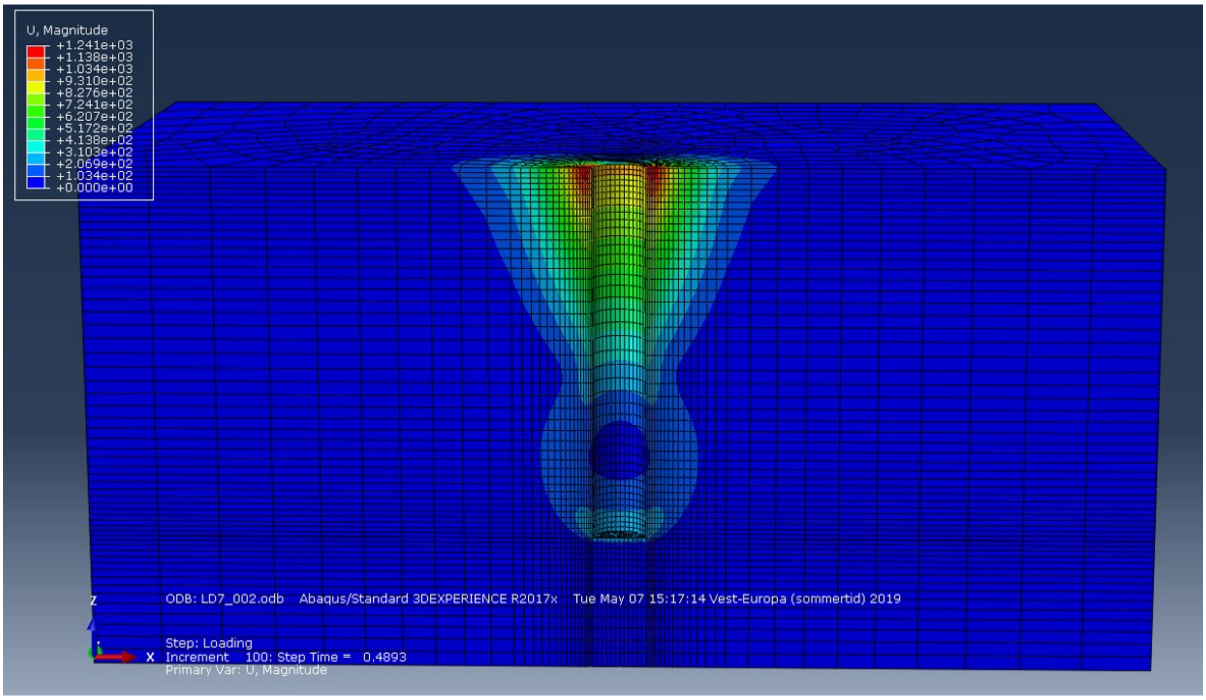

Figure 4.8: The soil displacement at failure presented in an undeformed model, without the pile visualized. L/D = 7, soil profile 1, γ_f^p= 0.02.

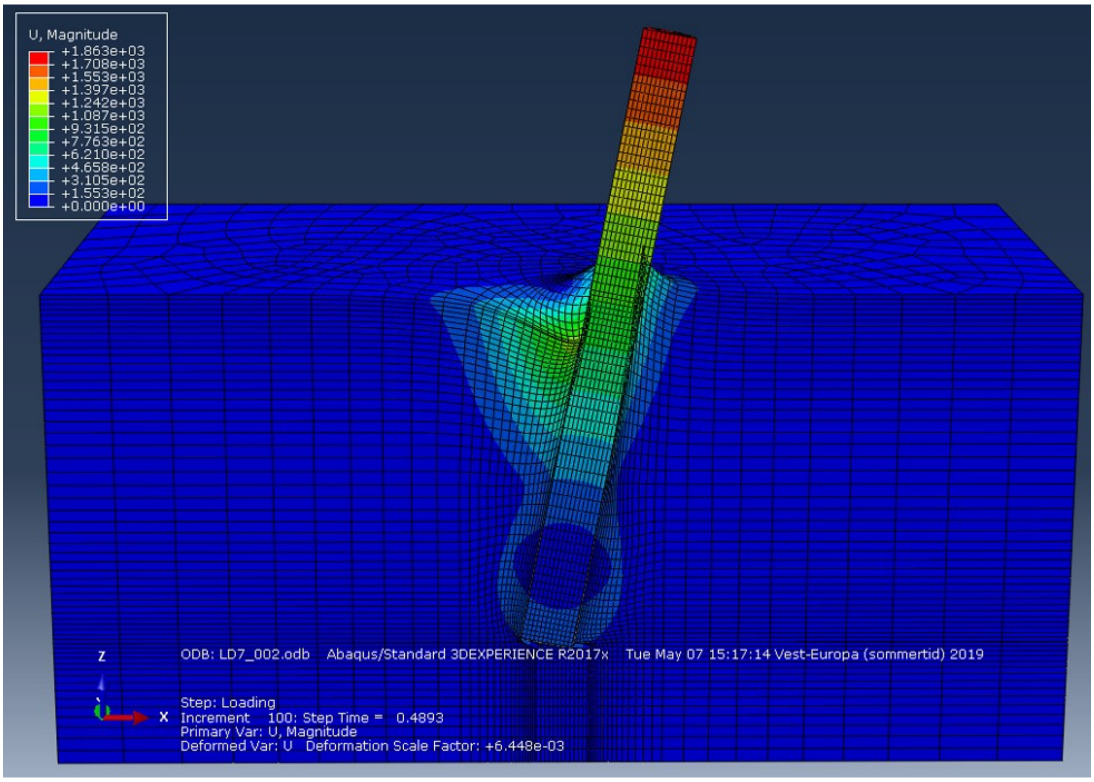

Figure 4.9: Model at failure, showing the displacement. L/D = 7, soil profile 1, γ_f^p= 0.02

4.5 Results

To increase the readability, the results presented herein are showing the lateral pile displacement for the soil profiles consisting of γ_f^p= 0.02 only. The full pile responses (deformation and cross-sectional force) from the comparison between the FEA and multi-spring model for all soil profiles are presented in Appendix A. Appendix B presents the monopile response analyses using the optimization tool. Although the Abaqus model does not catch the cross-section force response properly it is still included in the plots, as a rough estimate to give an indication of the total performance of the spring model.

As seen in Figure 4.12 and Figure 4.13, the multi-spring model performs well in the soft NC clay and the layered soil profiles for the longer piles (*L/D*-ratio of 7 and 10). An excellent match is observed for mostly all soil profiles in terms of deformation responses. For the piles with an *L/D*-ratio of 3 and 5 (Figure 4.10. and Figure 4.11. respectively) the multi-spring model seems to predict a softer response, relative to the response calculated by FEA. As seen in several of the results (Figure 4.10 (a), (b), Figure 4.11 (a), (b), Figure 4.12 (a)), the finite element model and the multi-spring model seems to interpret the pile response at high load levels differently.

Figure 4.14 presents the mobilized stresses in soil profile 4 at full mobilization for long piles in the finite element model. To investigate the influence of the top soft clay layer for the long piles, the deformation response in a soil profile consisting of 0.1 kPa shear strength in the top 12 meters of the seabed, and 100 kPa below is calculated for a pile with an *L/D*-ratio of 10. Plastic shear strain at failure is equal to 0.02. The results are compared to the finite element results presented in Figure 4.13 (d). The result is presented in Figure 4.15, showing that the shear strength of the top soil layer does not influence the pile response noticeably before reaching high stress mobilization levels.

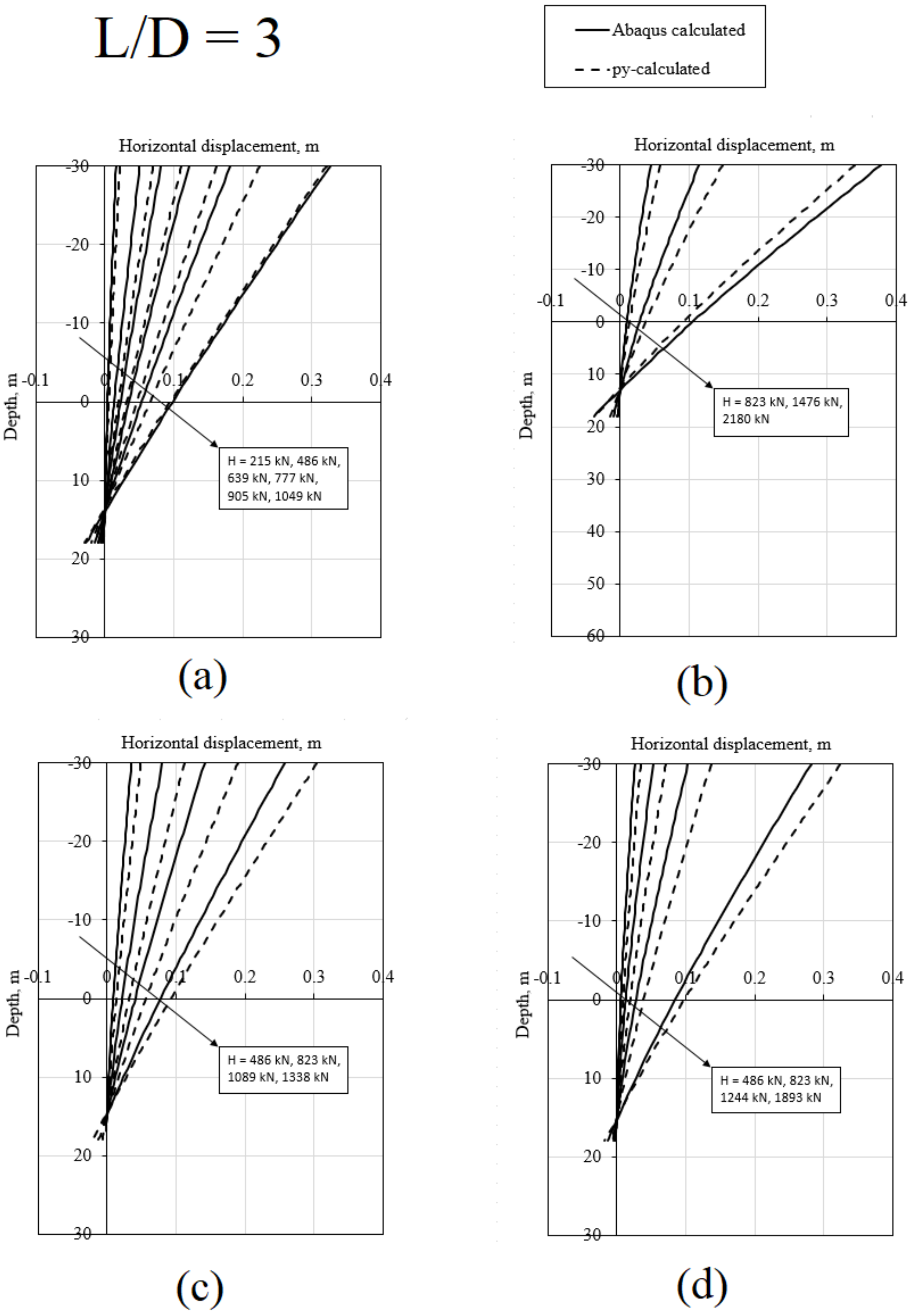

Figure 4.10: Comparison of lateral pile displacement for pile with an L/D-ratio of 3: (a) soil profile 1; (b) soil profile 2; (c) soil profile 3; (d) soil profile 4. γ_f^p= 0.02 for all soil profiles. The legend wrongfully says "py-calculated". The pile responses are calculated using the aforementioned multi-spring beam-column model.

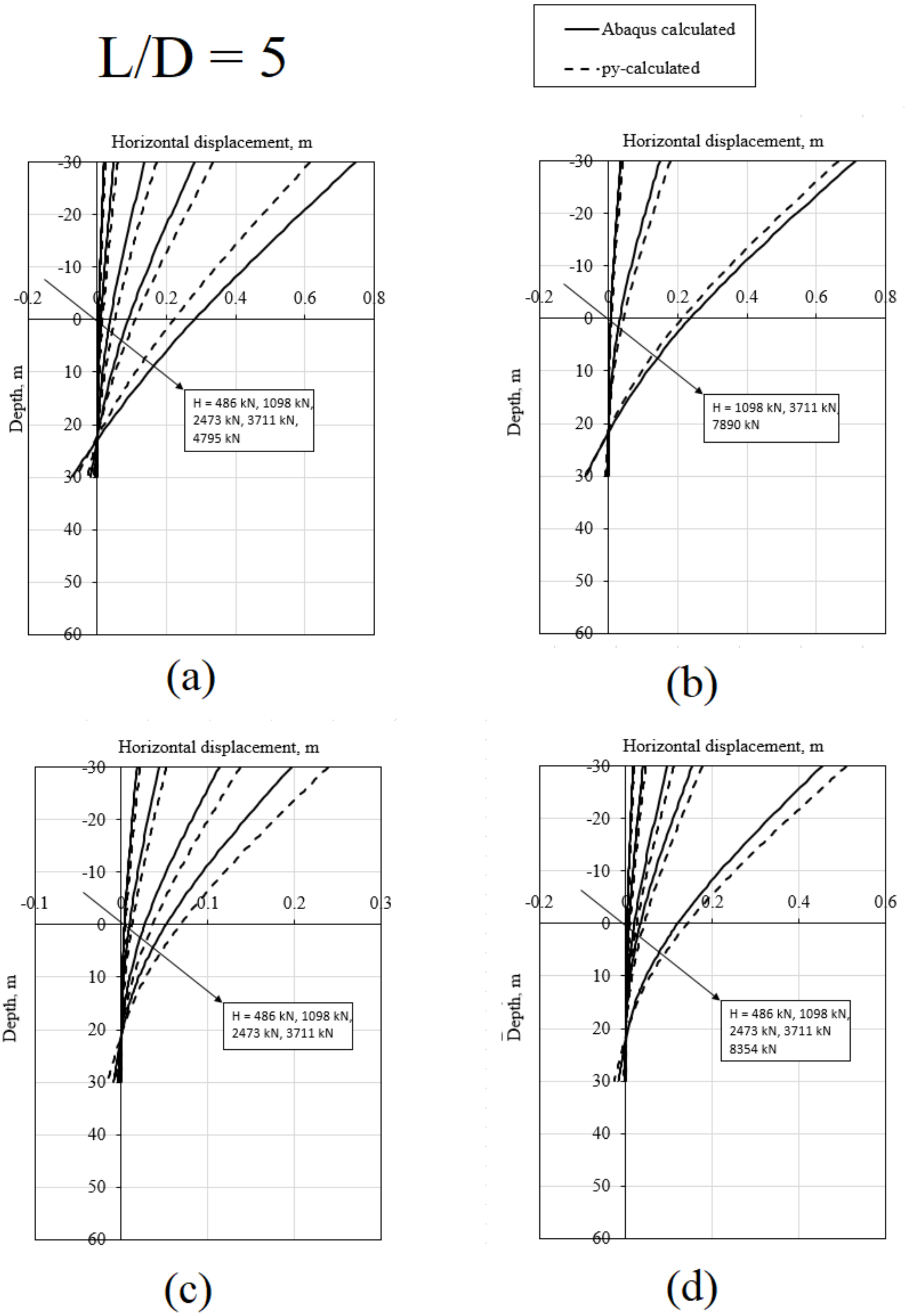

Figure 4.11: Comparison of lateral pile displacement for pile with an L/D-ratio of 5: (a) soil profile 1; (b) soil profile 2; (c) soil profile 3; (d) soil profile 4. γ_f^p= 0.02 for all soil profiles. The legend wrongfully says "py-calculated". The pile responses are calculated using the aforementioned multi-spring beam-column model.

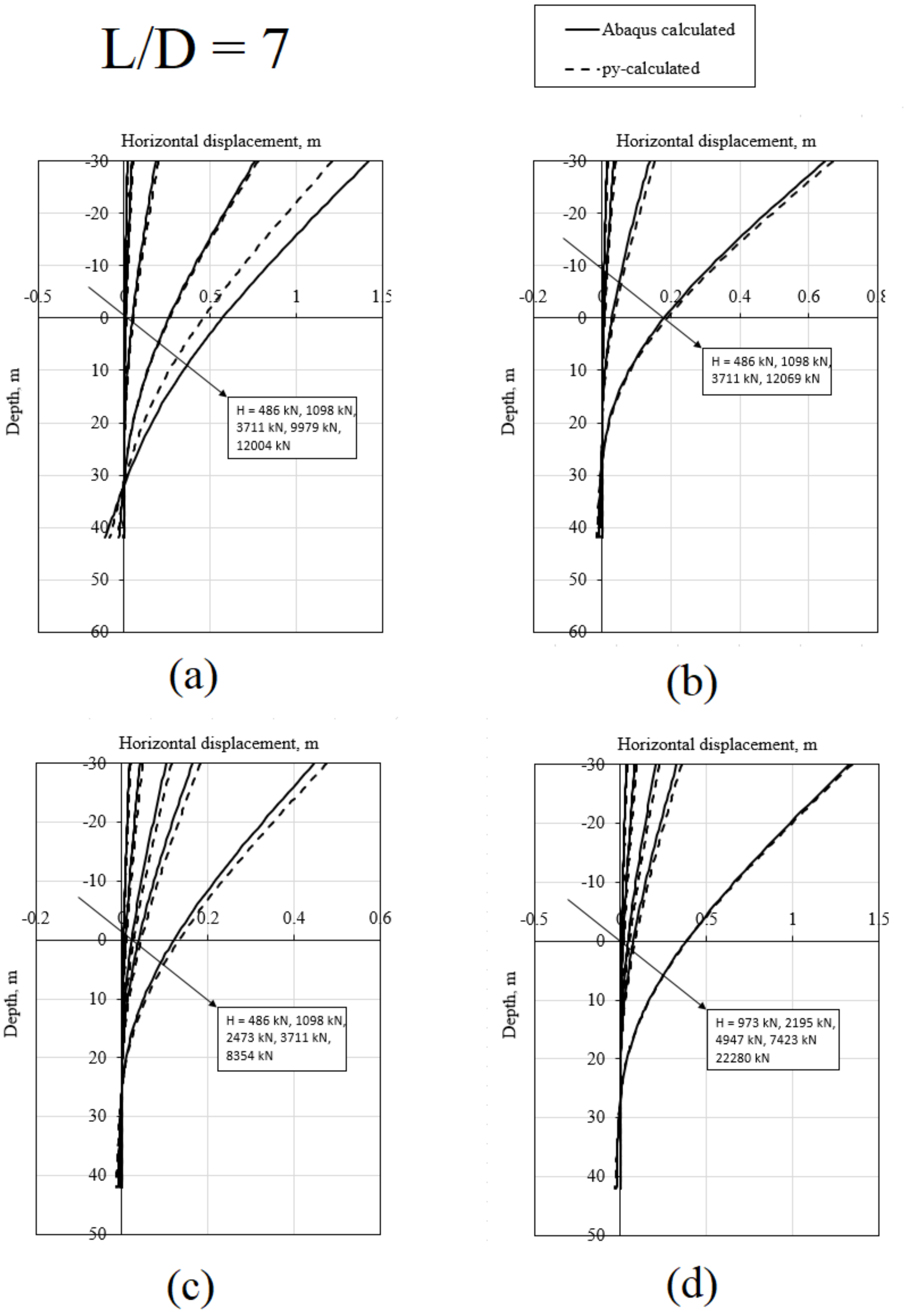

Figure 4.12: Comparison of lateral pile displacement for pile with an L/D-ratio of 7: (a) soil profile 1; (b) soil profile 2; (c) soil profile 3; (d) soil profile 4. γ_f^p= 0.02 for all soil profiles. The legend wrongfully says "py-calculated". The pile responses are calculated using the aforementioned multi-spring beam-column model.

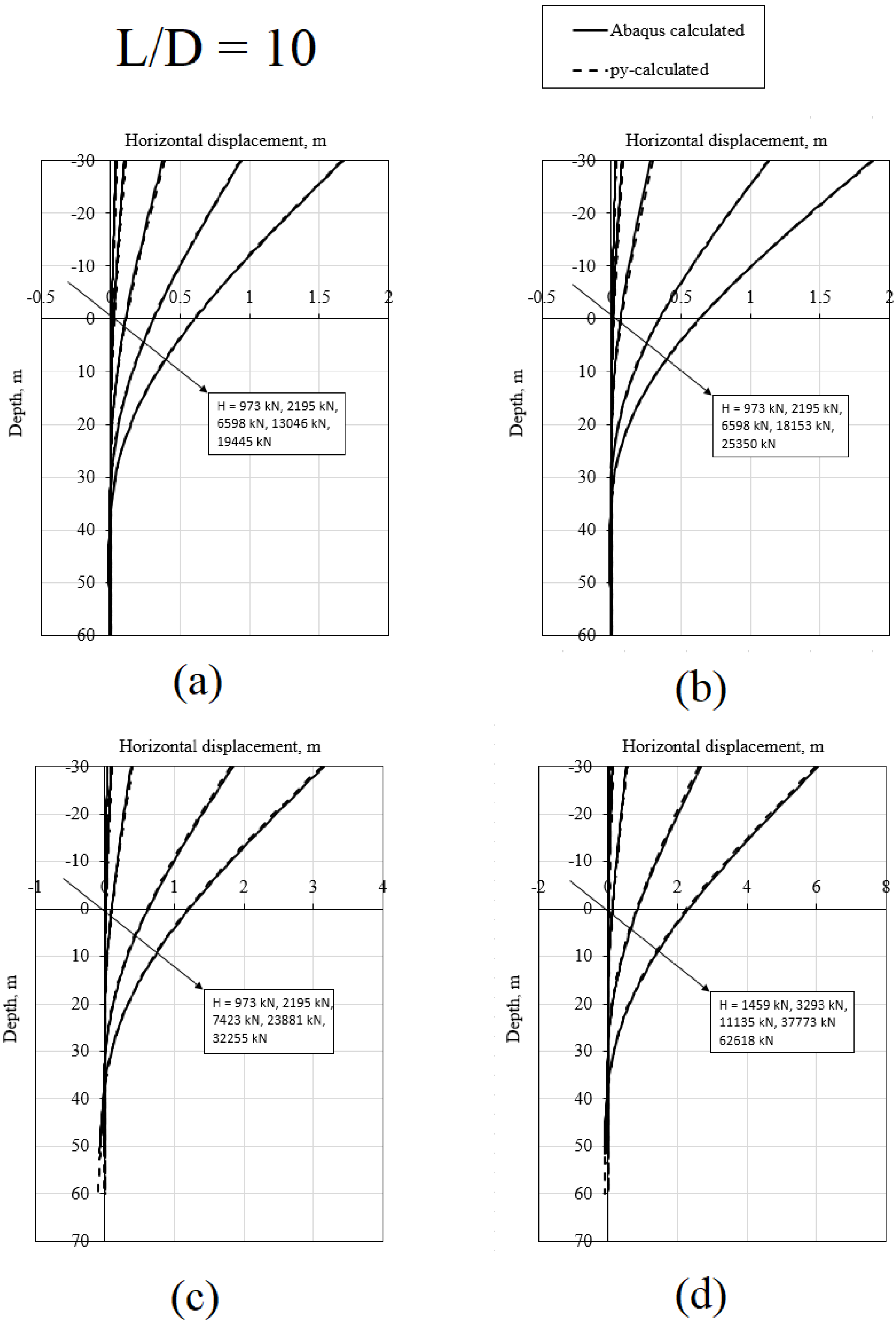

Figure 4.13: Comparison of lateral pile displacement for pile with an L/D-ratio of 10: (a) soil profile 1; (b) soil profile 2; (c) soil profile 3; (d) soil profile 4. γ_f^p= 0.02 for all soil profiles. The legend wrongfully says "py-calculated". The pile responses are calculated using the aforementioned multi-spring beam-column model.

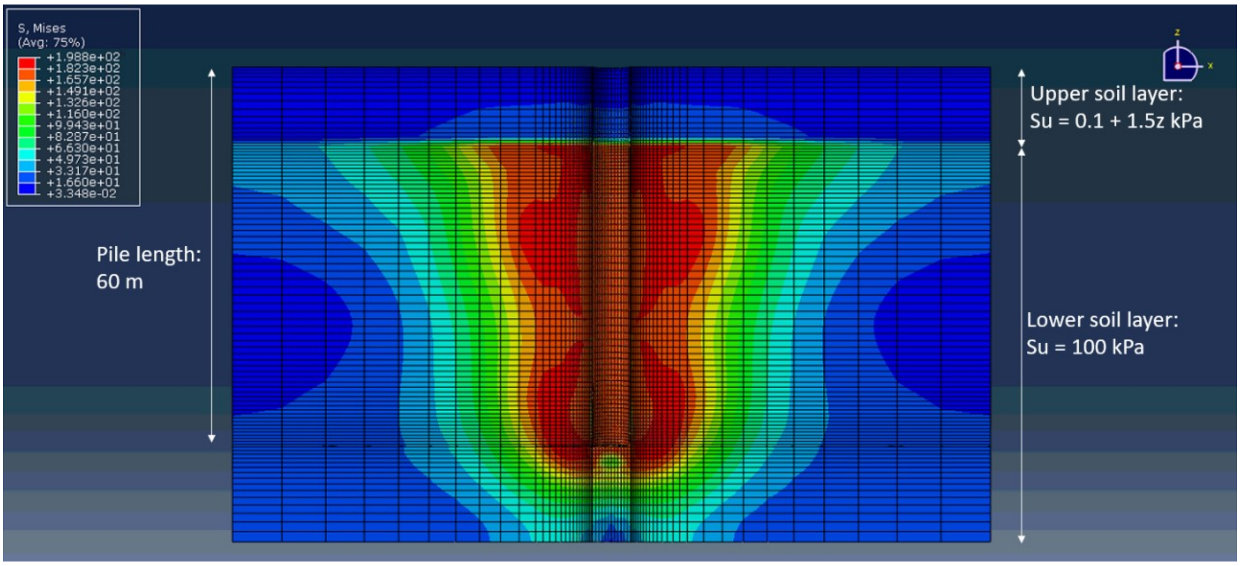

Figure 4.14: L/D = 10, γ_f^p= 0.02, soil profile 4. Soil stresses mobilized at failure.

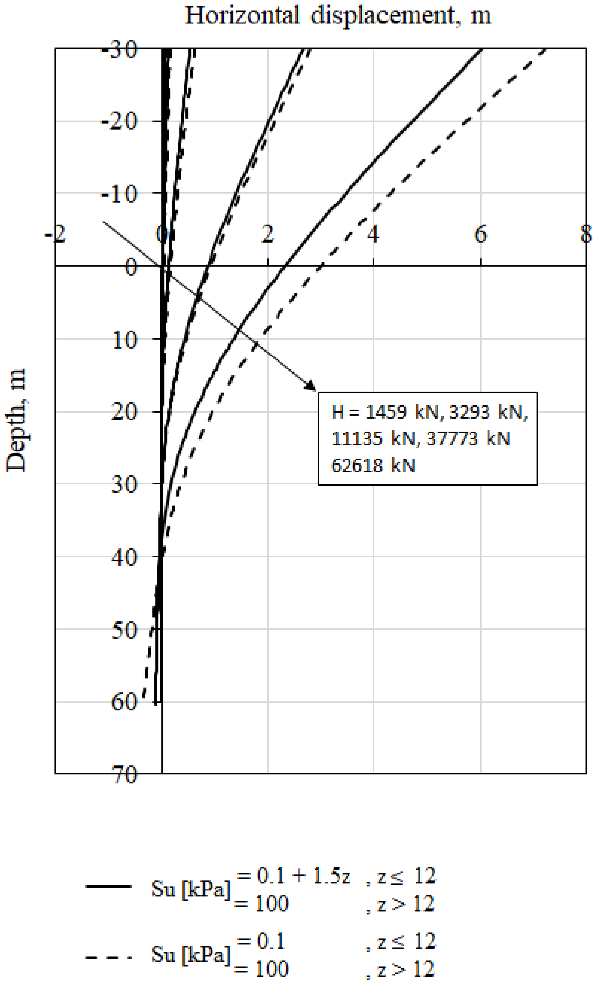

Figure 4.15: Pile deformation response with/without the soft NC layer. L/D=10, γ_f^p=0.02.

The multi-spring model appears to perform adequately for all pile types embedded in the stiff clay in soil profile 5. Thus, validating the multi-spring model as a proper design tool for mostly all types of piles in uniform stiff clay profiles. The results form a basis for determining what cases to be further investigated by the optimization tool.

Mostly all cases for the piles with an *L/D*-ratio of 3 and 5 embedded in the soft NC clay and the layered clay profiles seems to have a too soft response prediction relatively to the FEA results (Figure 4.10 and Figure 4.11). Thus, these piles are analyzed further by using the optimization tool to scale the stiffness (*p*-*y*) springs. The base shear and moment rotation springs are still using default parameters. An equally weighted combination of the Abaqus-calculated lateral pile displacement and cross-sectional rotation are used as the target pile response. The pile response comparison results are presented in Appendix B, with the corresponding *p*- and *y*-modifiers presented in Appendix C. The spring modifiers provides a significantly better accuracy of the predicted pile responses. The modifiers tend to be relatively constant for the entire pile length, indicating that the soil mechanisms are calculated correct, but not scaled properly by the spring model. Figure 4.16 visualizes the deformation response of a pile with an *L/D*-ratio of 5, embedded into soil profile 1, with the plastic failure strains equal to 0.02. The corresponding modifiers are visualized by Figure 4.17.

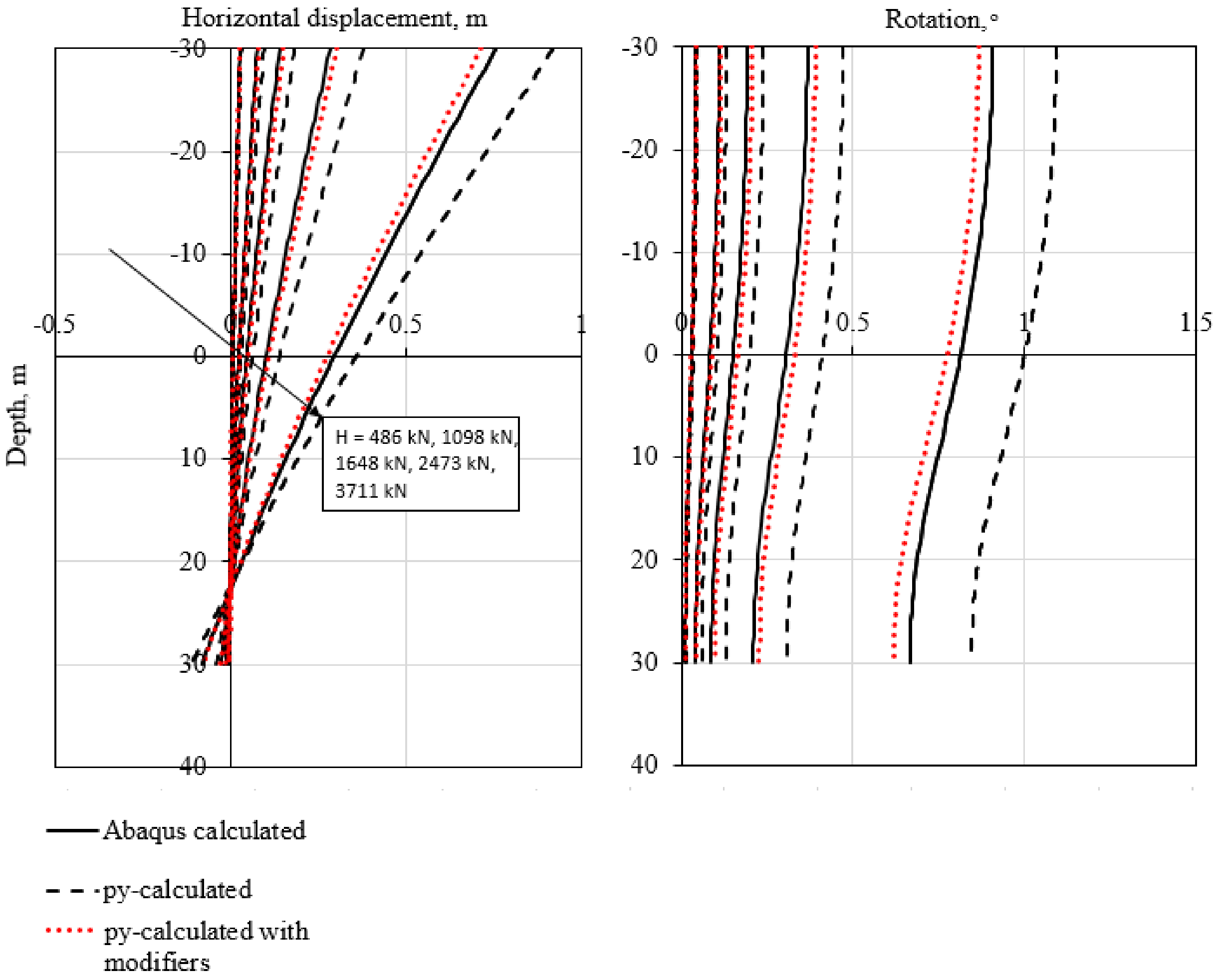

Figure 4.16: Predicted deformation using the optimized stiffness springs. Soil profile 1, L/D = 5, γ_f^p= 0.02. The legend wrongfully says "py-calculated". The pile responses are calculated using the aforementioned multi-spring beam-column model.

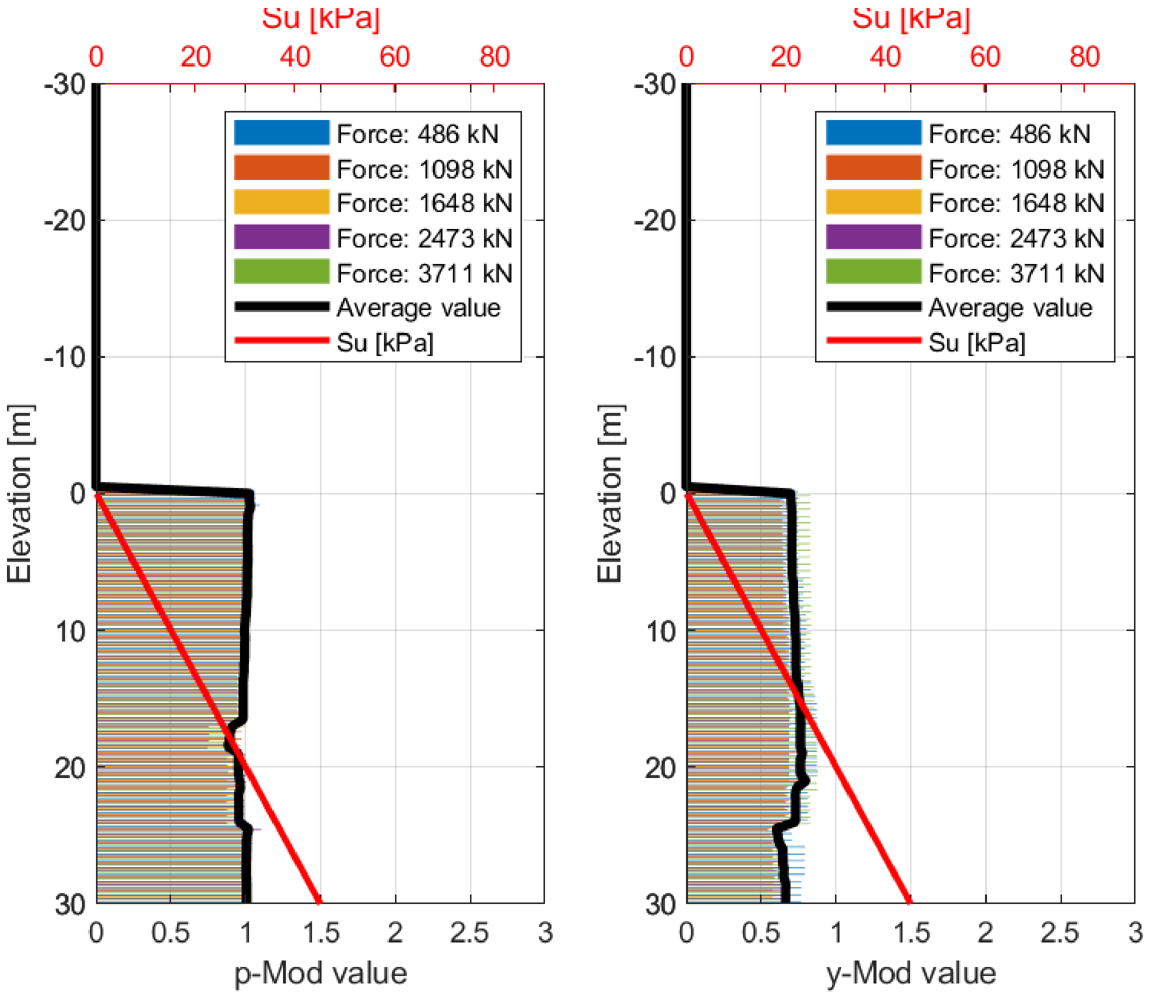

Figure 4.17: Stiffness spring modifiers applied.

4.6 Discussion

The discussion is divided into two separate parts. First the performance of the multi-spring model in the normally consolidated and the layered clay profile is discussed. Then, a discussion and further analyses of the stiffness corrections calculated by the optimization tool for the monopiles in normally consolidated and layered soil profiles are conducted.

4.6.1 Performance of the multi-spring model

The performance of the soil reaction spring model for various pile geometries are discussed, and noticeable results are highlighted.

L/D = 10

In general, the multi-spring model performs well, giving nearly identical results for the longer piles[1] for all soil profiles. Thus, it can be established that the multi-spring model performs well for longer monopiles (*L/D* = 10*)* in softer clays, as well as for the layered strength profiles. In the layered soil profiles, 80% of the pile is embedded into the stiffer bottom layer.

---

[1] Appendix: A.1.7., A.1.8, A.2.7., A.2.8., A.3.7., A.3.8., A.4.7., A.4.8., A.5.7. and A.5.8.

L/D = 7

The multi-spring model performs adequately for the piles with an *L/D*-ratio of 7. All piles and load levels give a good match[2], except at the load levels close to failure of the soft soil in soil profile 1. At these load levels[3] the mobilized soil strength is close to its capacity limit. This may lead to different interpretations in the Abaqus model relative to the numerical approach of NGI-PILE. Both approaches follow the same non-linear soil profile.

L/D = 3 & 5

The multi-spring model seems to predict the pile response of the monopiles (*L/D* = 3 and 5*)* in soil profile 5 adequately[4]. Thus, validating the applicability of the multi-spring model for monopile analyses in stiffer clay profiles.

For the normally consolidated, and the layered clay profiles the multi-spring model seems to predict a softer response than the FEA[5]. Thus, larger pile- displacements and rotations are observed.

Sources of error

Possible sources of error that may be of relevance are properties such as the meshing of the Abaqus model and the load step application. For several of the cases, the pile response at the highest load levels differ from patterns observed at earlier load levels[6]. Thus, it is assumed that the Abaqus model may not give a perfect description of the pile response at load levels close to failure. This phenomenon is explained by numerical overshoot due to discretization error. In some of the cases the phenomena made it look as if the response by the multi-spring model and the FEA-response correlates better at higher loads[7].

4.6.2 Monopile analyses using the optimization tool

With a basis in the results from the performance analyses (Appendix A), the monopiles are analyzed further using the optimization tool. Analyses for both the normally consolidated, and layered soil profiles are conducted. The optimization tool provides modifiers (Appendix C) that lead to an improvement in the pile response (Appendix B). The results are discussed in the following.

In general, the pile response calculated using the modified stiffness springs tend to give a better match to the FEA calculated pile response. All load levels seem to increase its accuracy, except for the highest load level. This is as excepted as the earlier load levels are at the steeper stage of the *p-y* curve, where a more linear type of curve is observed. As the optimal modifiers are calculated as the average of the different load level modifiers, the entire pile response is difficult to catch, as the pile response is non-linear.

---

[2] Appendix: A.1.5., A.1.6, A.2.5., A.2.6., A.3.5., A.3.6., A.4.5., A.4.6., A.5.5. and A.5.6.

[3] Appendix: A.1.5. and A.1.6., $H = 12004$ kN and $H = 11771$ kN, respectively

[4] Appendix: A.5.1., A.5.2., A.5.3. and A.5.4.

[5] Appendix: A.1.1., A.1.2., A.1.3, A.1.4, A.2.1., A.2.2., A.2.3., A.2.4., A.3.1., A.3.2., A.3.3., A.3.4., A.4.1., A.4.2., A.4.3. and A.4.4.

[6] Appendix: A.1.1., A.1.3., A.1.4., A.1.5., A.1.6., A.2.1., A.2.3., A.3.6., A.3.8., A.4.8., A.5.1., A.5.2., A.5.4., A.5.5. and A.5.6.

[7] Appendix: A.1.4. and A.3.6.

The modifiers may be visualized as stiffness corrections. An *p*-modifier below 1.0, and a *y*-modifier above 1.0 implies that the spring calculated response is too stiff relative to the soil and vice versa. All piles are optimized by iterating for the *y*-modifiers first. In general, all *y*-modifiers have a modifier value below 1.0, implying that the pile response calculated by the multi-spring model has too large deformations. This may be explained by the fact that the pile response is calculated by different strength mobilization levels. The Zhang and Andersen (2017) formulation was developed for slender piles in stiffer clay profiles. Thus, a high mobilization level for a slender pile implies that large portions of the soil adjacent to the pile adopt a plastic behavior, leading to large pile deformations. At the corresponding mobilization level for the monopiles in the softer clay profile, a smaller portion of the soil has adopted plastic behavior, thus lower deformations. This could be accounted for by applying lower scaling factors (ξ_1 and ξ_2) for the shear strains calculating the normalized displacement (*y/D*) in the Zhang and Andersen (2017) formulation.

The spring responses in the normally consolidated (soil profile 1 and 2) and the layered clay (soil profile 3 and 4) are explored in the following.

4.6.2.1 Normally consolidated clay

The calculated *p*- and *y*-modifiers for the normally consolidated clay profiles are relatively constant, thus it is assumed that the average value of the modifiers will give a representative description of the required spring corrections. The *p*-modifier is close to 1.0, thus for practical considerations it is assumed to have no influence on the scaling of the springs. To visualize the effect of the soil stress-strain relationship and the pile properties, the average *y*-modifiers are plotted against the *L/D* of the pile:

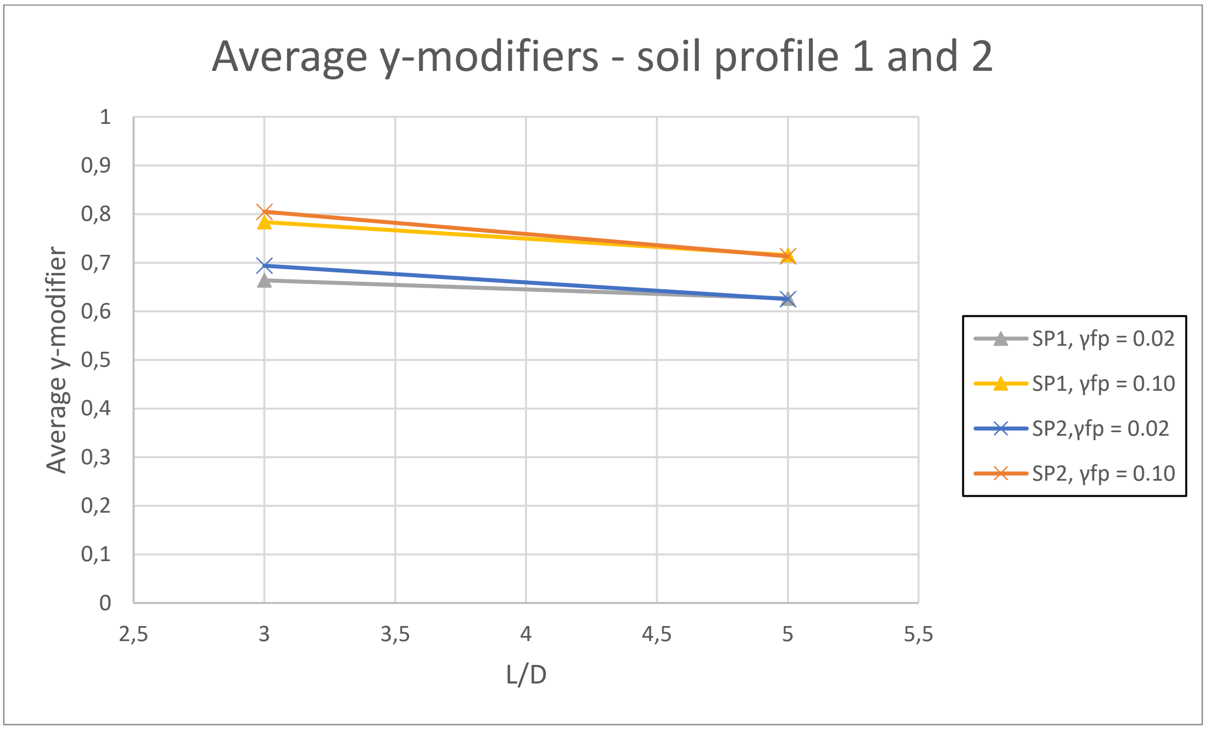

Figure 4.18: Average y-modifiers for the normally consolidated clay profile.

As seen in Figure 4.18, the effect of the pile dimensions (*L/D*) seem to be small as of practical considerations. The effect of the plastic failure strain has a direct impact on the calculated spring response. This is explained by the fact that a higher plastic failure strain will lead to larger soil strains prior to full soil mobilization. The deformation response calculated by the spring model is of a larger character (relative to the FEA pile response). Thus, it is sensible that the *y*-modifiers are closer to 1.0 at the higher plastic failure strains, as less corrections are needed to match the actual soil deformation. The effect of the plastic failure strain could be accounted for by conducting sensitivity studies of the plastic scaling coefficient, ξ_2 in the Zhang and Andersen (2017) formulation. There may be a possibility to formulate it as a function of the plastic failure strain.

4.6.2.2 Layered clay profile

There is a significant difference in the influence of the stiff bottom layer between the two different pile properties tested. In the cases regarding the piles with an *L/D*-ratio of 3, a third of the pile is embedded into the stiffer layer, and the bottom layer has close to no impact when comparing the calculated modifiers with the modifiers for the corresponding pile in soil profile 1. In the cases regarding the piles with an *L/D*-ratio of 5, 60% of the pile is embedded into the stiff layer. The *y*-modifier is in the same range as earlier, between 0.6 and 0.8. While the *p*-modifier tends to behave differently for the pile lengths embedded in the different soil layers. The effects are visualized by plotting the average *p*- and *y*-modifiers for the upper- and lower soil profile for the piles with an *L/D*-ratio of 5 (Appendix C.2.2.) in Figure 4.19.

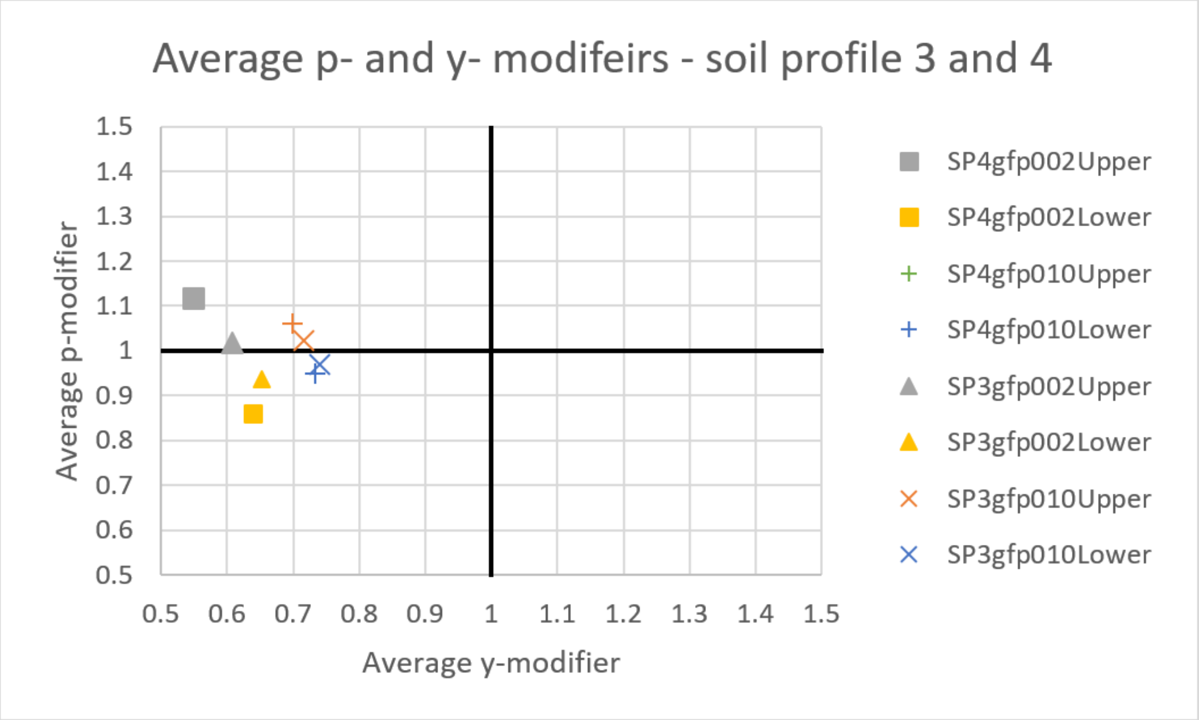

Figure 4.19: Average p- and y-modifiers for the layered soil profiles, with 60% of the pile embedded into the stiffer bottom soil layer (L/D = 5). The plastic failure strain is denoted as gfp.

As seen by Figure 4.19, the stiff lower soil layer influences the soft upper layer for all soil profile cases. The strength of the upper soil layer increases in all cases (average *p*-modifier above one) and decreases in the lower layer. The effect is particularly visible in the stiffer stress-strain profiles with a plastic failure strain of 0.10.

By these results, it is established that layering will not affect the pile response noticeably in cases where a stiff soil profile encircles less than a third of the bottom pile length. Monopiles embedded 60% into a stiffer lower layer are affected by the layering effect.

5 Pile damping

5.1 Introduction

An assessment of large-scale offshore wind power in the US showed that the support structures of a monopile contributed approximately 20-25% of the total capital cost (Musial & Ram, 2010). Damping is directly connected to the costs as it affects the result of the design load, which in turn influences the fatigue design of the structure. Higher damping can lead to lower design loads, and therefore a reduction of the material required. For an offshore wind turbine, the sources of damping are multiple, e.g. aerodynamic, hydrodynamic, structural and soil damping. Out of these sources of damping, the characterization of the soil damping has been considered the most complex parameter to model (Carswell et al., 2015). Darendeli (2001) presented a framework for estimating the damping for a specific soil profile as a function of *pre-consolidation stress* (σ_0'), *over consolidation ratio* (*OCR*), *plasticity index* (I_p), *number of loading cycles* (*N*), and the *loading frequency* (*f*). This section investigates if it is possible to find a connection between the estimated soil damping, and the pile damping without the need of using a comprehensive *finite element (FE)* tool. A framework of estimating the pile damping as a function of soil variables would be timesaving and applicable for practicing engineers, thus saving costs.

Using a pile slice model in Plaxis 3D (Plaxis, 2017), the damping at soil-pile interaction level (pile damping) is calculated by integrating the potential energy, E_{S0}, and the dissipated energy E_D over the soil at various displacement levels for eight different soil profiles. The pile damping is compared to the soil damping at element level for the respective soil profile to investigate what scaling factor would match pile- and soil damping the best.

To avoid misunderstandings, the damping within this section is referred to as *d,* and the diameter as *D*, unlike the theory presented in section 2.6.

5.2 Assumption

Zhang and Andersen (2017) demonstrated that it is possible to scale the soil-pile interaction (*p-y*) from the stress-strain response of the soil with simple scaling coefficients. It its postulated that a similar scaling law also exists for the soil damping. By establishing the fact that the *soil damping*, d_{soil}, at a specific point correspond to an equivalent *pile damping*, d_{pile}, the *pile-soil displacement* (*y/D*) can be scaled from the shear strain at the same damping ratio. The concept is visualized in Figure 5.1.

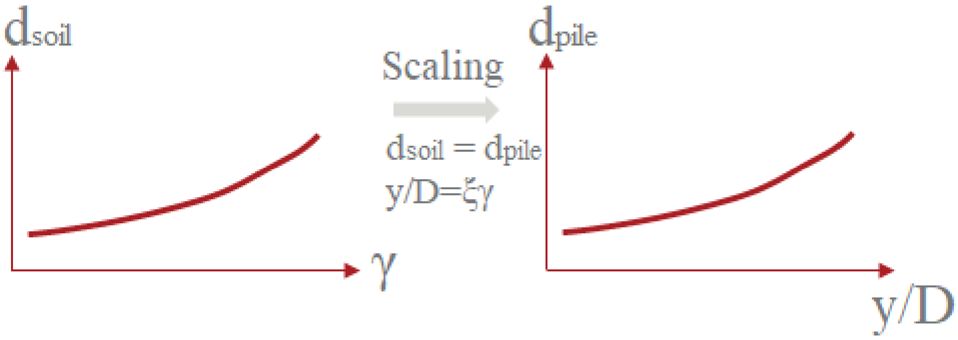

Figure 5.1: Damping scaling concept.

y is the pile displacement, D is the pile diameter, ξ is the scaling factor and γ is the shear strain for the soil. The concept is verified through FEA below.

5.3 Finite Element Model

5.3.1 Geometry and meshing

The focus of the testing is the connection between pile and soil damping. Thus, for simplicity the analysis is performed by modeling a representative horizontal slice of a pile (Figure 5.2), embedded into the ground. The model is 1 meter thick, with geometry as presented in Figure 5.3.

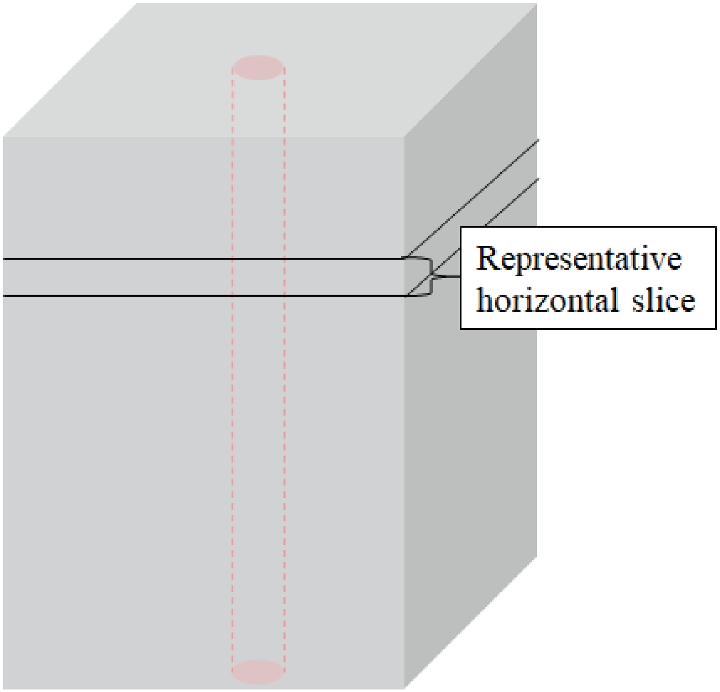

Figure 5.2: Representative horizontal slice of a pile embedded into the ground.

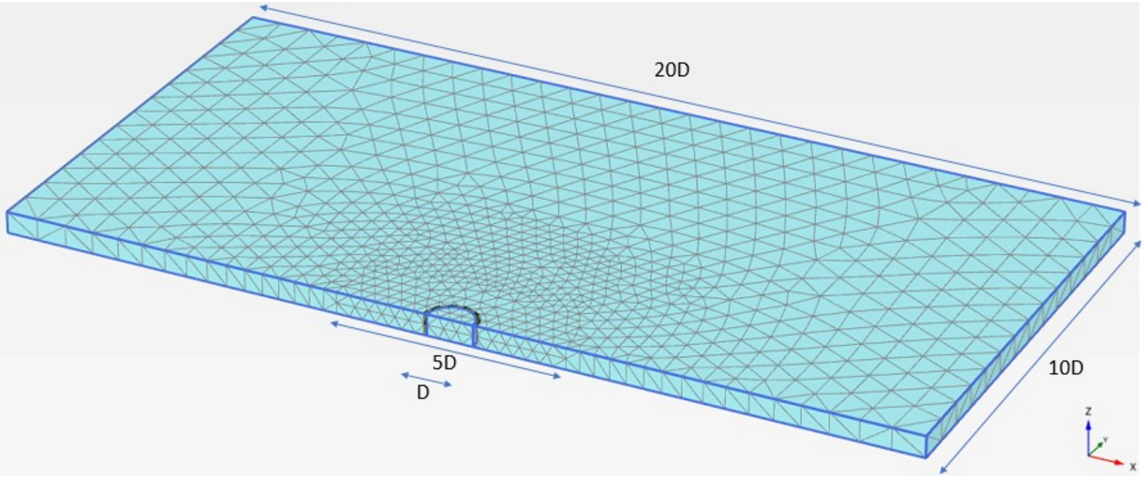

Figure 5.3: Geometry of the PLAXIS model. D is the pile diameter.

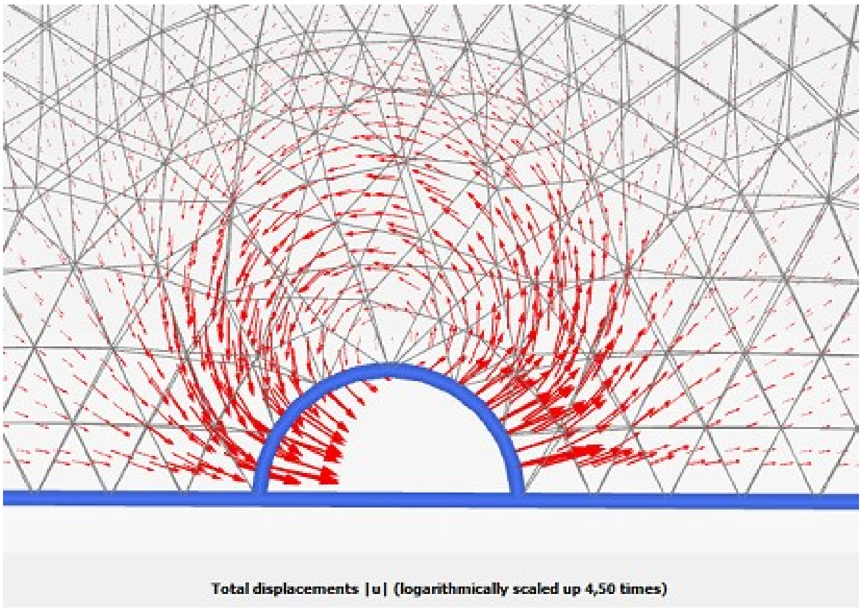

Figure 5.4: Localized flow around mechanism at failure.

Due to symmetry only half of the pile is modelled. The pile is modelled as a rigid body, with the force applied laterally in the center of the pile. All model boundaries are normally fixed, giving plane strain conditions. The pile interface is modeled as a rough interface, where separation is not allowed.

Due to computational efforts, the mesh within a cylindrical radius of 2.5*D* from pile center is meshed with a finer mesh. The mesh has been evaluated against the theoretical solutions of limiting bearing pressure of a circular cylinder, failing under plain strain flow around mechanism. Randolph and Houlsby (1984) showed that a fully rough interfaced pile has a theoretical bearing pressure of $11.94S_u$. The Plaxis model calculates a limiting bearing pressure of $12.47S_u$, which leads to a 4.4% numerical overshoot due to discretization error. The model will be used for analyses at load steps prior to fully soil mobilization, thus the meshing is assumed to perform adequately.

5.3.2 Soil model

The parametric analysis has basis in varying the stiffness variables *OCR* and I_P, while the pre-consolidation stress, number of loading cycles and loading frequency are kept constant. The following soil profiles are considered in the parametric analysis:

σ_0' [kPa]: 100

OCR: 1, 40

I_p [%]: 10, 20, 40, 60

N: 10

f [Hz]: 0.1

By using the model parameters presented by Darendeli (2001) for clays, the soil damping and normalized stiffness reduction (G/G_0) as a function of the shear strain is calculated. The calculated soil damping, and normalized stiffness reduction for the investigated soil profiles are presented below. Figure 5.5. and Figure 5.6. presents the normalized stiffness reduction and the soil damping, respectively, for soil profiles with an over consolidation ratio of 1. For the soil profiles with an over consolidation ratio of 40, the normalized stiffness reduction and the soil damping are presented in Figure 5.7 and Figure 5.8, respectively.

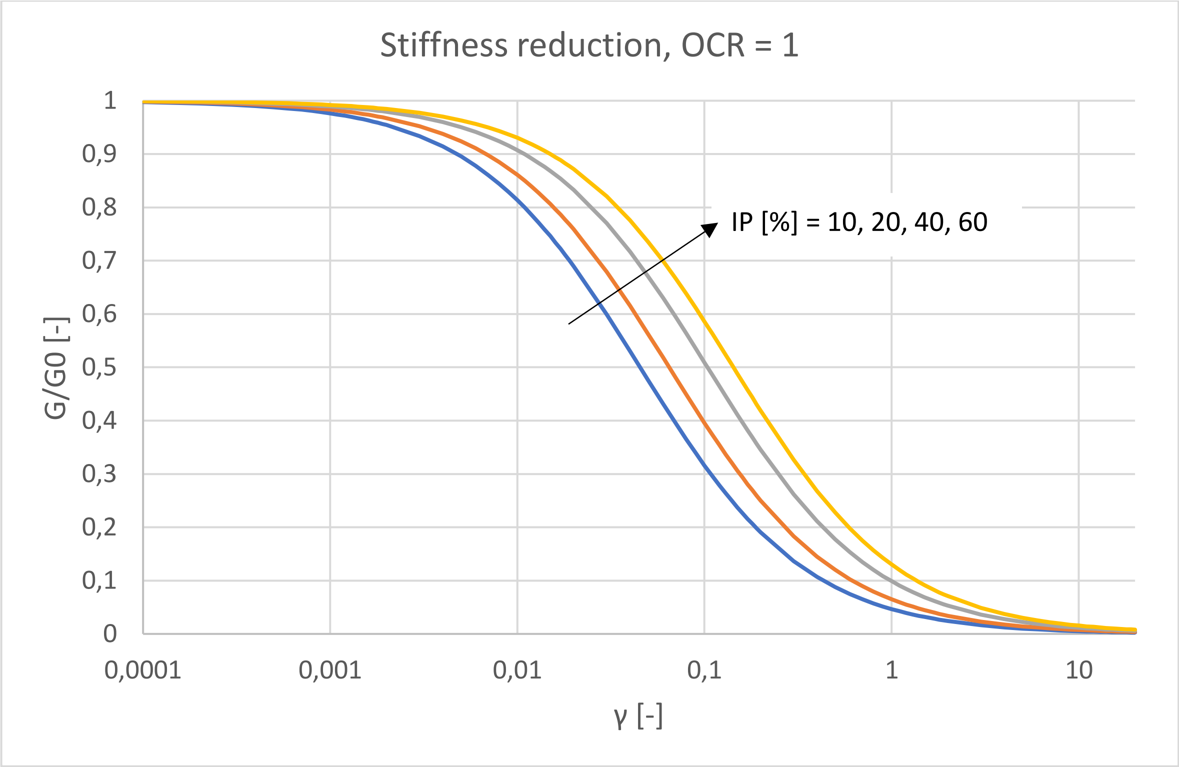

Figure 5.5: Normalized stiffness reduction curves with an OCR of 1.

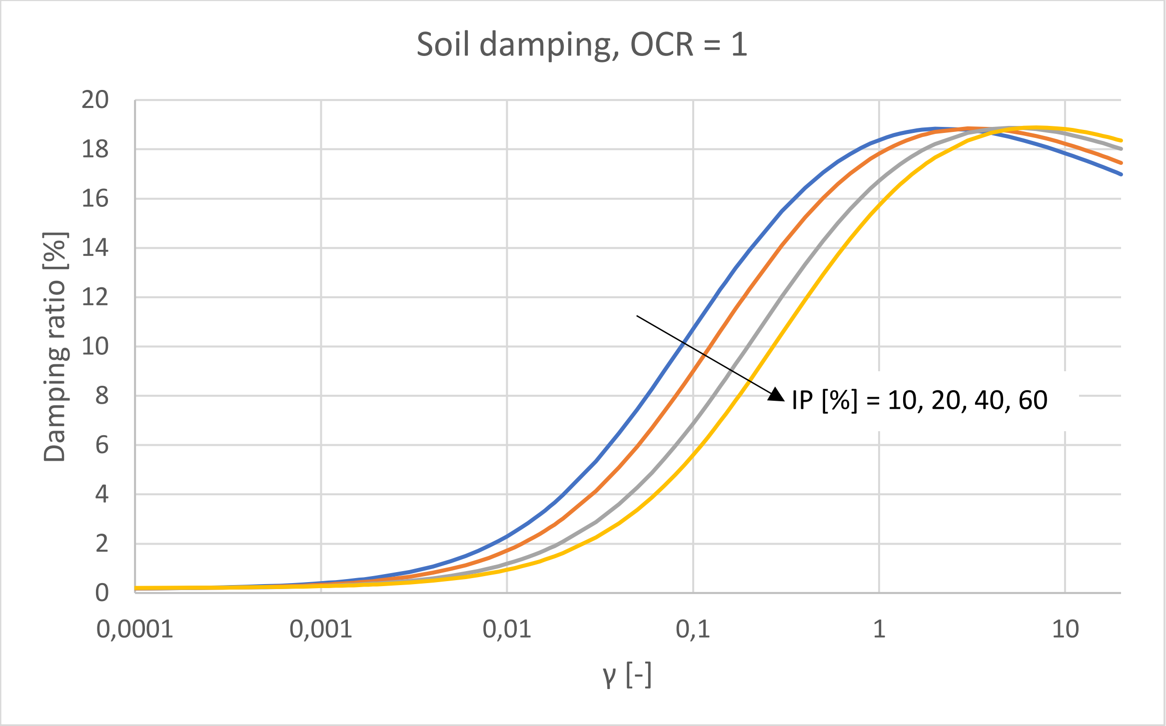

Figure 5.6: Estimated damping ratio. OCR = 1.

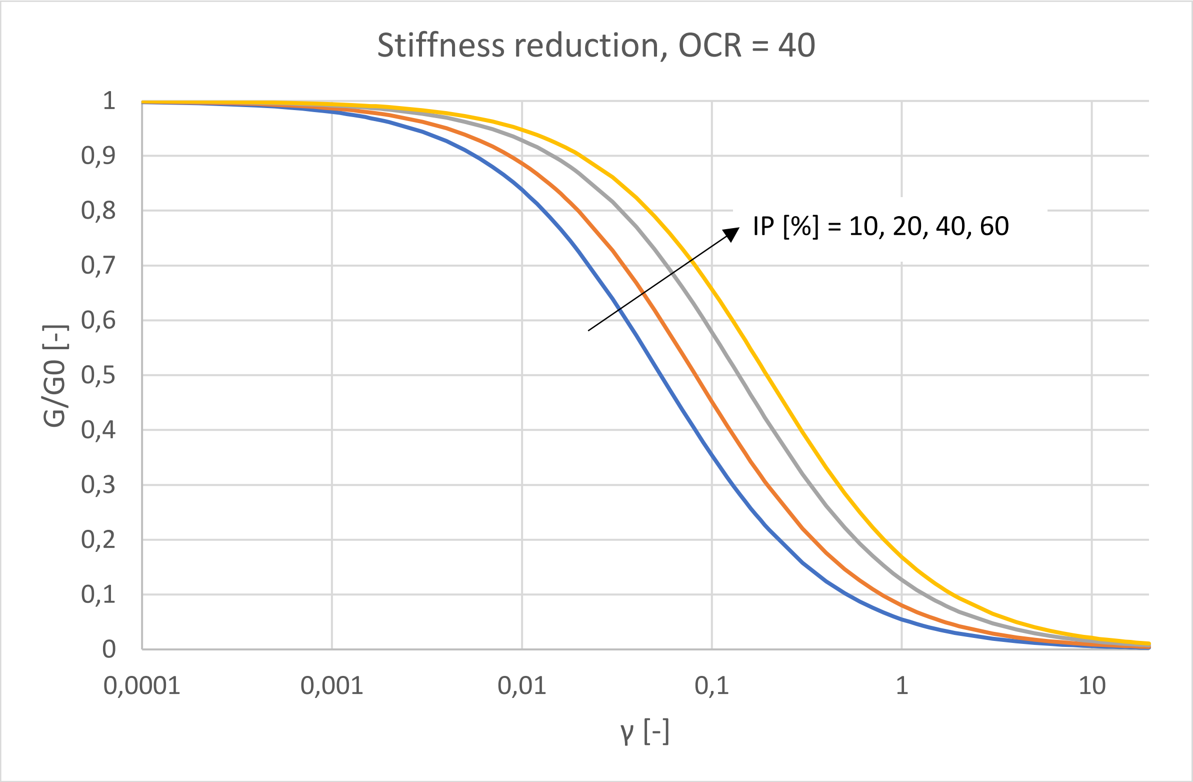

Figure 5.7: Normalized stiffness reduction curves with an OCR of 40.

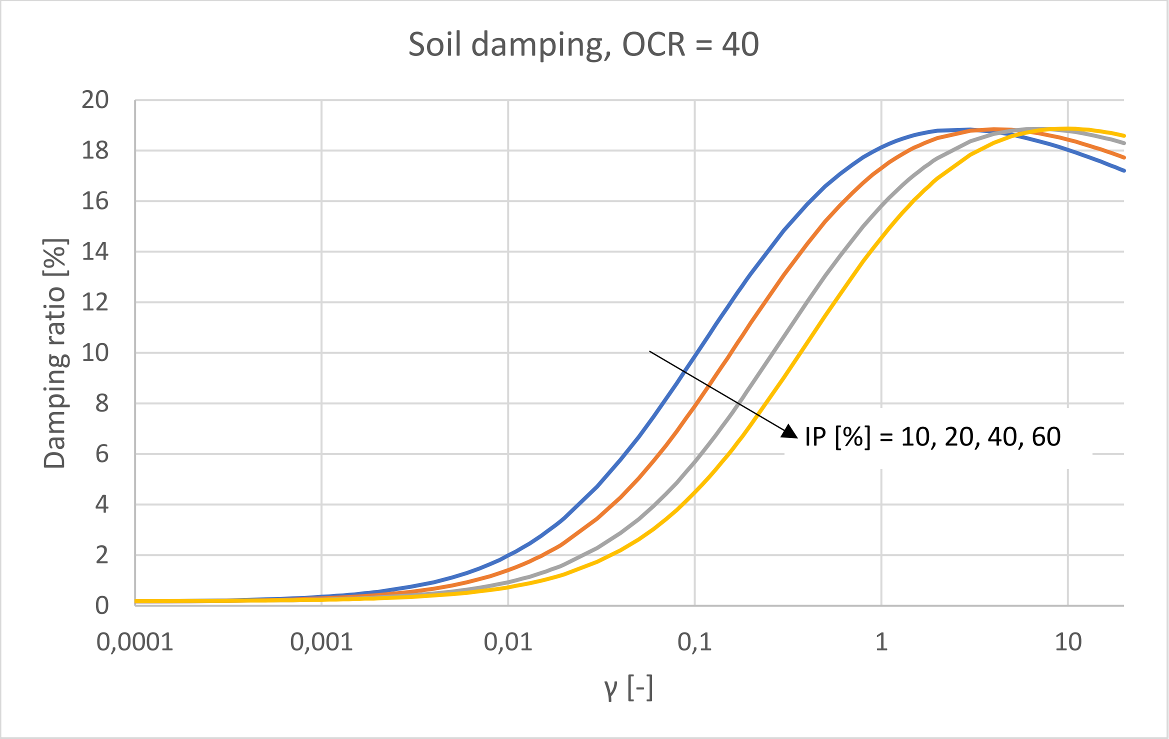

Figure 5.8: Estimated damping ratio. OCR = 40.

Following the empirical correlation presented by Andersen (2015) in the third McCelland lecture, an estimation for initial stiffness, *G₀*, is estimated by:

$$\frac{G_0}{\sigma_{ref}{}'} = \left(30 + \frac{75}{\frac{I_p}{100} + 0.03}\right) * OCR^{0.5}$$

$$\sigma'_{ref} = p_a * \left(\frac{\sigma_0{}'}{p_a}\right)^{0.9}$$

where p_a is the atmospheric pressure equal to *100 kPa*. The stress-strain response for the soil profile is found through the simple connection:

$$\tau(\gamma) = G(\gamma)\gamma$$

The soil is modeled using the NGI-ADP soil model (Grimstad et al., 2012). The shear strength and failure plastic strains are used as curve fitting parameters to match the stress-strain response calculated by the Darendeli model. An example comparison of the stress-strain response between the Darendeli model, and the NGI-ADP soil model for the soft clay profile with high plasticity (*OCR* of 1, *IP* of 60%) are presented in Figure 5.9. For this example, a shear strength of 20 kPa, and a plastic failure strain of 1.2% are found to give a good match. The G_0 is estimated using the above mentioned correlation, which results in a G_0/S_u ratio of 760 for this example case. As it is close to impossible to get an exact match between the different stress-strain profiles, the test is moderately limited, but as this exercise is conducted to investigate a hypothesis it is assumed that the limitation will not affect the result noteworthy.

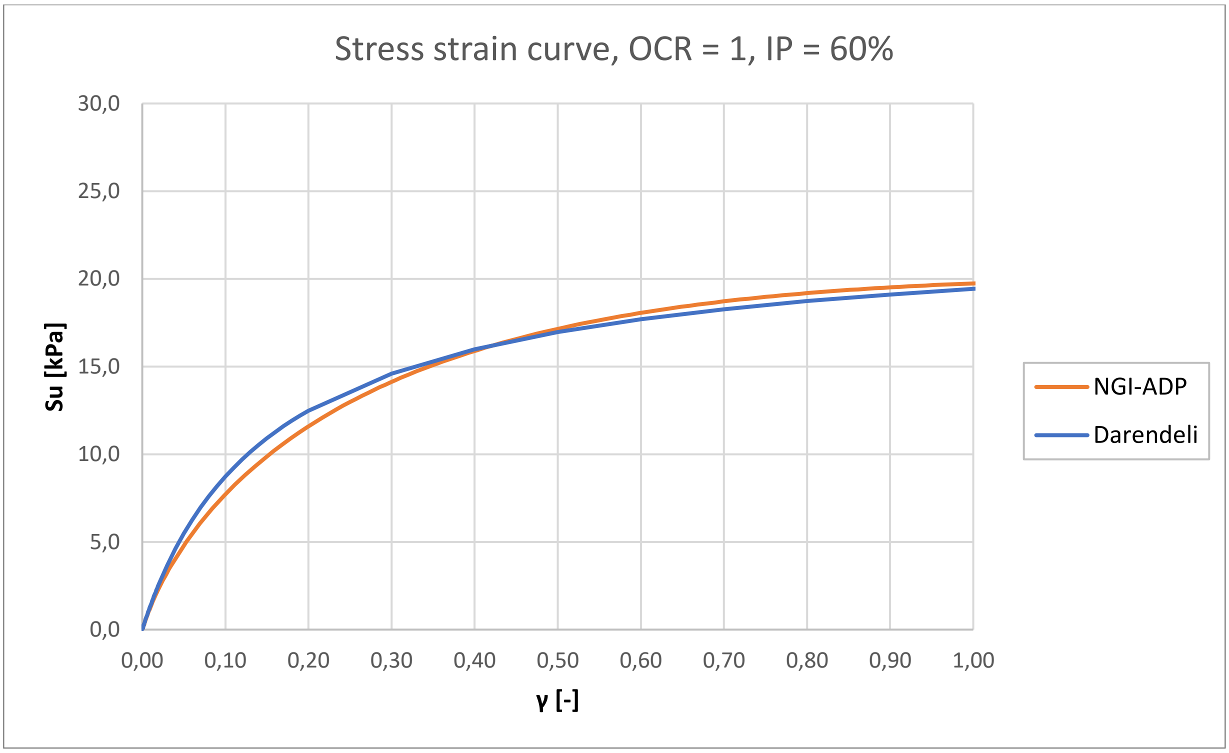

Figure 5.9: Stress-strain comparison between the Darendeli model and the NGI-ADP soil model.

5.3.3 Pile damping

The pile damping is calculated by finding the hysteric damping of the soil. The radiation damping is neglected, as the investigated frequency is below 1 Hz for all soil profiles (Carswell et al., 2015). The energy loss is found by calculating the potential energy and the dissipated energy. These are found by dividing the soil modeled in Plaxis 3D into small soil elements. The potential energy for each soil element, $E_{S0,i}$, is found by calculating the local energy density (stresses multiplied by strains) and multiplying it with the volume of the soil element, $V_{el,i}$:

$$E_{S0,i} = V_{el,i}\left(\sum \frac{1}{2}\sigma_{kk}\epsilon_{kk} + \sum \frac{1}{2}\tau_{kj}\gamma_{kj}\right)$$

The dissipated energy for one specific soil element, $E_{D,i}$, is found by rewriting the equation for the equivalent damping ratio:

$$d = \frac{1}{4\pi}\frac{E_D}{E_{S0}} \Rightarrow E_{D,i} = \ d_i 4\pi E_{S0,i}$$

where d_i is the local soil damping for at the considered soil element, found by the Darendeli damping curve, at the maximum shear strain of the soil element.

After finding the potential- and dissipated energy for each soil element, the total foundation damping is found by summing up all energy contributions:

$$d_{pile} = \frac{1}{4\pi}\frac{\sum_{i=1}^{n} E_{D,i}}{\sum_{i=1}^{n} E_{S0,i}}$$

In total eight soil profiles are analyzed. Each soil profile is tested at multiple deformation states, giving multiple data points for the damping comparison.

5.4 Results

As a re-confirmation, the *p-y* response of the pile in the FE-model is compared to *p-y* curves estimated by the Zhang and Andersen (2017) framework. As presented below (Figure 5.10), the FE-model and the model by Zhang and Andersen (2017) provides a good match for all soil profiles, reconfirming the generality of the framework.

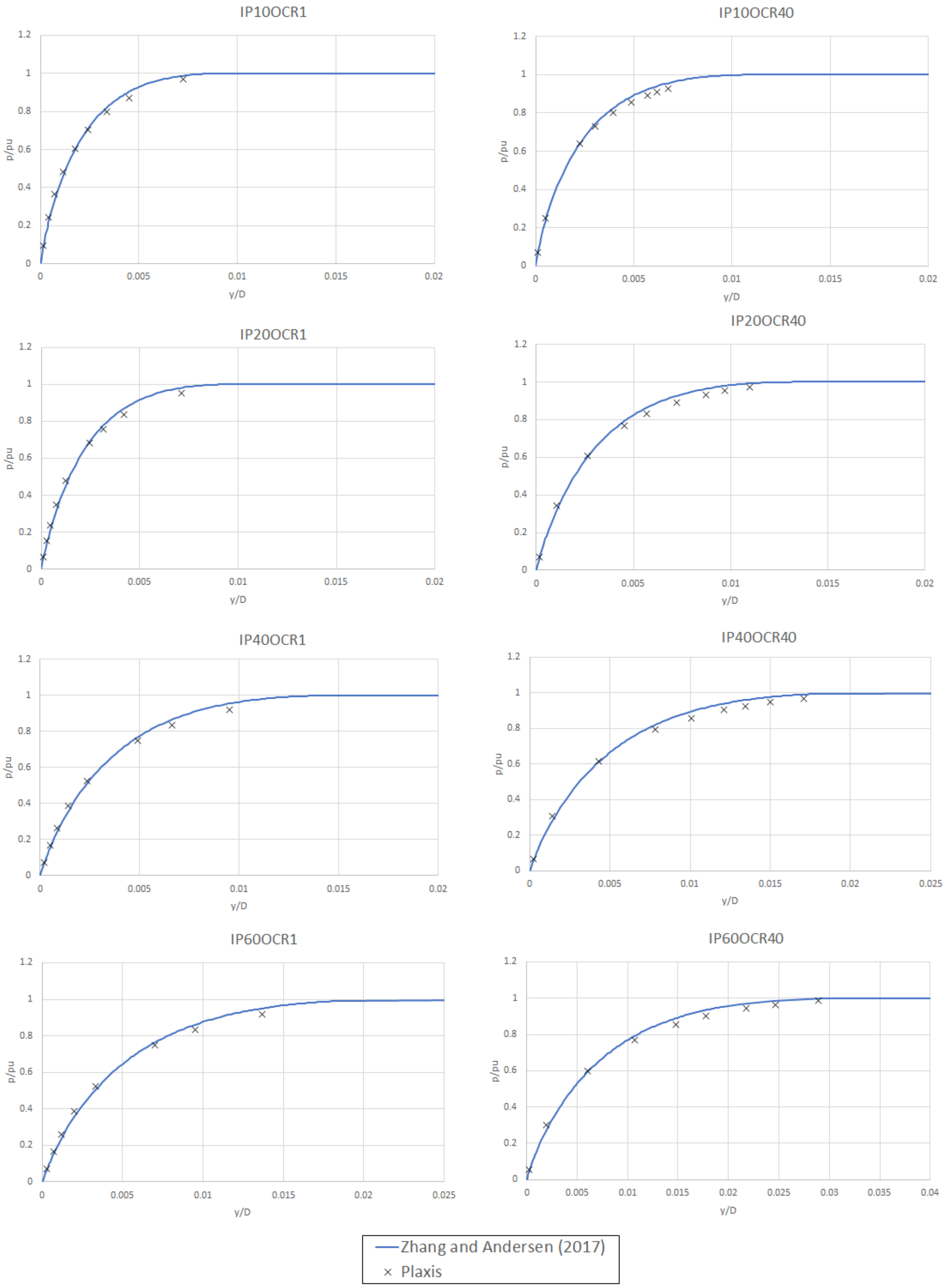
IP10OCR1
IP10OCR40
IP20OCR1
IP20OCR40
IP40OCR1
IP40OCR40
IP60OCR1
IP60OCR40

Figure 5.10: p-y response predicted by the FE-model along the p-y curves constructed from the stress-strain curves by Zhang and Andersen (2017).

By comparing the soil- and the pile damping for the different stiffness profiles, the corresponding scaling factors at different deformation stages are calculated. As presented in Figure 5.11 and Figure 5.12, the scaling factors varies between 3 and 3.75, and does not seem to be affected by the stiffness profiles. For practical purposes a constant value of 3.3 is suggested and tested.

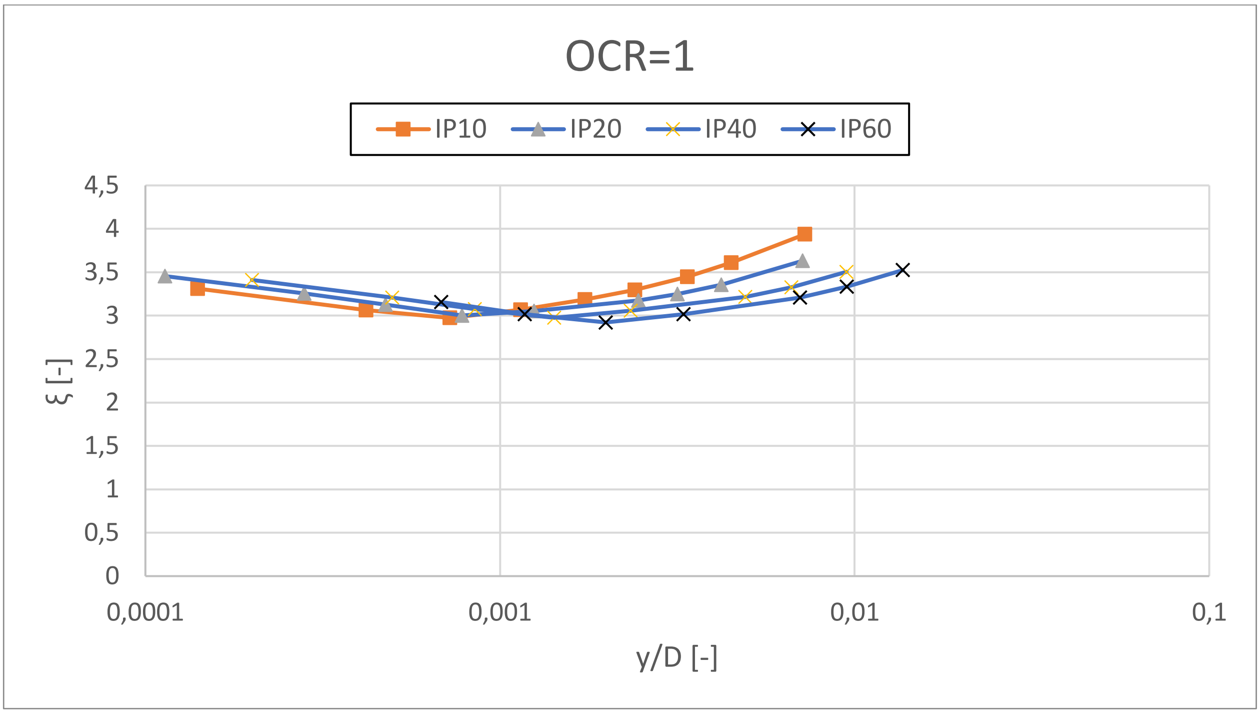

Figure 5.11: Back-calculated scaling factor for four different soil profiles with OCR=1 at different displacement levels. Note that the x-axis is log-scaled.

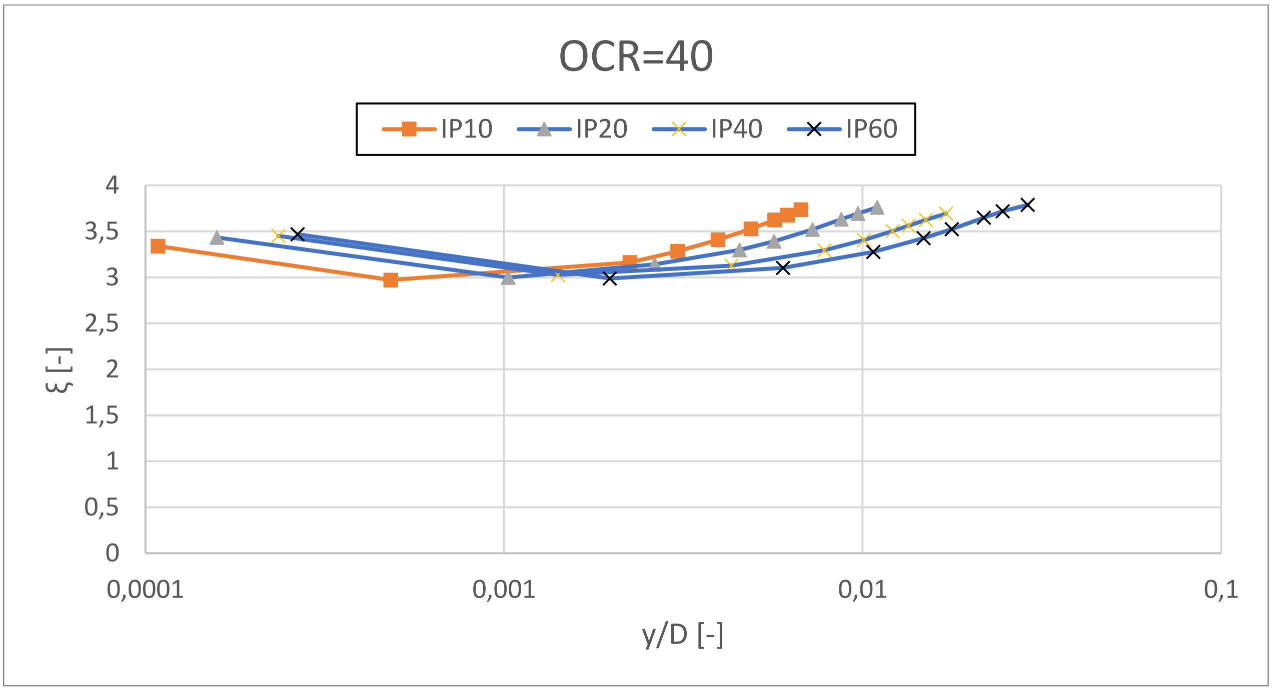

Figure 5.12: Back-calculated scaling factor for four different soil profiles with OCR=40 at different displacement levels. Note that the x-axis is log-scaled.

In general, the proposed scaling factor of 3.3 performs very well. The scaled soil damping gives a good match to the pile damping, estimated by the finite element analyses. The results of all damping calculations are presented in Figures 5.13-20. Figure 5.13 and Figure 5.20 shows the calculation results of the two limit cases, respectively a normally consolidated clay profile with a low plasticity index (*OCR*=1, I_P = 10%) and an over-consolidated clay profile with a high plasticity index (*OCR*=40, I_P = 40%). As the figures show, small deviations are experienced in the damping ranges 2.5% to 6% where the scaled soil damping underpredict the pile damping, and above 11% where the pile damping is overpredicted.

The estimated pile damping (*Darendeli scaled*) from the soil damping (*Darendeli*) and the FE-calculated pile damping (*Plaxis*) are compared. A good match between the FE-calculated damping and scaled pile damping is demonstrated. Note that the soil damping (blue line) is plotted against the shear strain, while the pile damping (grey line), and the Plaxis points are plotted against the normalized displacement, *y/D.* All calculation results are presented in the following.

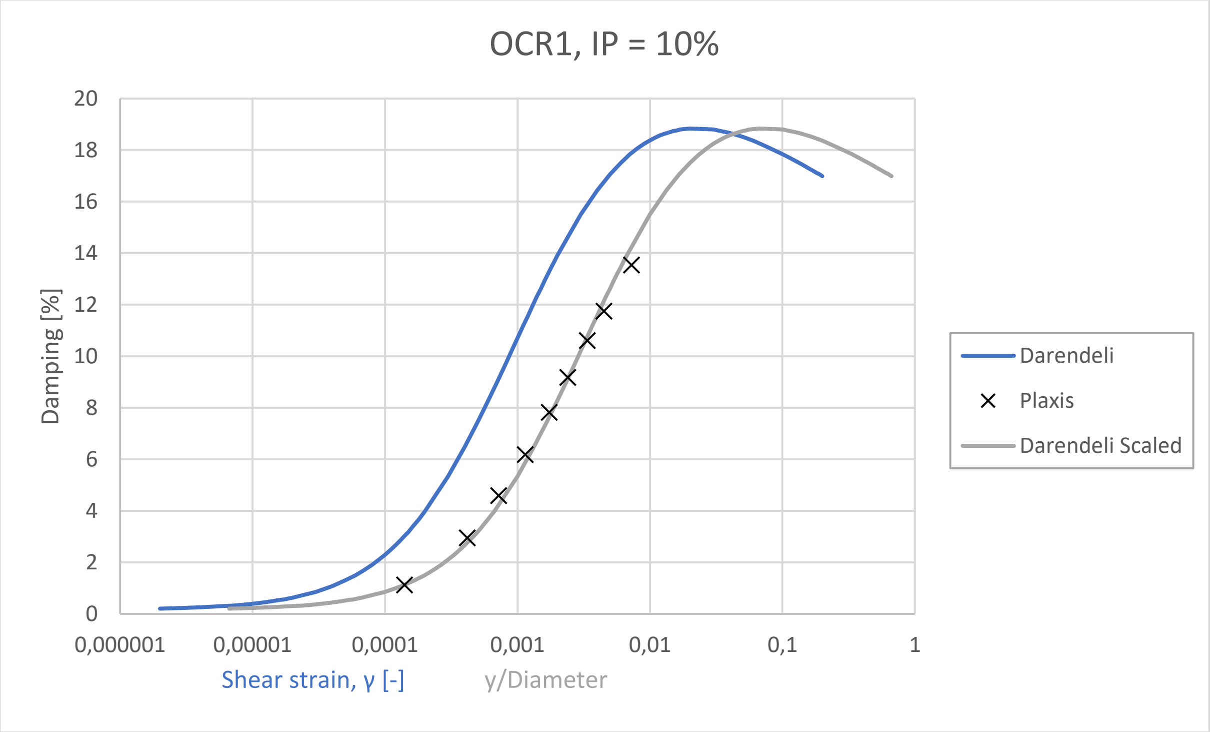

Figure 5.13: Estimated pile damping by scaling the soil damping. OCR=1, I_P=10%.

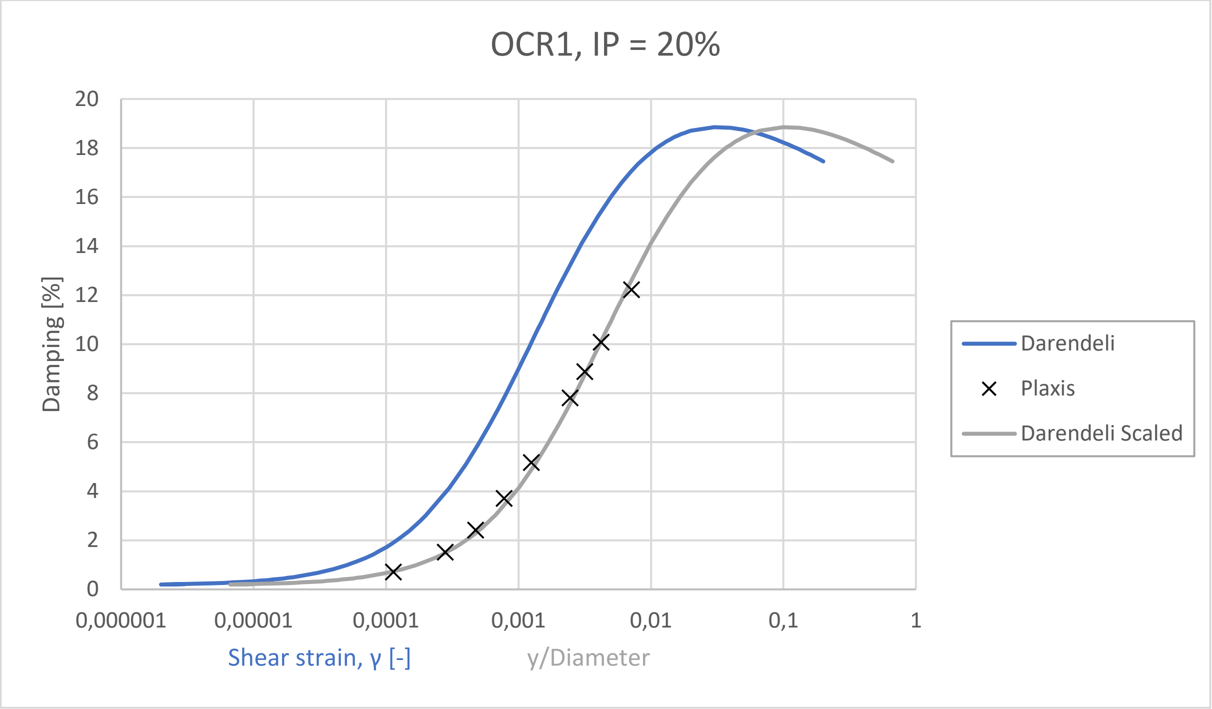

Figure 5.14: Estimated pile damping by scaling the soil damping. OCR=1, I_P=20%.

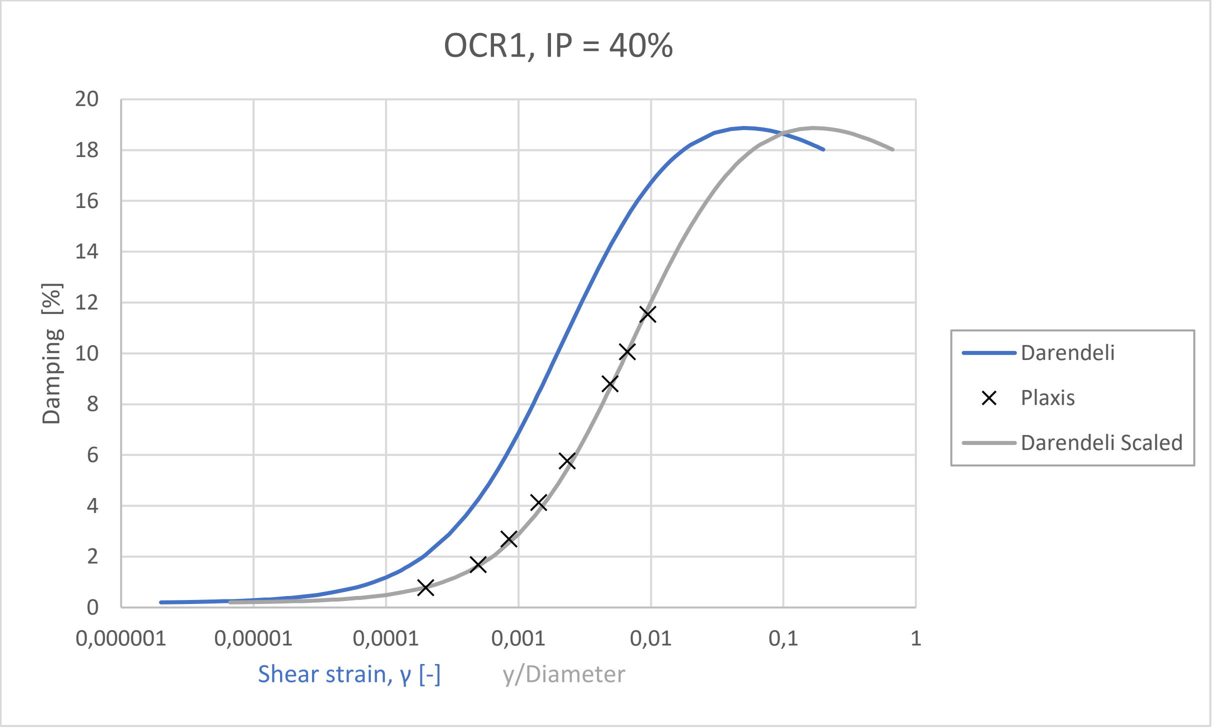

Figure 5.15: Estimated pile damping by scaling the soil damping. OCR=1, I_P=40%.

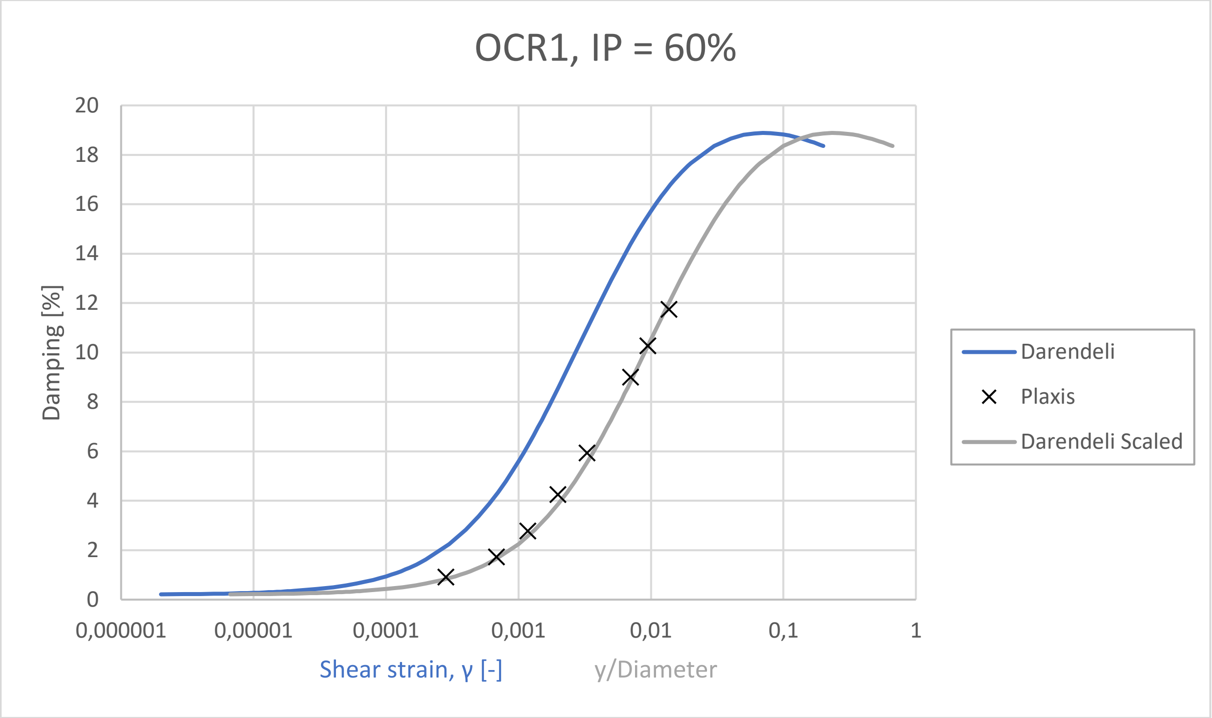

Figure 5.16: Estimated pile damping by scaling the soil damping. OCR=1, I_P=60%.

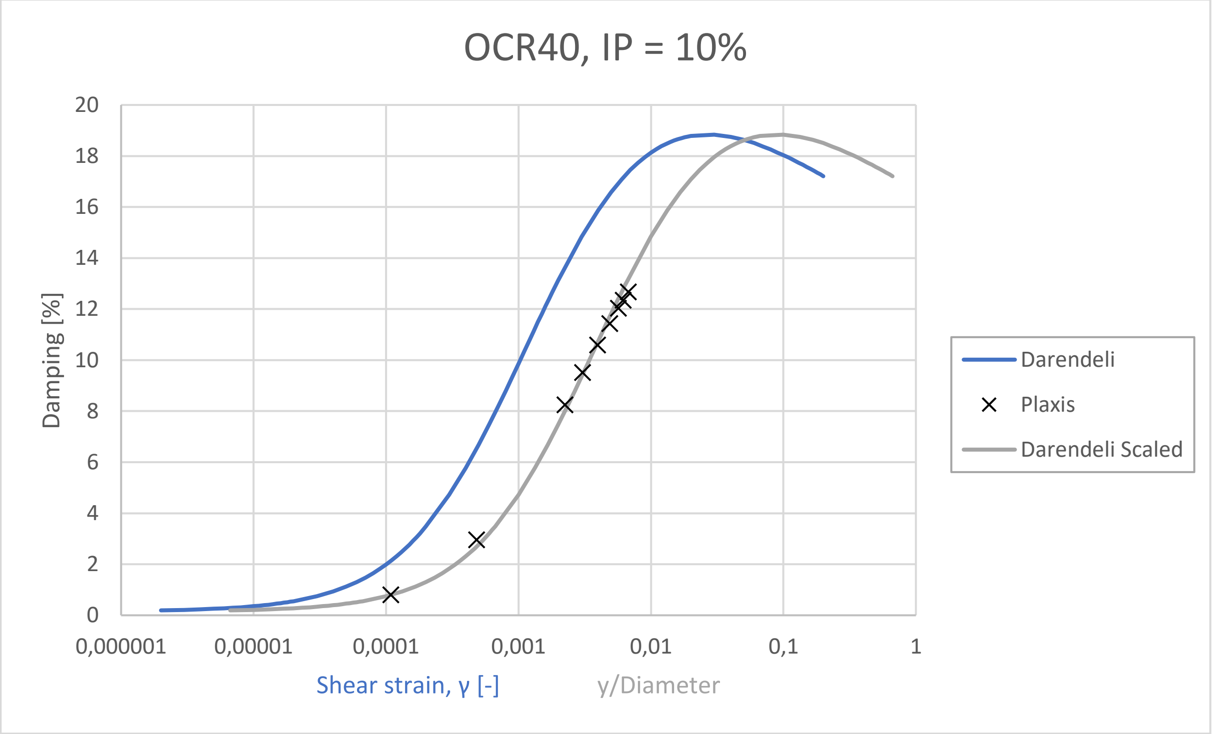

Figure 5.17: Estimated pile damping by scaling the soil damping. OCR=40, I_P=10%.

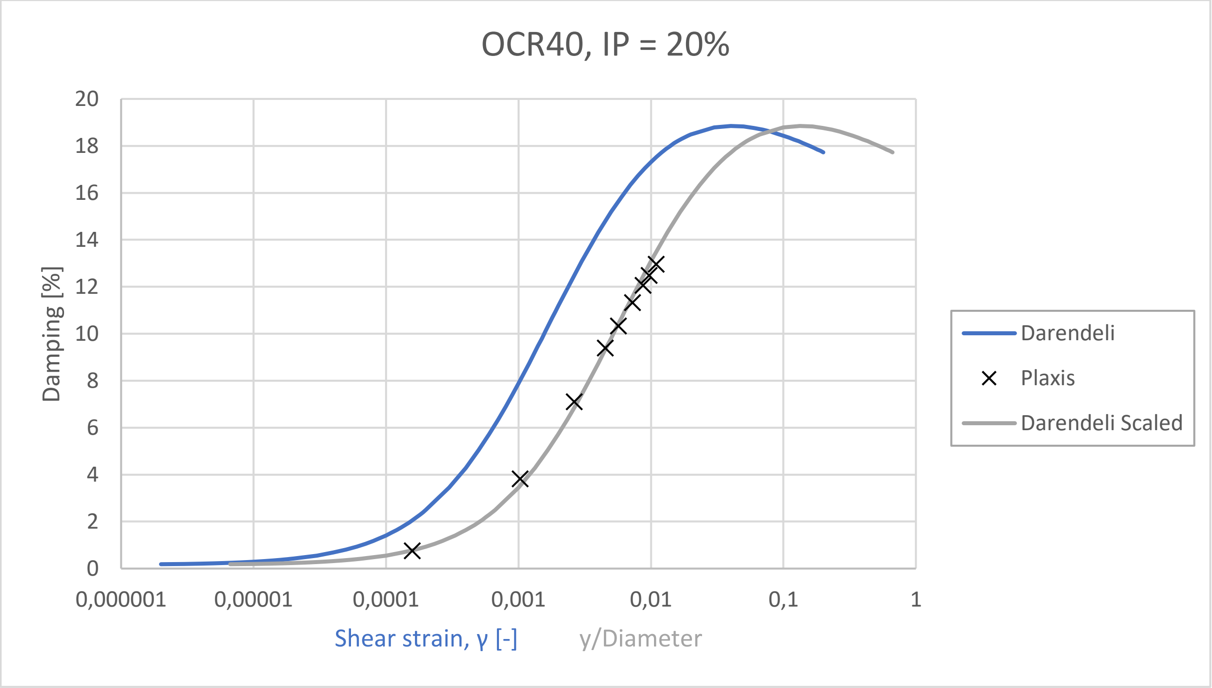

Figure 5.18: Estimated pile damping by scaling the soil damping. OCR=40, I_P=20%.

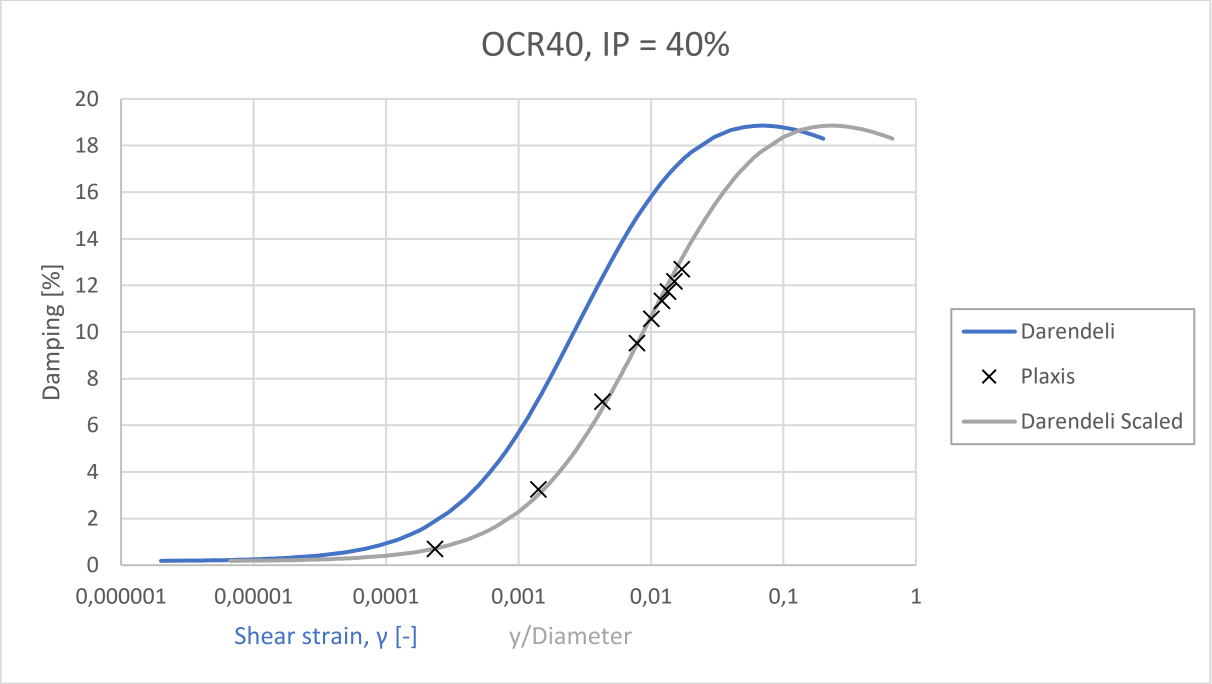

Figure 5.19: Estimated pile damping by scaling the soil damping. OCR=40, I_P=40%.

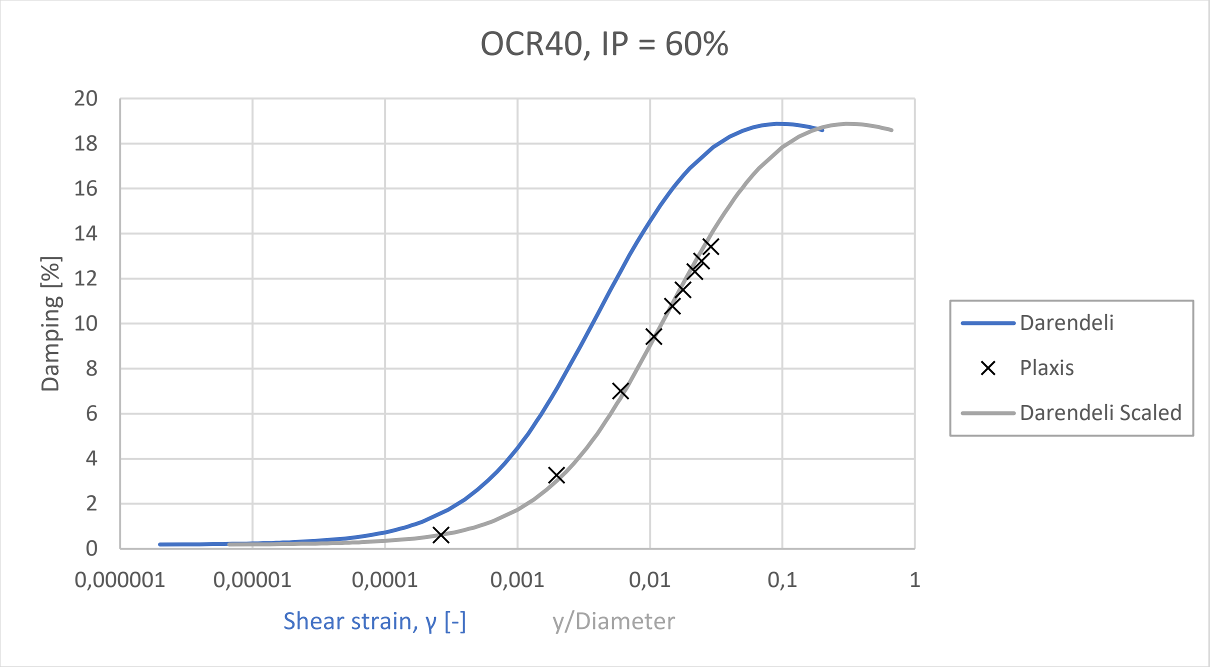

Figure 5.20: Estimated pile damping by scaling the soil damping. OCR=40, I_P=60%.

5.5 Conclusions

The following conclusions can be made based on the results presented above:

- The FEA re-confirm the scaling relationship between the stress-strain behavior of the soil at element level and soil-pile interaction *p-y* response.
- The hypothesis that it is possible to link the soil damping at element level to the pile damping at soil-pile interaction level is verified.
- A scaling factor of 3.3 is found to give a good estimation of the pile damping by scaling the damping response of the soil.

The proposed scaling factor of 3.3 is based on a study of relatively small parametric range. The effect of other variables such as the number of cycles, loading frequency and the pre-consolidation stress are not accounted for by the study conducted herein. These aspects need to be further investigated for a complete validation of the scaling factor.

By the framework presented in section 2.6.5., one may discuss the impact of each of the variables that are yet to be tested. The pre-consolidation stress has a direct impact on the estimated reference strain, γ_r. The reference strain is included in the calculation of the stiffness reduction curve, by moving the curve relative to the strain-axis. As seen through these analyses, the scaling factor does not vary appreciably relative to the stiffness reduction curve used for calculation. The stiffness reduction is independent of the loading frequency. It mostly affects the soil damping at small-strain area. What impact the variation of frequency remains unknown. The stiffness reduction curve is independent of the number of loading cycles. An increase in the number of loading cycles lead to a damping ratio reduction at the higher strain-values. As previously discussed, the estimated pile damping overpredict the actual pile damping at higher strains. Consequently, it can be conceived that the scaling factor may even be more precise for a higher number of cycles.

6 Conclusions and recommendation for further work

6.1 Conclusions

Several conclusions can be drawn based on the work carried out in this study:

1. A robust, efficient tool has been developed to calibrate soil reaction curves based on finite element analyses. The tool shows promising prospect for application in monopile design.
2. The performance of a proposed framework for analyzing monopile response in normally consolidated to lightly over-consolidated soft clays and layered soil profiles is examined. It is found that the proposed framework generally captures the monopile response well, particularly for *L/D* ratios equal or greater than 7. For piles with smaller *L/D* ratios, the framework generally predicts responses that fall on the softer side compared to FEA. Calibration exercise using the developed optimization tool demonstrates that much improved predictions can be achieved by using calibrated soil springs. The modifiers are found to be quite stable with depth. The *p*-modifier is found to be close to unity (meaning no adjustment) while the *y*-modifier is found to be less than 1.
3. A link between the soil damping at element level and at the soil-pile interaction level is confirmed, and for the parametric range tested, a scaling factor of 3.3 is revealed.

6.2 Recommendations for further work

There are several aspects that can be considered for future research:

1. The effect of soil anisotropy is yet to be investigated.
2. Further testing of the layering effect. In the analyses performed in this work, the only pile that had a noticeably effect of the layering was the pile embedded 60% into the stiffer soil layer. Further analyses with shallower embedment in the stronger layer could be useful.
3. Investigate the pile response in layered soil profiles consisting of a combination of sand and clay.
4. Further test the damping scaling model for wider parametric ranges. The effect of number of cycles, loading frequency and pre-consolidation stress are yet to be investigated.

References

4coffshore. (2018). Interactive Wind Farms map. Retrieved from https://www.4coffshore.com/offshorewind/

Abaqus, V. (2017). *Abaqus/CAE User's Manual*.

Andersen, K. H. (2015, June 10th, 2015). [3rd McClelland Lecture - Knut Andersen - Text].

API. (2014). API RP 2GEO. In *Geotechnical and Foundation Design Considerations*.

Bauchau, O. A., & Craig, J. I. (2009). Euler-Bernoulli beam theory. In O. A. Bauchau & J. I. Craig (Eds.), *Structural Analysis* (pp. 173-221). Dordrecht: Springer Netherlands.

Byrne, B., Mcadam, R., Burd, H., Houlsby, G., Martin, C., Gavin, K., . . . Taborda. (2015b). Field testing of large diameter piles under lateral loading for offshore wind applications. In.

Byrne, B., McAdam, R., Burd, H., Houlsby, G., Martin, C., Zdravković, L., . . . Sideri, M. (2015a). *New design methods for large diameter piles under lateral loading for offshore wind applications.* Paper presented at the 3rd International Symposium on Frontiers in Offshore Geotechnics (ISFOG 2015), Oslo, Norway, June.

Byrne, B., Mcadam, R., Burd, H., Houlsby, G., Martin, C., Zdravkovic, L., . . . Muir Wood, A. (2017). *PISA: New Design Methods for Offshore Wind Turbine Monopiles.* Paper presented at the Royal Geographical Society, London.

Carswell, W., Johansson, J., Løvholt, F., Arwade, S., Madshus, C., DeGroot, D., & Myers, A. (2015). Foundation damping and the dynamics of offshore wind turbine monopiles. *Renewable energy, 80*, 724-736.

Caselunghe, A., & Eriksson, J. (2012). Structural Element Approaches for Soil-Structure Interation. *Master's thesis*, 7.

Darendeli, M. B. (2001). Development of a new family of normalized modulus reduction and material damping curves.

DNVGL. (2018). *DNVGL-ST-0126 Support structures for wind turbines*. Retrieved from rules.dnvgl.com/docs/pdf/dnvgl/ST/2016-04/DNVGL-ST-0126.pdf

Grimstad, G., Andresen, L., & Jostad, H. P. (2012). NGI-ADP: Anisotropic shear strength model for clay. *International Journal for Numerical Analytical Methods in Geomechanics, 36*(4), 483-497.

Hong, Y., He, B., Wang, L., Wang, Z., Ng, C. W. W., & Mašín, D. (2017). Cyclic lateral response and failure mechanisms of semi-rigid pile in soft clay: centrifuge tests and numerical modelling. *Canadian Geotechnical Journal, 54*(6), 806-824.

IRENA. (2019). *Renewable Capacity Statistics 2019*. Retrieved from https://www.irena.org/publications/2019/Mar/Renewable-Capacity-Statistics-2019

Jeanjean, P. (2009). *Re-assessment of py curves for soft clays from centrifuge testing and finite element modeling.* Paper presented at the Offshore Technology Conference.

Martin, C., & Randolph, M. (2006). Upper-bound analysis of lateral pile capacity in cohesive soil. *Geotechnique, 56*(2), 141-145.

MASING, G. (1926). *Eigenspannumyen und verfeshungung beim messing.* Paper presented at the Proc. Inter. Congress for Applied Mechanics.

MATLAB (Producer). (2018, November 29 2018). PDF Documentation for MATLAB. Retrieved from https://www.mathworks.com/help/pdf_doc/matlab/index.html

Matlock, H. (1970). *Correlation for Design of Laterally Loaded Piles in Soft Clay*. Paper presented at the Offshore Technology Conference, Houston, Texas. https://doi.org/10.4043/1204-MS

Murff, J. D., & Hamilton, J. M. (1993). P-ultimate for undrained analysis of laterally loaded piles. *Journal of Geotechnical Engineering, 119*(1), 91-107.

Musial, W., & Ram, B. (2010). *Large-scale offshore wind power in the United States: Assessment of opportunities and barriers*. Retrieved from

Nichols, N. W., MJ, R., Mukherjee, K., Ayob, B., Sapihie, M., Clausen, C. J., & Lunne, T. (2014). *Effect of Lateral Soil Strength and Stiffness on Jacket Foundation Integrity and Design for South China Sea Sites.* Paper presented at the Offshore Technology Conference-Asia.

NORWEP. (2018). Global Offshore Wind Market Report 2018. Retrieved from https://www.norwep.com/Market-info/Markets/Norway/Events/Older/Old/Offshore-Wind-Market-Report-Roadshow-Bergen/Offshore-wind-market-report

Orsted. (2019). Hornseaproject - About the project. Retrieved from https://hornseaproject3.co.uk/en/About-the-Project#0

Plaxis, B. (2017). PLAXIS 3D 2017 reference manual. *Delft: PLAXIS BV*.

Powell, J., & Butcher, A. (2003). Characterisation of a glacial clay till at Cowden, Humberside. *Characterisation engineering properties of natural soils, 2*, 983-1020.

Randolph, M. F., & Houlsby, G. (1984). The limiting pressure on a circular pile loaded laterally in cohesive soil. *Geotechnique, 34*(4), 613-623.

Renzi, R., Maggioni, W., Smits, F., & Manes, V. (1991). *A centrifugal study on the behavior of suction piles.* Paper presented at the Proc. Int. Conf. on Centrifuge Modelling-Centrifuge.

Sagaseta, C., Whittle, A. J., & Santagata, M. (1997). Deformation analysis of shallow penetration in clay. *21*(10), 687-719. doi:10.1002/(sici)1096-9853(199710)21:10<687::Aid-nag897>3.0.Co;2-3

Salgado, R. (2008). *The Engineering of Foundations*: McGraw-Hill.

Seidel, M. (2014). Substructures for offshore wind turbines Current trends and developments. *Festschrift Peter Schaumann*, 363-368.

Technavio. (2019). Release of the Global Offshore Wind Power Market forcast for period 2019-2023. Retrieved from https://www.businesswire.com/news/home/20190528005658/en/

Yang, Z., & Jeremić, B. (2005). Study of soil layering effects on lateral loading behavior of piles. *Journal of Geotechnical Geoenvironmental Engineering, 131*(6), 762-770.

Yu, J., Huang, M., & Zhang, C. (2015). Three-dimensional upper-bound analysis for ultimate bearing capacity of laterally loaded rigid pile in undrained clay. *Canadian Geotechnical Journal, 52*(11), 1775-1790.

Zdravković, L., Taborda, D., Potts, D., Jardine, R., Sideri, M., Schroeder, F., . . . Houlsby, G. (2015). *Numerical modelling of large diameter piles under lateral loading for offshore wind applications.* Paper presented at the Proceeding 3rd International Symposium on Frontiers in Offshore Geotechnics. Norway:[sn].

Zhang, Y. (2019b). *A multi-spring model for monopile analysis in soft clays*. Submitted May 15th, 2019.

Zhang, Y., & Andersen, K. H. (2017). Scaling of lateral pile p - y response in clay from laboratory stress-strain curves. *Marine Structures, 53*, 124-135. doi:10.1016/j.marstruc.2017.02.002

Zhang, Y., & Andersen, K. H. (2019a). Soil reaction curves for monopiles in clay. *Marine Structures, 65*, 94-113.

Zhang, Y., Andersen, K. H., & Tedesco, G. (2016). Ultimate bearing capacity of laterally loaded piles in clay – Some practical considerations. *Marine Structures, 50*, 260-275. doi:10.1016/j.marstruc.2016.09.002

Appendices

Appendix A: Pile response by finite element analyses compared with multi-spring model

- A.1 Soil profile 1
- A.2 Soil profile 2
- A.3 Soil profile 3
- A.4 Soil profile 4
- A.5 Soil profile 5

Appendix B: Pile response analyses using the optimization tool

- B.1 Soil profile 1
- B.2 Soil profile 2
- B.3 Soil profile 3
- B.4 Soil profile 4

Appendix C: Stiffness spring modifiers

- C.1. Normally consolidated clay
- C.2. Layered soil profile

Appendix A

Pile response by finite element analyses compared with multi-spring model

Appendix A.1. Soil profile 1

A.1.1. L/D = 3. γ_f^p = 0.02

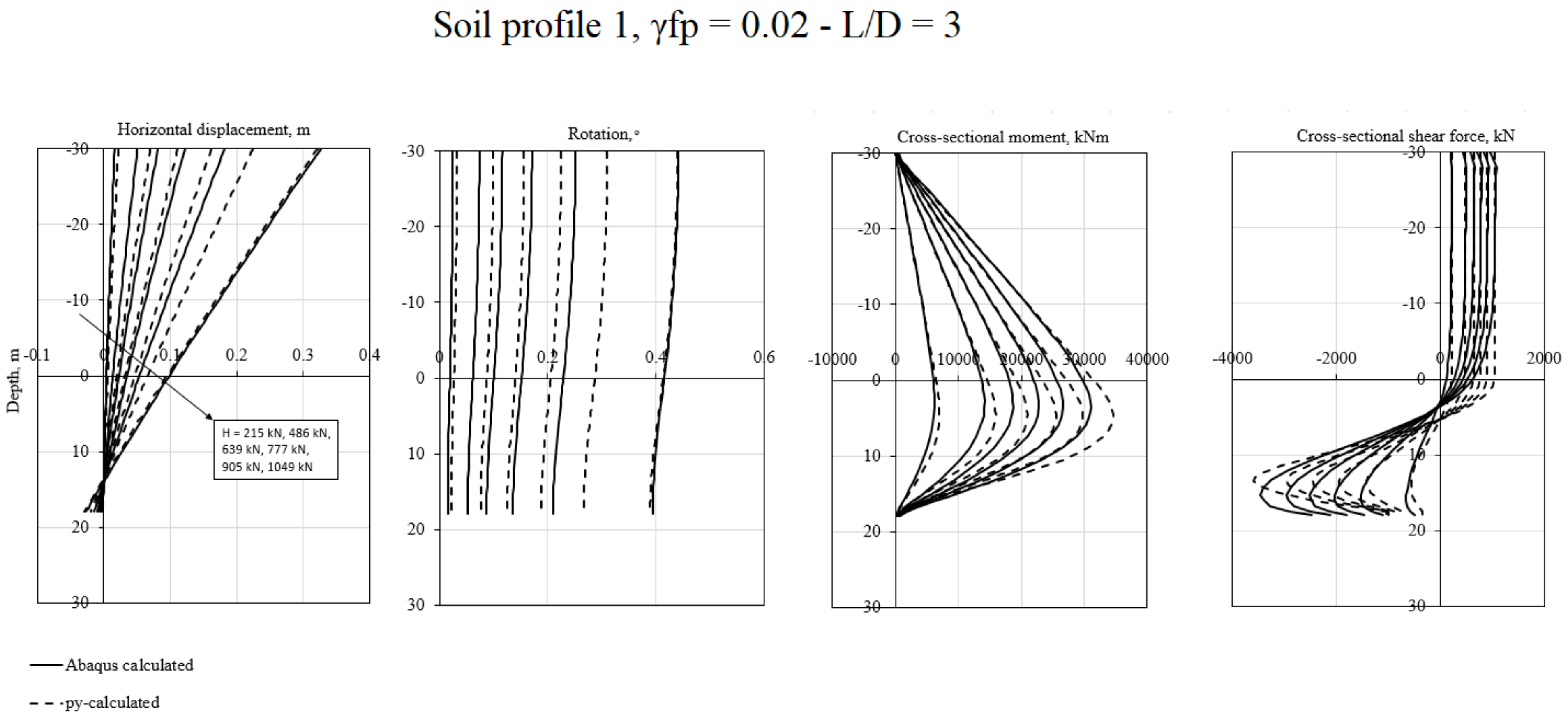

Figure A.1: Comparison of pile response – Soil profile 1, L/D=3, γ_f^p=0.02. The legend wrongfully says "py-calculated". The pile responses are calculated using the aforementioned multi-spring beam-column model.

A.1.2. L/D = 3. γ_f^p = 0.10

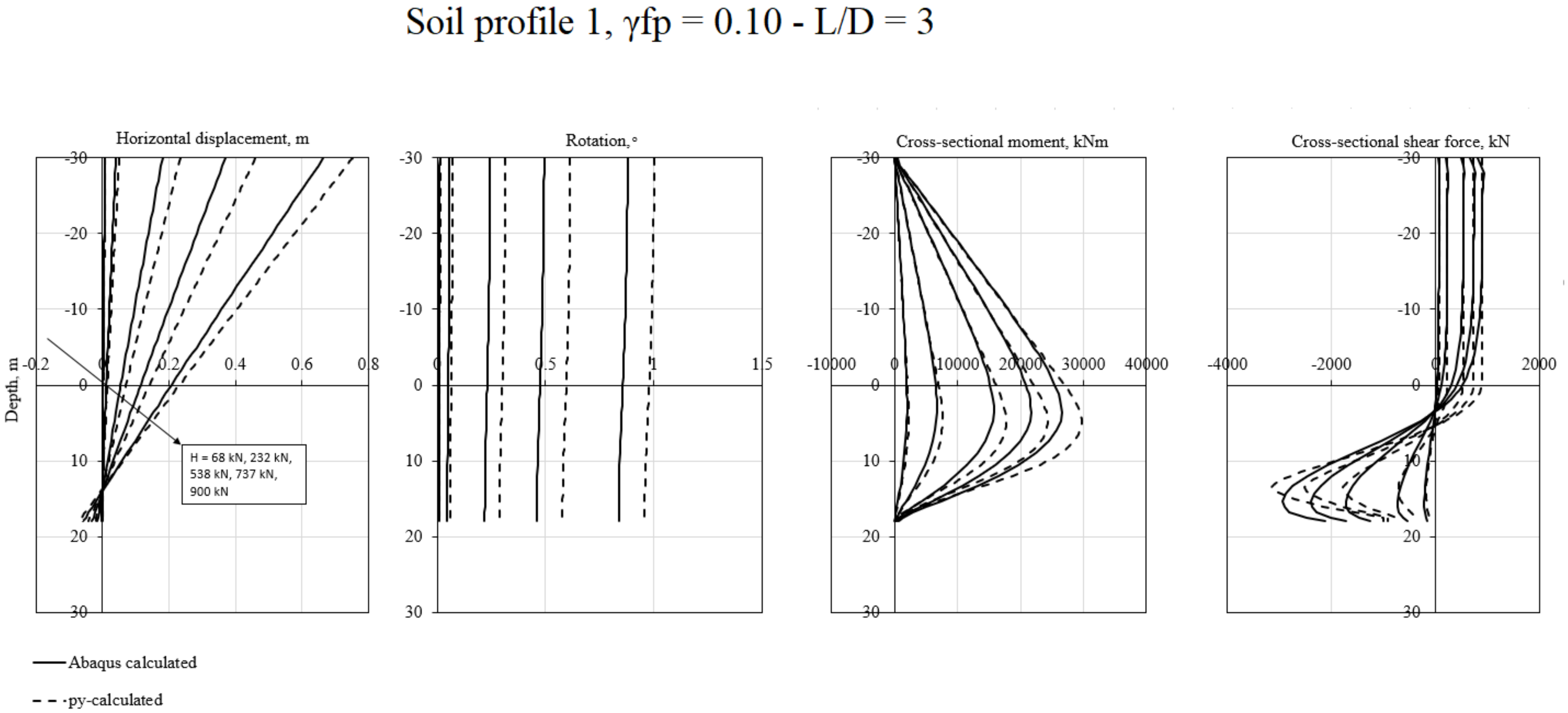

Soil profile 1, γfp = 0.10 - L/D = 3

Horizontal displacement, m

Rotation, °

Cross-sectional moment, kNm

Cross-sectional shear force, kN

Figure A.2: Comparison of pile response – Soil profile 1, L/D=3, γ_f^p=0.10. The legend wrongfully says "py-calculated". The pile responses are calculated using the aforementioned multi-spring beam-column model.

A.1.3. L/D = 5. γ_f^p = 0.02

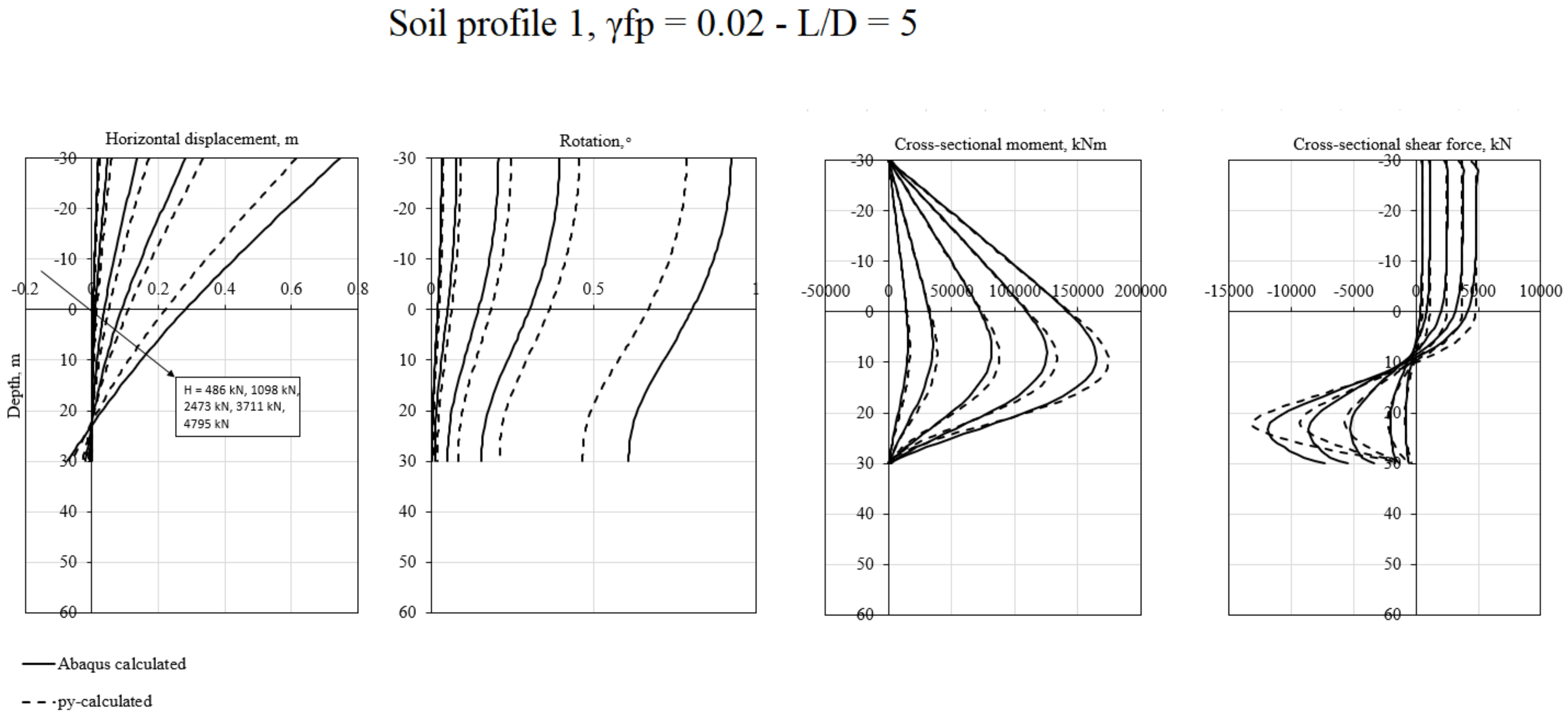

Figure A.3: Comparison of pile response – Soil profile 1, L/D=5, γ_f^p=0.02. The legend wrongfully says "py-calculated". The pile responses are calculated using the aforementioned multi-spring beam-column model.

A.1.4. L/D = 5. γ_f^p = 0.10

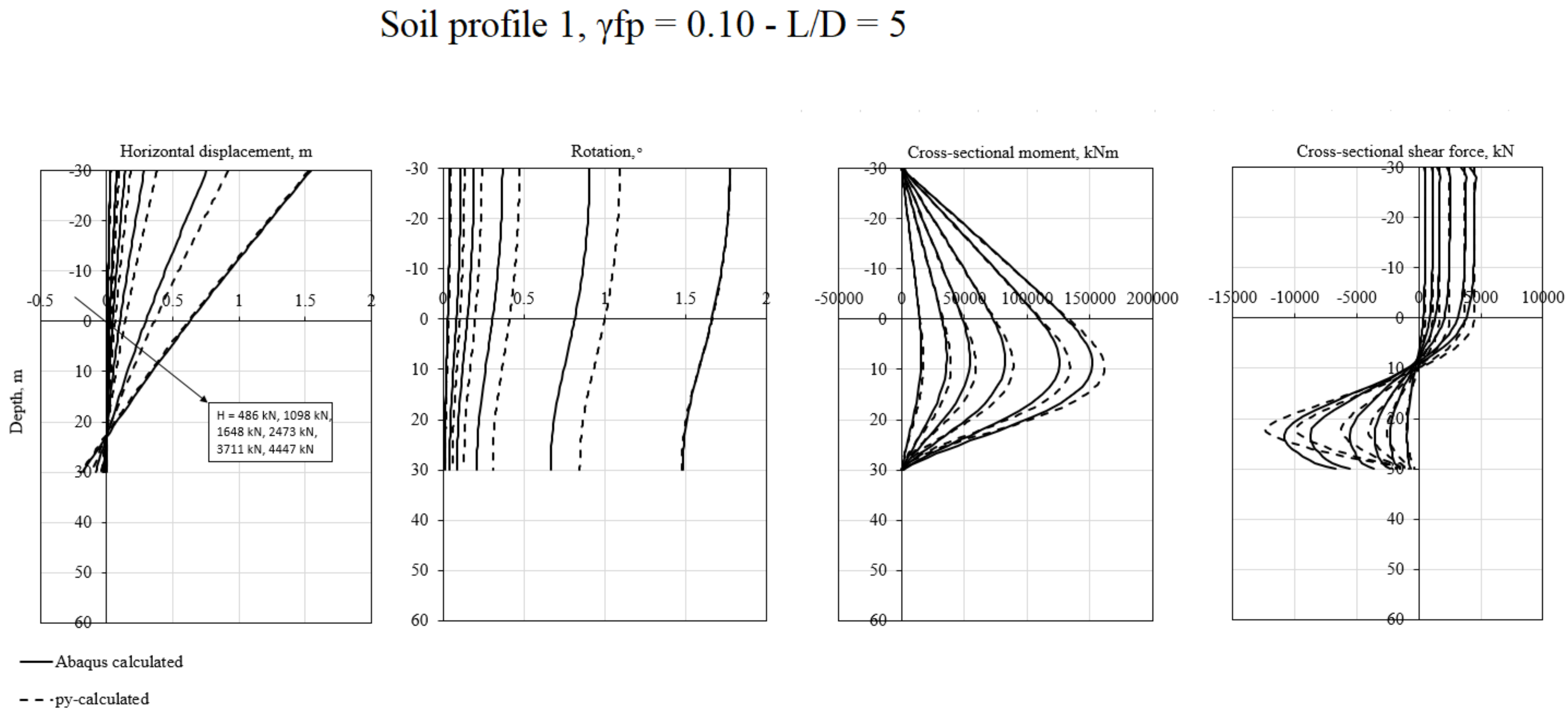

Figure A.4: Comparison of pile response – Soil profile 1, L/D=5, γ_f^p=0.10. The legend wrongfully says "py-calculated". The pile responses are calculated using the aforementioned multi-spring beam-column model.

A.1.5. L/D = 7. γ_f^p = 0.02

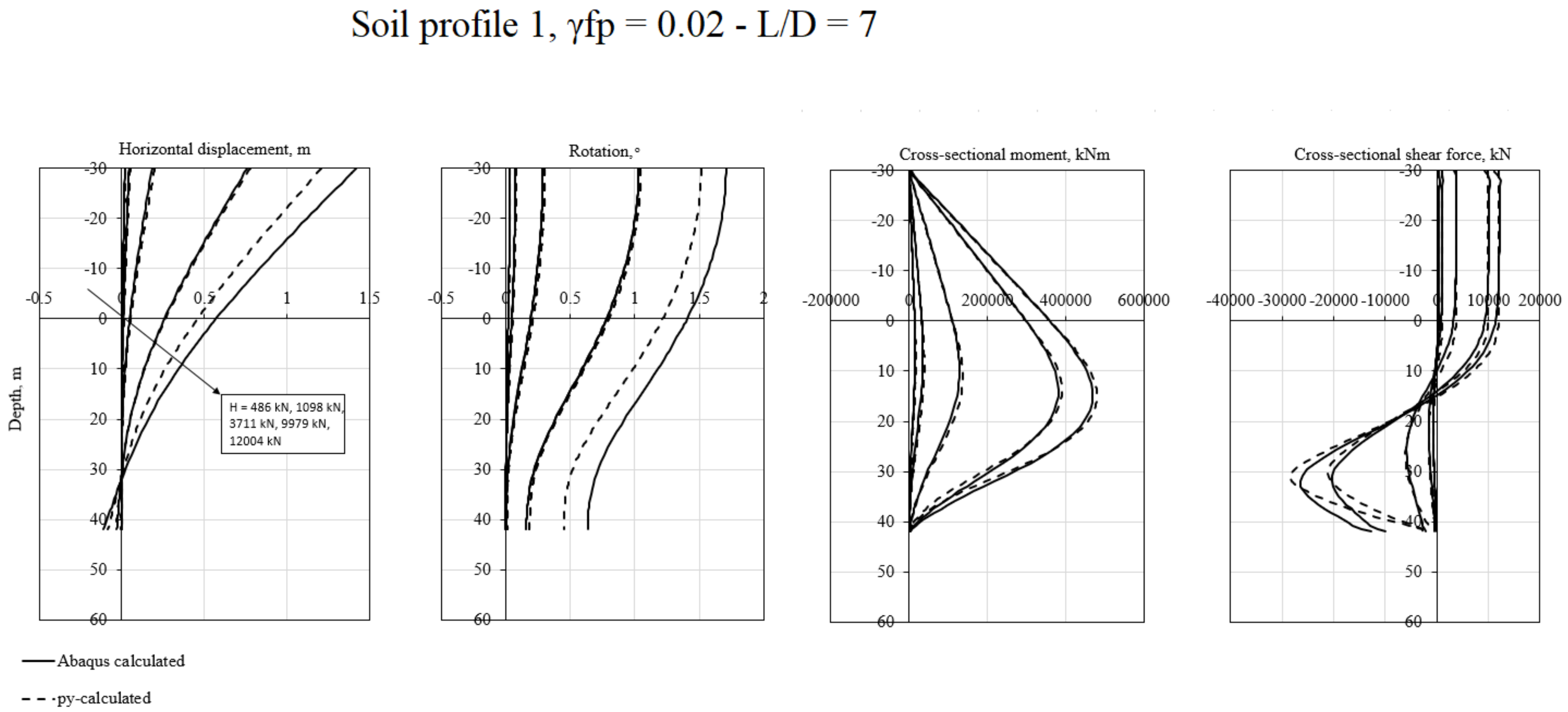

Figure A.5: Comparison of pile response – Soil profile 1, L/D=7, γ_f^p=0.02. The legend wrongfully says "py-calculated". The pile responses are calculated using the aforementioned multi-spring beam-column model.

A.1.6. L/D = 7. γ_f^p = 0.10

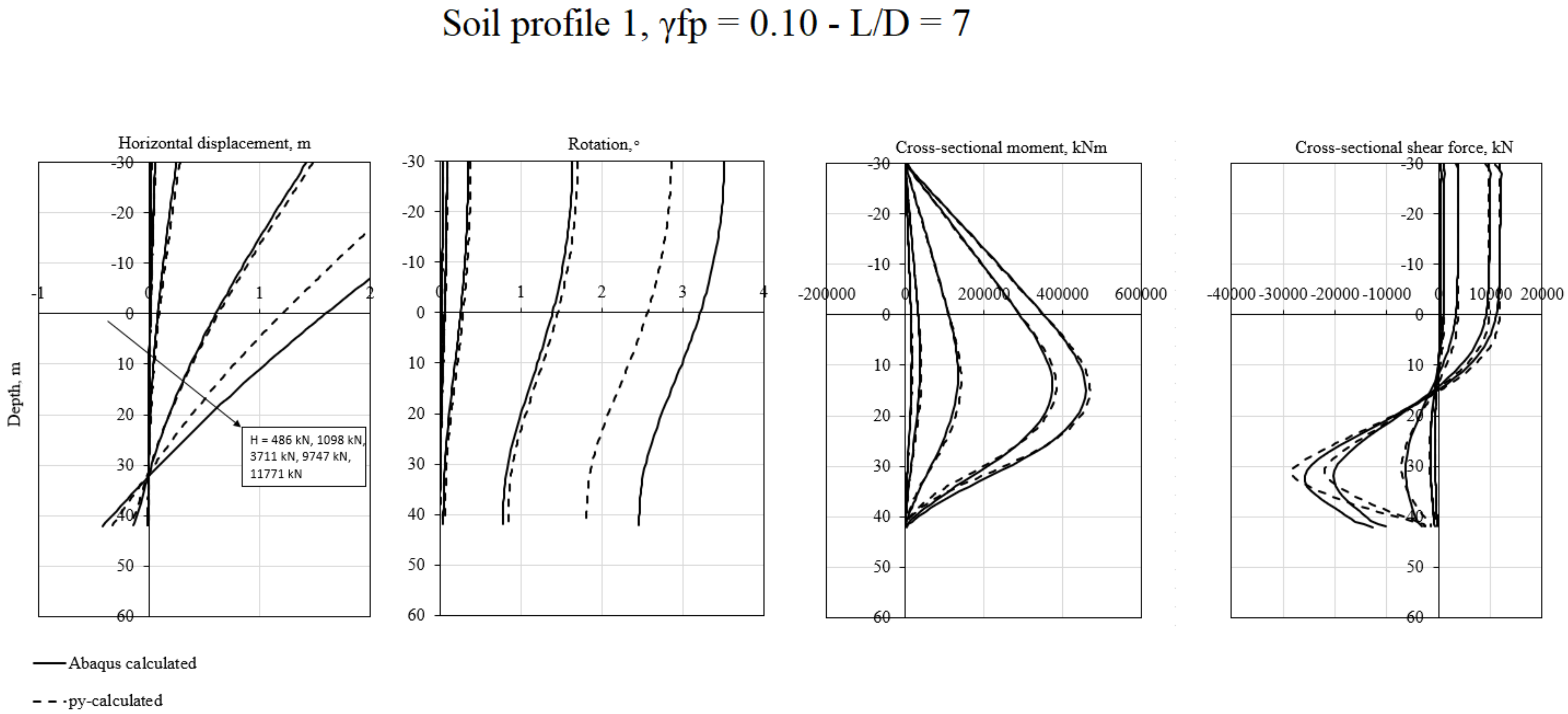

Figure A.6: Comparison of pile response – Soil profile 1, L/D=7, γ_f^p=0.10. The legend wrongfully says "py-calculated". The pile responses are calculated using the aforementioned multi-spring beam-column model.

A.1.7. L/D = 10. γ_f^p = 0.02

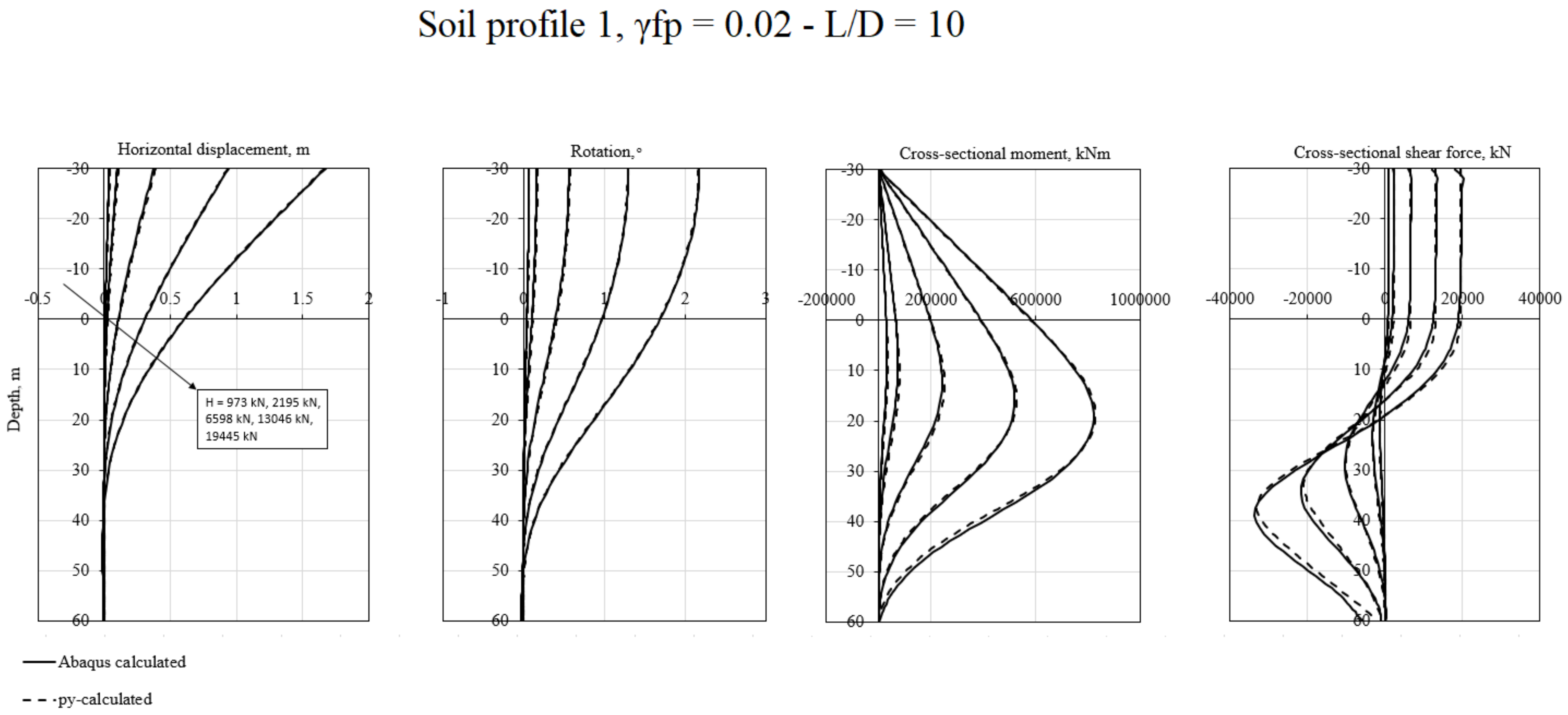

Figure A.7: Comparison of pile response – Soil profile 1, L/D=10, γ_f^p=0.02. The legend wrongfully says "py-calculated". The pile responses are calculated using the aforementioned multi-spring beam-column model.

A.1.8. L/D = 10. γ_f^p = 0.10

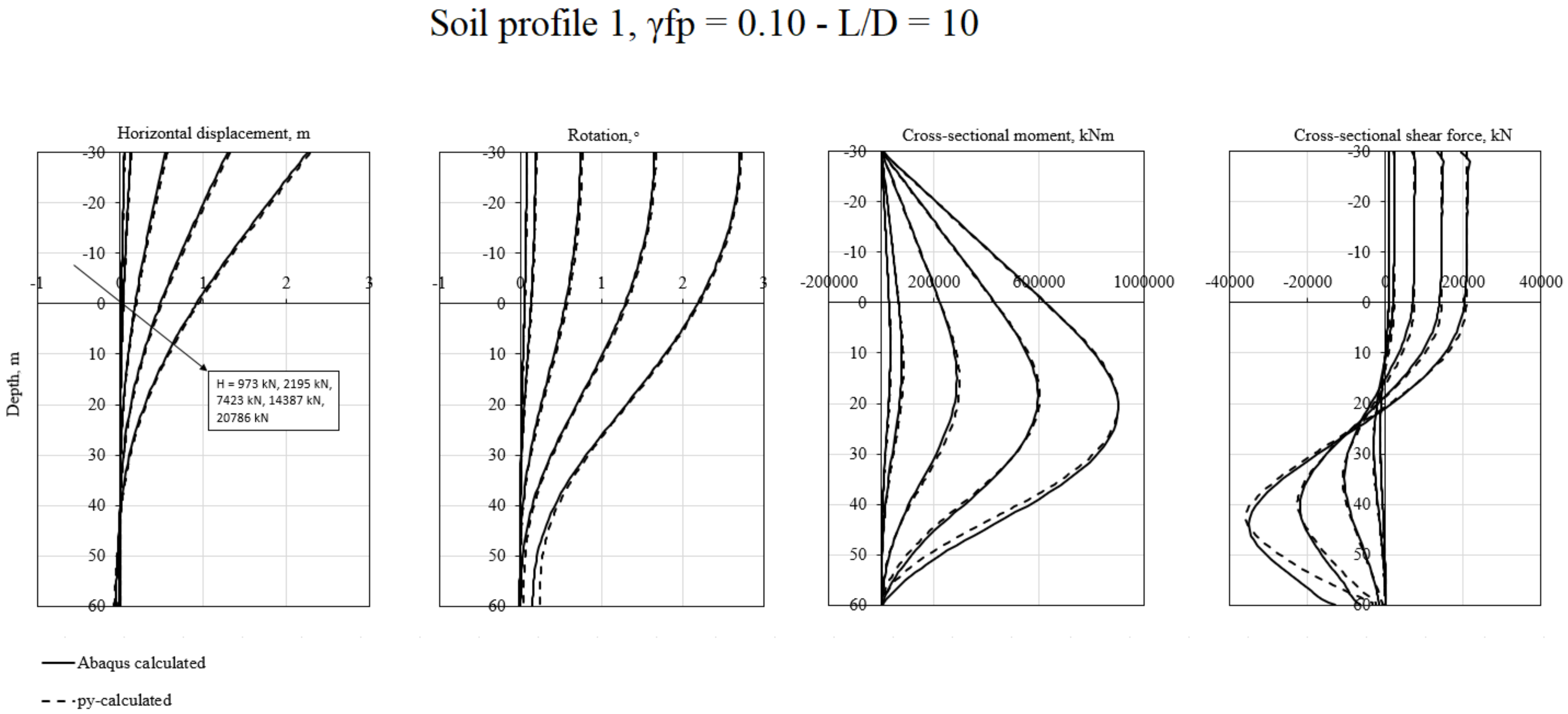

Figure A.8: Comparison of pile response – Soil profile 1, L/D=10, γ_f^p=0.10. The legend wrongfully says “py-calculated”. The pile responses are calculated using the aforementioned multi-spring beam-column model.

Appendix A.2. Soil profile 2

A.2.1. L/D = 3. γ_f^p = 0.02

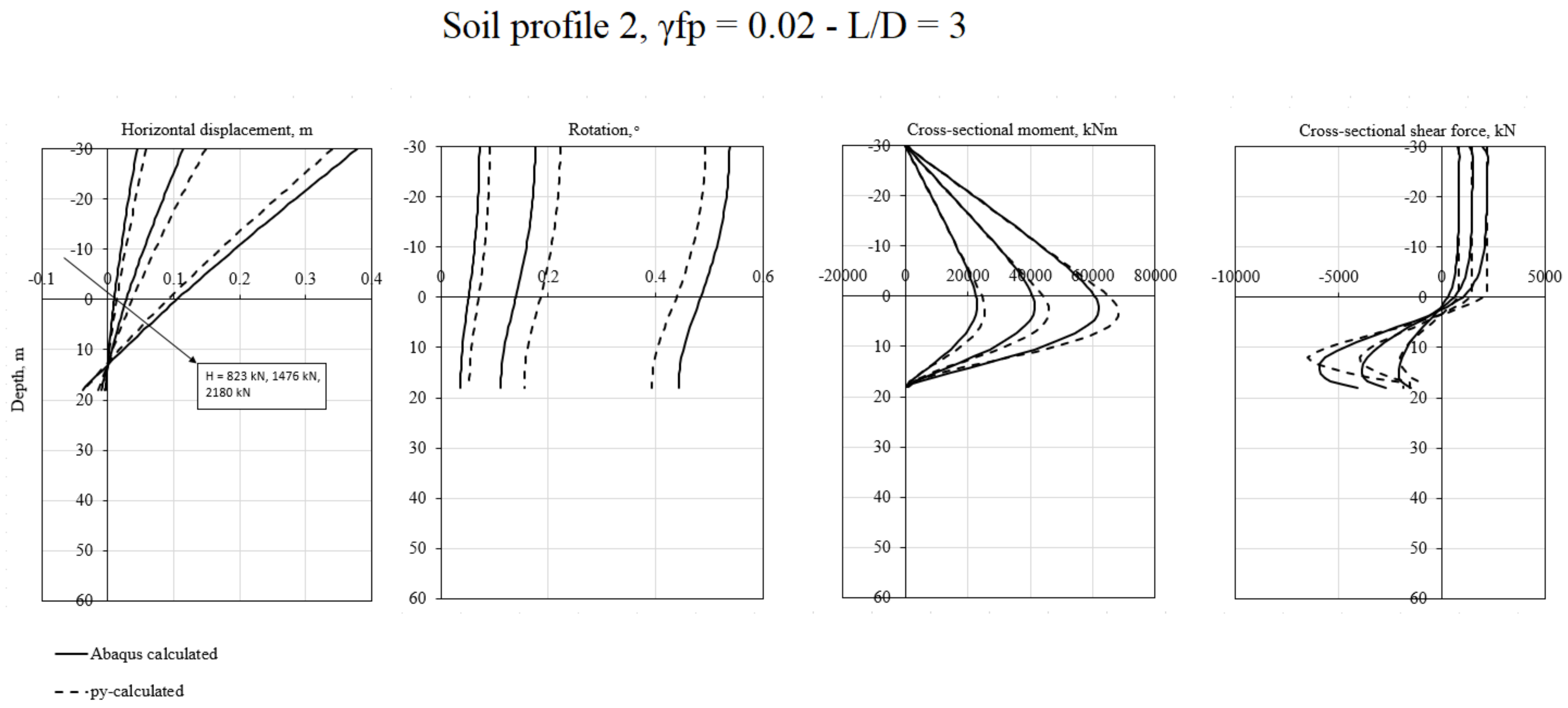

Figure A.9: Comparison of pile response – Soil profile 2, L/D=3, γ_f^p=0.02. The legend wrongfully says "py-calculated". The pile responses are calculated using the aforementioned multi-spring beam-column model.

A.2.2. L/D = 3. γ_f^p = 0.10

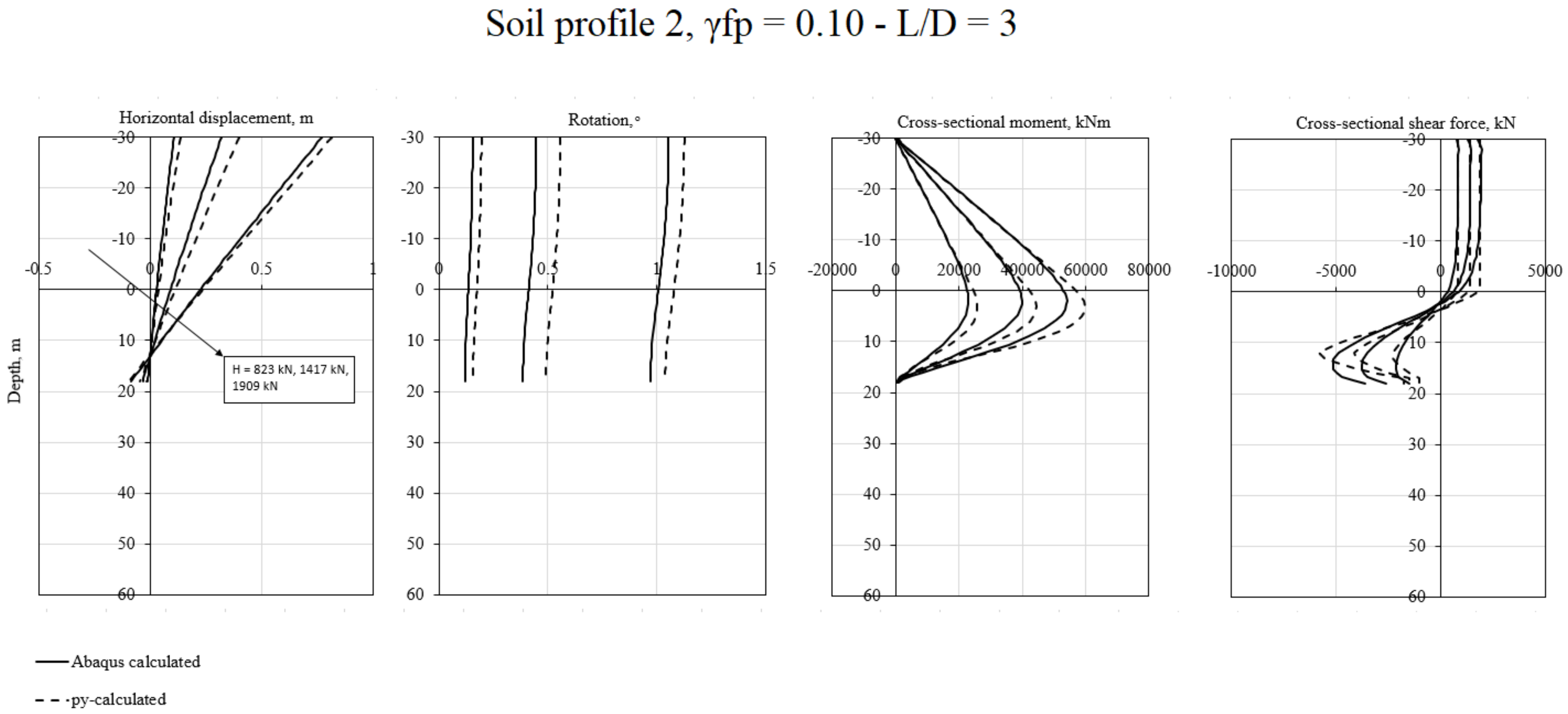

Figure A.10: Comparison of pile response – Soil profile 2, L/D=3, γ_f^p=0.10. The legend wrongfully says "py-calculated". The pile responses are calculated using the aforementioned multi-spring beam-column model.

A.2.3. L/D = 5. γ_f^p = 0.02

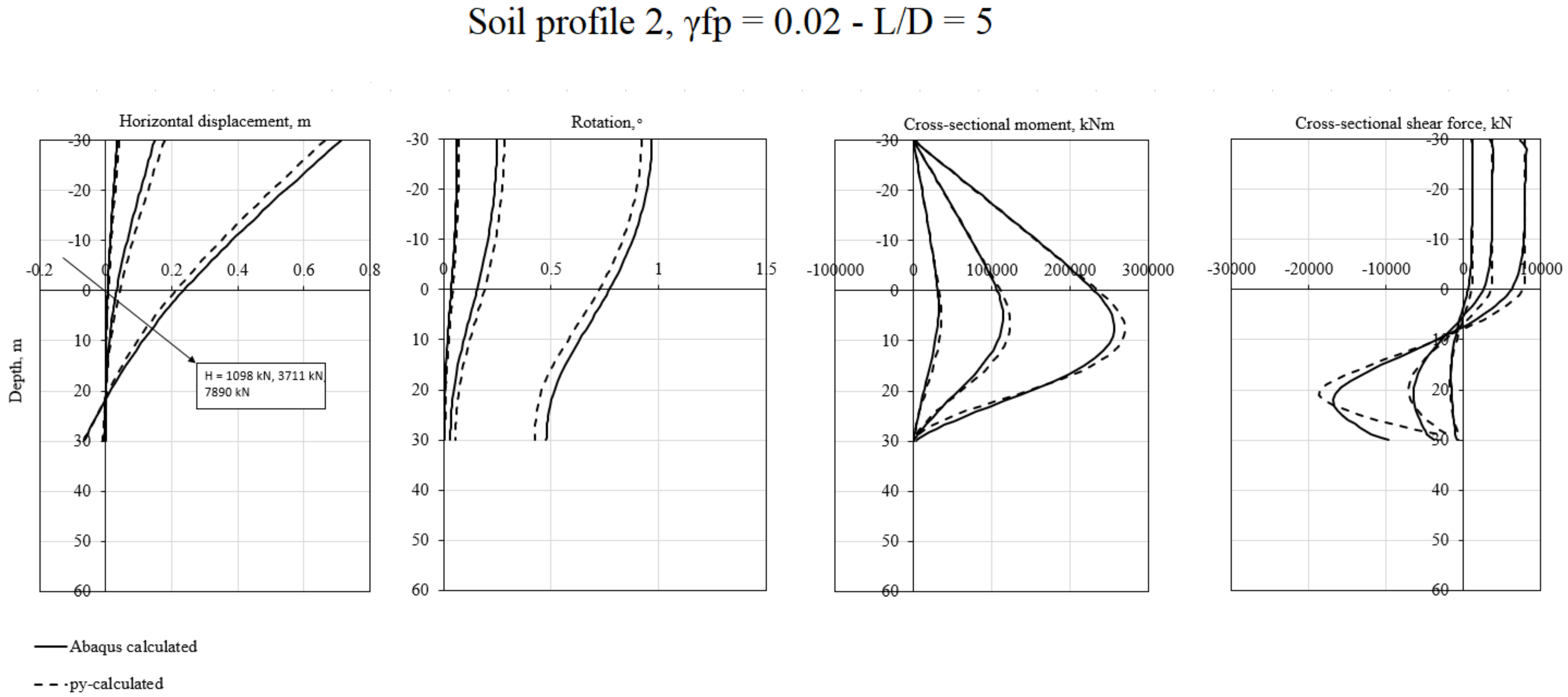

Figure A.11: Comparison of pile response – Soil profile 2, L/D=5, γ_f^p=0.02. The legend wrongfully says "py-calculated". The pile responses are calculated using the aforementioned multi-spring beam-column model.

A.2.4. L/D = 5. γ_f^p = 0.10

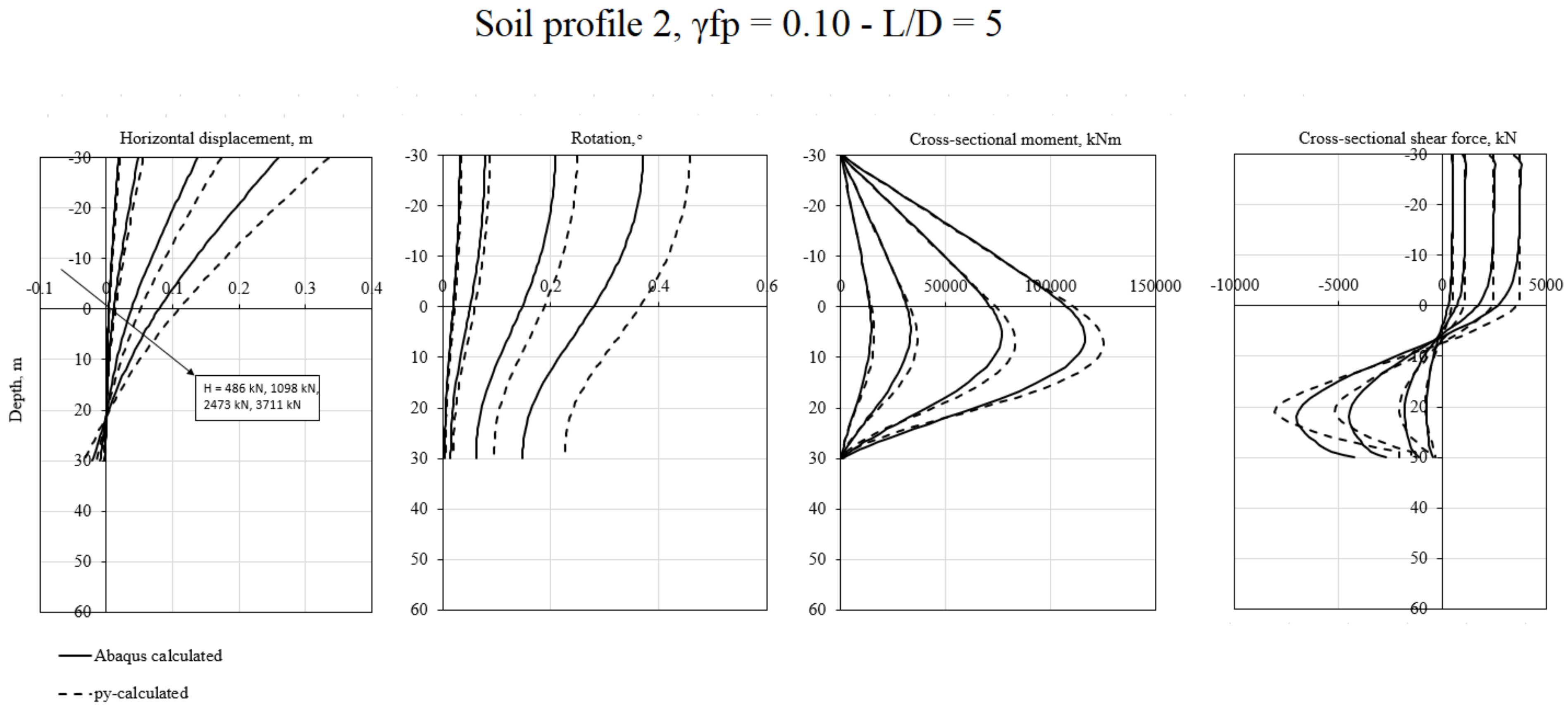

Figure A.12: Comparison of pile response – Soil profile 2, L/D=5, γ_f^p=0.10. The legend wrongfully says “py-calculated”. The pile responses are calculated using the aforementioned multi-spring beam-column model.

A.2.5. L/D = 7. γ_f^p = 0.02

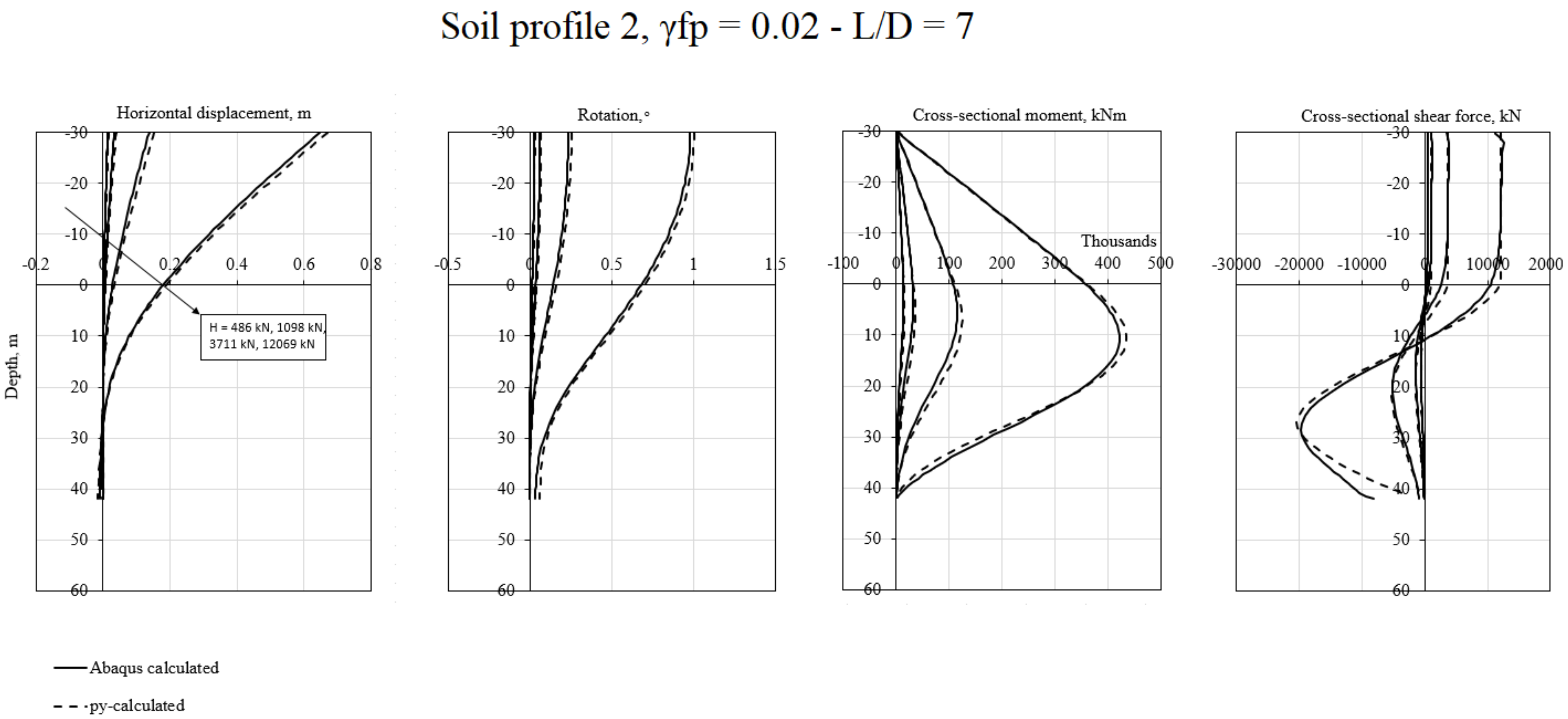

Figure A.13: Comparison of pile response – Soil profile 2, L/D=7, γ_f^p=0.02. The legend wrongfully says "py-calculated". The pile responses are calculated using the aforementioned multi-spring beam-column model.

A.2.6. L/D = 7. γ_f^p = 0.10

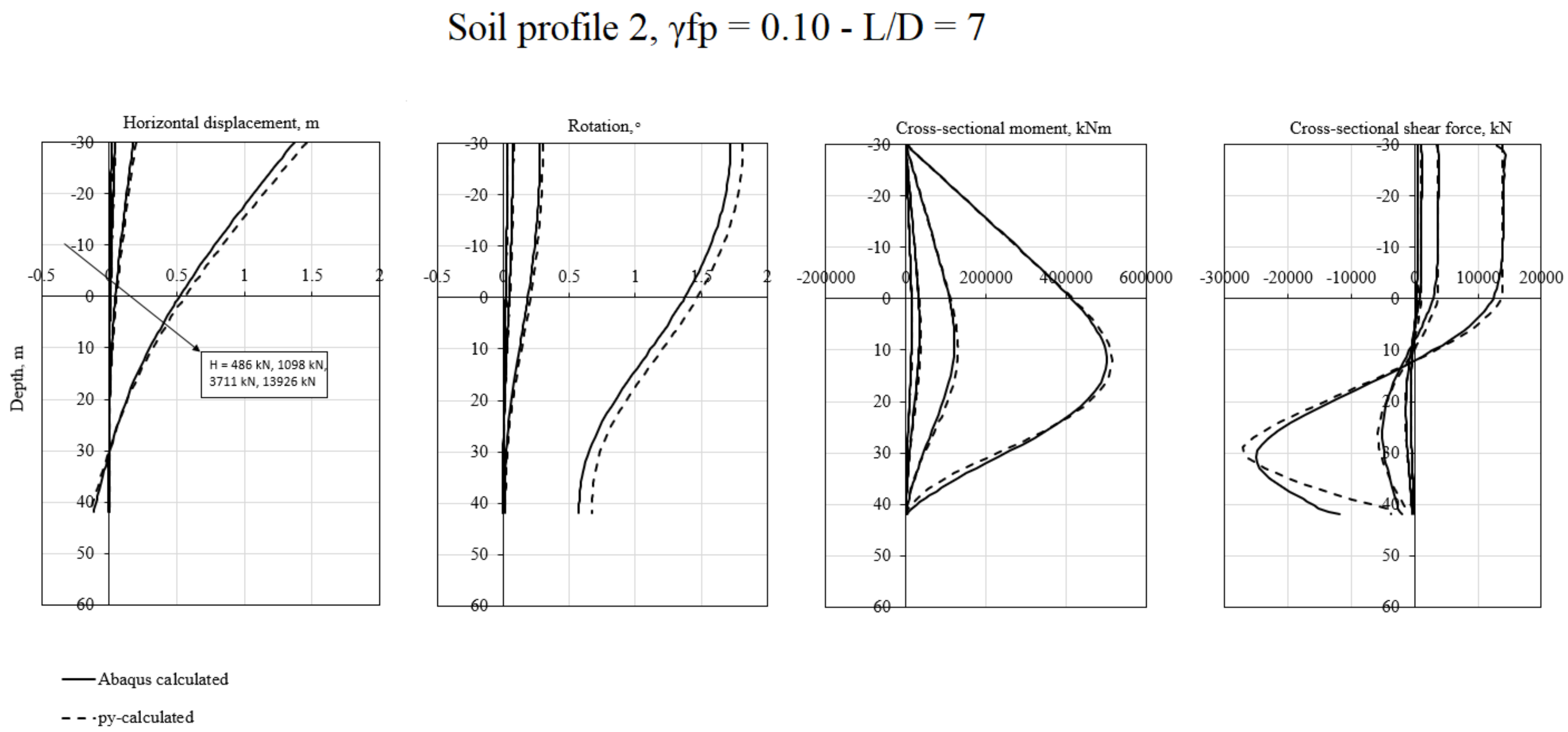

Figure A.14: Comparison of pile response – Soil profile 2, L/D=7, γ_f^p=0.10. The legend wrongfully says "py-calculated". The pile responses are calculated using the aforementioned multi-spring beam-column model.

A.2.7. L/D = 10. γ_f^p = 0.02

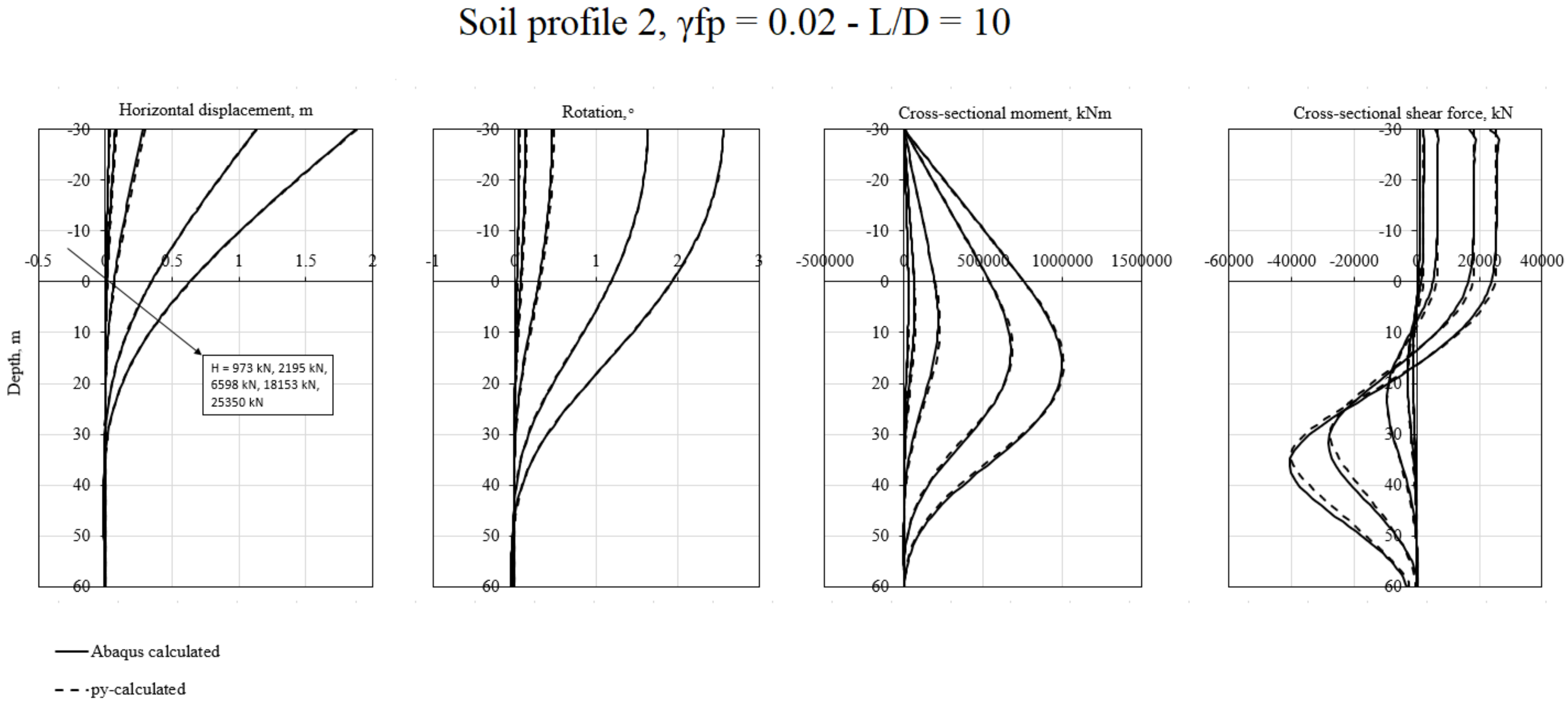

Figure A.15: Comparison of pile response – Soil profile 2, L/D=10, γ_f^p=0.02. The legend wrongfully says "py-calculated". The pile responses are calculated using the aforementioned multi-spring beam-column model.

A.2.8. L/D = 10. γ_f^p = 0.10

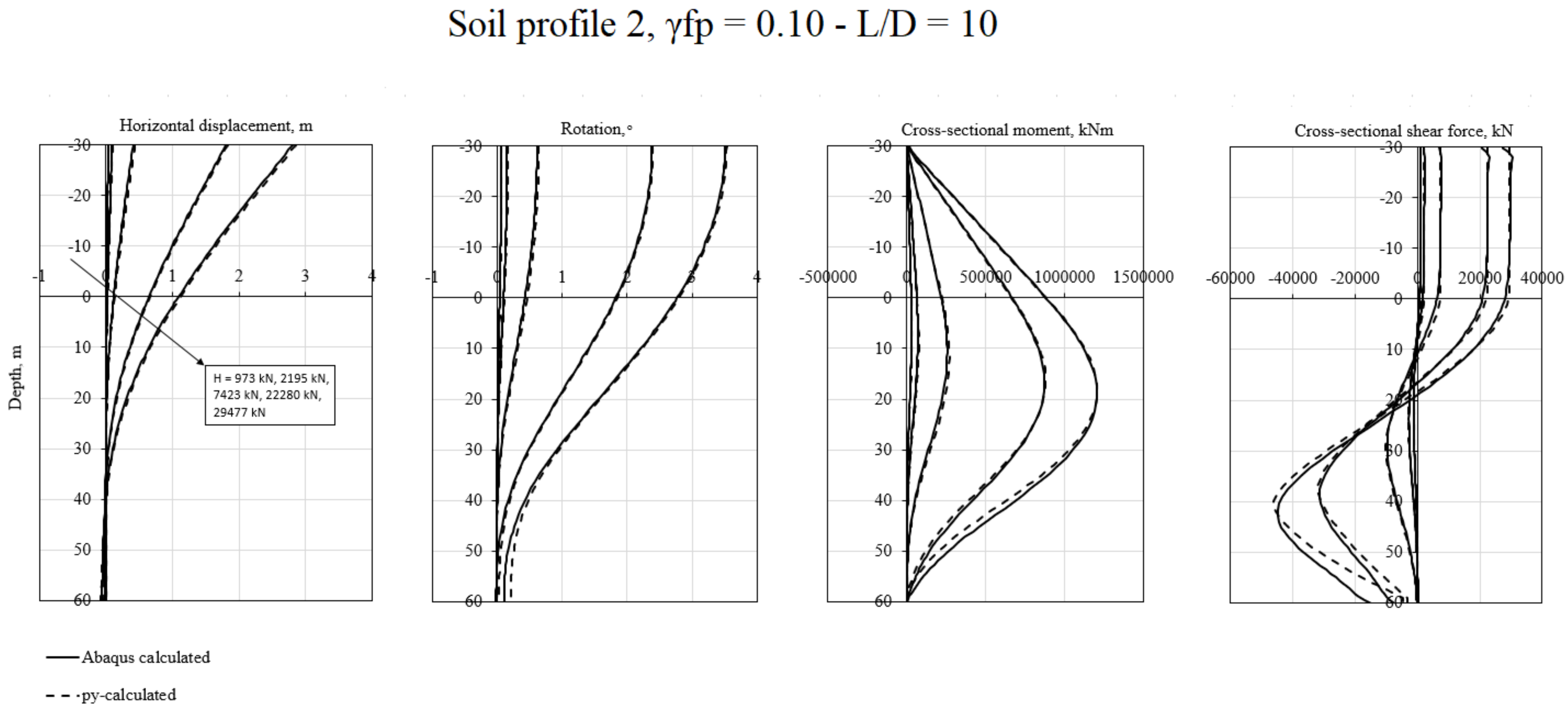

Figure A.16: Comparison of pile response – Soil profile 2, L/D=10, γ_f^p=0.10. The legend wrongfully says "py-calculated". The pile responses are calculated using the aforementioned multi-spring beam-column model.

Appendix A.3. Soil profile 3

A.3.1. L/D = 3. γ_f^p = 0.02

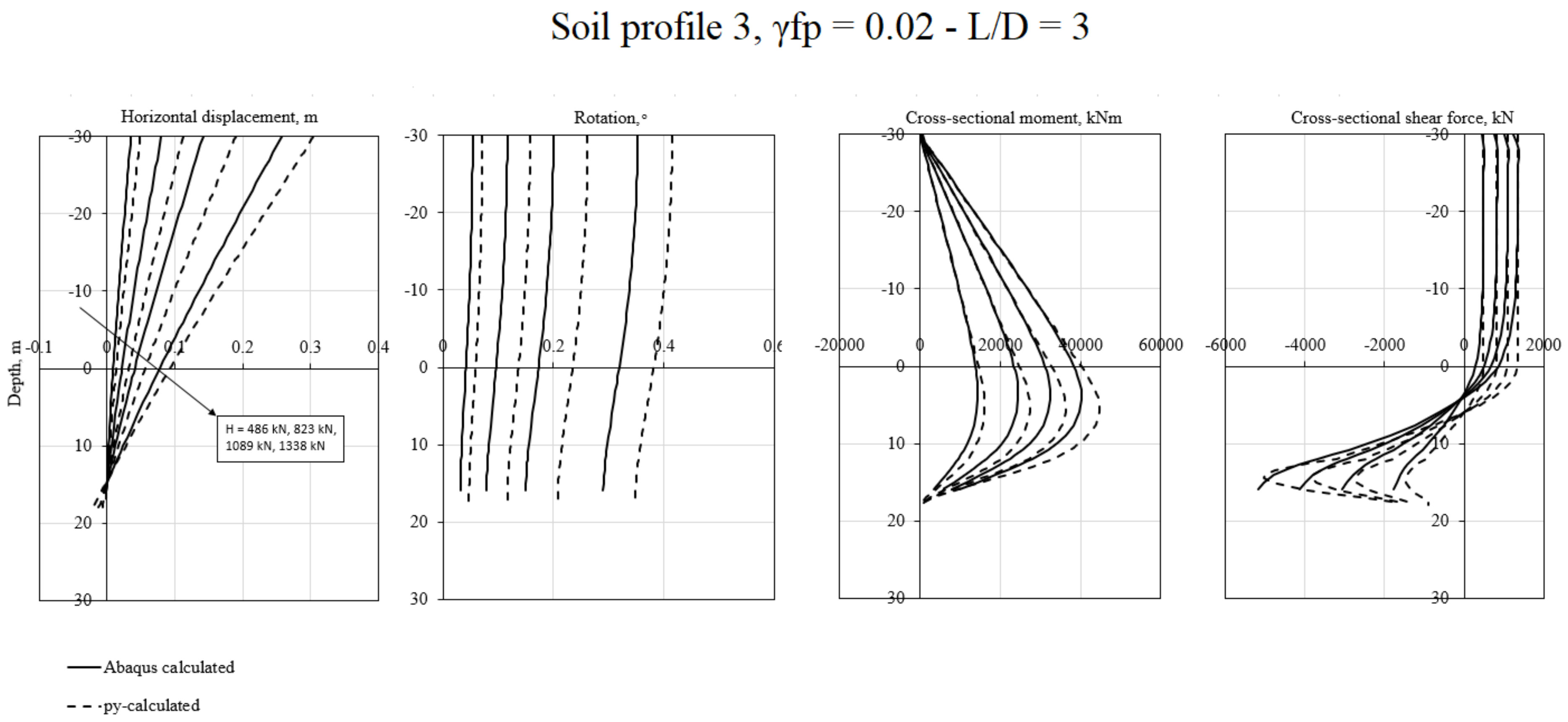

Figure A.17: Comparison of pile response – Soil profile 3, L/D=3, γ_f^p=0.02. The legend wrongfully says "py-calculated". The pile responses are calculated using the aforementioned multi-spring beam-column model.

A.3.2. L/D = 3. γ_f^p = 0.10

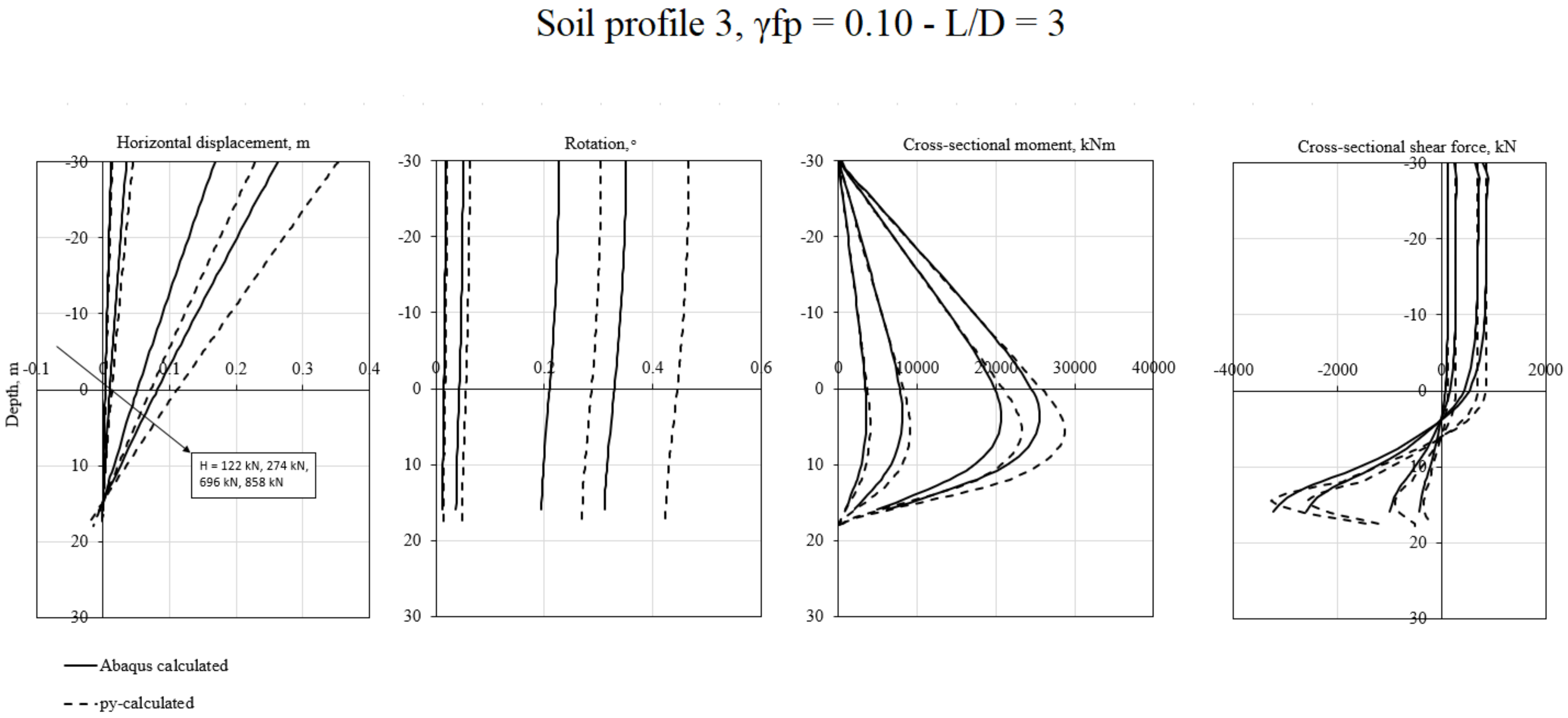

Figure A.18: Comparison of pile response – Soil profile 3, L/D=3, γ_f^p=0.10. The legend wrongfully says "py-calculated". The pile responses are calculated using the aforementioned multi-spring beam-column model.

A.3.3. L/D = 5. γ_f^p = 0.02

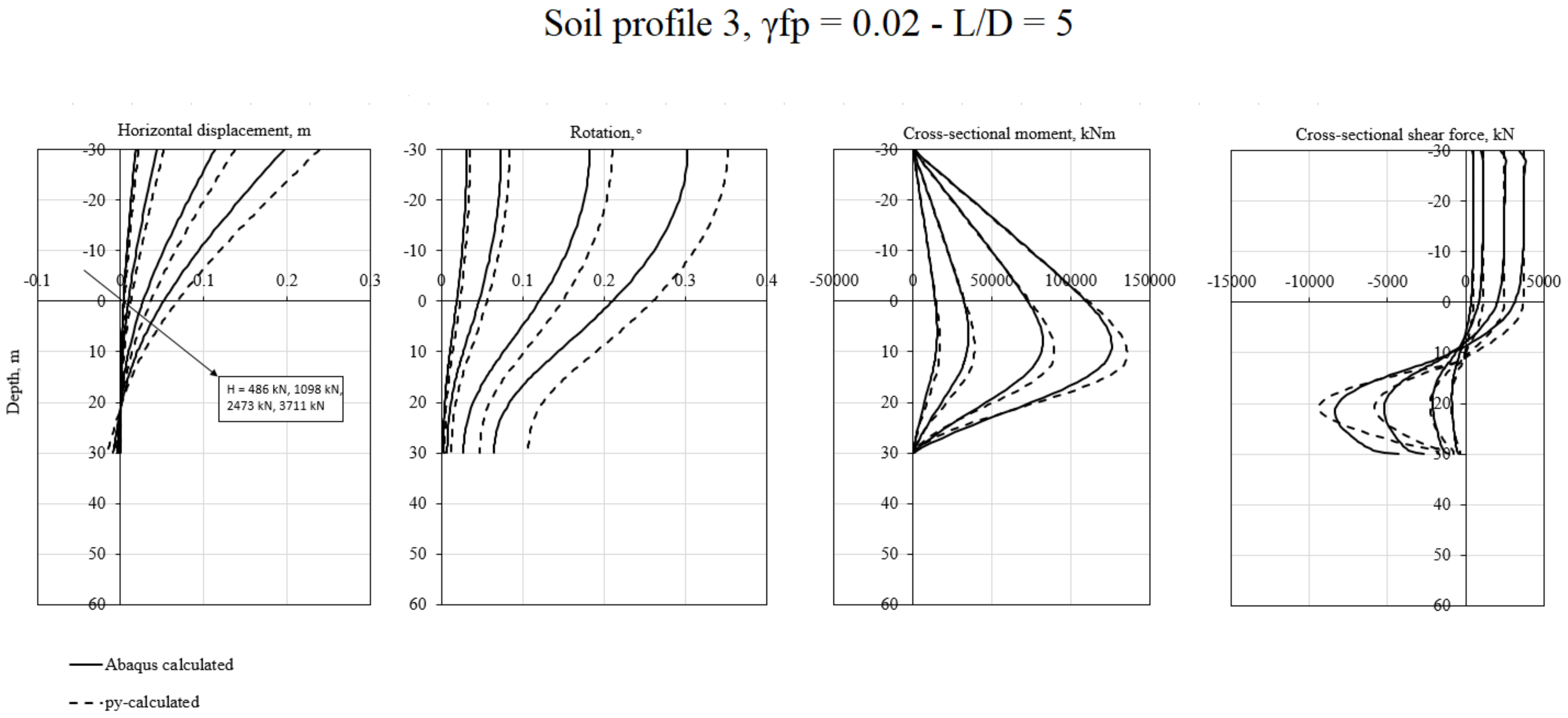

Figure A.19: Comparison of pile response – Soil profile 3, L/D=5, γ_f^p=0.02. The legend wrongfully says "py-calculated". The pile responses are calculated using the aforementioned multi-spring beam-column model.

A.3.4. L/D = 5. γ_f^p = 0.10

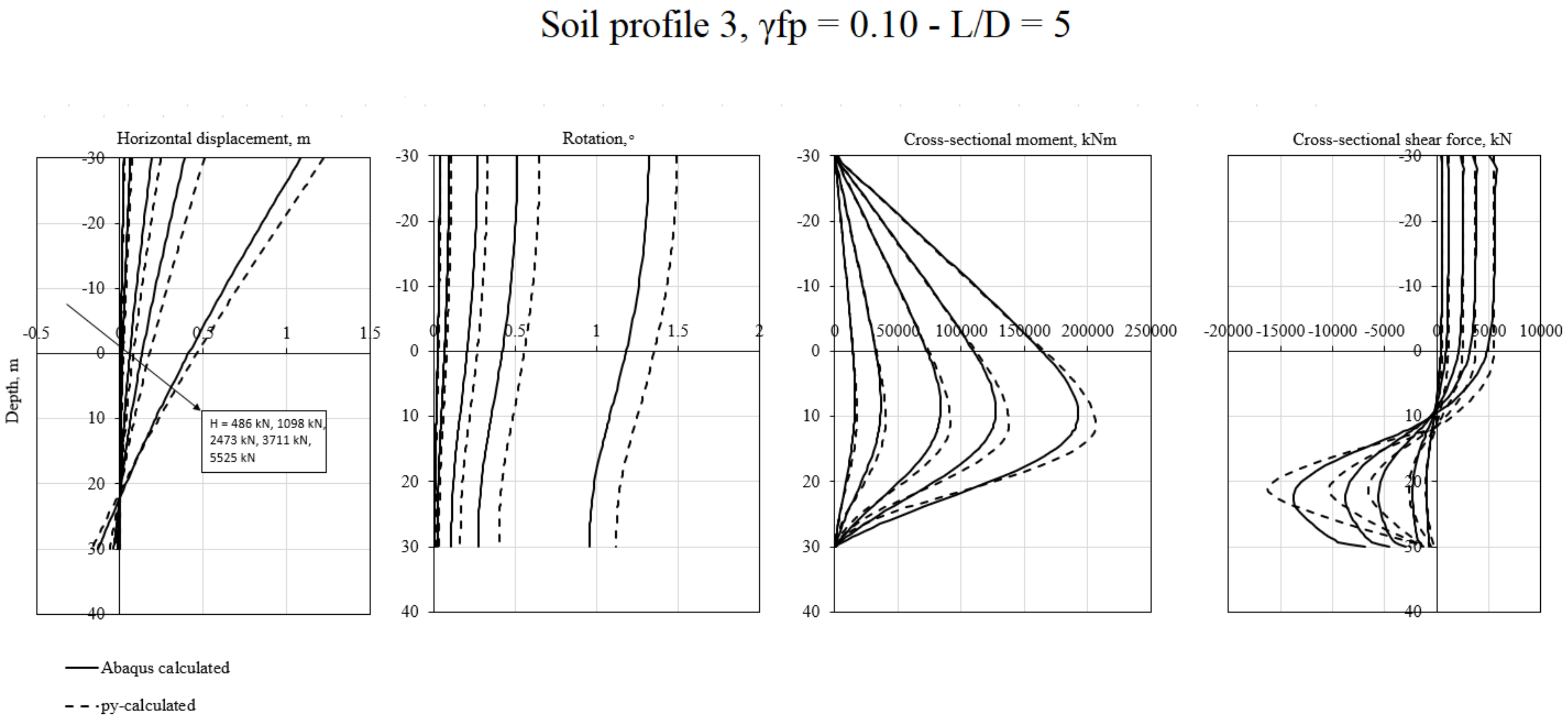

Figure A.20: Comparison of pile response – Soil profile 3, L/D=5, γ_f^p=0.10. The legend wrongfully says "py-calculated". The pile responses are calculated using the aforementioned multi-spring beam-column model.

A.3.5. L/D = 7. γ_f^p = 0.02

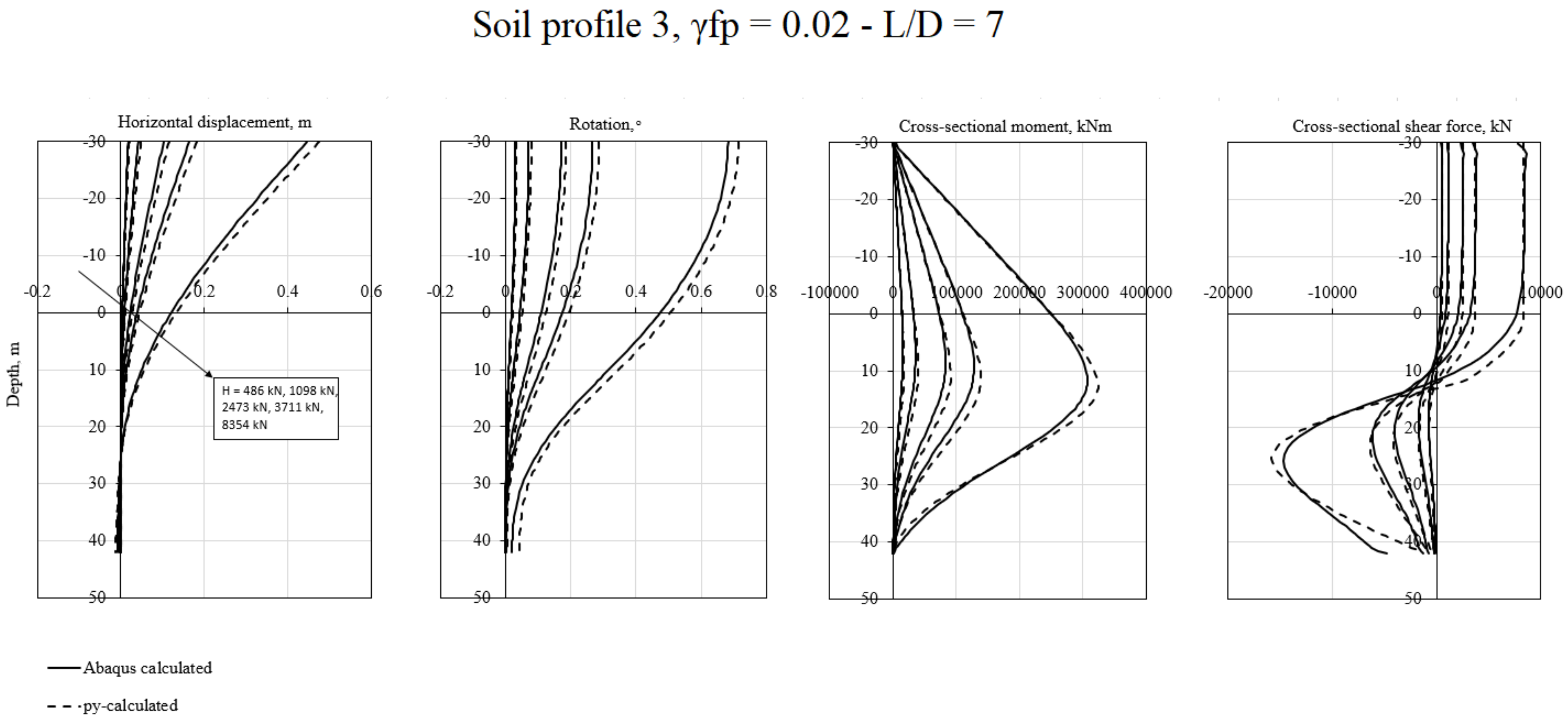

Figure A.21: Comparison of pile response – Soil profile 3, L/D=7, γ_f^p=0.02. The legend wrongfully says “py-calculated”. The pile responses are calculated using the aforementioned multi-spring beam-column model.

A.3.6. L/D = 7. γ_f^p = 0.10

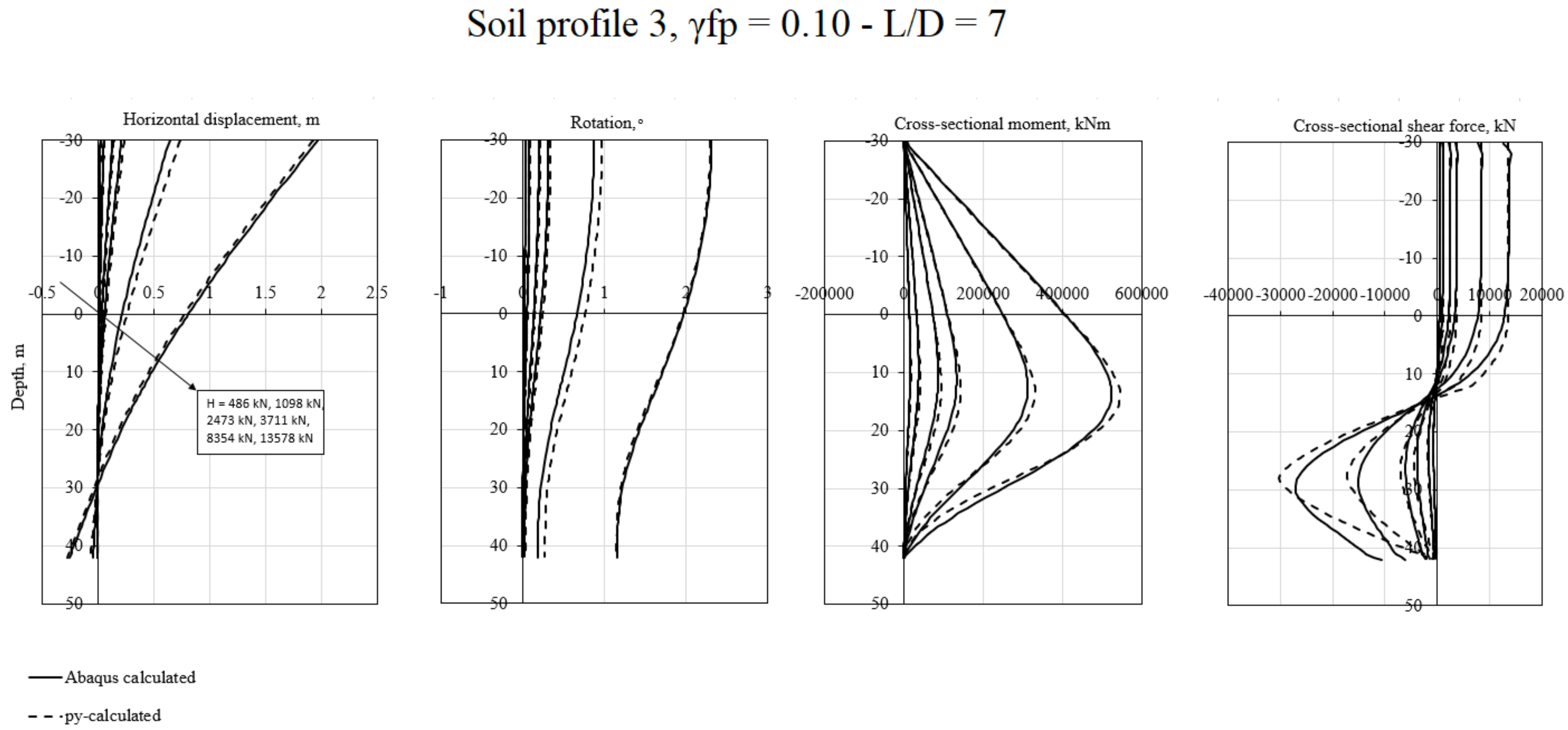

Figure A.22: Comparison of pile response – Soil profile 3, L/D=7, γ_f^p=0.10. The legend wrongfully says "py-calculated". The pile responses are calculated using the aforementioned multi-spring beam-column model.

A.3.7. L/D = 10. γ_f^p = 0.02

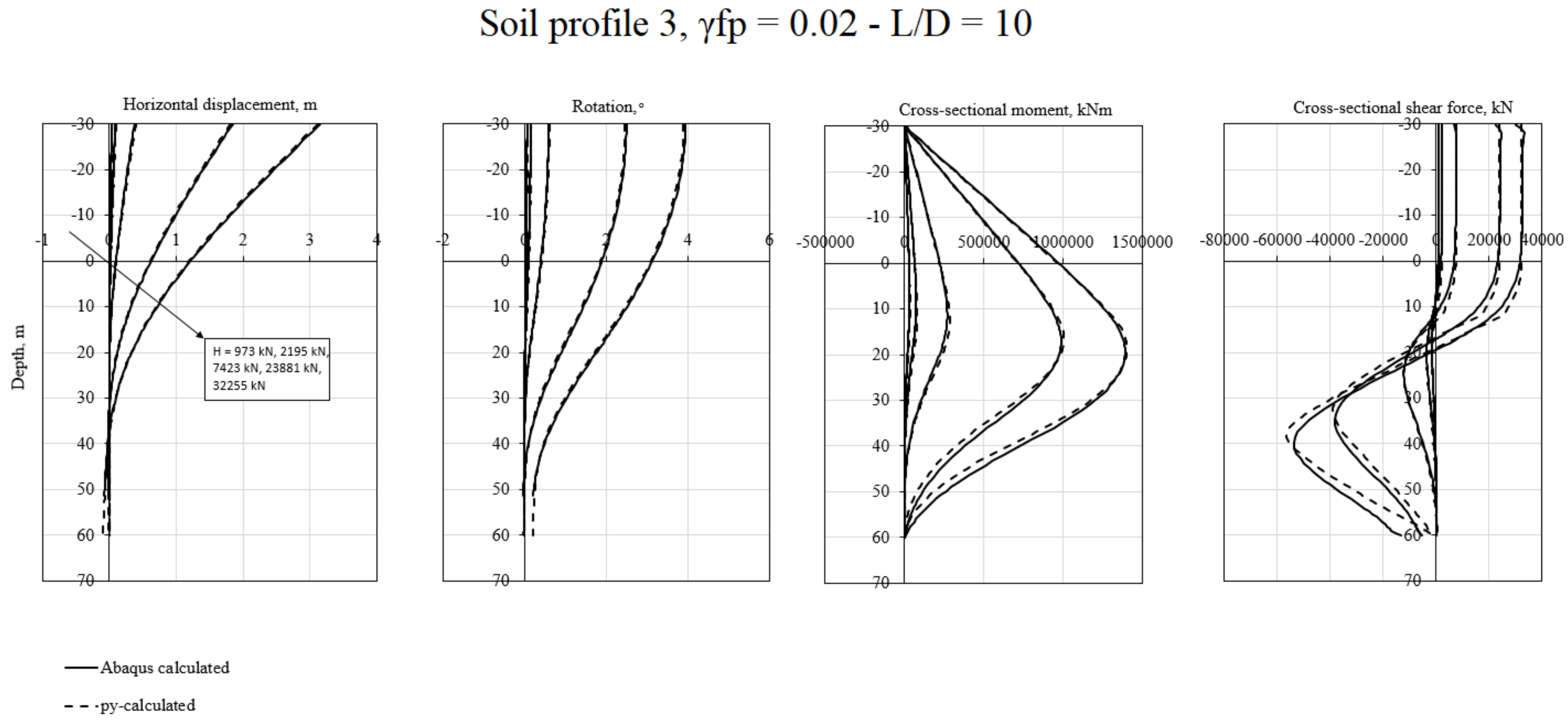

Figure A.23: Comparison of pile response – Soil profile 3, L/D=10, γ_f^p=0.02. The legend wrongfully says “py-calculated”. The pile responses are calculated using the aforementioned multi-spring beam-column model.

A.3.8. L/D = 10. γ_f^p = 0.10

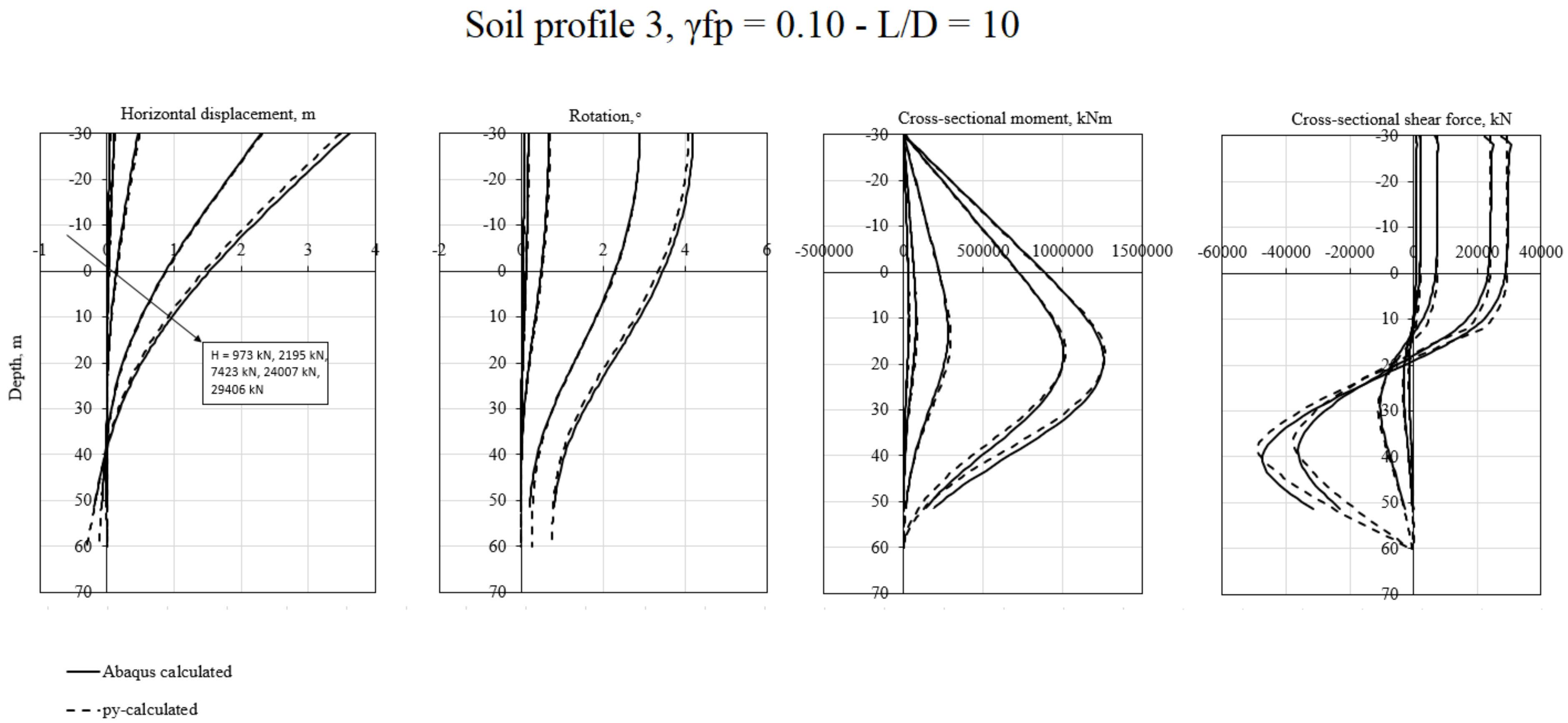

Figure A.24: Comparison of pile response – Soil profile 3, L/D=10, γ_f^p=0.10. The legend wrongfully says "py-calculated". The pile responses are calculated using the aforementioned multi-spring beam-column model.

Appendix A.4. Soil profile 4

A.4.1. L/D = 3. γ_f^p = 0.02

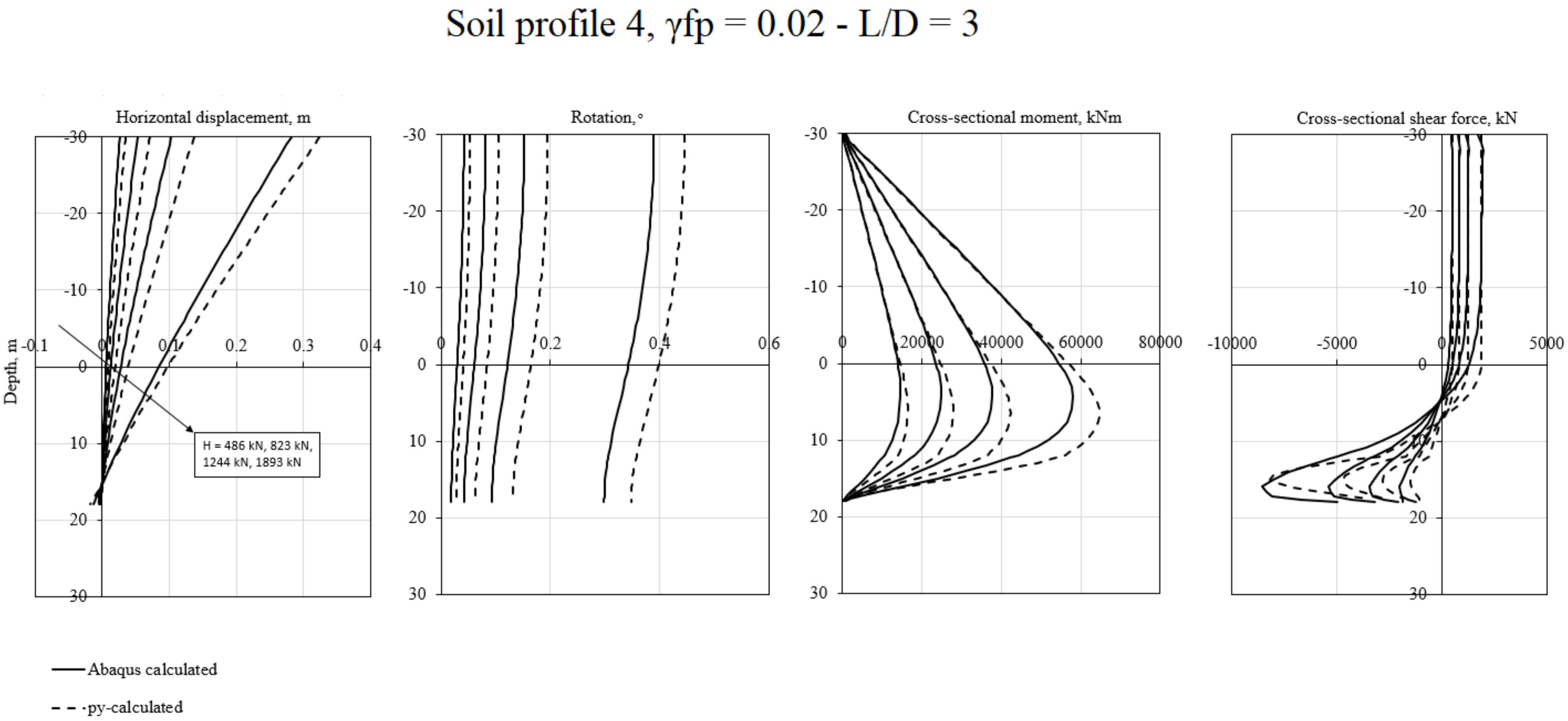

Figure A.25: Comparison of pile response – Soil profile 4, L/D=3, γ_f^p=0.02. The legend wrongfully says "py-calculated". The pile responses are calculated using the aforementioned multi-spring beam-column model.

A.4.2. L/D = 3. γ_f^p = 0.10

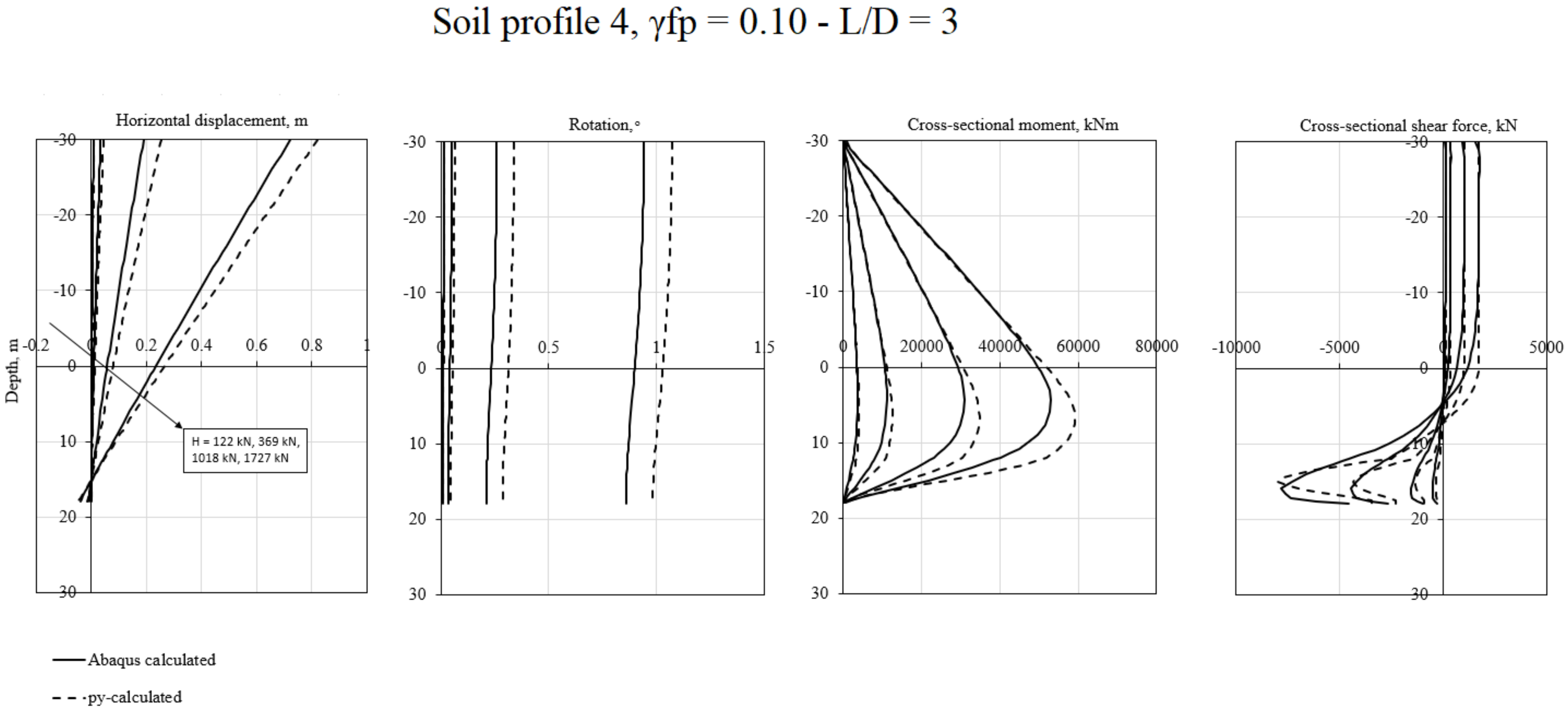

Figure A.26: Comparison of pile response – Soil profile 4, L/D=3, γ_f^p=0.10. The legend wrongfully says "py-calculated". The pile responses are calculated using the aforementioned multi-spring beam-column model.

A.4.3. L/D = 5. γ_f^p = 0.02

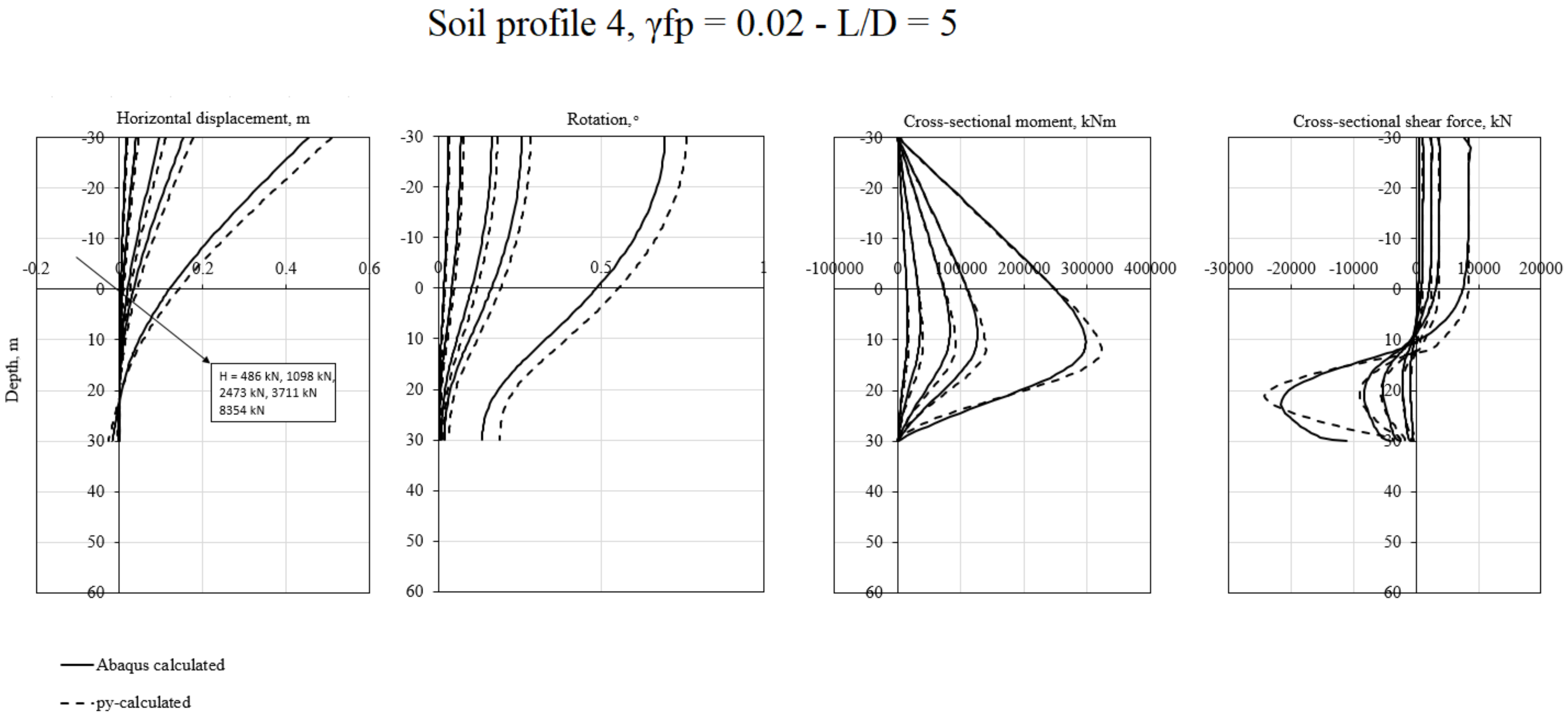

Figure A.27: Comparison of pile response – Soil profile 4, L/D=5, γ_f^p=0.02. The legend wrongfully says "py-calculated". The pile responses are calculated using the aforementioned multi-spring beam-column model.

A.4.4. L/D = 5. γ_f^p = 0.10

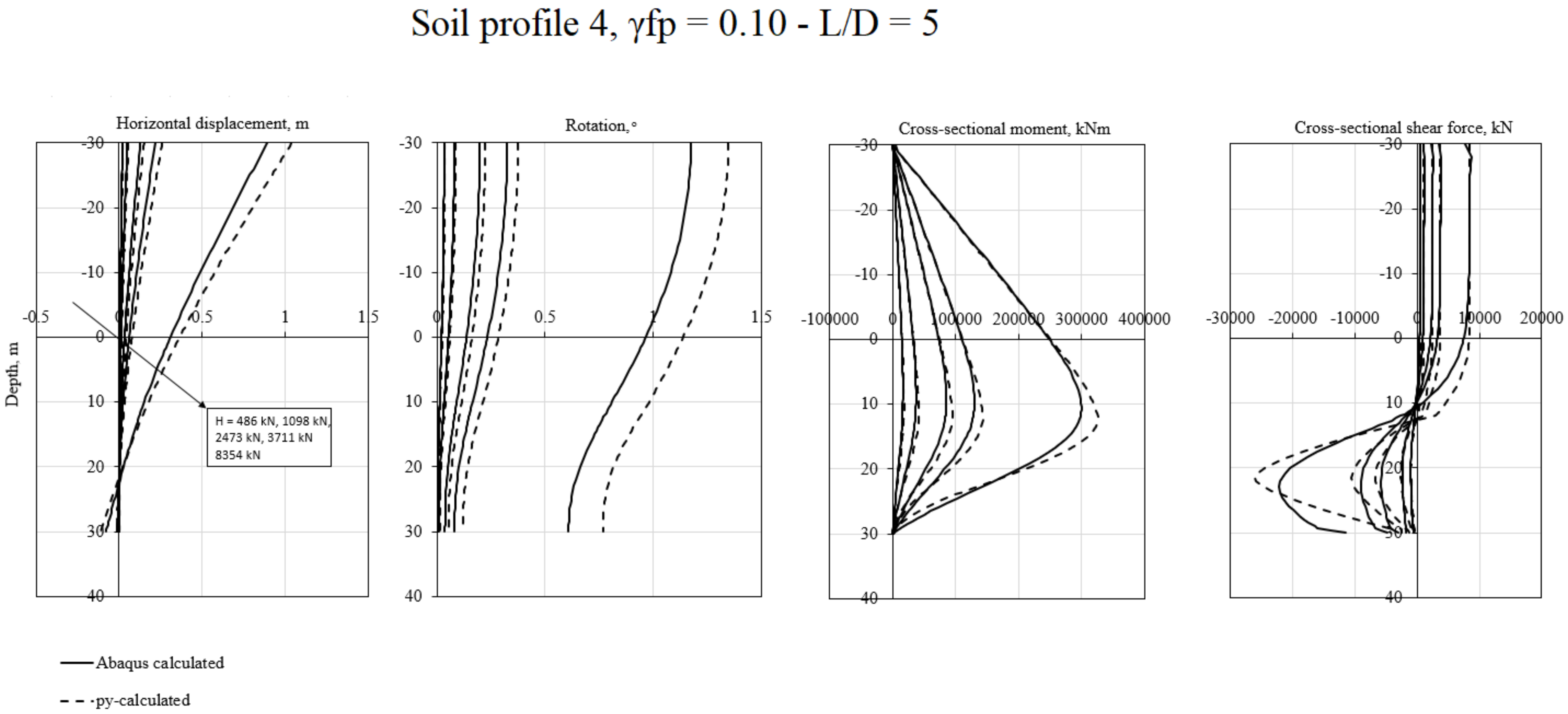

Figure A.28: Comparison of pile response – Soil profile 4, L/D=5, γ_f^p=0.10. The legend wrongfully says "py-calculated". The pile responses are calculated using the aforementioned multi-spring beam-column model.

A.4.5. L/D = 7. γ_f^p = 0.02

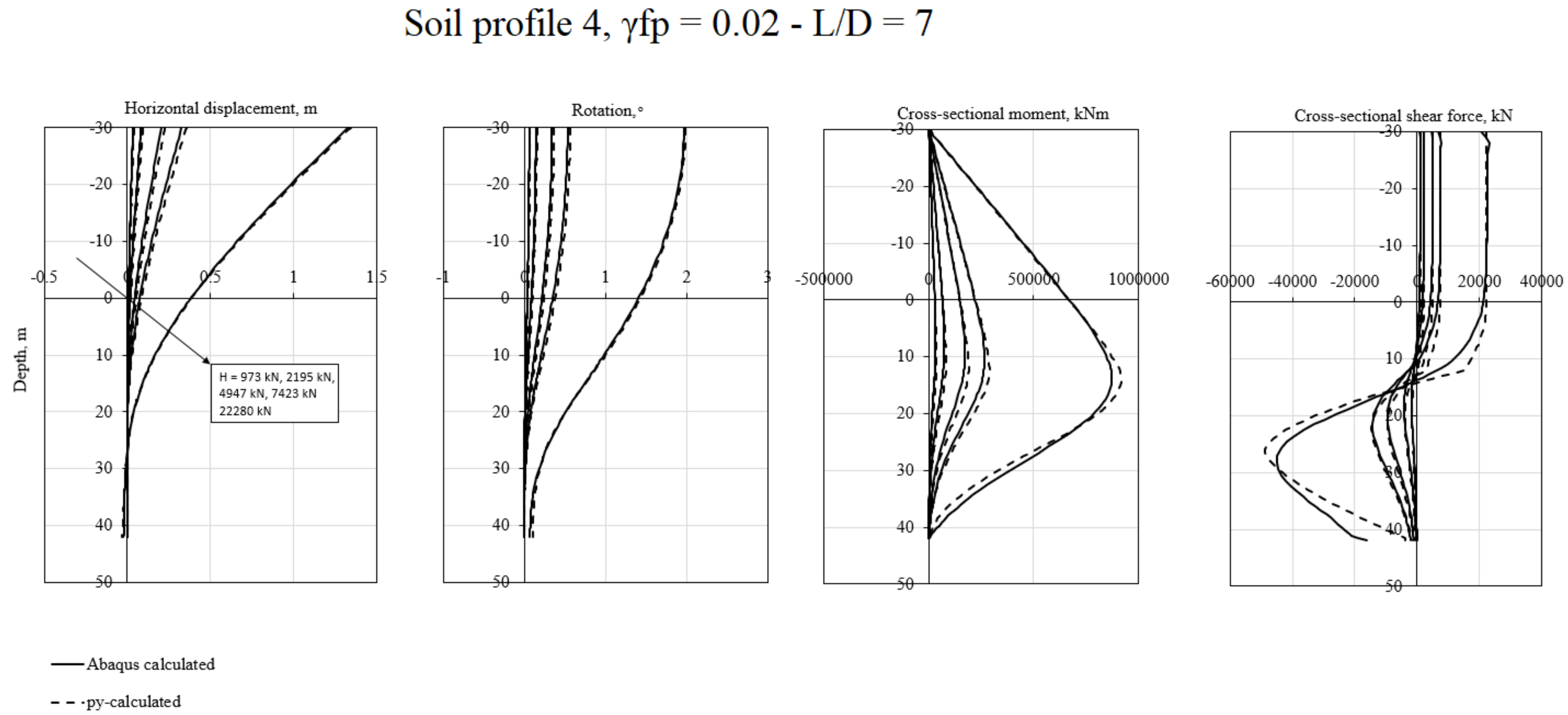

Figure A.29: Comparison of pile response – Soil profile 4, L/D=7, γ_f^p=0.02. The legend wrongfully says "py-calculated". The pile responses are calculated using the aforementioned multi-spring beam-column model.

A.4.6. L/D = 7. γ_f^p = 0.10

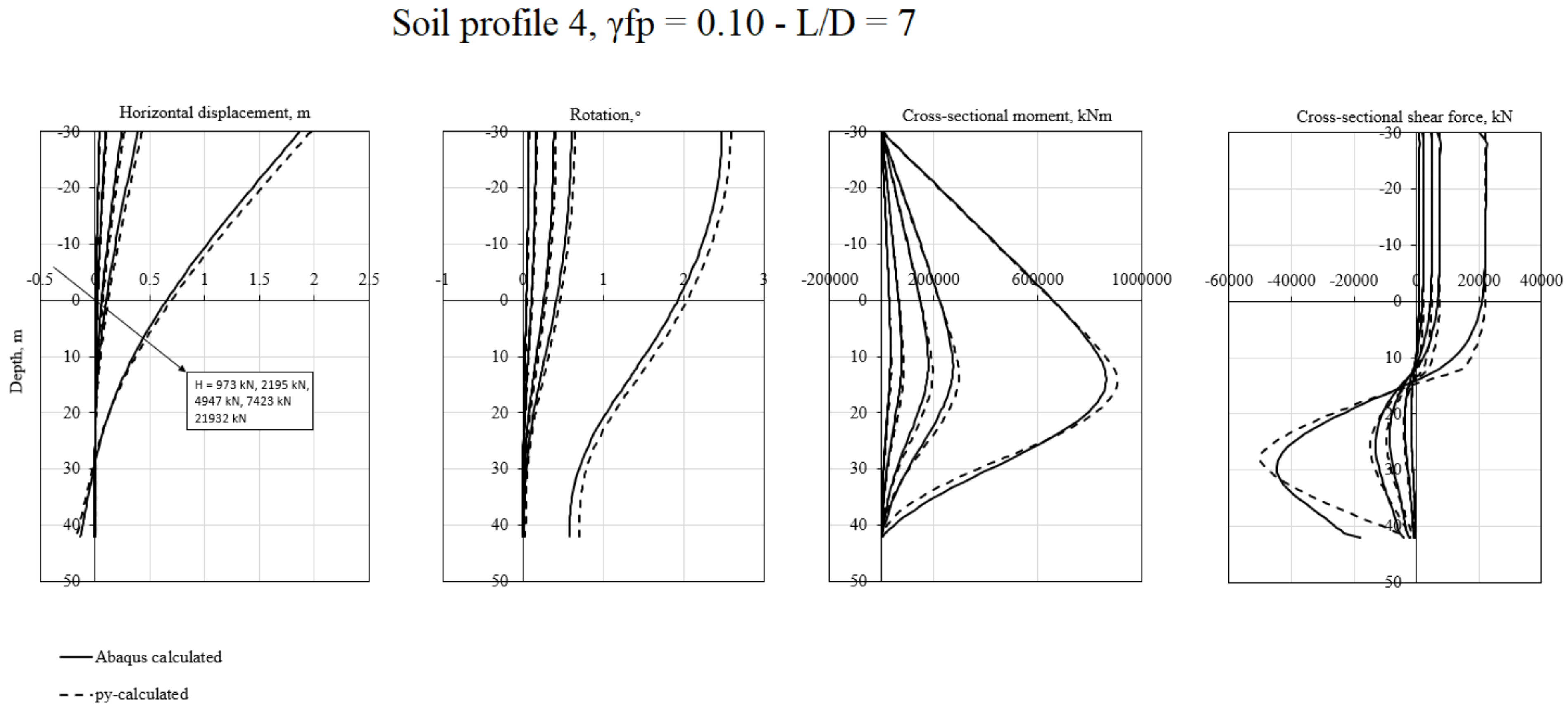

Figure A.30: Comparison of pile response – Soil profile 4, L/D=7, γ_f^p=0.10. The legend wrongfully says "py-calculated". The pile responses are calculated using the aforementioned multi-spring beam-column model.

A.4.7. L/D = 10. γ_f^p = 0.02

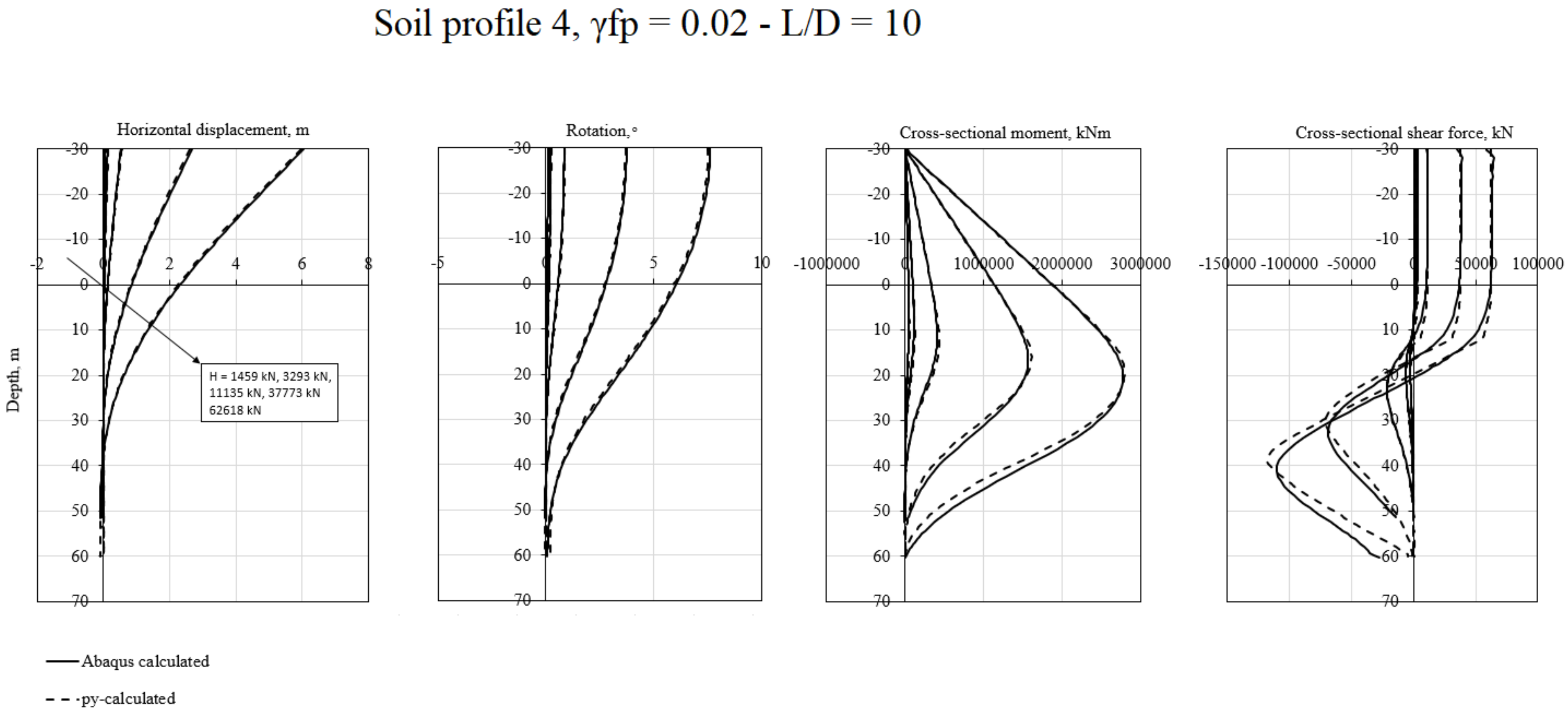

Figure A.31: Comparison of pile response – Soil profile 4, L/D=10, γ_f^p=0.02. The legend wrongfully says "py-calculated". The pile responses are calculated using the aforementioned multi-spring beam-column model.

A.4.8. L/D = 10. γ_f^p = 0.10

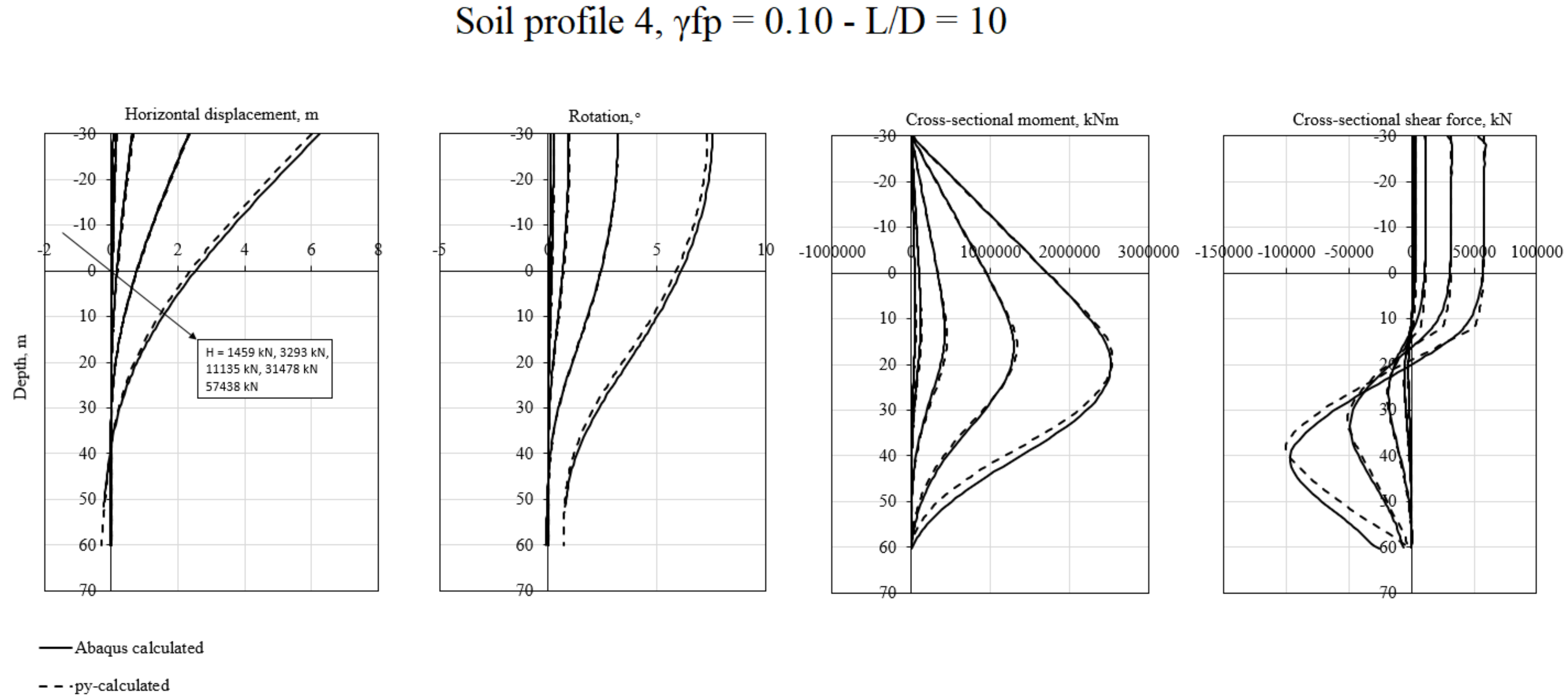

Figure A.32: Comparison of pile response – Soil profile 4, L/D=10, γ_f^p=0.10. The legend wrongfully says "py-calculated". The pile responses are calculated using the aforementioned multi-spring beam-column model.

Appendix A.5. Soil profile 5

A.5.1. L/D = 3. $\gamma_f^p = 0.02$

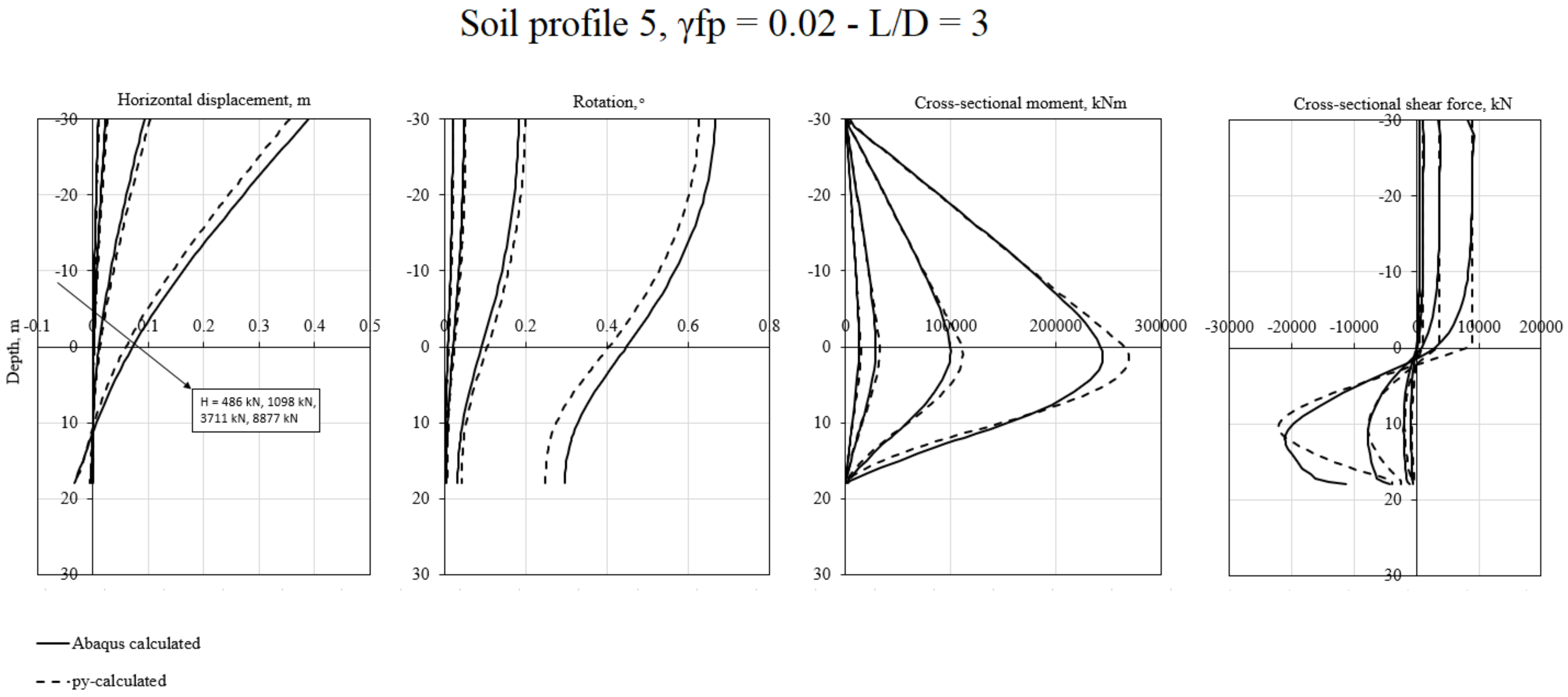

Figure A.33: Comparison of pile response – Soil profile 5, L/D=3, γ_f^p=0.02. The legend wrongfully says "py-calculated". The pile responses are calculated using the aforementioned multi-spring beam-column model.

A.5.2. L/D = 3. γ_f^p = 0.10

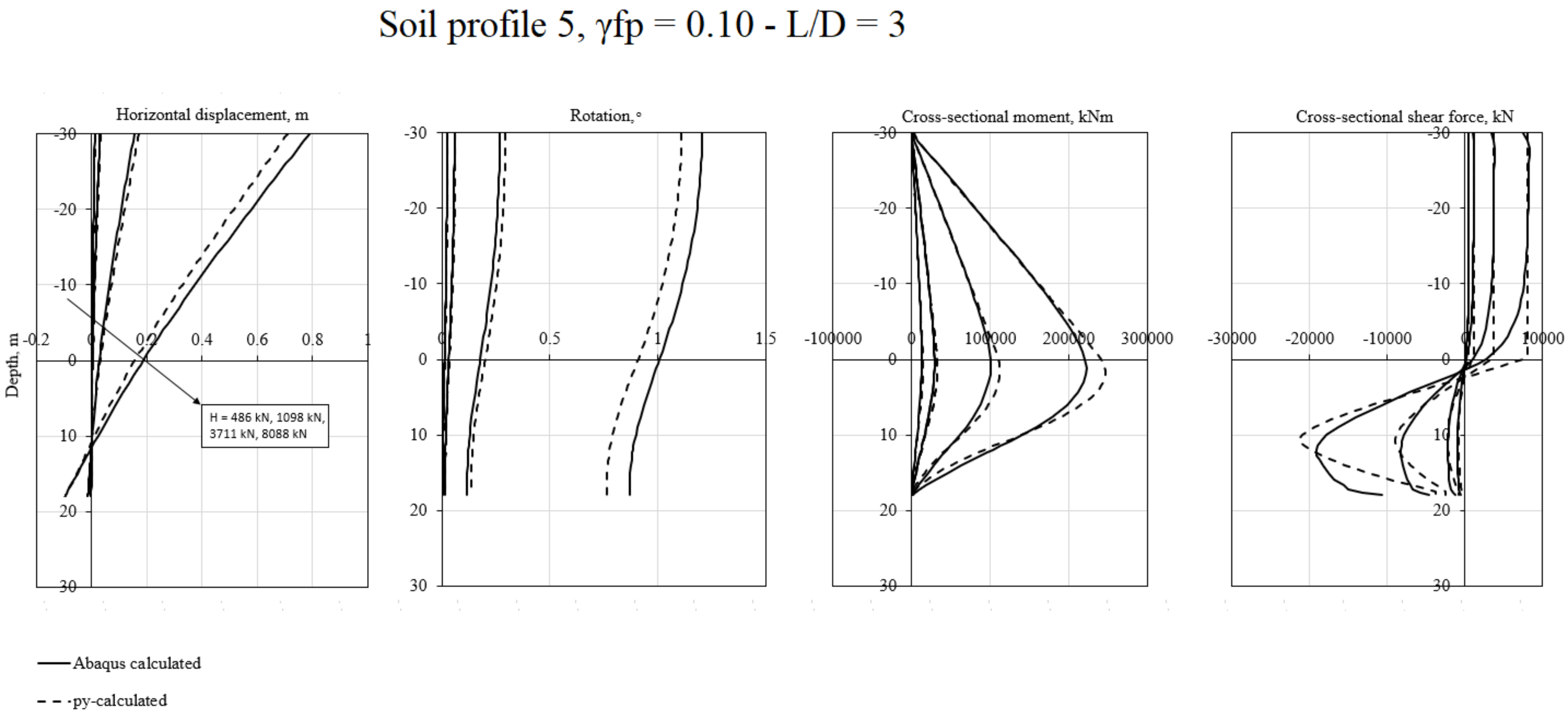

Figure A.34: Comparison of pile response – Soil profile 5, L/D=3, γ_f^p=0.10. The legend wrongfully says "py-calculated". The pile responses are calculated using the aforementioned multi-spring beam-column model.

A.5.3. L/D = 5. γ_f^p = 0.02

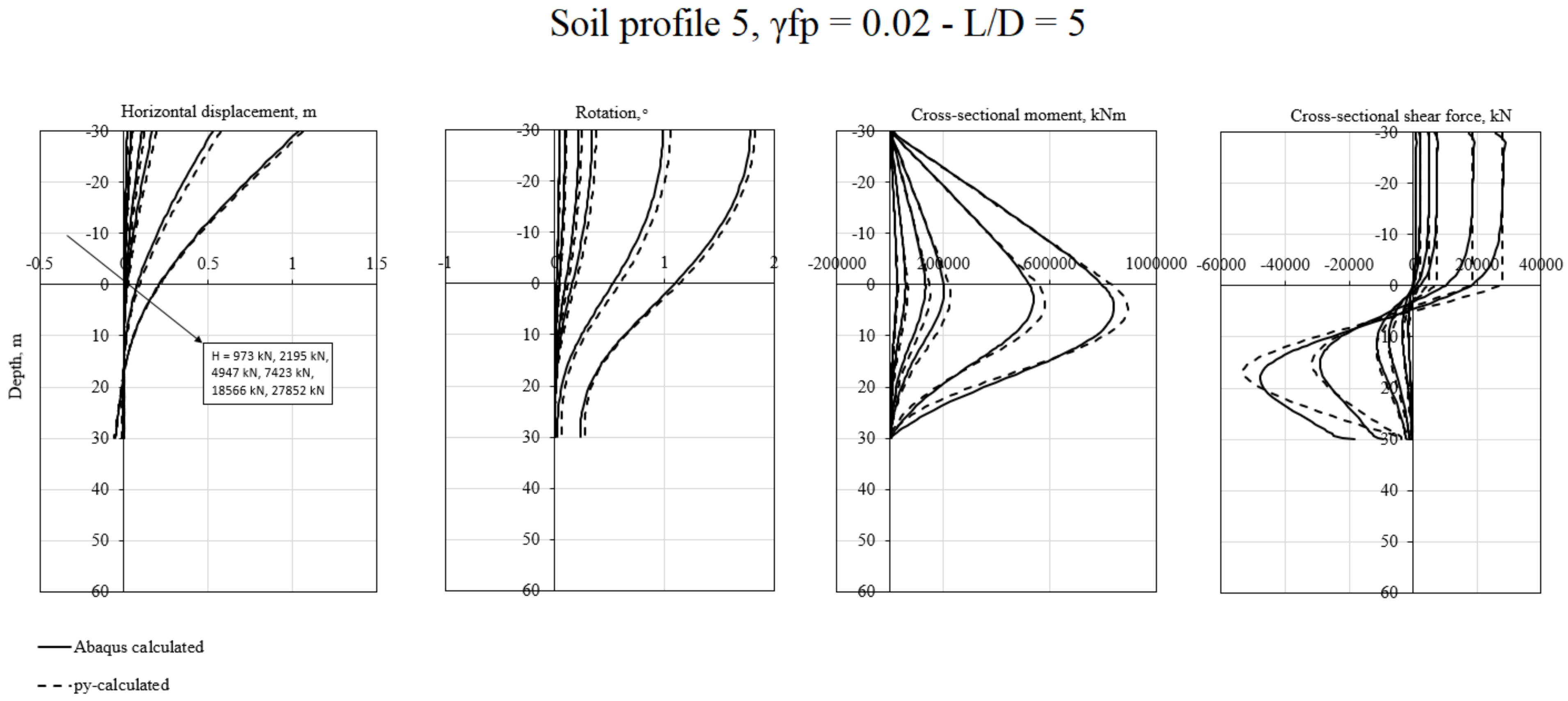

Figure A.35: Comparison of pile response – Soil profile 5, L/D=5, γ_f^p=0.02. The legend wrongfully says "py-calculated". The pile responses are calculated using the aforementioned multi-spring beam-column model.

A.5.4. L/D = 5. γ_f^p = 0.10

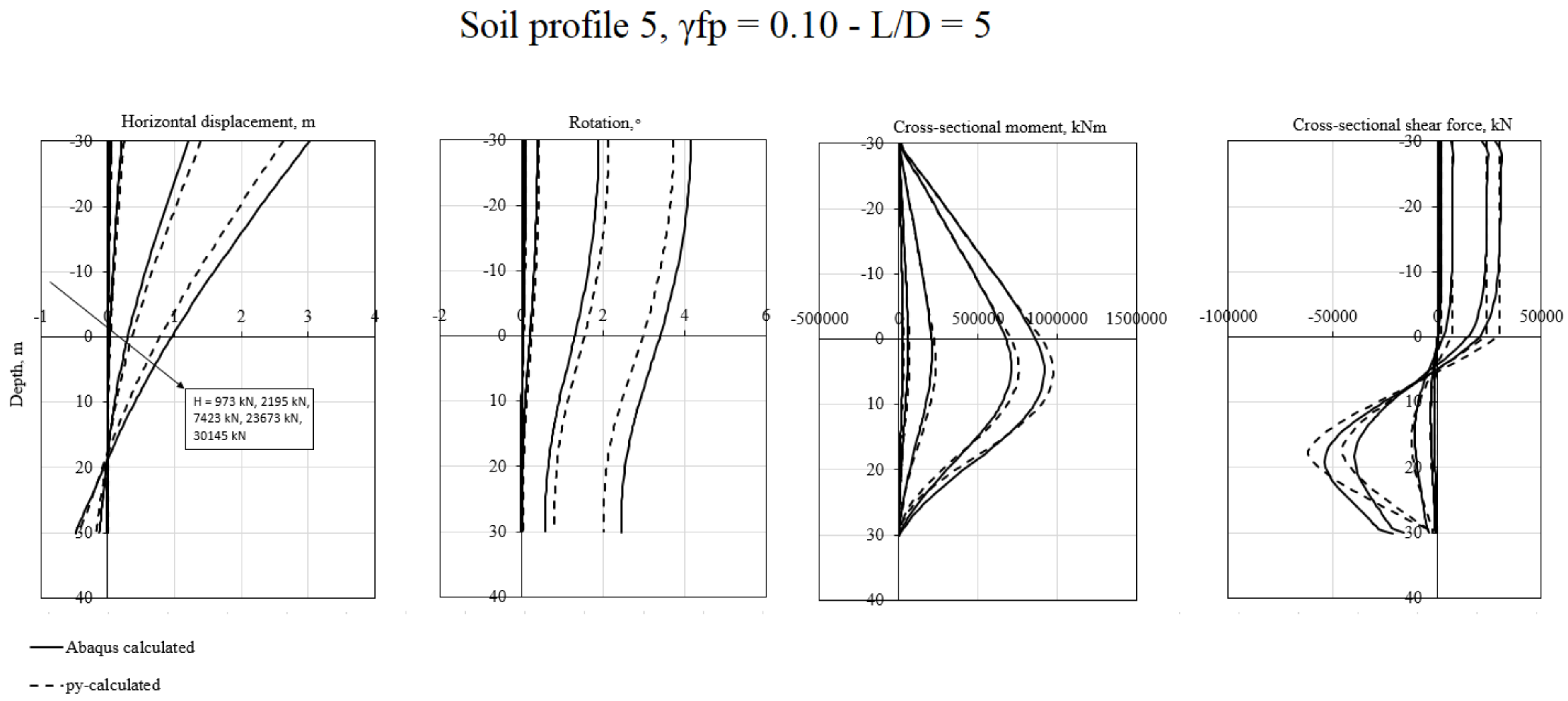

Figure A.36: Comparison of pile response – Soil profile 5, L/D=5, γ_f^p=0.10. The legend wrongfully says "py-calculated". The pile responses are calculated using the aforementioned multi-spring beam-column model.

A.5.5. L/D = 7. γ_f^p = 0.02

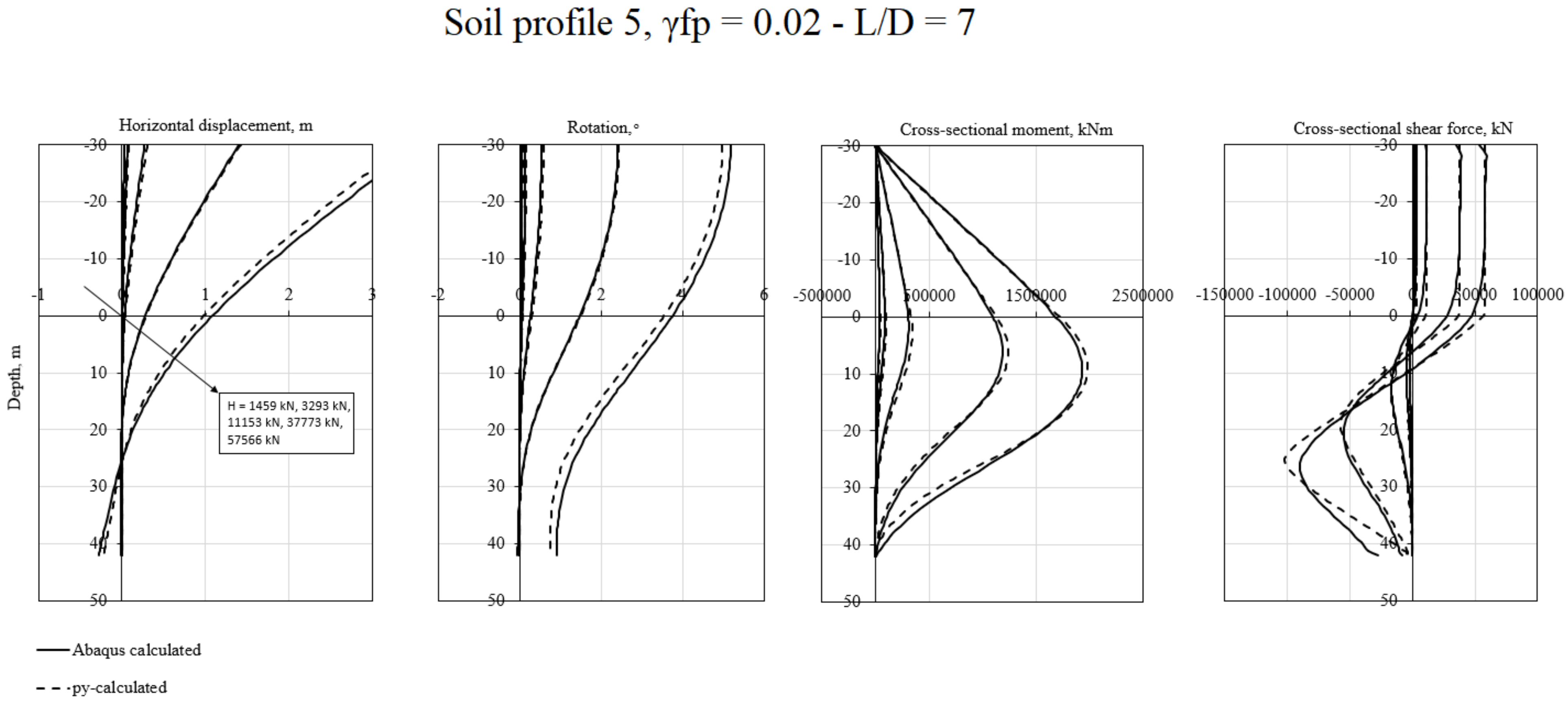

Figure A.37: Comparison of pile response – Soil profile 5, L/D=7, γ_f^p=0.02. The legend wrongfully says “py-calculated”. The pile responses are calculated using the aforementioned multi-spring beam-column model.

A.5.6. L/D = 7. $\gamma_f^p = 0.10$

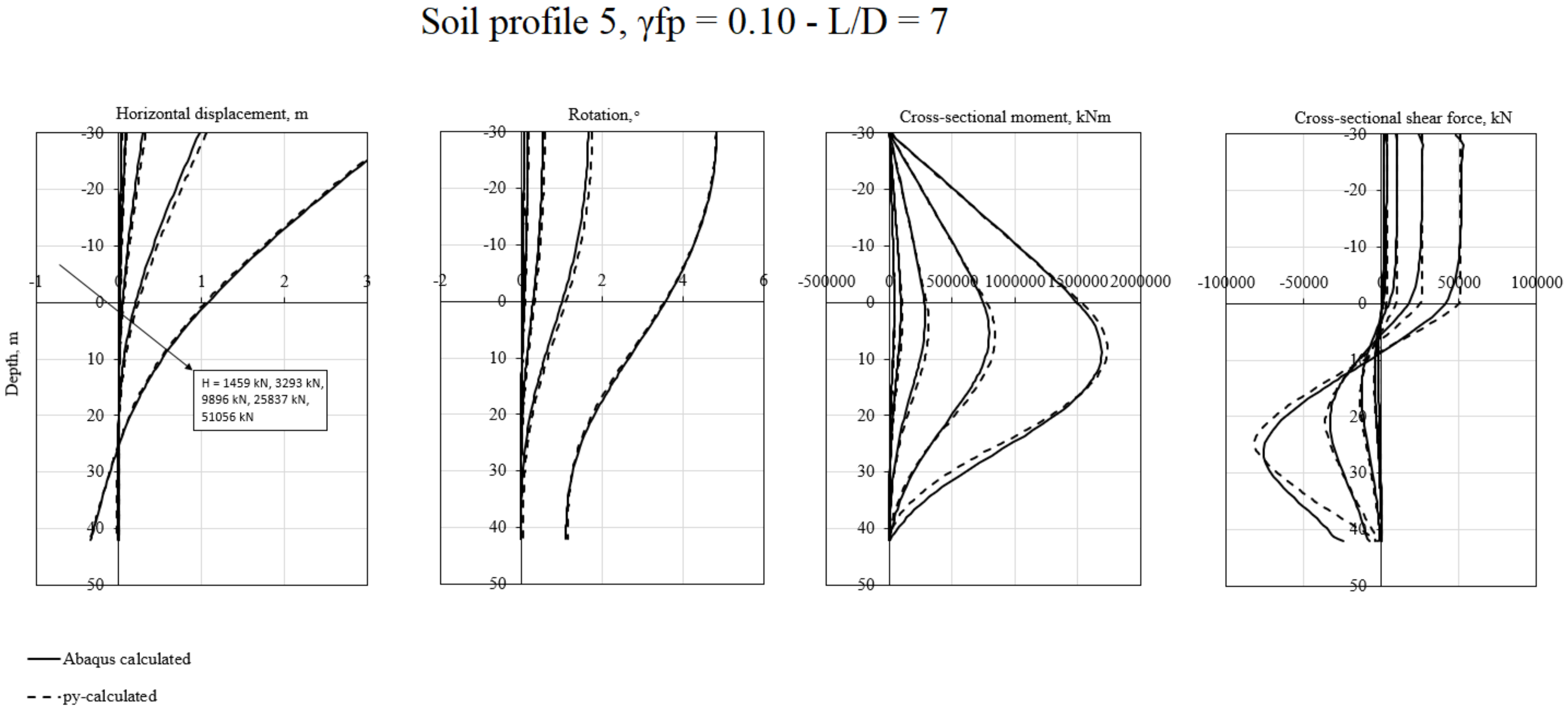

Figure A.38: Comparison of pile response – Soil profile 5, L/D=7, γ_f^p=0.10. The legend wrongfully says "py-calculated". The pile responses are calculated using the aforementioned multi-spring beam-column model.

A.5.7. L/D = 10. γ_f^p = 0.02

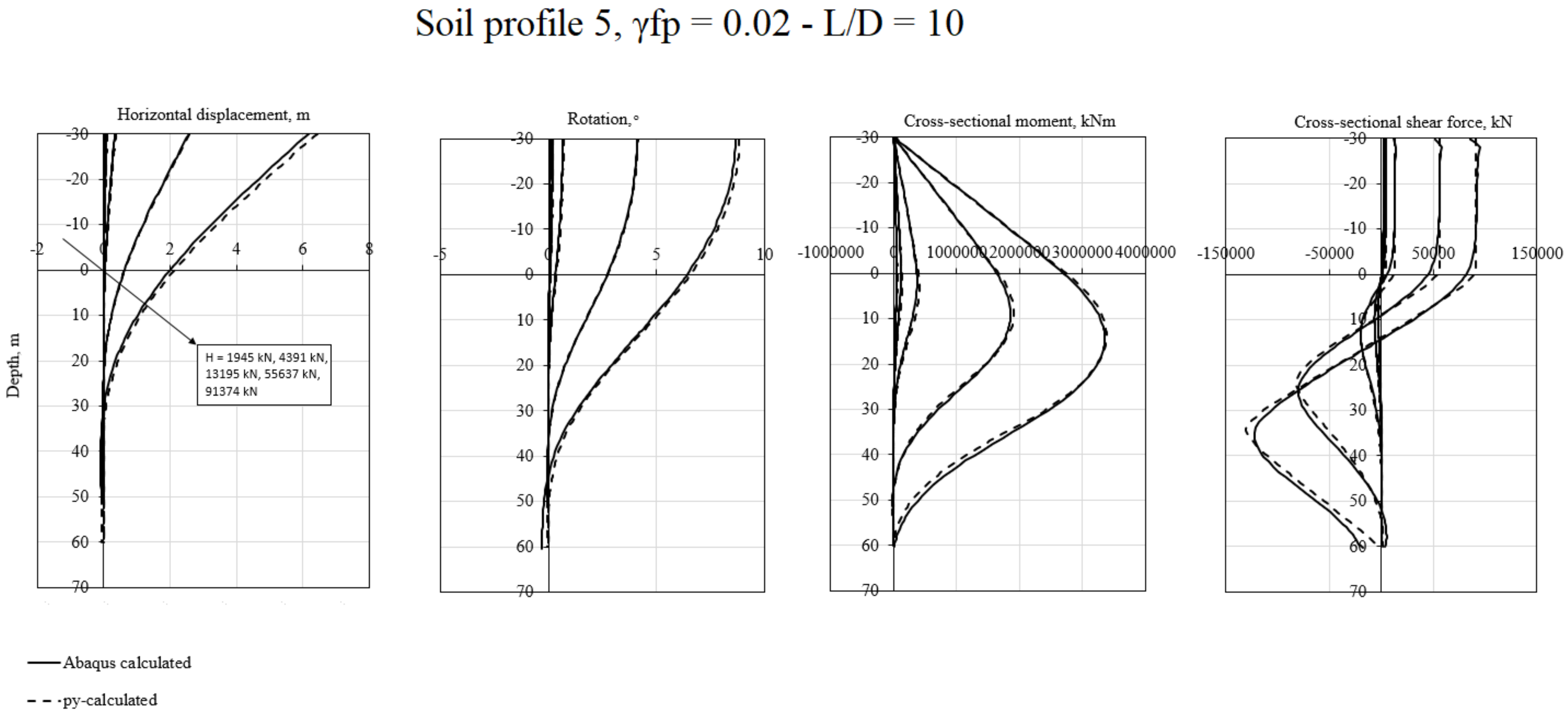

Figure A.39: Comparison of pile response – Soil profile 5, L/D=10, γ_f^p=0.02. The legend wrongfully says "py-calculated". The pile responses are calculated using the aforementioned multi-spring beam-column model.

A.5.8. L/D = 10. γ_f^p = 0.10

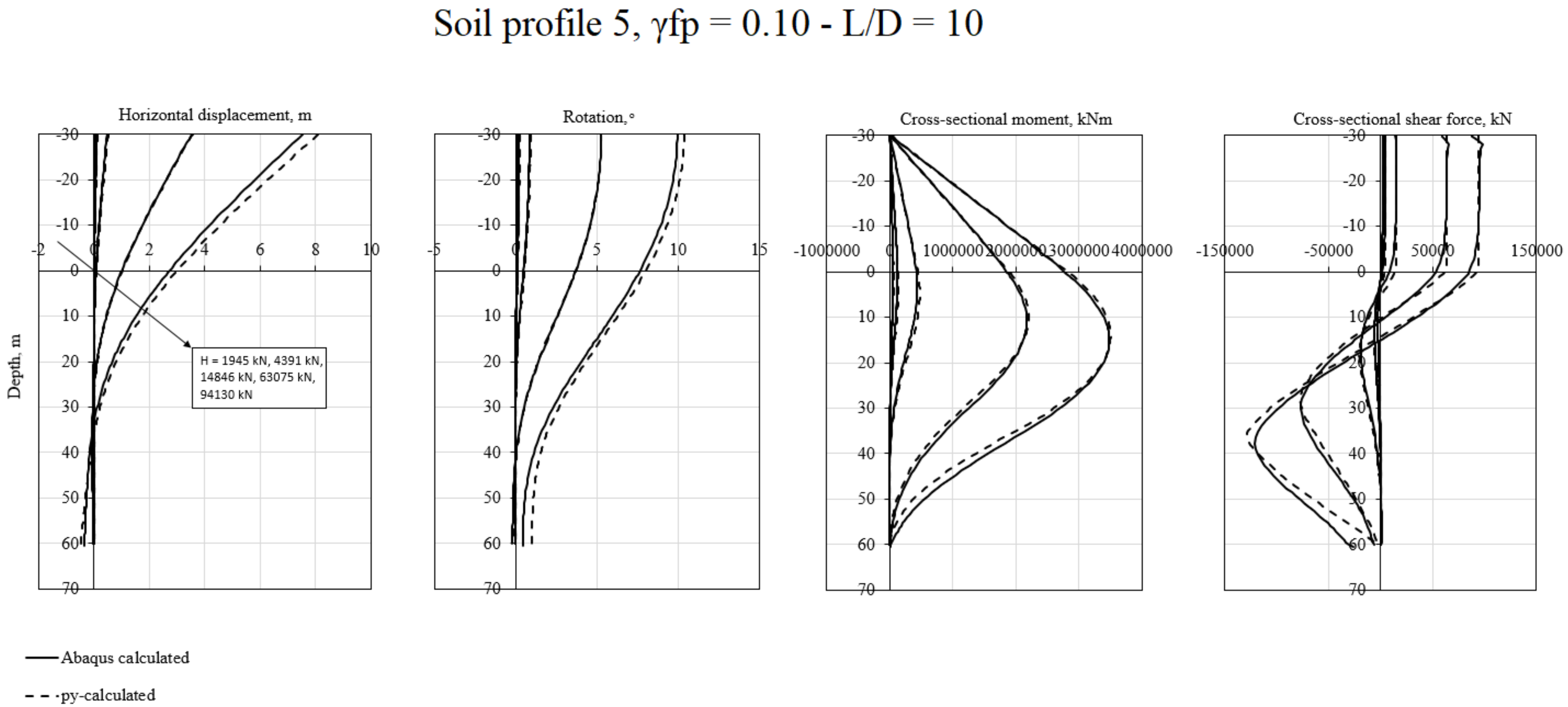

Figure A.40: Comparison of pile response – Soil profile 5, L/D=10, γ_f^p=0.10. The legend wrongfully says "py-calculated". The pile responses are calculated using the aforementioned multi-spring beam-column model.

Appendix B

Pile response analyses using the optimization tool

Appendix B.1. Soil profile 1

B.1.1. L/D = 3. γ_f^p = 0.02

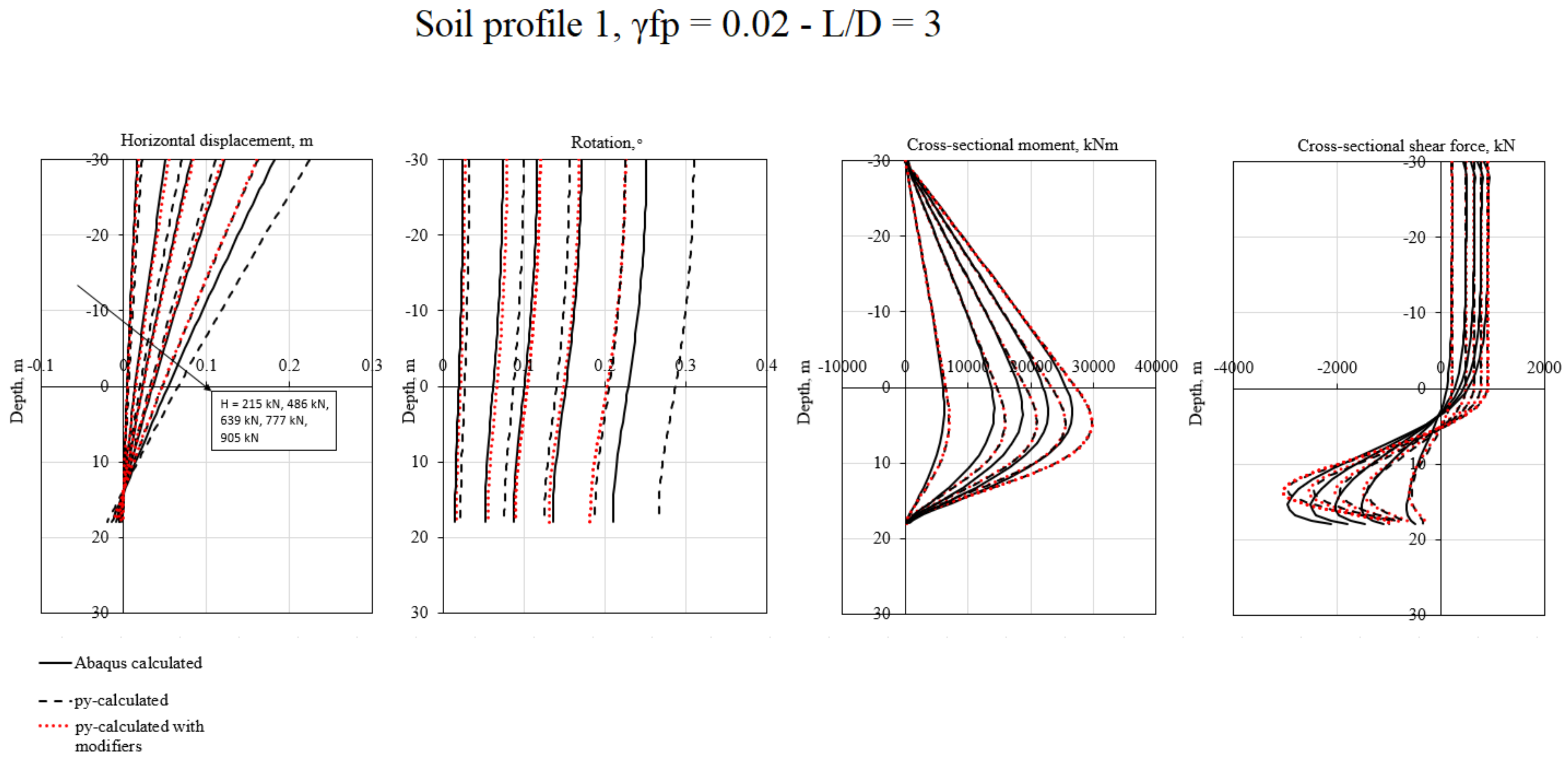

Figure B.1: Optimized pile response – Soil profile 1, L/D=3, γ_f^p=0.02.

Table B.1: Normalized error reduction, soil profile 1, γ_f^p = 0.02, L/D = 3.

Pile load [kN]		Error reduction [%]
215	Displacement	77.98
	Rotation	74.97
	Combined	**76.47**
486	Displacement	84.04
	Rotation	83.62
	Combined	**83.88**
639	Displacement	89.03
	Rotation	93.07
	Combined	**91.28**
777	Displacement	79.99
	Rotation	92.17
	Combined	**86.61**
905	Displacement	42.67
	Rotation	51.93
	Combined	**47.66**

B.1.2. L/D = 3. γ_f^p = 0.10

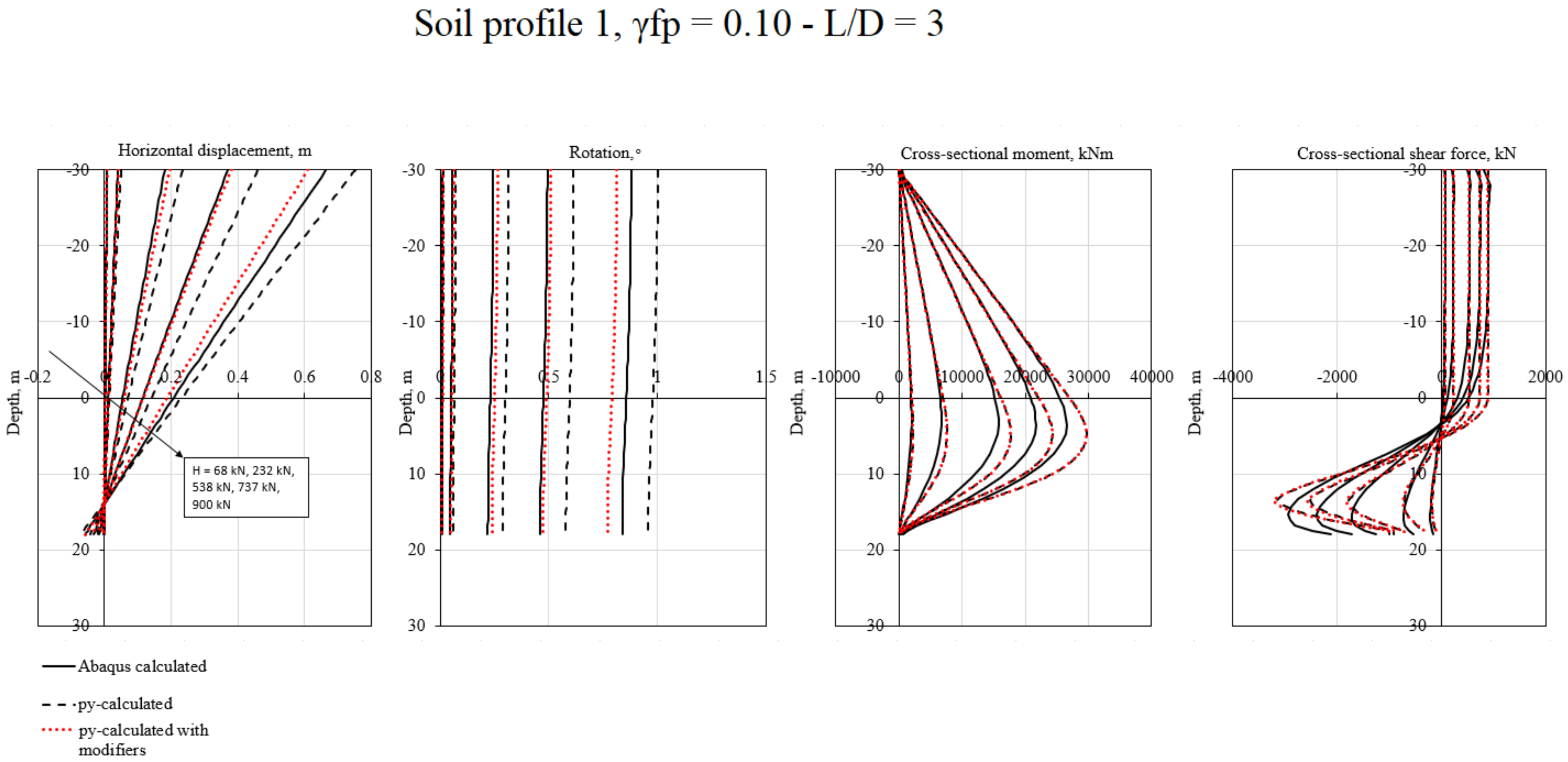

Figure B.2: Optimized pile response – Soil profile 1, L/D=3, γ_f^p=0.10.

Table B.2: Normalized error reduction, soil profile 1, γ_f^p = 0.10, L/D = 3.

Pile load [kN]		Error reduction [%]
68	Displacement	47.67
	Rotation	49.77
	Combined	**48.38**
232	Displacement	73.67
	Rotation	72.20
	Combined	**72.93**
538	Displacement	73.28
	Rotation	72.60
	Combined	**72.93**
737	Displacement	81.46
	Rotation	88.30
	Combined	**85.28**
900	Displacement	25.95
	Rotation	43.38
	Combined	**35.34**

B.1.3. L/D = 5. γ_f^p = 0.02

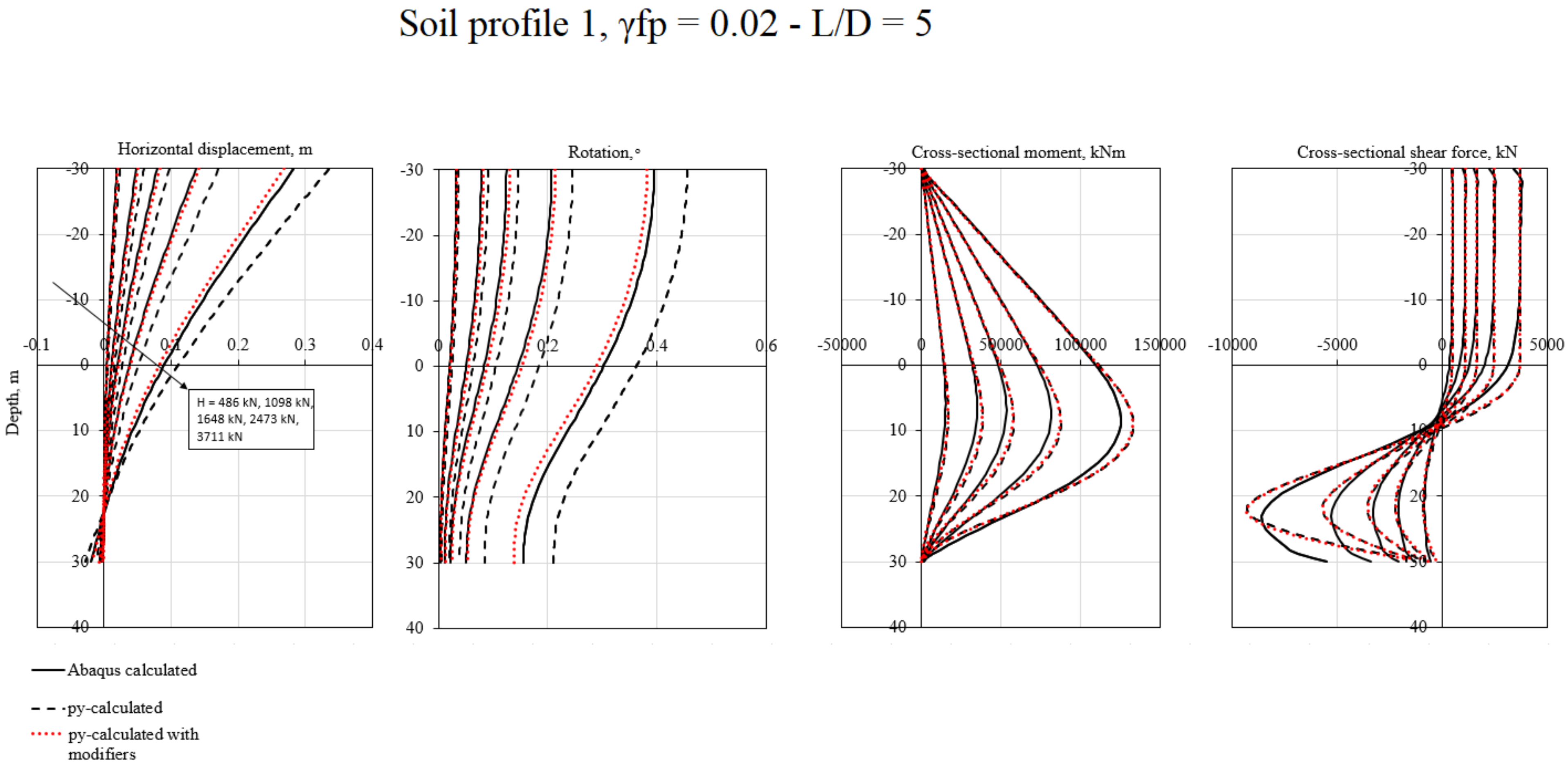

Figure B.3: Optimized pile response – Soil profile 1, L/D=5, γ_f^p=0.02.

Table B.3: Normalized error reduction, soil profile 1, γ_f^p = 0.02, L/D = 5.

Pile load [kN]		Error reduction [%]
486	Displacement	88.38
	Rotation	88.19
	Combined	**89.19**
1098	Displacement	88.11
	Rotation	84.81
	Combined	**86.89**
1648	Displacement	88.45
	Rotation	85.40
	Combined	**87.22**
2473	Displacement	91.90
	Rotation	91.76
	Combined	**92.15**
3711	Displacement	60.37
	Rotation	69.08
	Combined	**64.84**

B.1.4. L/D = 5. γ_f^p = 0.10

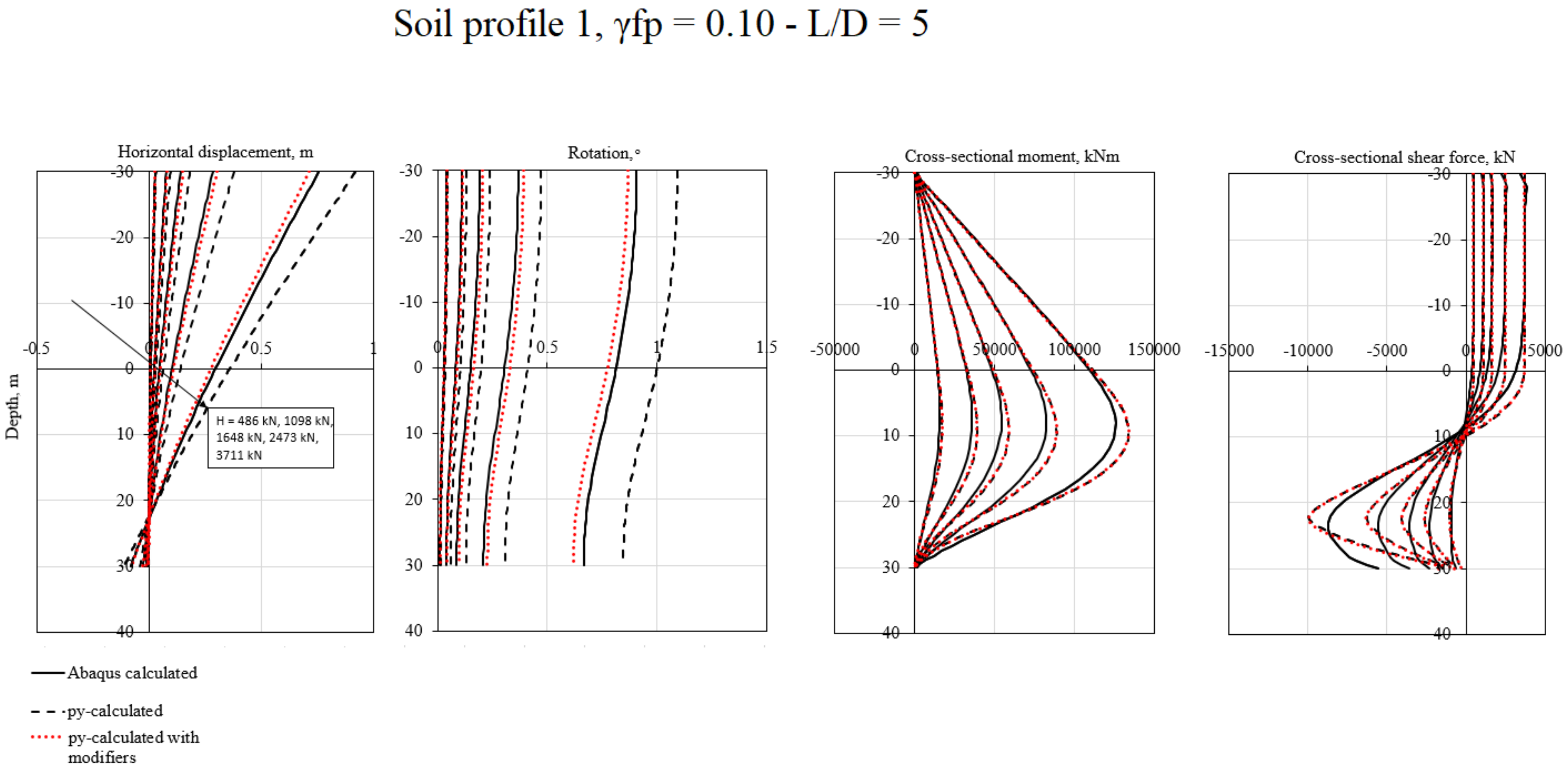

Figure B.4: Optimized pile response – Soil profile 1, L/D=5, γ_f^p=0.10.

Table B.4: Normalized error reduction, soil profile 1, γ_f^p = 0.10, L/D = 5.

Pile load [kN]		Error reduction [%]
486	Displacement	62.91
	Rotation	75.47
	Combined	**68.72**
1098	Displacement	85.46
	Rotation	82.10
	Combined	**83.92**
1648	Displacement	77.82
	Rotation	75.70
	Combined	**76.82**
2473	Displacement	82.27
	Rotation	80.60
	Combined	**81.46**
3711	Displacement	67.02
	Rotation	75.48
	Combined	**71.61**

Appendix B.2. Soil profile 2

B.2.1. L/D = 3. γ_f^p = 0.02

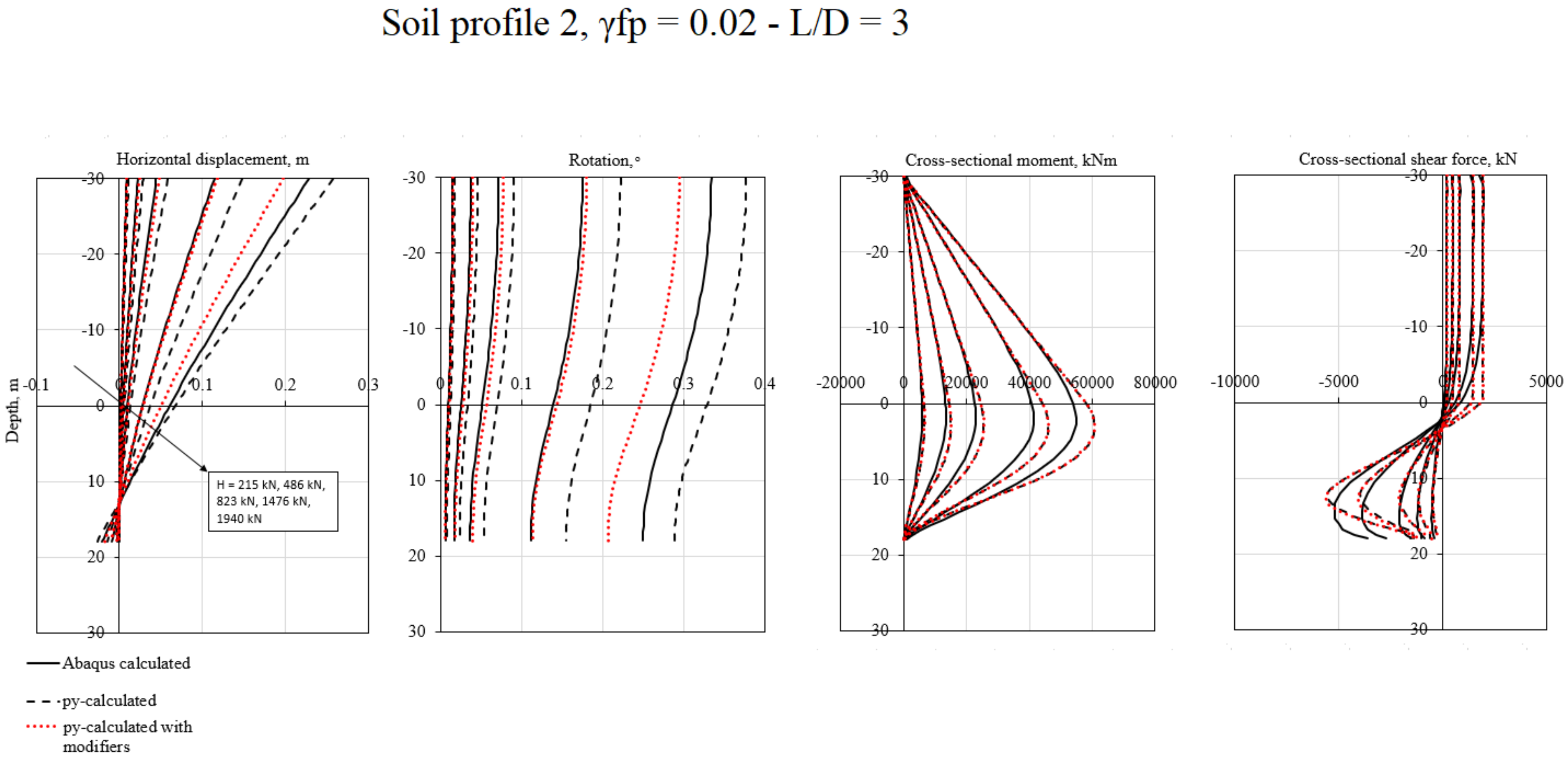

Figure B.5: Optimized pile response – Soil profile 2, L/D=3, γ_f^p=0.02.

Table B.5: Normalized error reduction, soil profile 2, γ_f^p = 0.02, L/D = 3.

Pile load [kN]		Error reduction [%]
215	Displacement	84.39
	Rotation	83.67
	Combined	**84.26**
486	Displacement	80.10
	Rotation	77.58
	Combined	**78.92**
823	Displacement	78.75
	Rotation	77.73
	Combined	**78.31**
1476	Displacement	85.89
	Rotation	94.41
	Combined	**90.53**
1940	Displacement	-0.72
	Rotation	-6.43
	Combined	**-3.81**

B.2.2. L/D = 3. γ_f^p = 0.10

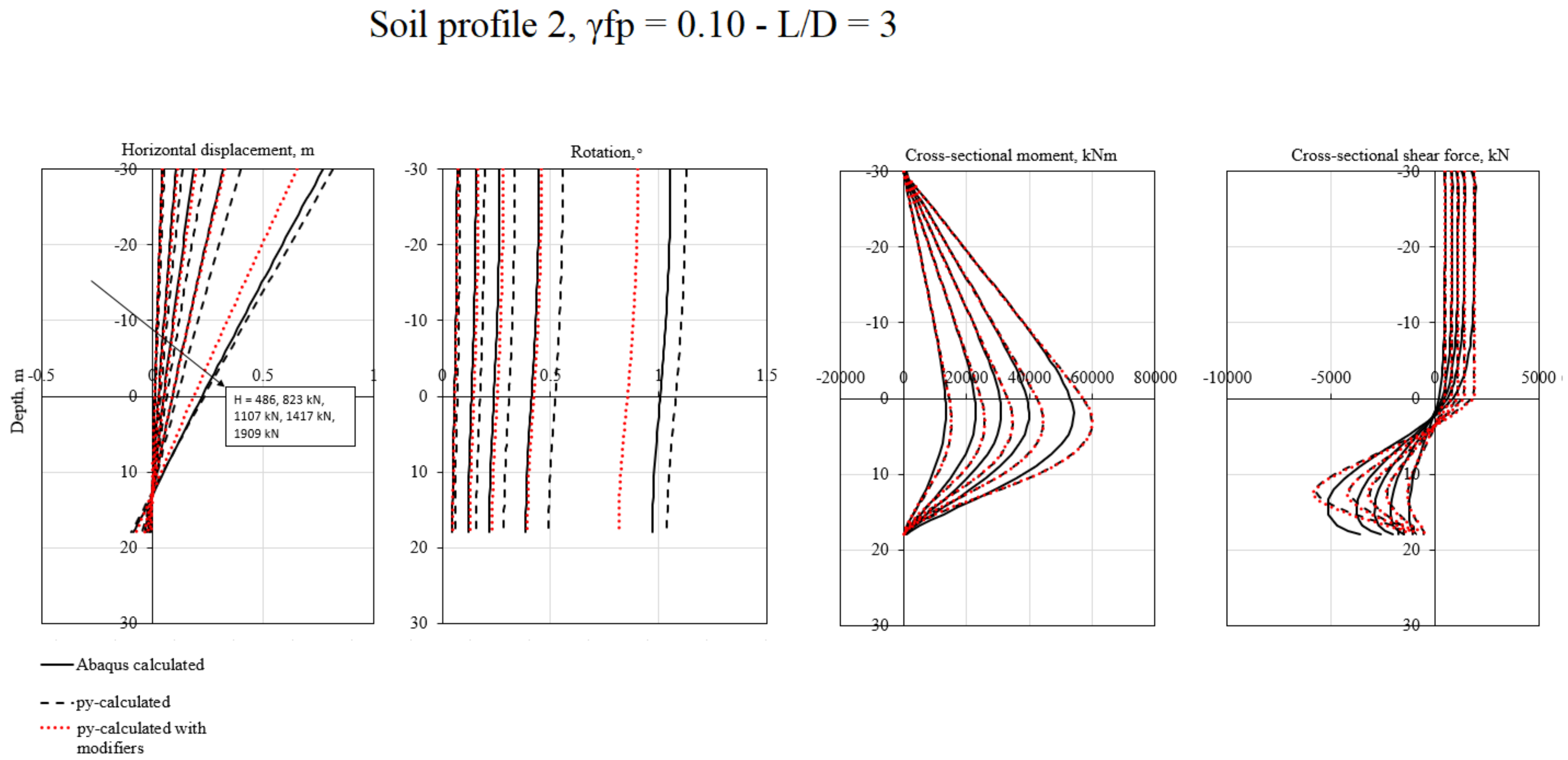

Figure B.6: Optimized pile response – Soil profile 2, L/D=3, γ_f^p=0.10.

Table B.6: Normalized error reduction, soil profile 2, γ_f^p=0.10, L/D=3.

Pile load [kN]		Error reduction [%]
486	Displacement	76.63
	Rotation	83.16
	Combined	**80.25**
823	Displacement	71.62
	Rotation	75.15
	Combined	**73.53**
1107	Displacement	75.58
	Rotation	79.38
	Combined	**77.69**
1417	Displacement	77.15
	Rotation	91.90
	Combined	**85.21**
1909	Displacement	-50.46
	Rotation	-117.00
	Combined	**-79.07**

B.2.3. L/D = 5. γ_f^p = 0.02

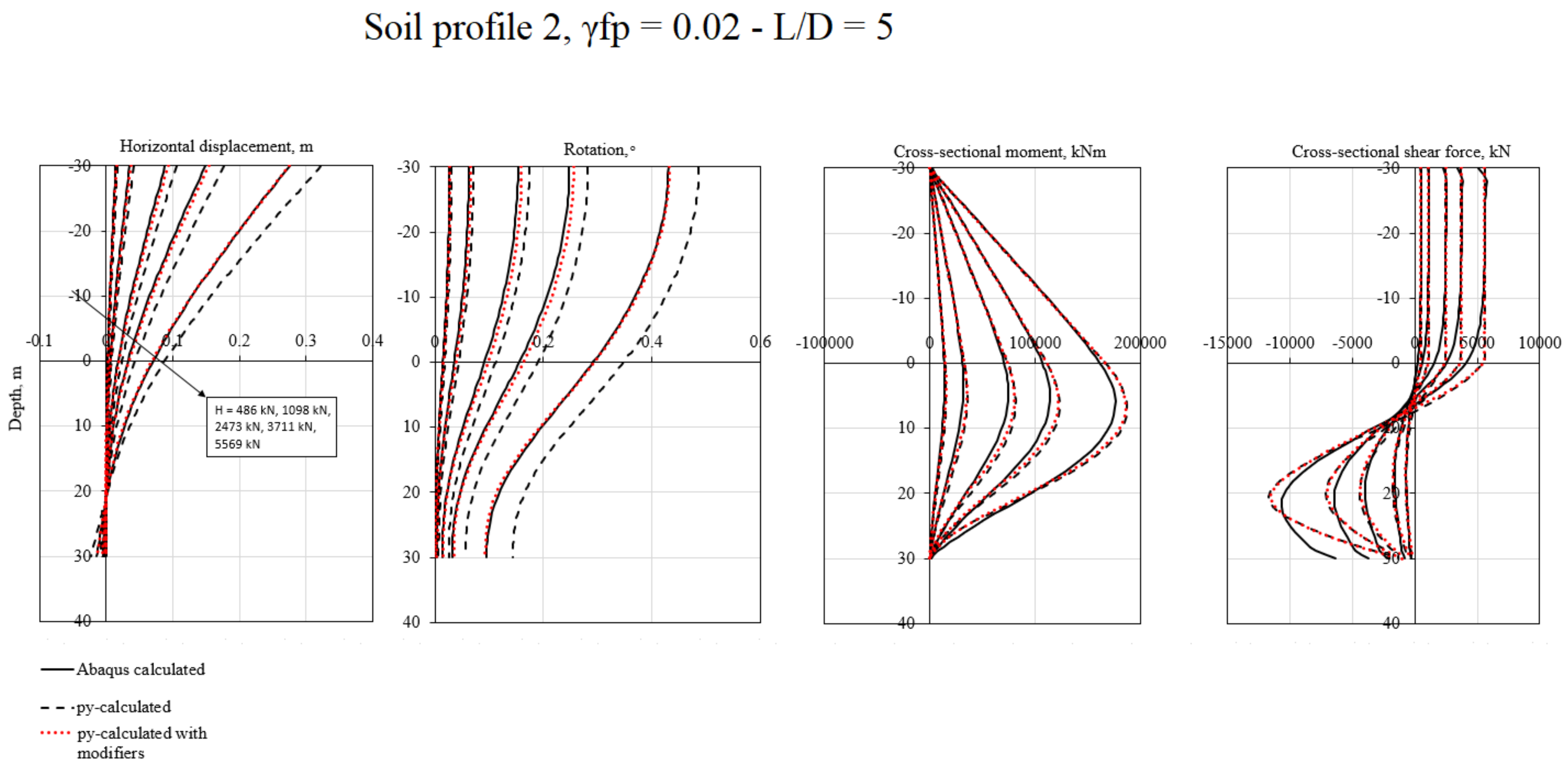

Figure B.7: Optimized pile response – Soil profile 2, L/D=5, γ_f^p=0.02.

Table B.7: Normalized error reduction, soil profile 2, γ_f^p=0.02, L/D=5.

Pile load [kN]		Error reduction [%]
486	Displacement	82.15
	Rotation	90.80
	Combined	**87.93**
1098	Displacement	86.85
	Rotation	90.80
	Combined	**89.94**
2473	Displacement	88.77
	Rotation	88.49
	Combined	**89.26**
3711	Displacement	89.39
	Rotation	90.92
	Combined	**90.68**
5569	Displacement	81.83
	Rotation	92.66
	Combined	**87.43**

B.2.4. L/D = 5. γ_f^p = 0.10

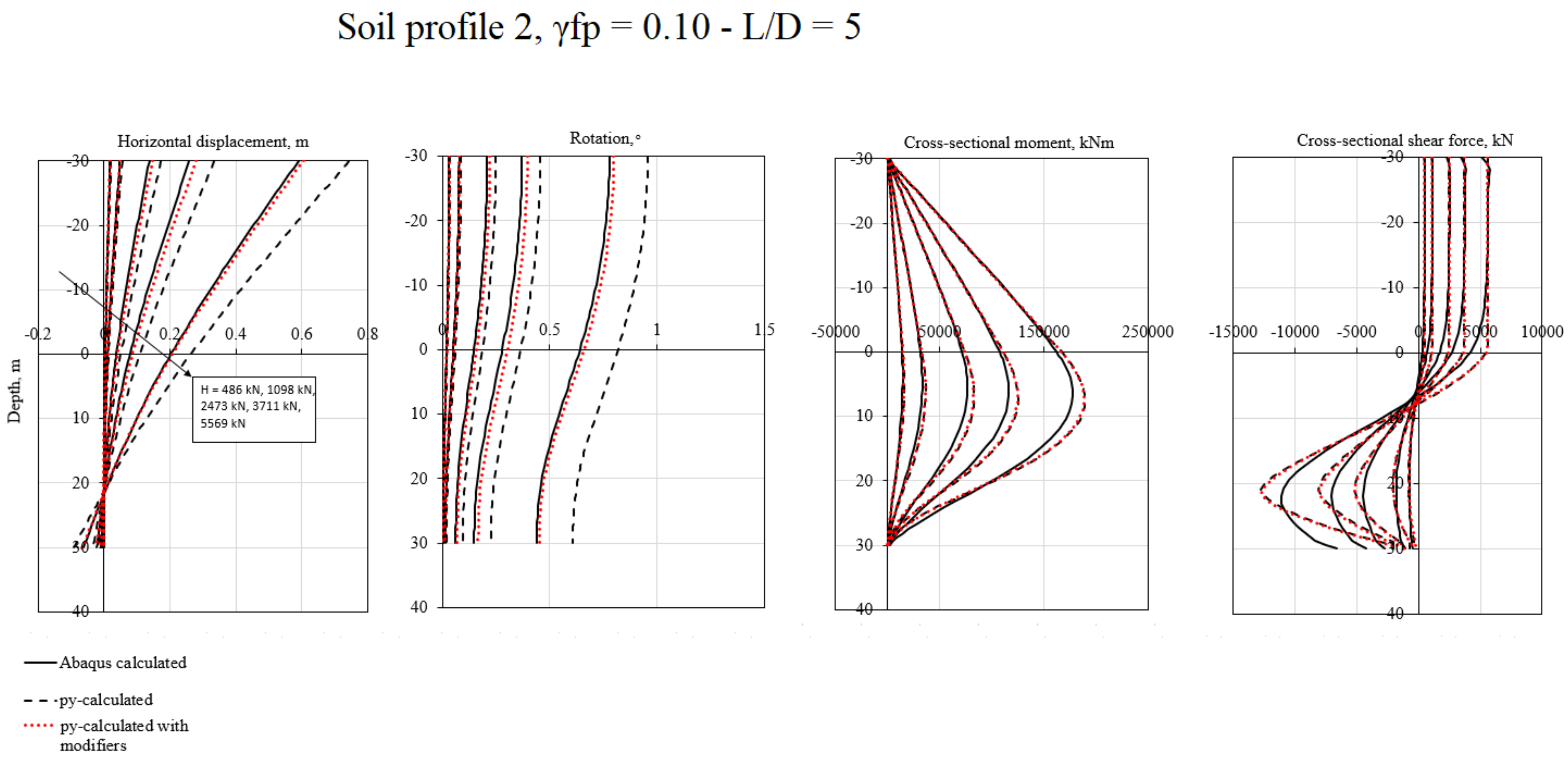

Figure B.8: Optimized pile response – Soil profile 2, L/D=5, γ_f^p=0.10.

Table B.8: Normalized error reduction, soil profile 2, γ_f^p=0.10, L/D=5.

Pile load [kN]		Error reduction [%]
486	Displacement	56.69
	Rotation	72.71
	Combined	**64.51**
1098	Displacement	80.18
	Rotation	83.04
	Combined	**81.29**
2473	Displacement	79.58
	Rotation	76.39
	Combined	**78.08**
3711	Displacement	78.38
	Rotation	76.04
	Combined	**77.24**
5569	Displacement	88.45
	Rotation	92.05
	Combined	**90.52**

Appendix B.3. Soil profile 3

B.3.1. L/D = 3. γ_f^p = 0.02

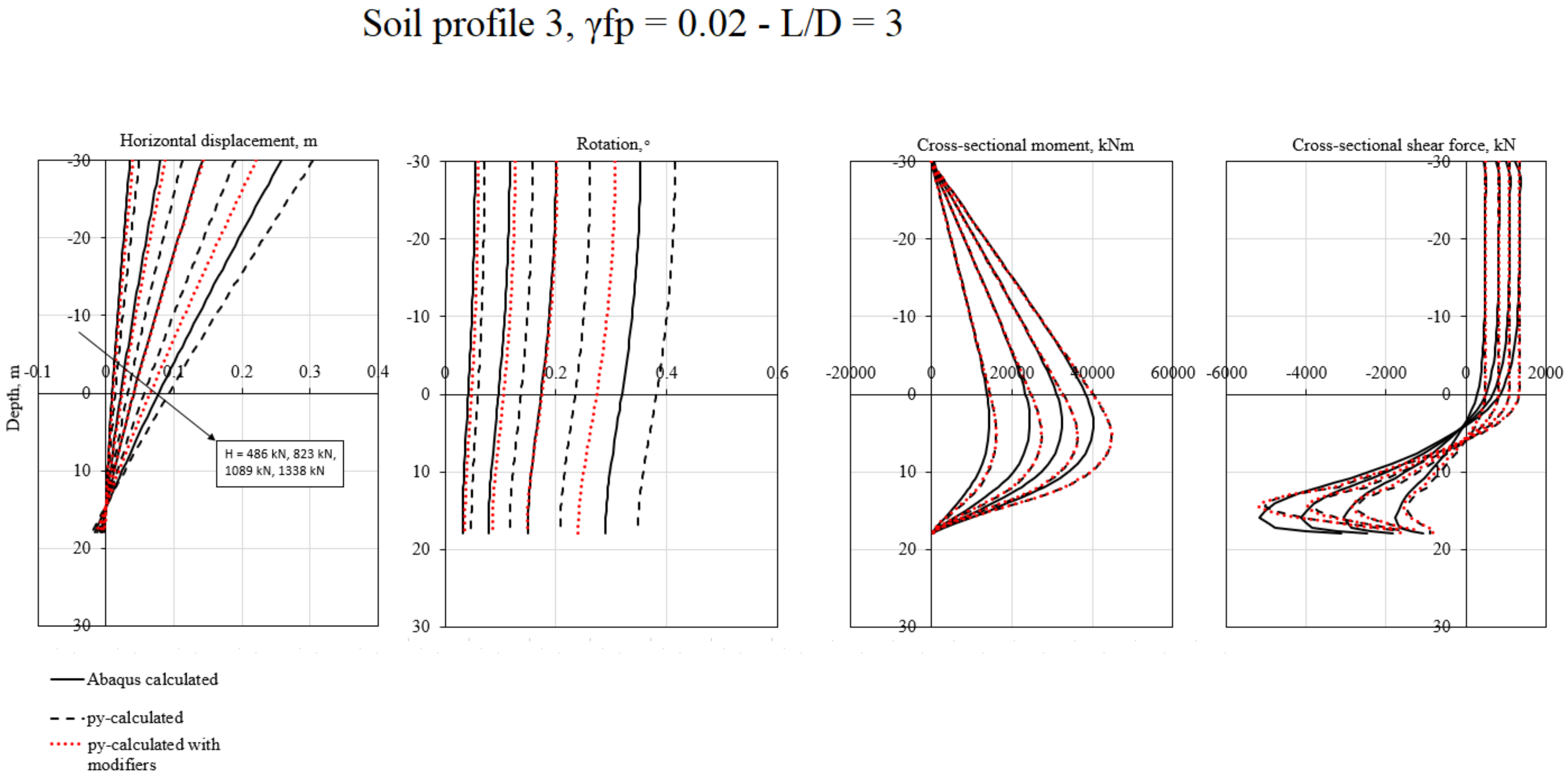

Figure B.9: Optimized pile response – Soil profile 3, L/D=3, γ_f^p=0.02.

Table B.9: Normalized error reduction, soil profile 3, γ_f^p=0.02, L/D=3.

Pile load [kN]		Error reduction [%]
486	Displacement	71.68
	Rotation	70.03
	Combined	**70.94**
823	Displacement	81.27
	Rotation	79.77
	Combined	**80.57**
1089	Displacement	93.74
	Rotation	98.39
	Combined	**96.30**
1338	Displacement	4.38
	Rotation	20.90
	Combined	**13.64**

B.3.2. L/D = 3. γ_f^p = 0.10

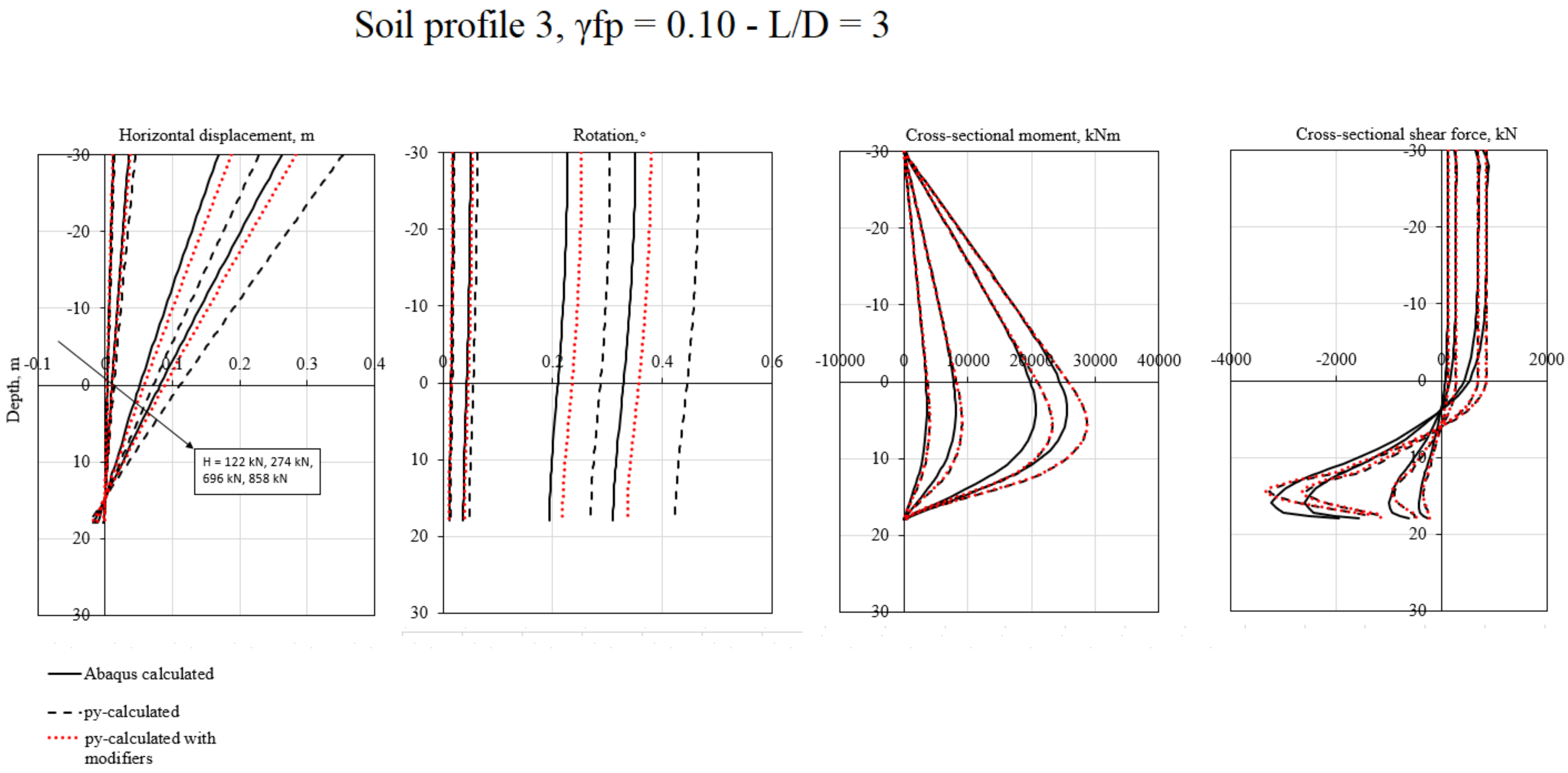

Figure B.10: Optimized pile response – Soil profile 3, L/D=3, γ_f^p=0.10.

Table B.10: Normalized error reduction, soil profile 3, γ_f^p=0.10, L/D=3.

Pile load [kN]		Error reduction [%]
122	Displacement	66.78
	Rotation	63.84
	Combined	**64.64**
274	Displacement	79.61
	Rotation	78.23
	Combined	**79.00**
696	Displacement	69.28
	Rotation	67.80
	Combined	**68.51**
858	Displacement	78.18
	Rotation	76.71
	Combined	**77.41**

B.3.3. L/D = 5. γ_f^p = 0.02

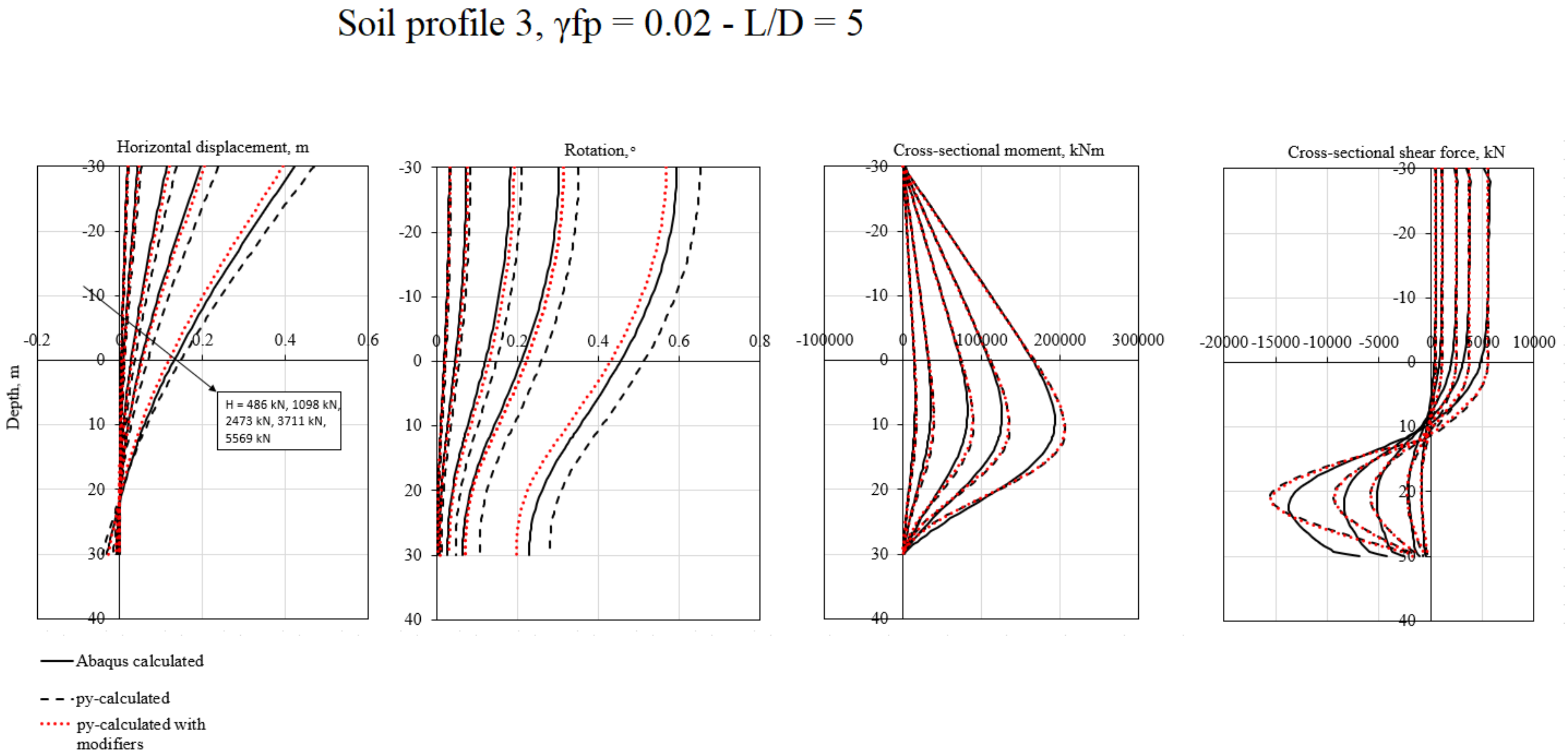

Figure B.11: Optimized pile response – Soil profile 3, L/D=5, γ_f^p=0.02.

Table B.11: Normalized error reduction, soil profile 3, γ_f^p=0.02, L/D=5.

Pile load [kN]		Error reduction [%]
486	Displacement	82.24
	Rotation	80.97
	Combined	**82.58**
1098	Displacement	81.49
	Rotation	78.61
	Combined	**80.74**
2473	Displacement	80.23
	Rotation	77.21
	Combined	**79.05**
3711	Displacement	85.21
	Rotation	84.16
	Combined	**85.00**
5569	Displacement	24.33
	Rotation	38.63
	Combined	**31.33**

B.3.4. L/D = 5. γ_f^p = 0.10

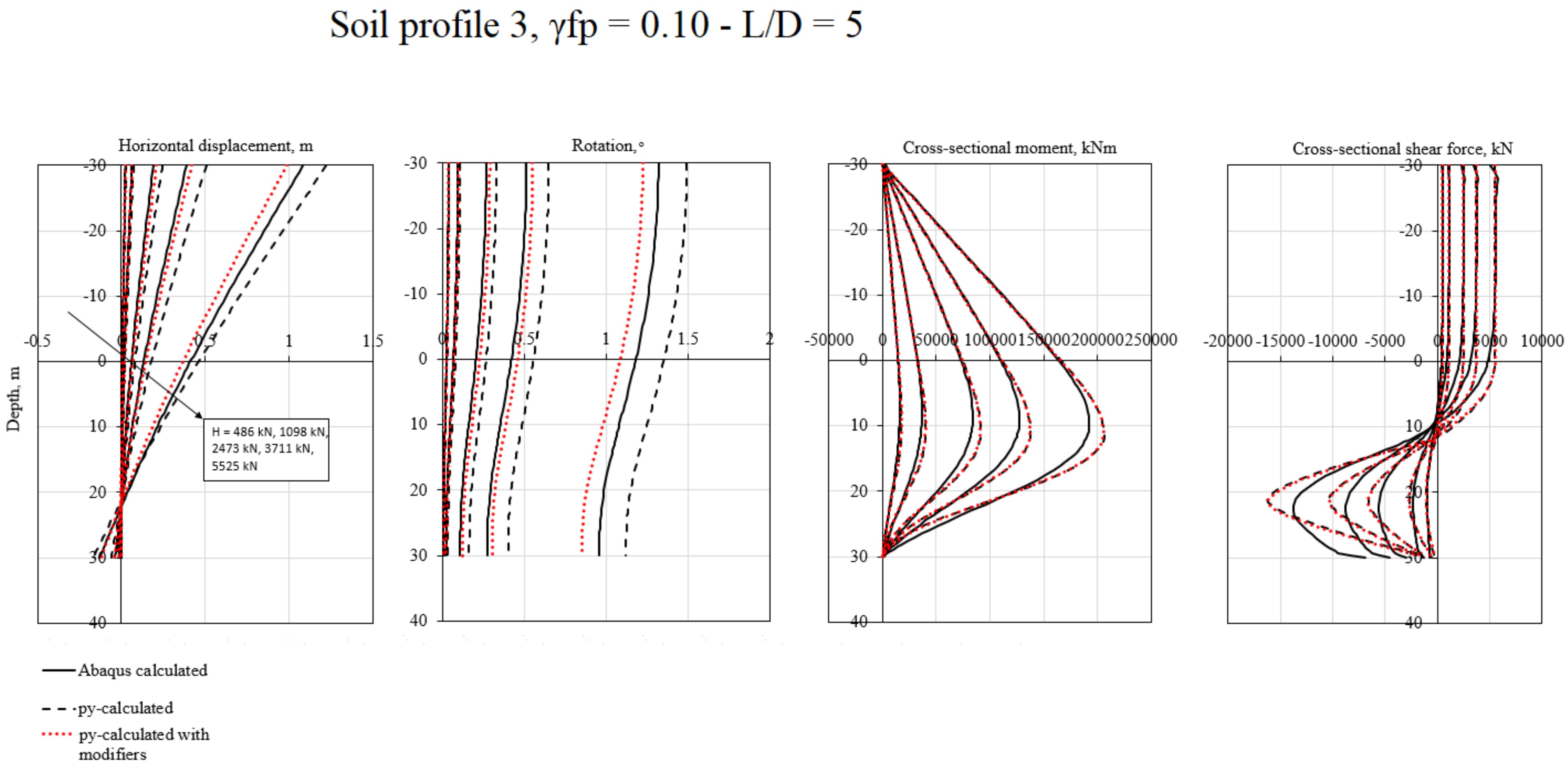

Figure B.12: Optimized pile response – Soil profile 3, L/D=5, γ_f^p=0.10.

Table B.12: Normalized error reduction, soil profile 3, γ_f^p=0.10, L/D=5.

Pile load [kN]		Error reduction [%]
486	Displacement	80.66
	Rotation	80.15
	Combined	**79.86**
1098	Displacement	89.28
	Rotation	84.24
	Combined	**87.12**
2473	Displacement	70.78
	Rotation	69.02
	Combined	**69.99**
3711	Displacement	76.73
	Rotation	75.77
	Combined	**76.30**
5525	Displacement	31.93
	Rotation	38.60
	Combined	**35.15**

Appendix B.4. Soil profile 4

B.4.1. L/D = 3. γ_f^p = 0.02

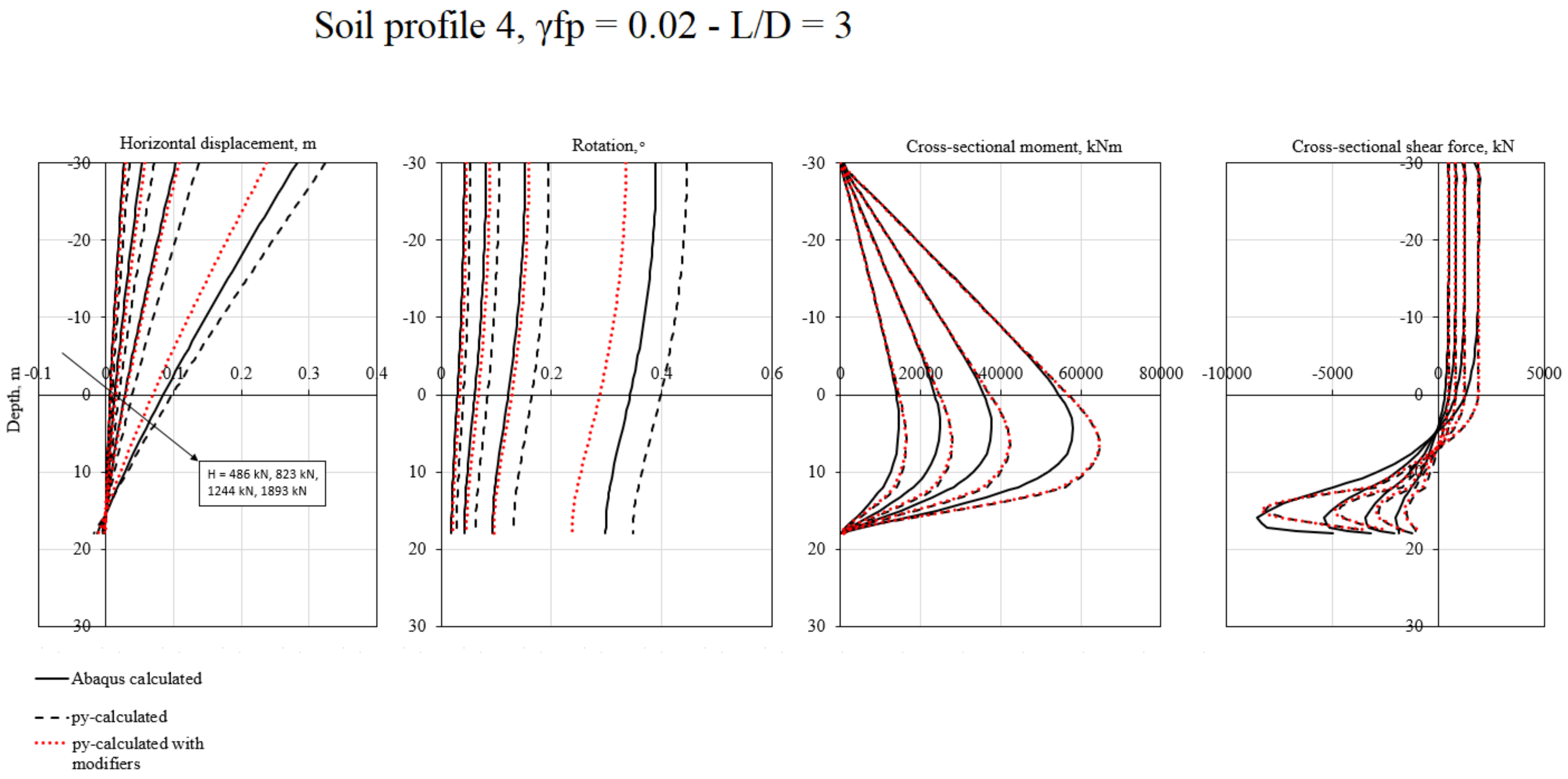

Figure B.13: Optimized pile response – Soil profile 4, L/D=3, γ_f^p=0.02.

Table B.13: Normalized error reduction, soil profile 4, γ_f^p=0.02, L/D=3.

Pile load [kN]		Error reduction [%]
486	Displacement	70.56
	Rotation	69.64
	Combined	**70.36**
823	Displacement	77.27
	Rotation	76.53
	Combined	**77.12**
1244	Displacement	90.69
	Rotation	89.46
	Combined	**90.26**
1893	Displacement	-38.68
	Rotation	-10.45
	Combined	**-23.30**

B.4.2. L/D = 3. γ_f^p = 0.10

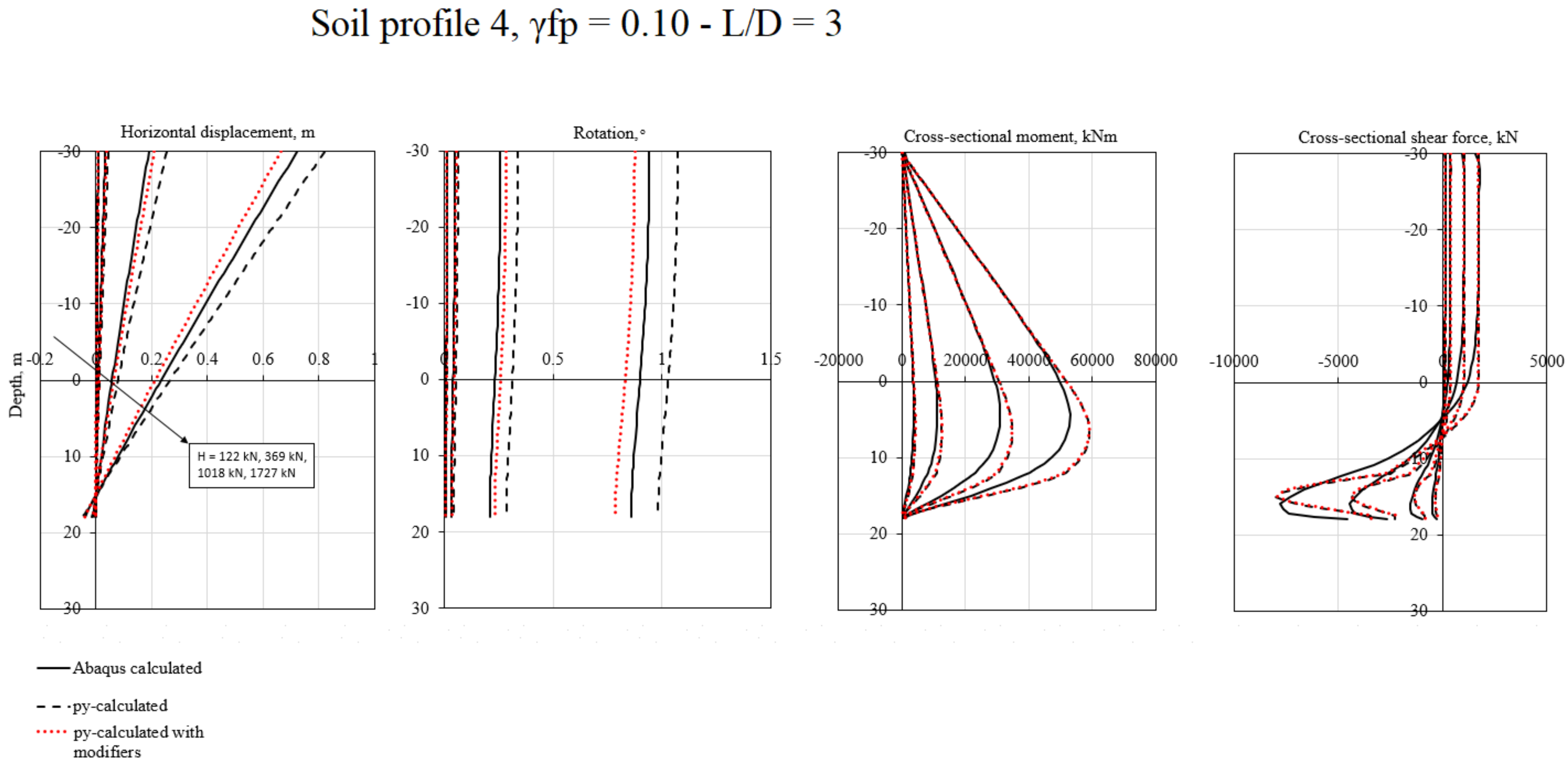

Figure B.14: Optimized pile response – Soil profile 4, L/D=3, γ_f^p=0.10.

Table B.14: Normalized error reduction, soil profile 4, γ_f^p=0.10, L/D=3.

Pile load [kN]		Error reduction [%]
122	Displacement	84.45
	Rotation	69.29
	Combined	**77.02**
369	Displacement	73.50
	Rotation	70.71
	Combined	**72.23**
1018	Displacement	73.65
	Rotation	69.57
	Combined	**71.51**
1727	Displacement	-1.48
	Rotation	44.13
	Combined	**24.40**

B.4.3. L/D = 5. γ_f^p = 0.02

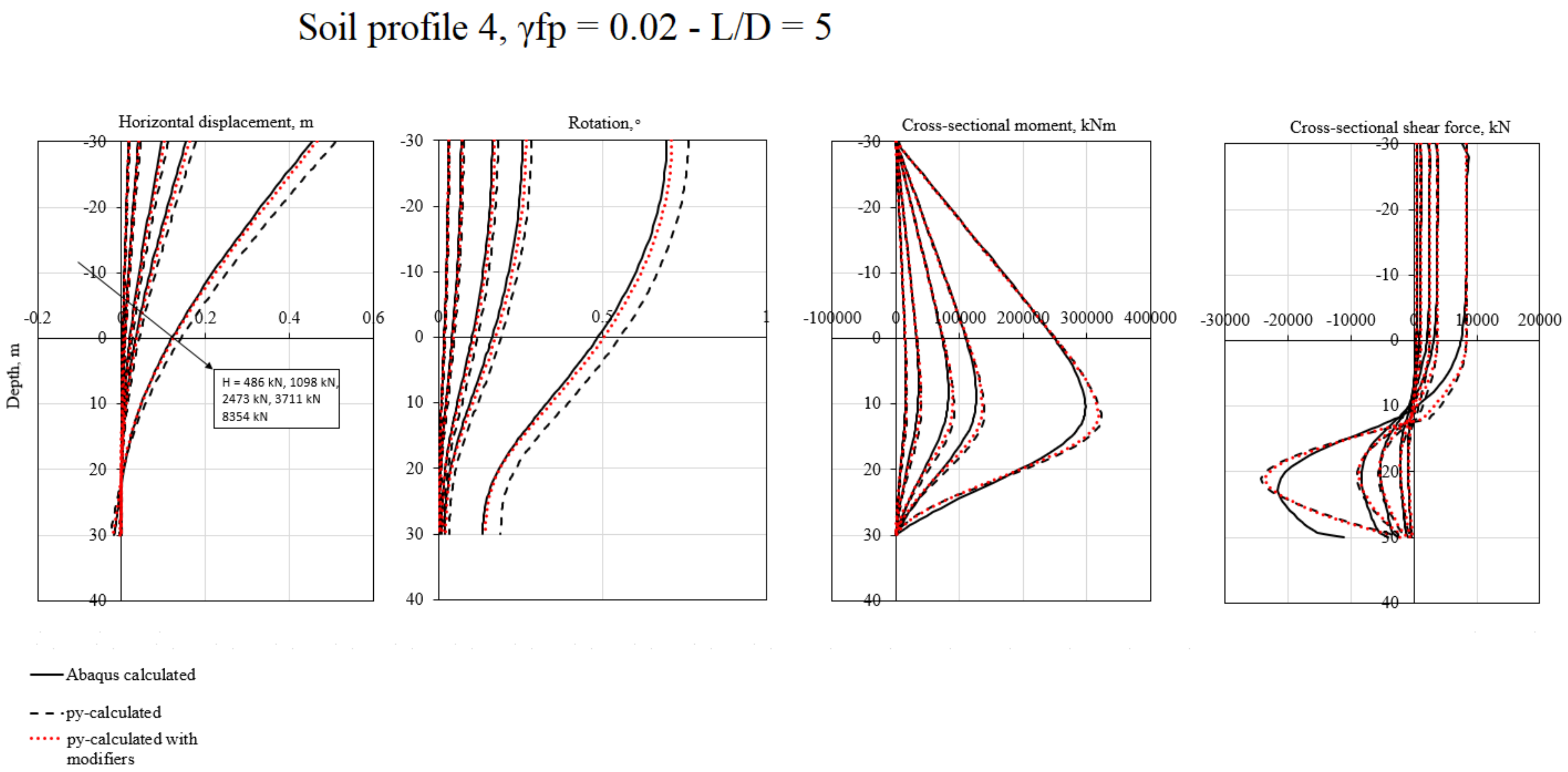

Figure B.15: Optimized pile response – Soil profile 4, L/D=5, γ_f^p=0.02.

Table B.15: Normalized error reduction, soil profile 4, γ_f^p=0.02, L/D=5.

Pile load [kN]		Error reduction [%]
486	Displacement	84.09
	Rotation	87.55
	Combined	**89.28**
1098	Displacement	82.24
	Rotation	86.21
	Combined	**87.27**
2473	Displacement	80.06
	Rotation	80.10
	Combined	**81.66**
3711	Displacement	77.16
	Rotation	75.51
	Combined	**77.19**
8354	Displacement	73.97
	Rotation	85.79
	Combined	**81.43**

B.4.4. L/D = 5. γ_f^p = 0.10

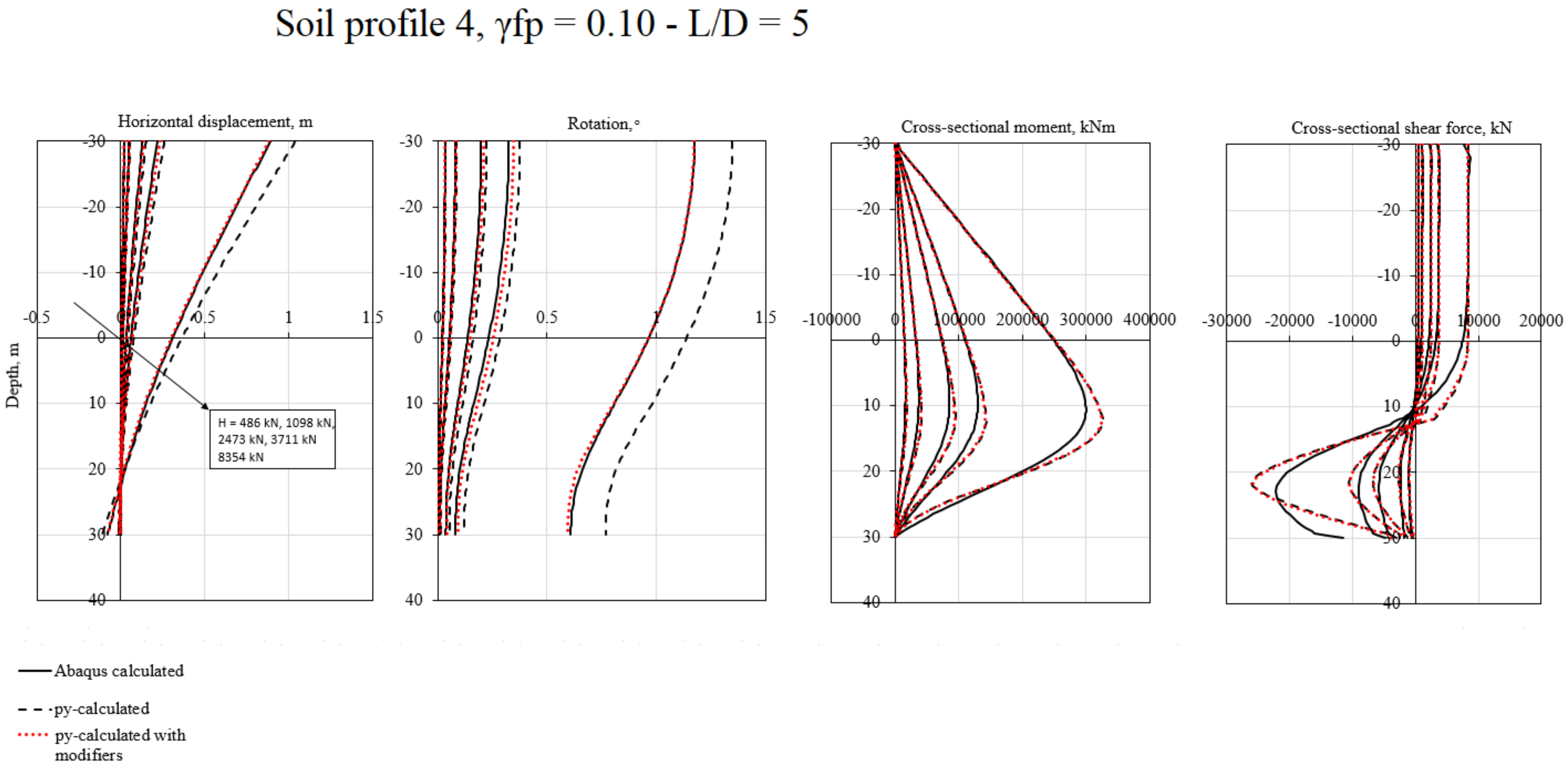

Figure B.16: Optimized pile response – Soil profile 4, L/D=5, γ_f^p=0.10.

Table B.16: Normalized error reduction, soil profile 4, γ_f^p=0.10, L/D=5.

Pile load [kN]		Error reduction [%]
486	Displacement	82.65
	Rotation	83.91
	Combined	**85.14**
1098	Displacement	74.75
	Rotation	71.38
	Combined	**72.18**
2473	Displacement	76.71
	Rotation	72.33
	Combined	**75.02**
3711	Displacement	70.23
	Rotation	67.02
	Combined	**68.88**
8354	Displacement	65.26
	Rotation	93.07
	Combined	**79.77**

Appendix C

Stiffness spring modifiers

Appendix C.1. Normally consolidated clay

Table C.1.1. NC-Clay. L/D=3.

γ_f^p	Soil profile 1	Soil profile 2
2 %	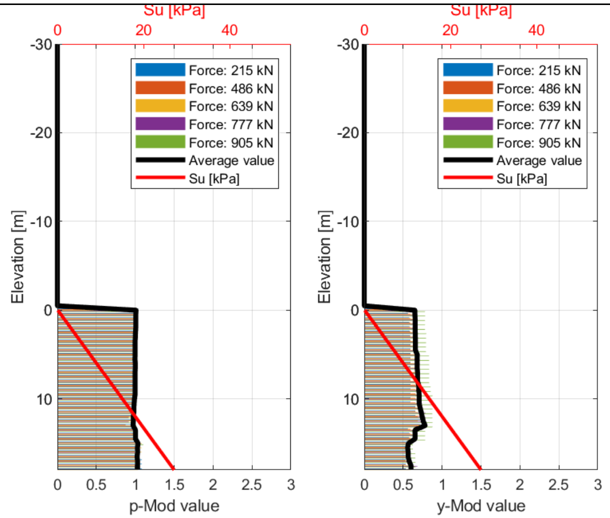	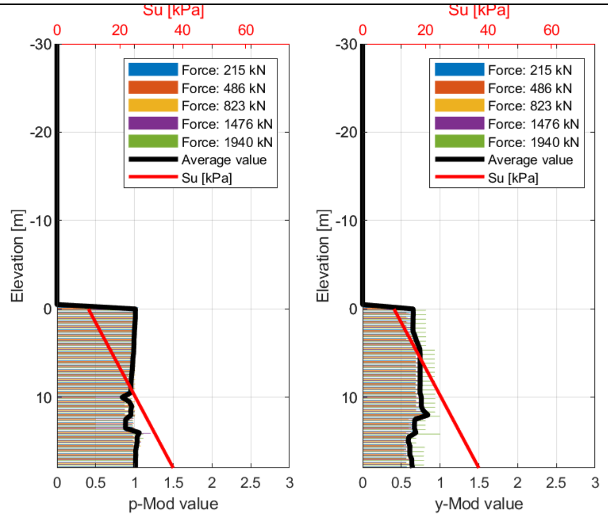
10 %	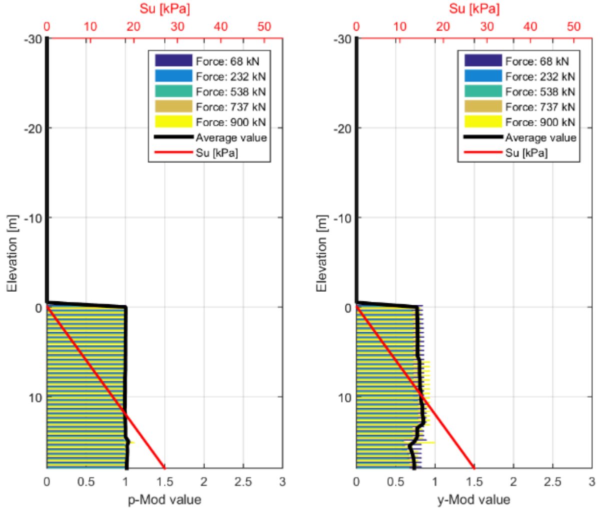	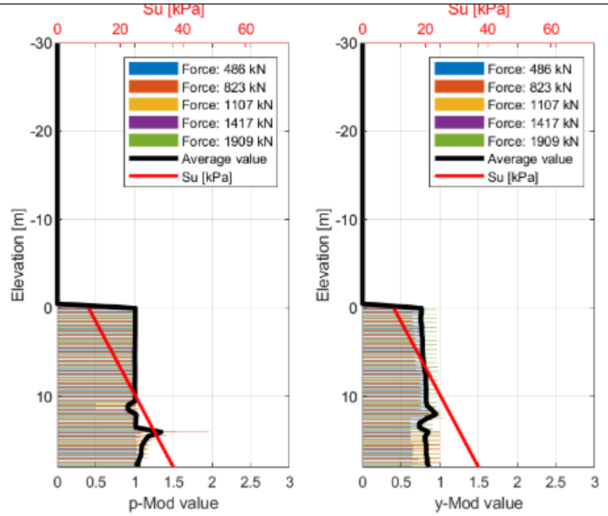

Table C.1.2. NC-Clay. L/D=5.

γ_f^p	Soil profile 1	Soil profile 2
2 %	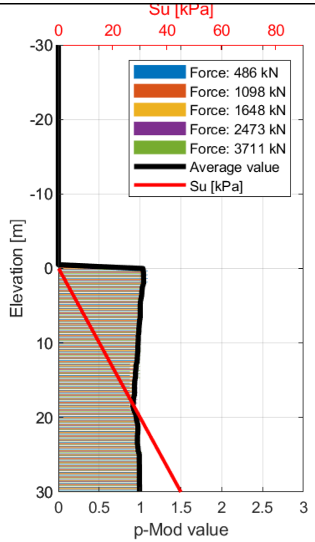 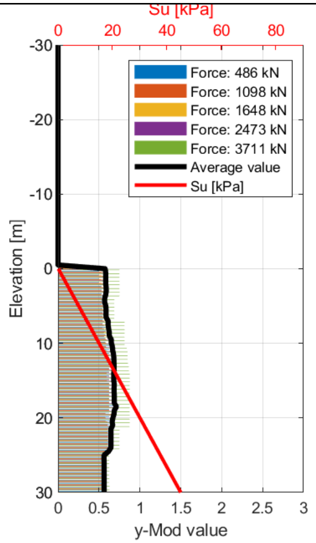	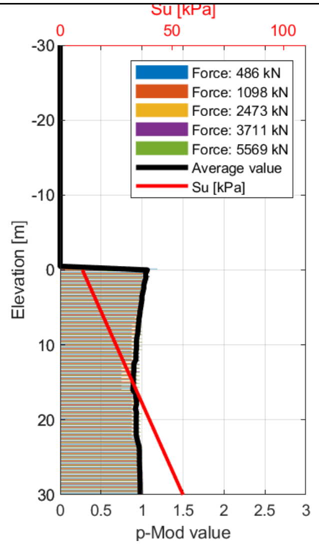 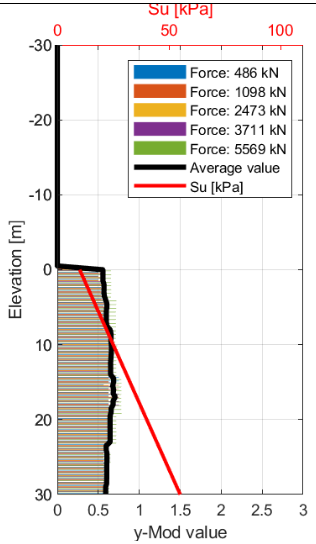
10 %	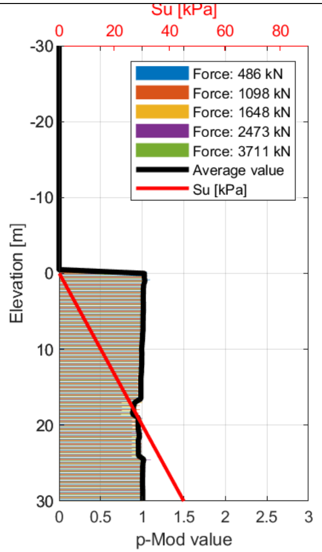 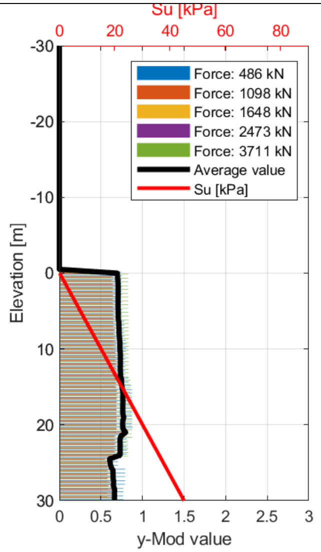	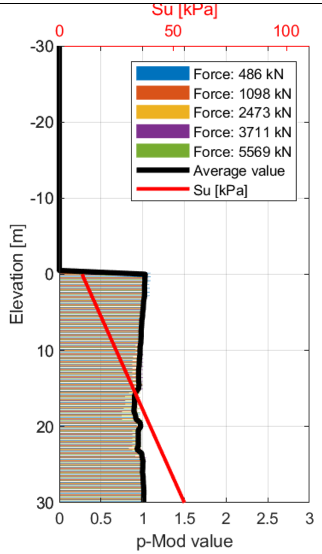 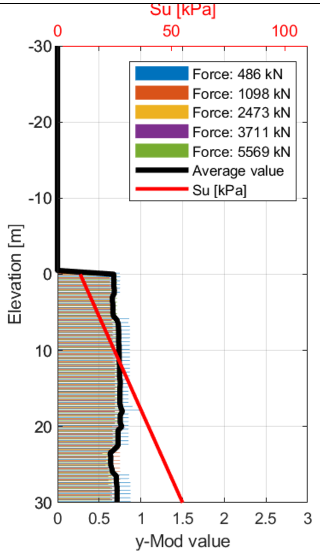

Table C.2.1. Layered soil profile. L/D=3.

γ_f^p	Soil profile 3	Soil profile 4
2 %	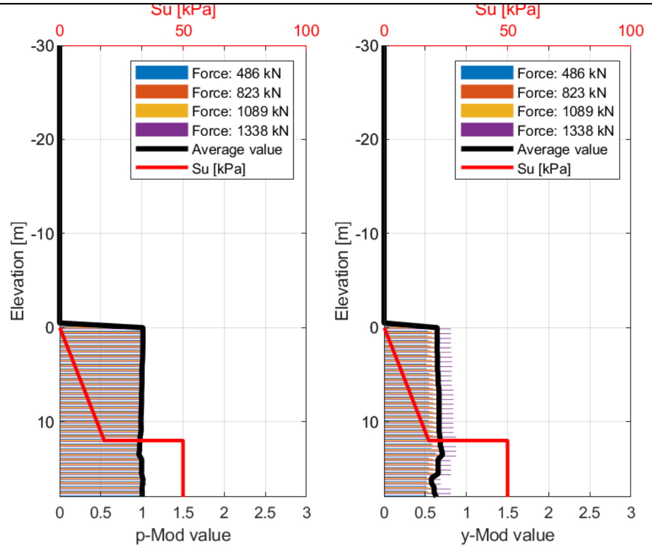	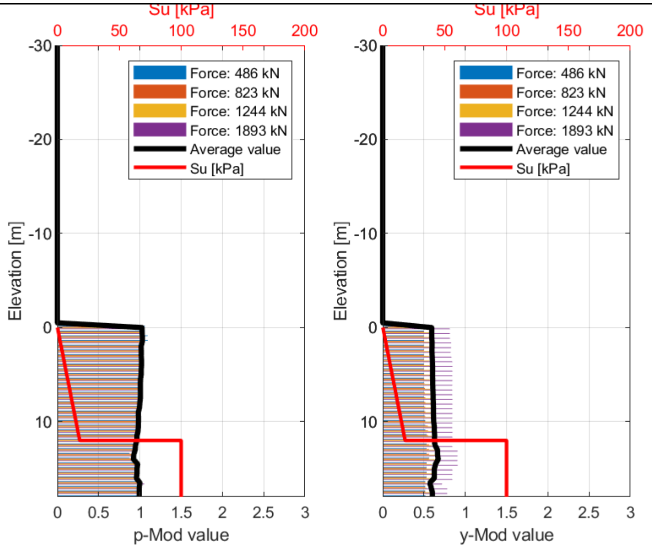
10 %	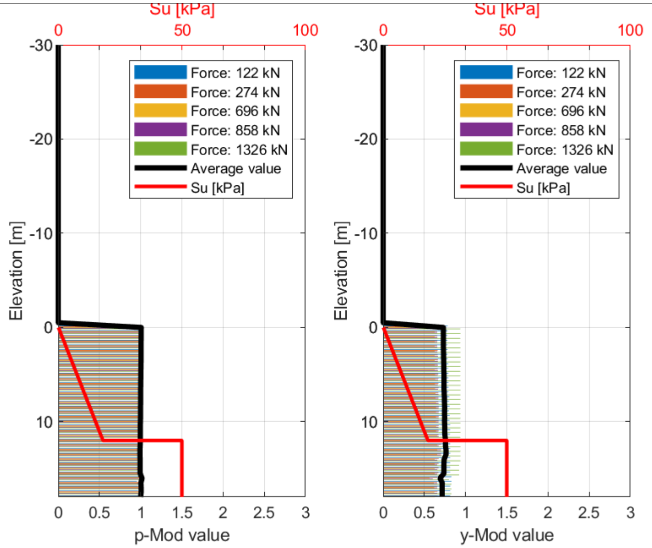	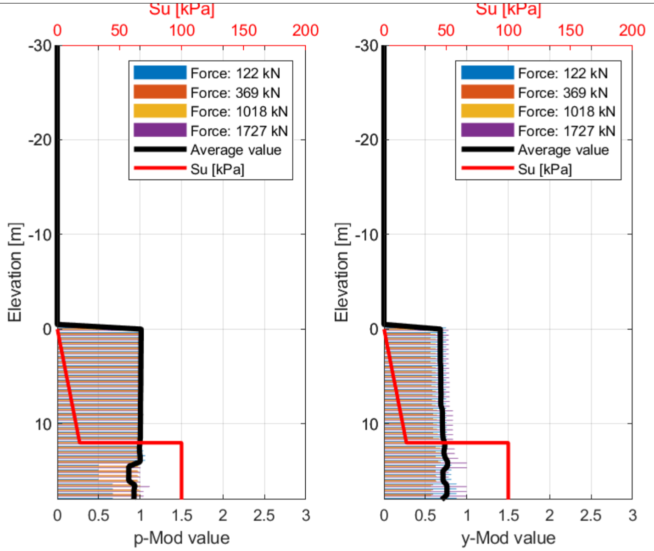

Table C.2.2. Layered soil profile. L/D=5.

γ_f^p	Soil profile 3	Soil profile 4
2 %	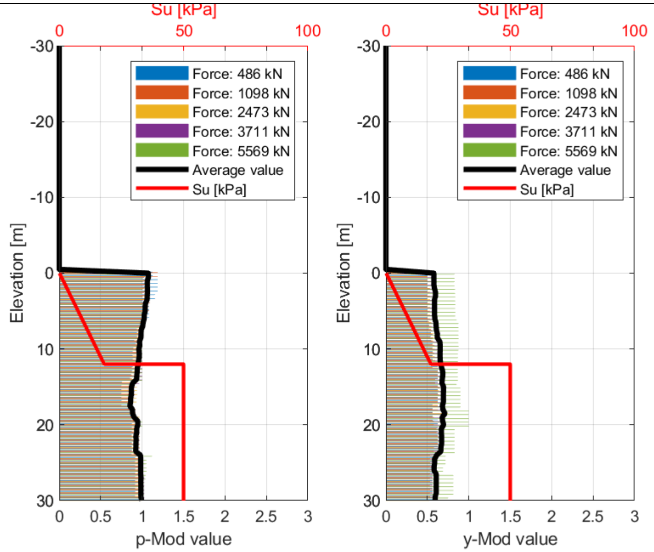	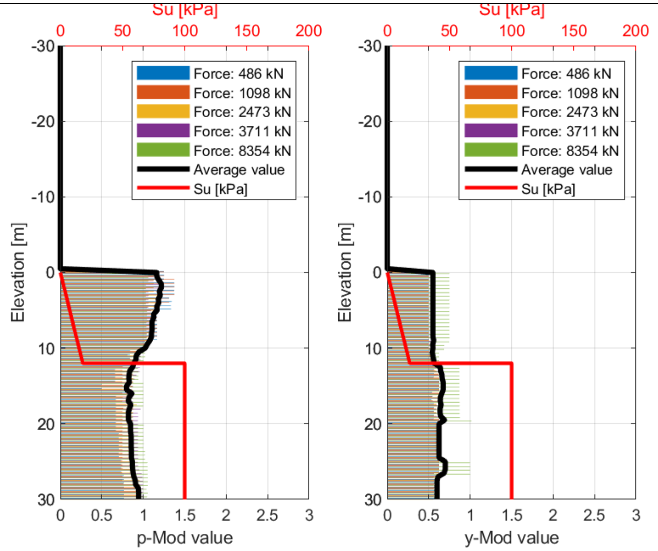
10 %